Title

Ca Isotopes in Igneous and High-Temperature Metamorphic Systems and the Hydrothermal Chemistry of Paleoseawater

Author

Antonelli, Michael A

Publication Date

2018

Ca Isotopes in Igneous and High-Temperature Metamorphic Systems and the Hydrothermal Chemistry of Paleoseawater

By

Michael A. Antonelli

A dissertation submitted in partial satisfaction of the

requirements for the degree of

Doctor of Philosophy

in

Earth and Planetary Science

in the

Graduate Division

of the

University of California, Berkeley

Committee in charge:

Professor Donald J. DePaolo, Chair
Professor David L. Shuster
Professor Todd E. Dawson

Fall 2018

Ca Isotopes in Igneous and High-Temperature Metamorphic Systems and the Hydrothermal Chemistry of Paleoseawater

Michael A. Antonelli

Abstract

Ca Isotopes in Igneous and High-Temperature Metamorphic Systems and the Hydrothermal Chemistry of Paleoseawater

by

Michael A. Antonelli

Doctor of Philosophy in Earth and Planetary Science

University of California, Berkeley

Professor Donald J. DePaolo, Chair

In the last two decades it has been increasingly recognized that Ca isotope fractionation at high-temperatures can greatly exceed fractionation at surface conditions. These effects have been used to trace recycling of crustal materials into the mantle, to estimate equilibration temperatures in mantle rocks, and to understand kinetic isotope fractionation during diffusion in experimental melts. However, little is known about the competition between kinetic and equilibrium Ca isotope effects in natural samples, which suggests that the use of stable Ca isotope variations as a proxy for carbonate recycling (or for mantle temperature) is significantly underdetermined.

The Ca isotope evolution of continental crust, which is currently understudied, is intimately linked to the geochemical evolution of Earth's mantle, oceans, and atmosphere. As such, this dissertation focuses dominantly on understanding radiogenic, kinetic, and equilibrium Ca isotope variations in igneous and metamorphic rocks from the continental crust, but also includes radiogenic Sr isotope models of hydrothermal circulation at mid-ocean ridges, which are critical to understanding continental weathering rates and the geochemical evolution of seawater over time.

Chapter 2 explores the potential feed-back between the chemical and isotopic composition of paleoseawater and high-temperature hydrothermal fluids, which has been implied by Sr-isotope measurements in hydrothermal minerals over time (Antonelli et al., 2017). Chapter 3 presents results from radiogenic Ca isotope measurements in lower-crustal rocks and minerals, confirming that K is effectively lost from the lower crust during high-T metamorphism (Antonelli et al., 2018). Chapter 4 focuses on stable Ca isotope measurements in lower-crustal rocks and minerals, demonstrating that kinetic Ca effects are abundant in nature, both at the whole-rock and inter-mineral scales, and that they can be used to understand paragenesis and Ca diffusion in lower-crustal rocks (Antonelli et al., 2019b). Chapter 5 presents stable Ca isotope results from volcanic and sub-volcanic rocks and minerals, which imply that Ca isotopes can be used to estimate crystal growth-rates in igneous crystals (*e.g.* phenocrysts, comb-layers, and orbicules) and that associated volcanic eruption/recharge events are generally short-lived (Antonelli et al., 2019a).

To my mother and grandparents, Paule, Simone, and Maurice Malartre, and to my father, Prof. Peter L. Antonelli, who first sparked my passion for rocks and minerals.

Table of Contents

List of Figures

Chapter 2

Chapter 3

Chapter 4

Chapter 5

List of Tables

Chapter 3

Chapter 4

Chapter 5

Acknowledgements

Along with my parents and grandparents, I would also like to dedicate this work to my partner Erin Nordquist, my niece and nephew Paul and Rebecca, my brothers Mark and David (and their mother Marylu), my uncles Olivier and Pierre Malartre, my great-uncles Jacky and Bernard Leclert, my cousins, Julien, Sophie, Virginie, Nicolas, Clara, and Arthur, and my friends Jonny Maynard & Adam Seniuk. All of you have been a great source of support in spite of the distance.

I would first like to thank my advisor Donald J. DePaolo for sharing numerous lessons on how to best approach scientific problems and how to succeed in science. Don has given me both the freedom and the resources to follow my interests, along with first-hand examples of how to effectively give presentations, communicate results, and apply for funding. His mentorship has been invaluable. I would also like to thank my past advisors, Tom Chacko, Karlis Muehlenbachs, and especially James Farquhar, for sharing with me their combined isotopic and petrologic knowledge and for providing advice and moral support during tougher parts of the last decade.

A great deal of insight was gained by collaborating with various researchers, including Nick Pester, Shaun Brown, Tom Chacko, Ed Grew, Daniela Rubatto, Martin Schiller, Edwin Schauble, Tushar Mittal, Barbara Tripoli, Jim Watkins, and Anders McCarthy. Your help has been greatly appreciated! Tom Owens, Wenbo Yang, Sean Mulcahy, Nick Botto, Tim Teague, and especially Shaun Brown are also owed special thanks for their help trouble-shooting my analyses.

My geochemical colleagues/friends Daniel Eldridge, Stefan Peters, Noah Jemison, Vera Fernandes, Anirban Basu, Markus Bill, Brian Harms, Chris Yakymchuk, Nick Pester, Jesse Hahm, Drew Syverson, Thomas Kruijer, Mathieu Amor, Mathieu Touboul, Kathrin Schiller, Hannah Bourne, Chelsea Willett, Anna Clinger, Ming Tang, Elizabeth Niespolo, Courtney Sprain, Eric Sonnenthal, Isabel Fendley, Andrew Turner, Max Thiemens, Francois Tissot, Alex McCoy-West, and Mark Thiemens, amongst others, have also been a tremendous boon during my studies, thank you all! I would similarly like to acknowledge several current/past graduate students, including Mamun Miah, Francois Soubiran, Harry Lisabeth, Ben Fildier, Ben Thurnhoffer, Sevan Adourian, Stephen Breen, Jesse Day, Ahmed Alaoui, Robert Citron, Brent Trevisan, David Mangiante, Newton Nguyen, William Hawley, Ari Melinger Cohen, Nate Lindsey, Yuem Park, Kevin Miller, Robert Martin-Short, and Simen Linge Johnson for their friendship and coeval hardships. A special thanks is especially owed to my friends Tushar Mittal and Brenhin Keller, with whom discussions and collaborations have been particularly fruitful.

My gratitude is extended to Duane Froese, Karlis Muehlenbachs, Tom Chacko, Sarah Gleeson, Chris Herd, Kurt Konhauser, and Larry Heaman for helping to get me hooked on geochemistry in my undergraduate years, Alberto Reyes, Fabrice Calmels, and Britta Jensen for ill-advisedly taking a young version of myself out to the field, George Leitmann for his perspective and friendship during my years in Berkeley, and Todd Dawson & David Shuster for their isotopic knowledge, friendship, and advice.

Finally, I would like to thank Christina Tibbs, Roberto McCoy, Kuhuk Goyal, Remi Taranta, David Grigorian, Esteban Gonzalez, Harry Lisabeth, Jonny Maynard, Paul Antonelli, Nicolas Malartre, Edgar Silva, Dylan Ladd, and Joseph Lent (amongst many others), for their friendship and their dedication to our musical endeavors over the years, which tend to be the most effective recourse when isotopic mechanisms become incogitable.

Chapter 1

Introduction

The evolution of Earth's mantle, continents, atmosphere, and oceans are intimately linked to each other and cannot be studied in isolation. Built out of primitive solar system materials and containing large amounts of water, Earth is the only planet in our solar system with differentiated continental crust and active plate-tectonics. The unique geological evolution of our planet has led to formation of the Earth's oceans, atmosphere, and continents, and has also played a key role in the evolution of life, which (as far as we know) is a feature unique to the Earth. However, understanding the various processes which formed our planet is complicated by several factors, including the very large time scales involved.

Isotope geochemistry is the best way to understand the timing and nature of different events in Earth's deep geologic past. Geochemists generally combine measurements of radiogenic and stable isotopes, in order to constrain the timing and the nature of geologic events, respectively. Radiogenic isotopes, created through radioactive decay, are used to place absolute age constraints on events that occurred in the past, but are also used to trace mixing between different Earth-system reservoirs. This common application depends on the uneven distribution of parent isotopes in different reservoirs, and the consequent increase in daughter isotopes in those reservoirs over time. For example, Rb and K are concentrated in continental crust relative to the mantle, allowing for enrichments of ^{87}Sr (the product of ^{87}Rb decay) and ^{40}Ca (the product of ^{40}K decay) in the continents over geologic time.

On the other hand, separation (*aka* fractionation) of stable isotopes that are not the product of radioactive decay depends mainly on isotopic mass differences and Ca-O bond strengths. These stable isotope variations are generally measured in order to quantify physical parameters for past chemical reactions (*e.g.* temperature-pressure conditions and reaction rates/extents). Calcium isotopes are especially useful for constraining past events in geological materials because of the large number of stable isotopes (six total: ^{40}Ca, ^{42}Ca, ^{43}Ca, ^{44}Ca, ^{46}Ca, and ^{48}Ca), large relative mass differences (~10% for ^{44}Ca *vs.* ^{40}Ca), single redox state at mantle, crustal, and surface conditions (Ca^{2+}), and the partially radiogenic origin of ^{40}Ca. Sr isotopes (3 total: ^{86}Sr, ^{87}Sr, and ^{88}Sr) have much smaller relative mass differences, and are thus more useful for radiometric dating and/or for tracing the relative contributions of different Earth-system reservoirs into mixed pools (*e.g.* seawater) over time.

Chapter 2 of this dissertation presents a study interpreting seawater ^{87}Sr/^{86}Sr ratios over the last ~500 million years. Previous work investigating Sr-isotope ratios in paleoseawater generally conclude that periods of high continental weathering led to higher seawater ^{87}Sr/^{86}Sr while periods of high mid-ocean ridge (MOR) spreading (greater MOR hydrothermal fluxes) led to lower seawater ^{87}Sr/^{86}Sr. These records have thus been used to reconstruct Earth's atmospheric CO_2 levels, which can be positively correlated to continental weathering rates, over geologic time. Along with Sr-isotope variations in paleoseawater, various lines of evidence suggest that major element concentrations (*e.g.* Ca, Mg, and SO_4) have also cyclically varied over the last 500 million years. However, previous models using seawater ^{87}Sr/^{86}Sr for reconstructions of global weathering rates (and atmospheric CO_2) have not taken into account the potential effects of seawater ^{87}Sr/^{87}Sr and major element variations on MOR hydrothermal fluid compositions over time, which are generally assumed to have constant (modern) ^{87}Sr/^{86}Sr. Developing a charge-balance model calibrated to modern seawater and hydrothermal fluids, I use the paleoseawater ^{87}Sr/^{86}Sr and major element (Mg, Ca, SO_4, and Sr) records in order to predict hydrothermal fluid Sr-isotope and chemical compositions over time. I find that this model successfully predicts high ^{87}Sr/^{86}Sr in Cretaceous and Permian hydrothermal fluids, as implied by studies of ophiolite epidosites. This model suggests that the composition of MOR hydrothermal fluids varies cyclically with ocean chemistry, and serves as a small negative feedback on mantle Ca and Sr inputs when seawater has high Ca/SO_4 and low Mg. These results imply that MOR hydrothermal inputs are not constant through time and that seawater composition itself needs to be taken into account when attempting to model the seawater ^{87}Sr/^{86}Sr record. The model also suggests that lower amounts of continental weathering or greater amounts of low-temperature hydrothermal circulation than currently predicted are required to explain seawater ^{87}Sr/^{86}Sr during the Cretaceous. This study was published in *Proceedings of the National Academy of Sciences (PNAS)* (Antonelli et al., 2017).

Chapter 3 presents results from an investigation into the radiogenic Ca isotope composition of lower continental crust. Although it is generally accepted that K is partitioned into continents (*vs.* mantle) during magmatic differentiation, it is uncertain how K behaves once inside the continental crust. Understanding the behavior and distribution of K in the continental crust is important because K was the most abundant source of radioactive heat on the early Earth. The process of continental stabilization (*aka* cratonization) requires coupling between the lower crust and sub-continental lithospheric mantle (SCLM), which necessitates radiogenic heat depletion in the lower crust. Several studies have suggested that Rb and U are lost from the lower crust and concentrated in the upper crust during lower crustal metamorphism, implying that K behaves in a similar fashion. However, a direct measurement of K-loss in lower crustal rocks has remained elusive. In this chapter, I show that low-K minerals in the lower crust (such as garnet) can contain large radiogenic ^{40}Ca enrichments. These radiogenic enrichments can be used to constrain K/Ca in metamorphic protolith rocks, which are much higher than measured in the rocks today. This directly confirms for the first time that K is efficiently extracted from the lower crust during high-T metamorphism. I also present results from a non-modal batch melting model that suggests 20-30% partial melting generally explains the K/Ca decreases in lower crustal granulites. This study has been re-submitted with revisions to *Geochemical Perspectives Letters* (Antonelli et al., 2018).

Chapter 4 presents the results of stable Ca isotope measurements (including ^{48}Ca) in a large number of high-T metamorphic rocks and minerals. It also contains density-functional theory (DFT) models for silicate minerals, and numerical diffusion models for Ca isotope fractionation in whole-rocks during lower crustal metamorphism. At upper granulite-facies conditions (~900°C) the predicted equilibrium Ca isotope fractionations do not exceed ~0.8‰, yet we find a range 5 times larger than this in metamorphic whole-rock samples, and ~10 times larger in mineral separates. This suggests that large kinetic Ca isotope fractionations occur during lower-crustal metamorphism. I introduce and successfully test a new proxy, Δ^{48}Ca’, which quantifies deviations from equilibrium mass-dependent behavior in triple-isotope space, and confirm that the large observed Ca isotope effects in both whole-rocks and minerals are kinetic in origin. Given that the effects are kinetic, I use available thermochronological constraints for the Napier Complex and numerical diffusion modeling to constrain Ca diffusivities and isotopic fractionation factors during long-lived lower-crustal metamorphism, and find that the isotopic data are generally consistent with previous estimates for Ca transport via grain-boundary and volume-diffusion in metamorphic rocks (10^{-10} – 10^{-7} m^2/yr). The data also suggest that inter-mineral Ca isotope disequilibria are related to pressure-temperature-time (P-T-t) evolution in different sample localities. I find that retrograde garnet formation, which occurs during isobaric cooling from ultra-high temperatures, is correlated with negative disequilibrium garnet-mineral Ca isotope fractionations, whereas prograde (clockwise P-T-t) and magmatic garnet formation appear to occur closer to equilibrium. The inter-mineral Ca isotopic disequilibria are observed to deviate further from predicted equilibrium values with increasing whole-rock and garnet Mg#, plagioclase anorthite contents, and orthopyroxene Ca/Mg, all of which generally increase with temperature. Taken at face value, this suggests that the activation of various diffusion pathways, which also depends significantly on temperature, is responsible for the large Ca isotope effects observed in lower-crustal rocks and minerals.

Although the necessary information required to use Ca isotopes as a geothermometer across a wide-range of sample-types and mineralogies are provided in this chapter, I urge future researchers to carefully consider whether or not their samples are actually at equilibrium before using Ca isotopes as a temperature proxy. Likewise, the prevalence of kinetic Ca isotope effects in natural samples suggests that Ca isotopes should not be used to trace carbonate subduction into the mantle, unless first taking into account (i) the large number of kinetic processes that occur during primary carbonate precipitation from seawater, (ii) the relative amounts of recycled sedimentary *vs.* high-T vein carbonates that are subducted, and (iii) the kinetic/unmixing effects that undoubtedly occur during subduction, dehydration, partial-melting, transport, and crystallization. This study has been submitted to *Earth and Planetary Science Letters* (Antonelli et al., 2019b).

Chapter 5 presents stable Ca isotope measurements in volcanic and sub-volcanic minerals and whole rocks. I first analyze rapidly-cooled experimental tonalites, confirming that phenocryst growth can lead to large disequilibrium Ca isotopic fractionations (> 2‰) in magmatic systems. I also analyze Ca isotope variations in a large number of natural igneous samples from several different localities. These include samples of volcanic phenocryst minerals and associated matrix, micro-drilled transects across two dioritic orbicules, and many plagioclase separates from comb-layers, orbicules, and related sub-volcanic rocks in Northern California. Based on the model of Watson and Muller (2009), I find that measured Δ^{44}Ca values are consistent with rapid disequilibrium plagioclase growth (at rates > ~6-15 cm/yr) during orbicule- and comb-layer formation (within sub-volcanic conduits), and during phenocryst formation prior to the 1915 Mt. Lassen dacite eruption. Pairing these growth rate estimates with maximum crystal sizes suggests that individual orbicule- and comb-layers (~1 cm) are formed in just one or two months, which corroborates previous estimates for rapid crystal growth, based on plagioclase textures.

Pairing the isotopic measurements with crystal-size distribution (CSD) analyses in the volcanic samples, I find that plagioclase phenocryst separates in Mt. Lassen Dacite and Deadman's dome (which yield resolvable $\Delta^{44}Ca_{\text{plagioclase-matrix}}$), indicate crystallization time-scales of ~5 and ~30 days, respectively. Although there are some uncertainties regarding the relationship between various phenocryst populations (measured by CSD) within a sample and the analyzed mineral separates, the results serve as additional support for recent volcanic models where crystal-rich magmas are stored for extended periods of time at relatively low temperatures (*aka* 'cold-storage') and ephemerally re-activated by injection of new magma into the sub-volcanic systems. Finally, I show that, all else being equal, increasing water contents in rapidly-cooled tonalites lead to decreasing $\Delta^{44}Ca_{plag\text{-}glass}$ fractionations, as a probable result of increasing Ca diffusivities. Thus, the youngest phenocryst populations in a volcanic sample (which form rapidly, after magmatic eruption/degassing) are most likely to contain the largest disequilibrium Ca isotope effects. Although further experimental confirmation is required, these results suggest that volatiles may not greatly affect the fractionation factors (*e.g.* D_{44}/D_{40}) for Ca isotope diffusion in magmas, which is in accordance with recent observations for Li isotope diffusion in hydrous silicate liquids. This study is in preparation for *Earth and Planetary Science Letters* (Antonelli et al., 2019a).

Chapter 2

Effect of paleo-seawater composition on hydrothermal reactions in mid-ocean ridges

2.1. Overview

Variations in the Mg, Ca, Sr, and SO_4 concentrations of paleoseawater can affect the chemical exchange between seawater and oceanic basalt in hydrothermal systems at mid-ocean ridges (MOR). We present a model for evaluating the nature and magnitude of these previously unappreciated effects, using available estimates of paleoseawater composition over Phanerozoic time as inputs and $^{87}Sr/^{86}Sr$ of ophiolite epidosites and epidote-quartz veins as constraints. The results suggest that modern hydrothermal fluids are not typical due to low Ca and Sr relative to Mg and SO_4 in modern seawater. At other times during the last 500 Myr, particularly during the Cretaceous and Ordovician, hydrothermal fluids had more seawater-derived Sr and Ca, a prediction that is supported by Sr isotope data. The predicted $^{87}Sr/^{86}Sr$ of vent fluids varies cyclically in concert with ocean chemistry, with some values much higher than the modern value of ~0.7037. The seawater chemistry effects can be expressed in terms of the transfer efficiency of basaltic Ca and Sr to seawater in hydrothermal systems, which varies by a factor of ~1.6 over the Phanerozoic, with minima when seawater Mg and SO_4 are low. This effect provides a modest negative feedback on seawater composition and $^{87}Sr/^{86}Sr$ changes. For the mid-Cretaceous, the low $^{87}Sr/^{86}Sr$ of seawater requires either exceptionally large amounts of low-temperature exchange with oceanic crust or that the weathering flux of continentally-derived Sr was especially small. The model also has implications for MOR hydrothermal systems in the Precambrian, when low seawater SO_4 could help explain low seawater $^{87}Sr/^{86}Sr$.

2.2. Introduction

Mid-ocean ridge (MOR) hydrothermal circulation, fuelled by persistent heat from shallow magma reservoirs, is a key component in the long-term regulation of global climate and ocean chemistry (Berner and Kothavala, 2001). Hydrothermal fluids that emerge from these systems, at temperatures up to ~400 ˚C, are chemically distinct from seawater due to reactions with newly forming oceanic crust. Relative to seawater, fluids emanating from modern MOR hydrothermal systems are enriched in Ca and transition metals, have lower pH and Eh, and have little to no Mg and SO_4 (Elderfield and Schultz, 1996; German and Seyfried, 2014; Staudigel, 2013; Von Damm et al., 1985).

Hydrothermal circulation at MOR is dominated by two important chemical reactions: the removal of seawater SO_4 through mineral precipitation with seawater Ca, and the removal of seawater Mg through precipitation of hydroxy-silicate minerals (German and Seyfried, 2014; Seyfried and

Bischoff, 1981, 1979). Seawater SO_4 is primarily lost through the formation of anhydrite ($CaSO_4$) early during hydrothermal circulation, as anhydrite precipitation occurs by simply heating seawater >130 °C (Bischoff and Seyfried, 1978). There can also be minor losses of SO_4 through thermochemical sulfate reduction (Ono et al., 2007; Peters et al., 2010) and bacterial processes.

Seawater Mg is lost from hydrothermal fluids at both low and high temperatures, by exchange of seawater Mg for basaltic Ca through the transformation of primary igneous minerals to alteration phases such as montmorillonite and chlorite (German and Seyfried, 2014). This Mg:Ca exchange process is accompanied by the generation of acidity and the release of basaltic Ca (and Sr) into the hydrothermal fluids (Berndt et al., 1988; Seyfried and Bischoff, 1981).

The overall chemical and isotopic exchange in modern MOR hydrothermal systems is partly determined by the peculiarities of modern seawater, which has relatively high dissolved [Mg] (53 mmol/kg) and [SO_4] (28 mmol/kg) (brackets indicate concentration), and relatively low dissolved [Ca] (10 mmol/kg) and [Sr] (91 µmol/kg). At various times in the geologic past these proportions (53:10:28:91) were much different (Fig. 2.1). The origins of these variations are not well understood (Lowenstein et al., 2013), but their existence has substantial consequences for the evolution of fluids during hydrothermal circulation.

2.3. Paleoseawater chemical variations

The record of seawater [Mg], [Ca], and [SO_4] through the Phanerozoic is largely derived from fluid-inclusion measurements in marine halite (Horita et al., 2002; Lowenstein et al., 2013, 2003) (Fig. 2.1), but is corroborated in general terms by other observations. During the Cretaceous and Devonian periods, seawater apparently had substantially lower [Mg] and [SO_4], and higher [Ca] relative to modern seawater. In the late Permian and Cambrian, seawater compositions were more similar to modern. Support for such historical variability in seawater composition comes from: i) the alternating dominance of aragonite *vs.* calcite as the primary biogenic carbonate mineral (Lowenstein et al., 2013), ii) Mg/Ca ratios in hydrothermal veins (Rausch et al., 2013), iii) δ^{44}Ca variations in evaporite deposits (Blättler and Higgins, 2014), iv) sulfur isotope models (Algeo et al., 2015; Bernasconi et al., 2017), and v) Mg/Ca ratios in calcifying marine organisms (Dickson, 2002).

Estimates for paleoseawater [Sr] are not as well developed and not all consistent. Most evidence from altered ophiolite assemblages and the fossil record indicate elevated [Sr] in seawater during times of elevated [Ca] (Coogan, 2009; Gothmann et al., 2015; Steuber and Veizer, 2002), with fairly small overall changes to the seawater Sr/Ca ratio. However, lower than modern Sr/Ca ratios for the period between 30-180 Ma have also been proposed based on analyses of carbonate veins in altered oceanic crust (Coggon et al., 2010). For the purpose of evaluating our model we have constructed a notional Phanerozoic seawater [Sr] curve (Fig. 2.1) based on combining the Sr/Ca record from invertebrates (Steuber and Veizer, 2002) and benthic foraminifera (Lear et al., 2003) with the record for seawater [Ca] (adopting the assumptions of previous authors), but compare this with results using constant modern seawater [Sr] which approximates the results of lower Sr/Ca estimates (Coggon et al., 2010).

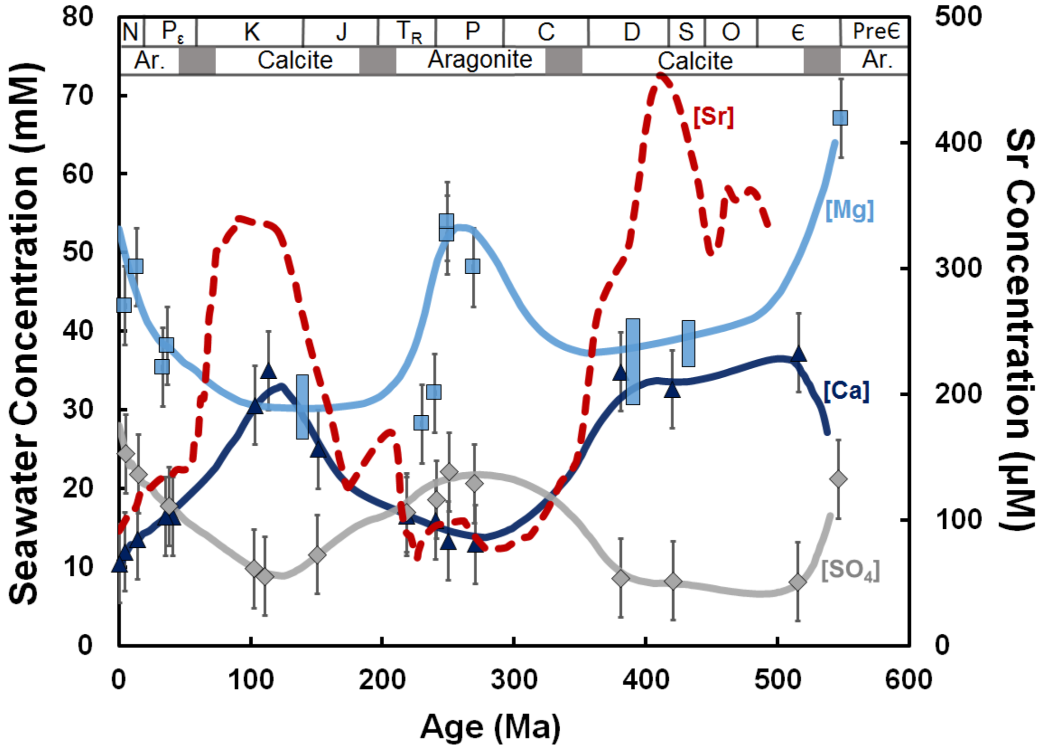

Fig. 2.1. Compilation of data for seawater [Mg], [Ca], [SO_4], and [Sr] estimates over the Phanerozoic. Data for [Mg] (light blue squares and rectangles), [Ca] (dark blue triangles), and [SO_4] (grey diamonds), are in mmol/kg and derive from fluid inclusions in marine halite (Horita et al., 2002; Lowenstein et al., 2003). Large light blue rectangles are [Mg] estimates based on measured Ca/SO_4. Rough seawater [Sr] estimates (in µmol/kg, dashed red line) were calculated from the [Ca] estimates, based on consistent binned Sr/Ca measurements in low-Mg biological calcite over the Phanerozoic from various studies (Lear et al., 2003; Steuber and Veizer, 2002), but are subject to uncertainties. Lower estimates of seawater Sr/Ca (Coggon et al., 2010) lead to approx. modern Sr concentrations from 30-180 Ma. Geologic eras and periods of calcite and aragonite seas are demarcated at the top of the graph.

2.4. Hydrothermal Charge-balance model

Hydrothermal flow through mid-ocean ridge systems is complicated in several ways. Some fluids enter the oceanic crust close to the ridge, where they are rapidly heated as they percolate downwards and are then vented back to the ocean quickly (German and Seyfried, 2014). Other fluids enter the crust much farther from the ridge, have a longer and slower transit through the system, and may or may not be heated to the high temperatures characterizing the axial portions of the system. Although it is difficult to account for the complexity in a simple model, certain material and charge balance constraints are likely to be met by the dissolved ions in the fluids.

Our approach is to use knowledge of modern systems to establish a model that we then apply to ancient systems. Modern high-T hydrothermal fluids that vent back to the ocean have zero [Mg], elevated [Ca], zero [SO_4], and slightly elevated [Sr] that is largely, but not completely, derived from basalt based on $^{87}Sr/^{86}Sr$ evidence (Amini et al., 2008; Bach and Humphris, 1999; Coogan and Dosso, 2012; Elderfield and Schultz, 1996; German and Seyfried, 2014; Von Damm et al., 1985). Analyses of modern high-T vent fluids suggest that the overall change in fluid chemistry, especially for the three major ions Mg, Ca, and SO_4, can be constrained by charge balance. The positively charged seawater Mg^{2+} and Ca^{2+}, and negatively charged SO_4^{2-} ions are removed from the fluids, yet the seawater proportions (53:10:28) are such that there is a total positive charge excess per kilogram of fluid equal to $[Mg^{2+}]_{sw} + [Ca^{2+}]_{sw} – [SO_4^{2-}]_{sw}$. As end-member hydrothermal fluids have zero [Mg], charge balance is maintained through the net release of Ca^{2+} from basalt. According to this model, the final average Ca concentration in venting hydrothermal fluids (~35 mmol/kg) can be calculated from the initial seawater concentrations as:

$$[Ca]_{hyd} = [Mg]_{sw} + [Ca]_{sw} - [SO_4]_{sw} \qquad \text{[Eq. 2.1]}$$

Where $[Ca]_{hyd}$ is the Ca concentration in high-T hydrothermal fluids, and $[Mg]_{sw}$, $[Ca]_{sw}$, and $[SO_4]_{sw}$ are the magnesium, calcium, and sulfate concentrations in seawater, respectively. More rigorous reaction-path modeling, which includes other cations (such as Na, K, Fe) and processes such as albitization and the formation of actinolite (SI Appendix, SI Text, Fig. S2.1), corroborates this charge balance equation.

The hydrothermal Ca is a combination of seawater Ca plus Ca released from basalt. The minimum amount of Ca released from basalt must be equal to $[Ca]_{hyd}$ - $[Ca]_{sw}$. However, there is evidence that in lower temperature parts of the hydrothermal circulation system, virtually all of the seawater Ca is removed through precipitation of anhydrite ($CaSO_4$) (Amini et al., 2008), so that virtually all of the Ca in the venting fluids is derived from basalt. This inference is strongly supported by the observation that ~80% of the Sr in end-member vent fluids is also derived from basalt (Bach and Humphris, 1999; Coogan and Dosso, 2012; Elderfield and Schultz, 1996; German and Seyfried, 2014; Von Damm et al., 1985). The key aspects of our model relate to the sources of hydrothermal Ca and Sr which, based on equation [2.1], should have been substantially different in the geologic past due to differences in the proportions of dissolved Ca, Mg and SO_4 relative to the modern system. Since ultimately we wish to relate the changes in hydrothermal geochemistry to changes in Sr isotopes, it is important to correctly model the behavior of Sr relative to Ca.

Our model for fluid evolution in MOR systems, which is meant to describe the global average MOR hydrothermal fluid evolution, can be expressed in four steps (SI Appendix, Fig. S2.2):

1. As seawater flows into fractures in warm basalt and is heated above 130°C, $CaSO_4$ (anhydrite) precipitates, removing essentially all of the original dissolved seawater Ca or SO_4, depending on which is present in larger concentration, and a fraction of the dissolved seawater Sr that depends on the amount of Ca removed.
2. With continued heating and flow, but still at moderate temperature, basalt releases Ca along with Sr in exchange for Mg until any remaining seawater SO_4 is precipitated as $CaSO_4$. In this secondary phase of anhydrite formation, which applies only when $[SO_4]_{sw} > [Ca]_{sw}$, the anhydrite incorporates Sr from both seawater and basalt. The Mg released from basalt is continually returned to the solid phase as secondary hydroxylated Mg minerals. (In real systems there is overlap between steps 1 and 2.)
3. At high-T (>250°C) Ca and Mg continue to be released from basalt, but all of the Mg is returned to the solid phase as secondary hydroxylated Mg minerals; the most prominent being chlorite, whereas the released Ca and accompanying Sr mostly accumulate in the fluid.
4. With continued heating, additional Ca and Sr from the fluids exchanges with Ca and Sr in the basalts with no change in total fluid concentration of either element (we subsequently refer to this as high-T Ca, Sr exchange).

This model allows us to make predictions about how differences in seawater composition in the geologic past will be manifest as changes in the extent of Ca, Mg, SO_4, and Sr exchange between seawater and oceanic crust, ultimately evidenced by changes in the $^{87}Sr/^{86}Sr$ of hydrothermal vent fluids. The test of the model comes from measured values of $^{87}Sr/^{86}Sr$ in high temperature vein epidote samples from ophiolites (Alexander et al., 1993; Bickle and Teagle, 1992; Fonneland-Jorgensen et al., 2005; Kawahata et al., 2001, 1987; McCulloch et al., 1981; Turchyn et al., 2013).

In Fig. 2.2 we illustrate the model described above, where modern seawater ([Mg]:[Ca]:[SO_4] of 53:10:28 mmol/kg) leads to vent fluid with $[Ca]_{hyd}$ = 35 mmol/kg and zero [Mg], which is approximately the same as for average modern vent fluids and for reaction path simulations (SI Appendix, SI Text, Fig S1a,c). For paleoseawater with a Cretaceous composition (30:30:10), only 1/3 of $[Ca]_{sw}$ can be removed through anhydrite precipitation in step-1 (because $[Ca]_{sw} > [SO_4]_{sw}$), step-2 does not occur, and the fluids emerge with $[Ca]_{hyd}$ = 50 mmol/kg, some 20 mmol/kg of which is inherited from the incoming seawater (Figs. 2, SI Appendix, Fig. S2.1b). In our model, the oceanic crust is a source for Ca at all values of seawater [Ca], [Mg] and [SO_4]*.

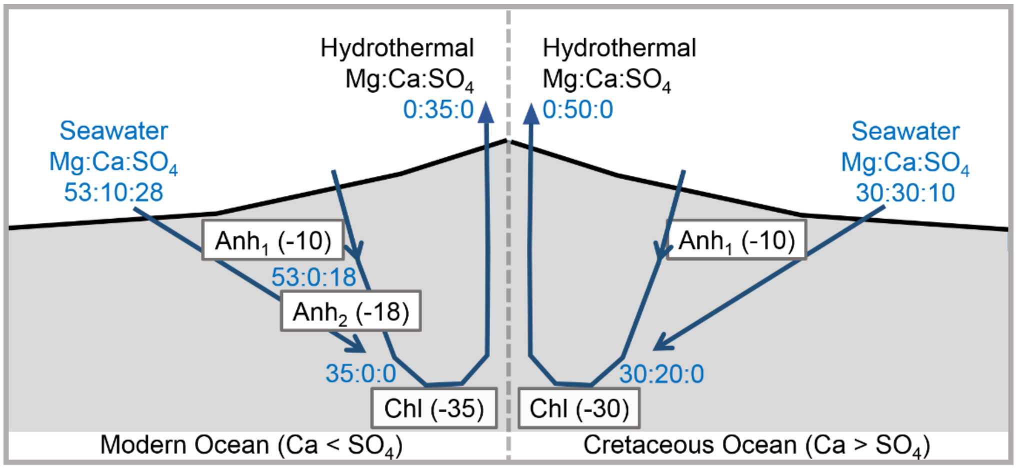

Fig. 2.2. Schematic representation of hydrothermal budgets for Mg, Ca, and SO_4. The numbers in blue are concentrations in mmol/kg for [Mg]:[Ca]:[SO_4] based on the charge balance calculations presented below and formalized in equation [2.1]. Numbers in brackets reflect mmol/kg of SO_4 lost from seawater to anhydrite-1 (Anh_1), and anhydrite-2 (Anh_2), and mmol/kg of Mg lost from seawater to chlorite and other silicates (Chl).

2.5. Strontium isotope evolution in hydrothermal fluids

To estimate the $^{87}Sr/^{86}Sr$ of hydrothermal fluids, we extend the charge-balance model assuming that Sr passively follows Ca during anhydrite precipitation, basalt dissolution, and chlorite/epidote precipitation. During anhydrite precipitation (Step 1), seawater Sr is assumed to be removed in anhydrite with a Sr/Ca ratio of 0.003 (R_{Anh}). For modern seawater, this is a simplification roughly equivalent to removing 99% of seawater Ca as anhydrite with a Sr/Ca distribution coefficient of 0.1 [the average equilibrium experimental value (Shikazono and Holland, 1983)]. The predicted anhydrite Sr/Ca agrees with data from modern seafloor anhydrite deposits (Kuhn et al., 2003; Teagle et al., 1998). When $[Ca]_{sw} < [SO_4]_{sw}$, such as in the modern oceans, there is further

---

*It has also been proposed that [Ca] vs. [Mg] data for paleoseawater produce a pattern that points towards basalt as a sink for seawater Ca when it is present at levels greater than ~20 mmol/kg, and as a source for Ca at lower levels (Kump, 2008). However, a chemical mechanism for this idea has not been proposed, and replacement of seawater Mg by basaltic Ca appears to be thermodynamically favorable at all temperatures (SI Appendix, SI Text, Fig. S2.1).

anhydrite precipitation until sulfate is fully removed (Step 2). This second phase of anhydrite precipitation occurs as Ca is released from the basalts. It is assumed that basaltic Sr is released with basaltic Ca in proportion to the bulk basalt concentrations (Staudigel, 2013) (R_{bslt} = basalt Sr/Ca = 0.002) and incorporated into anhydrite using the ratio R_{Anh}, as illustrated in SI Appendix (Fig. S2.3). The continued release of basaltic Ca during Step 3 is also accompanied by a proportional release of basaltic Sr using the ratio R_{bslt}.

Model steps 1-3 arrive at the correct $[Sr]_{hyd}$ for average modern vent fluids (~110 µmol/kg, where $[Sr]_{sw}$ = 91 µmol/kg, SI Appendix, Fig. S2.4), but produce a value of $^{87}Sr/^{86}Sr$ that is slightly higher than the observed average value of ~0.7037 (Bach and Humphris, 1999). We infer that this mismatch indicates that there is further high-T Ca, Sr exchange between hydrothermal fluid and basalt (Step 4). This "exchange" occurs as a result of continued dissolution of Mg, Ca, Sr-bearing primary minerals and precipitation of secondary minerals that also contain these elements; it is assumed to leave the fluid [Ca] and [Sr] unchanged (and [Mg] = 0), but results in a further shift of fluid $^{87}Sr/^{86}Sr$ toward basalt values. Assuming Sr and Ca are exchanged in the proportion R_{bslt}, a fraction of about 0.1 (denoted θ_{exch}, SI Appendix, SI Text) of the total Ca in modern hydrothermal vent fluids (~35 mmol/kg), must exchange with basalt in order to produce the low $^{87}Sr/^{86}Sr$ of average modern vent fluids (0.7037). Exchange processes are documented by several lines of evidence, at low temperature in the $^{87}Sr/^{86}Sr$ of basalt-hosted carbonate veins and anhydrite deposits, and at high temperature in the isotopic compositions of altered ophiolite assemblages (Berndt et al., 1988; Teagle et al., 2003). For simplicity, in the model we assume that the exchange happens after all of the Mg has been removed from the fluid.

The model Sr concentration of hydrothermal vent fluids can be expressed as:

$$[Sr]_{hyd} = [Sr]_{sw} - [Sr]_{anh} + [Sr]_{bslt} \qquad \text{[Eq. 2.2]}$$

Where $[Sr]_{sw}$ is the strontium concentration of seawater, $[Sr]_{anh}$ is the strontium lost during anhydrite precipitation, and $[Sr]_{bslt}$ is the strontium gained from the basalts. The isotopic composition of Sr is calculated by mixing the seawater Sr remaining after anhydrite precipitation with the Sr released from basalt during Ca-Mg exchange, according to:

$$\left(\frac{^{87}Sr}{^{86}Sr}\right)_{hyd} = \frac{[Sr]_{hyd,sw}}{[Sr]_{hyd}}\left(\frac{^{87}Sr}{^{86}Sr}\right)_{sw} + \frac{[Sr]_{hyd,bslt}}{[Sr]_{hyd}}\left(\frac{^{87}Sr}{^{86}Sr}\right)_{bslt} \qquad \text{[Eq. 2.3]}$$

Where $[Sr]_{hyd,sw}$, $[Sr]_{hyd,bslt}$, and $[Sr]_{hyd}$ are the seawater Sr, basaltic Sr, and total Sr concentrations in the output hydrothermal fluids, respectively; $(^{87}Sr/^{86}Sr)_{sw}$ is the strontium isotope ratio of seawater, and $(^{87}Sr/^{86}Sr)_{Bslt}$ is the strontium isotope ratio of basalt (assumed = 0.7025).

The use of an average $^{87}Sr/^{86}Sr$ of modern vent fluids (= 0.7037) to calibrate our model could be questioned based on the observation that $^{87}Sr/^{86}Sr$ is somewhat variable between ridges and is loosely correlated with spreading rates (Bach and Humphris, 1999). Although there is variability, the data as reported yield a mean and standard deviation for different ridges of 0.7037 ± 0.0004, which is not so large as to invalidate use of the average. Causes of $^{87}Sr/^{86}Sr$ variability are most simply related to variability in Ca concentrations. The average [Ca] of modern hydrothermal vents represents a combination of fluids that have undergone full titration of seawater Mg, and then approached equilibrium with basalt at different temperatures (SI Appendix, SI Text, Fig. S2.1). At lower temperatures albitization increases [Ca] (in exchange for seawater Na), and at higher temperatures amphibole formation lowers [Ca] (replaced mostly by basaltic Na and Fe). Along with differences in temperature, variability in fluid residence times also affects reaction extent, and may help explain low-temperature vents with fully titrated [Mg] and high ^{87}Sr/^{86}Sr (Elderfield et al., 1999; Mottl and Wheat, 1994). Since Sr follows Ca exchange and the replacement of seawater Mg by basaltic Ca is thermodynamically favorable at all temperatures, a charge-balance model is a logical approach to integrating variable fluid histories (SI Appendix, SI Text, Fig. S2.2). When applying the model to other times in the geologic past, it is straightforward to account for possible variations in global spreading rate using the correlation of (Bach and Humphris, 1999), but global rates are unlikely to have varied by more than about 20% relative to modern (Rowley, 2002), which would correspond to an increase in average ^{87}Sr/^{86}Sr of only about 0.0002.

We relate the Ca-Mg-SO_4 chemistry of hydrothermal systems to Sr isotopes because the Sr isotopic record of high-T hydrothermal precipitates is the primary test of our model, and has direct implications for the interpretation of paleoseawater ^{87}Sr/^{86}Sr. To most simply replicate modern systems, and in accordance with our reaction-path simulations (SI Appendix, SI Text) and with natural and experimental observations (Bischoff and Seyfried, 1978; Seyfried and Bischoff, 1981, 1979; Teagle et al., 2003), anhydrite precipitation is separated into two phases (SI Appendix, Fig. S2.2). Anhydrite-1 is derived entirely from seawater, whereas anhydrite-2 includes variable proportions of basaltic calcium and strontium (as observed in modern ocean drill cores). Therefore equation [2.2] can be expanded to:

$$[Sr]_{hyd} = [Sr]_{sw} - [Sr]_{anh1} - [Sr]_{anh2,sw} + [Sr]_{bslt1} + [Sr]_{bslt2} \qquad \text{[Eq. 2.4]}$$

Where $[Sr]_{anh1}$ is the seawater Sr lost during the first phase of anhydrite precipitation, $[Sr]_{anh2,sw}$ is the seawater Sr lost to anhydrite-2, $[Sr]_{bslt1}$ is the basaltic Sr remaining in the fluid after formation of anhydrite-2, and $[Sr]_{bslt2}$ is the basaltic Sr gained during the final exchange of seawater Mg for basaltic Ca. The final Ca,Sr exchange required to explain the isotope data (θ_{exch}, SI Appendix, SI Text) does not affect any concentrations within the hydrothermal fluids, and is not explicitly denoted in equation [2.4]. The [Sr] in the fluids and minerals discussed is only a minor component, and thus has been ignored in terms of its effects on charge-balance.

To calculate hydrothermal fluid ^{87}Sr/^{86}Sr for Phanerozoic paleoseawater, we replace the terms in mixing equation [2.3] with those from our charge-balance equations (defined in SI Appendix, SI Text) in order to arrive at our final model. It is important to note that a four-isotope approach (Kristall et al., 2017) is not necessary for our purposes, as we use only the seawater record as input values. When accounting for the different sinks and sources for seawater and basaltic Sr during hydrothermal circulation, including high-T exchange (model step 4), we arrive at:

$$\left(\frac{^{87}Sr}{^{86}Sr}\right)_{hyd} = \frac{[Sr]_{sw} - [Sr]_{anh1} - [Sr]_{anh2,SW} - [Sr]_{exch,sw}}{[Sr]_{hyd}}\left(\frac{^{87}Sr}{^{86}Sr}\right)_{sw} + \frac{[Sr]_{bslt1} + [Sr]_{bslt2} - [Sr]_{exch,bslt} + [Sr]_{exch}}{[Sr]_{hyd}}\left(\frac{^{87}Sr}{^{86}Sr}\right)_{bslt} \qquad \text{[Eq. 2.5]}$$

Where $[Sr]_{exch,sw}$ and $[Sr]_{exch,bslt}$ are the amounts of seawater and basaltic strontium within the hydrothermal fluids that are exchanged with the basalt during step 4, respectively (SI Appendix, SI Text), and their sum is $[Sr]_{exch}$. Our final charge-balance model for average high-T hydrothermal ^{87}Sr/^{86}Sr over the Phanerozoic takes into account the gains and losses in Sr during anhydrite precipitation, basalt dissolution, and exchange of Sr between hydrothermal fluids and basalt; all of which are calibrated to modern hydrothermal vent fluid compositions.

2.6. Variability in hydrothermal $^{87}Sr/^{86}Sr$ over the Phanerozoic

Applying the model to paleoseawater requires the record of seawater [Mg], [Ca], [SO_4], and [Sr] (Fig. 2.1), and the record of paleoseawater $^{87}Sr/^{86}Sr$ (Fig. 2.3) derived from measurements of marine carbonate (Prokoph et al., 2008). The result is a calculated curve representing the predicted $^{87}Sr/^{86}Sr$ of average *high-temperature* MOR hydrothermal fluids through time, where the past ~150 Ma are generally better constrained than the rest due to availability of published data (Fig. 2.3). Using the seawater Sr concentration history from Fig. 2.1, the model-predicted values of $^{87}Sr/^{86}Sr$ for hydrothermal fluids vary over a large range from about 0.7030, which is lower than modern vent fluids, to about 0.7075, which is much higher than modern vent fluids. The corresponding fraction of recycled seawater Sr in venting hydrothermal fluid varies from about 20% to 80% during the Phanerozoic, and is maximized during periods of high seawater [Ca] and [Sr] and low seawater [Mg] and [SO_4]. The relationship between the fraction of recycled seawater Sr and the vent fluid $^{87}Sr/^{86}Sr$ is not simple because the seawater $^{87}Sr/^{86}Sr$ is also changing with time.

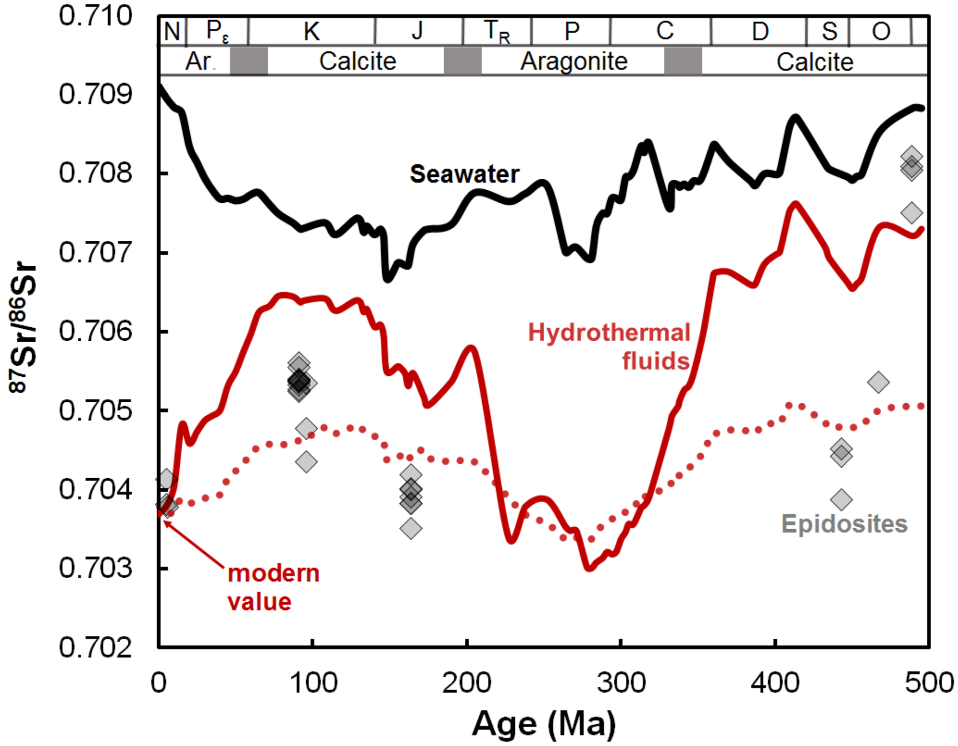

Fig. 2.3. Calculated hydrothermal strontium compositions through time, based on equation [2.5], varying input seawater [Mg], [Ca], [SO_4], [Sr], and $^{87}Sr/^{86}Sr$ composition. [Mg], [Ca], [SO_4], and [Sr] data are the same as for Fig. 2.1. Black line is seawater $^{87}Sr/^{86}Sr$ composition through time (Prokoph et al., 2008), red line is the calculated $^{87}Sr/^{86}Sr$ of output hydrothermal fluid. Dotted red line is model result for hydrothermal $^{87}Sr/^{86}Sr$ using constant modern seawater [Sr], which is approx. consistent with lower estimates of Sr/Ca for ~30-180 Ma (Coggon et al., 2010). Grey diamonds are $^{87}Sr/^{86}Sr$ data from epidosites and epidote-quartz veins from ophiolites and oceanic drill-cores (Alexander et al., 1993; Bickle and Teagle, 1992; Fonneland-Jorgensen et al., 2005; Kawahata et al., 2001, 1987; McCulloch et al., 1981; Turchyn et al., 2013). Several of the late Cambrian epidosite samples plotting highest above our model predictions have $\delta^{18}O$ values indicative of metamorphic resetting (Turchyn et al., 2013).

The relatively few available strontium isotope data from ophiolite epidosite and epidote-quartz veins are plotted in Figure 2.3 for comparison, based on the inference that they best record high-T

MOR-type hydrothermal fluids through time. Epidote forms at temperatures greater than ~300°C, and is likely to precipitate from fully evolved vent fluids. Furthermore, epidosites and epidote-quartz veins in particular are thought to form preferentially along concentrated flow-paths where water/rock ratios are high (Alexander et al., 1993; André and Deutsch, 1986; Berndt et al., 1989; Muehlenbachs et al., 2003) and are thus likely to be the best records of high-T fluids through time. Epidosites and epidote-quartz veins from the two youngest oceanic crustal sections [Pito Deep and Site 504B (Barker et al., 2010; Kawahata et al., 1987)] have $^{87}Sr/^{86}Sr$ values that are close to typical average modern vent fluids, reinforcing the hypothesis that they record vent fluid chemistry in older rocks.

The available epidosite/epidote-quartz Sr isotope data (Fig. 2.3) are broadly consistent with the model. For the Cretaceous period, the Sr isotopes in epidosites and epidote-quartz veins from Troodos and Oman indicate that the model predicts the correct sense of change, but yields an amplitude that is too large. For other periods there are few ophiolite data, and the seawater concentration estimates for Sr are less reliable, but the model generally corroborates high observed $^{87}Sr/^{86}Sr$ in Ordovician epidotes when using the seawater [Sr] curve from Figure 2.1. The curves shown in Figure 2.3 are mostly illustrative of how the seawater chemical changes shown would translate into changes in $^{87}Sr/^{86}Sr$ of hydrothermal fluid dissolved Sr. The fact that the observed variations in ophiolite $^{87}Sr/^{86}Sr$ are not as extreme as predicted by the model could indicate that the Ca, Mg, SO_4, and Sr variations in paleoseawater were not as extreme as shown in Figure 2.1.

Lower estimates of Cretaceous seawater Sr/Ca (Coggon et al., 2010), as roughly approximated by the constant seawater [Sr] calculations (Fig. 2.3), yield predicted hydrothermal $^{87}Sr/^{86}Sr$ somewhat too low relative to the available data. Our conclusion is that the model captures essential aspects of the exchange at mid-ocean ridges and the available data, but requires more data to be sufficiently refined for accurate predictions of paleo-hydrothermal behavior. In particular, it is important to accurately model the behavior of Sr relative to Ca, something that can be done only crudely with currently available experimental and field data (Kuhn et al., 2003; Shikazono and Holland, 1983; Teagle et al., 1998).

Another potential issue concerns the role of carbonate in the hydrothermal systems. There is evidence for elevated amounts of carbonate precipitation in oceanic crust at certain times in the geologic past (Coogan and Dosso, 2015; Gillis and Coogan, 2011). In the modern ocean, the amount of dissolved carbonate in seawater (~2 mmol/kg as opposed to 28 mmol/kg SO_4), which would precipitate in an analogous manner to sulfate as fluids are heated, serves as only a small sink for seawater Ca and Mg. If dissolved inorganic carbon were present in the oceans at higher concentration in the geologic past, it could potentially affect the charge balance. However, estimates suggest that total dissolved carbon in the oceans has not changed significantly over the past 70 million years (Zeebe, 2012).

2.7. Hydrothermal Ca and Sr fluxes through time

Our model provides an approach for estimating the effects of seawater chemistry on chemical exchange between seawater and oceanic crust in the *high temperature* parts of MOR circulation systems. The removal of Mg and SO_4 from seawater in our model is not different from previous studies [(Lowenstein et al., 2013) and references therein]; at all times these components are fully removed from the circulating seawater at and near MOR's. Overall, our modeling indicates that seafloor hydrothermal systems respond to changes in the chemical composition of seawater, but this is unlikely to be a major cause of seawater chemical variations.

The model generates estimates of seawater and basaltic [Ca] and [Sr] in hydrothermal vent fluids. The total amount of Ca and Sr transferred from basalt to the oceans is the product of these concentrations and the total amount of fluid flowing through MOR hydrothermal systems globally. Calculated values for the relative fluxes of high-T hydrothermal [Ca] and [Sr] derived from basalt (per unit expelled hydrothermal fluid) vary by a factor of ~1.6 throughout the Phanerozoic, with a notable low in the Cretaceous (Fig. 2.4a). The transfer of Sr and Ca from basalt to the oceans (Fig. 2.4a) is less efficient during periods when seawater [Mg] and [SO_4] are low compared to [Ca] and [Sr]. This behavior serves as a small negative feedback on seawater [Ca] and [Sr] (Fig. 2.4b), and also has implications for $^{87}Sr/^{86}Sr$ and ^{40}Ca in seawater throughout Earth history (Caro et al., 2010).

Over the Phanerozoic, the model shows a gradual decrease in the efficiency of Sr and Ca transfer from basalts with decreasing age, as a result of generally decreasing seawater [Mg]/[SO_4] towards the present day. This Phanerozoic trend is reversed in the Late Cenozoic, and is also punctuated by a relatively short pulse during the Permian, when seawater compositions were similar to modern.

An interesting aspect of our results is that while Cretaceous seawater $^{87}Sr/^{86}Sr$ was relatively low (Fig. 2.3), our model suggests that MOR hydrothermal systems were less efficient at transferring Sr from oceanic crust to seawater (Fig. 2.4a). Possibly counterbalancing this effect is the amount of global hydrothermal fluid flux, which some have inferred was higher than modern in the Cretaceous (Engebretson et al., 1992; Gaffin, 1987) as a consequence of globally higher seafloor generation rates Our results therefore suggest that either low temperature exchange of Sr between basalt and seawater (including weathering of ocean-island basalts) was responsible for a large fraction of the overall basalt-seawater exchange (Allègre et al., 2010; Coogan and Dosso, 2015; Kristall et al., 2017), or conversely, that there was an exceptionally small continental weathering flux of radiogenic Sr during the Cretaceous. Supporting the prior interpretation are records of low-temperature hydrothermal crust alteration (Coogan and Dosso, 2015), which suggest that higher water temperatures increased the magnitude of low-temperature basalt-seawater exchange. Such small temperature differences (~10 C), however, would have little effect on our results for high-T fluids.

Seawater SO_4 levels alone can affect the transfer of basaltic Sr to the oceans because basaltic Sr can be captured in anhydrite. If decoupled from oscillations in seawater [Mg] and [Ca] (such as those that occur during the Phanerozoic), low seawater [SO_4] leads to an increase in basaltic Sr delivery to the oceans per unit of hydrothermal fluid. This result may be important for understanding hydrothermal circulation during the Archean and Proterozoic, when seawater [SO_4] may have been especially low (Crowe et al., 2014; Kump and Seyfried, 2005; Lowenstein et al., 2013). Neoproterozoic $^{87}Sr/^{86}Sr$ values, for example, are generally lower than for the Phanerozoic (Halverson et al., 2007), which could be partially explained by contemporaneously low levels of seawater [SO_4]. Sulfate could also affect the exchange of radiogenic ^{40}Ca between seawater and the oceanic crust (Kump, 2008).

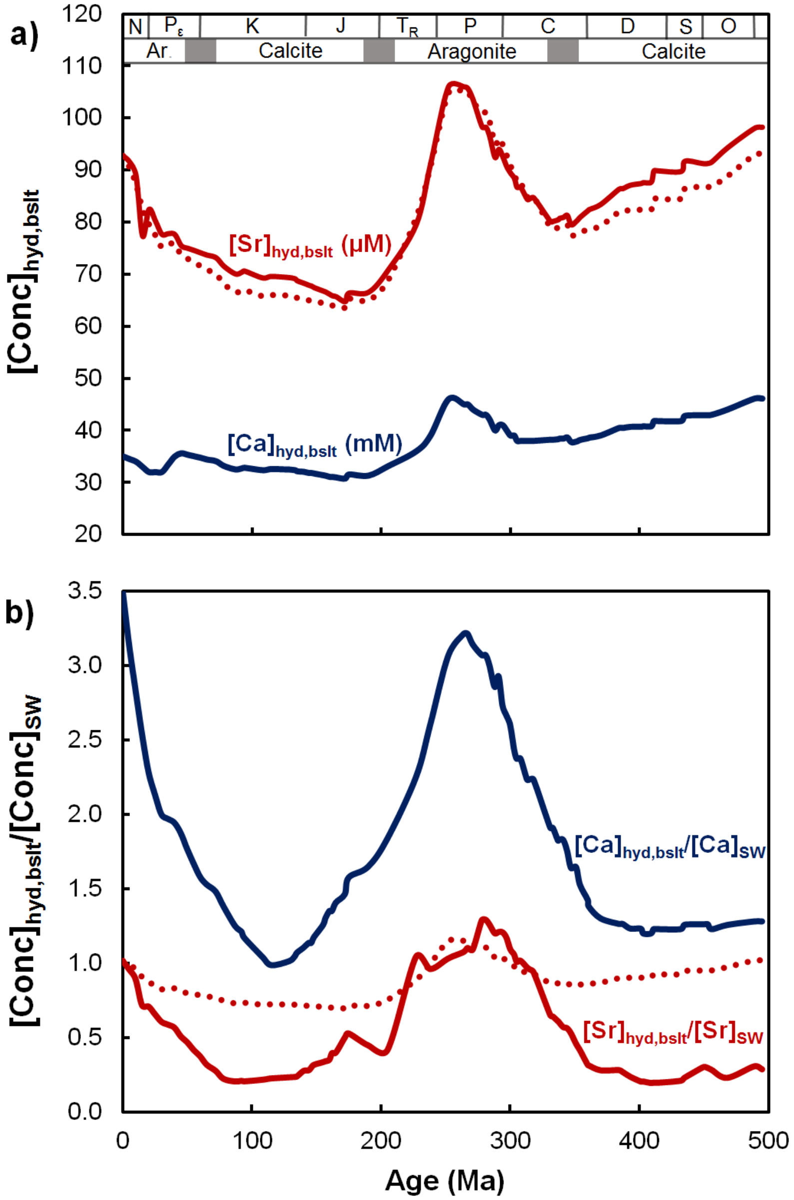

Fig. 2.4a,b. Calculated basaltic [Ca] and [Sr] in hydrothermal fluids through time, based on equation [2.5], varying input seawater [Mg], [Ca], [SO_4], and [Sr] (Fig. 2.1). a) Basaltic [Ca] (dark blue) and basaltic [Sr] (red) within hydrothermal fluids through time, and b) in hydrothermal fluids relative to seawater [Ca] and [Sr]. Dotted red lines are model results using constant modern seawater [Sr].

The fate of seawater sulfate in oceanic crust, however, is poorly constrained (Halevy et al., 2012; Tostevin et al., 2014); anhydrite is likely to be a sink for oceanic sulfate, despite its retrograde solubility, but it is uncertain how much of it is fixed into the crust versus dissolved back into the oceans prior to subduction. Sulfur isotope studies demonstrate that seawater sulfate has been incorporated into the mantle throughout geologic time [e.g. (Canfield, 2004; Kagoshima et al., 2015)] and models indicate that only ~20-35% of the modern sulfur burial flux is in the form of pyrite (Tostevin et al., 2014), which suggests that the remaining sulfur sink is initially in the form of sulfate or sulfur intermediates, but this estimate can vary significantly based on the amount of recycled evaporite material in rivers (Halevy et al., 2012). Although we have not attempted to create a global model for seawater [Ca] and [Sr] through time, differences in low-temperature fluxes and retrograde outputs from altered oceanic crust [e.g. (Coogan and Dosso, 2015; Kristall et al., 2017)], along with potential differences in reaction rates caused by paleoseawater variability, would be important to consider [a dual-porosity model is presented in the SI Text to explore the effects of reaction rate differences on hydrothermal exchange (SI Appendix, SI Text, Fig. S2.5)]. On the other hand, if our calculations, relating to high temperature hydrothermal fluids, were to represent the average exchange of Sr between oceanic basalt and the oceans, it would require re-evaluation of the relationship between the seawater $^{87}Sr/^{86}Sr$ curve and continental weathering fluxes.

2.8. Supplementary Information

2.8.1. Reaction-path modeling

Equilibrium reaction path models were constructed to test the relative effects of precursor seawater chemistry on the Ca concentration of mid-ocean ridge hydrothermal fluids in the context of the charge-balance simplification presented in the main text (equation [2.1]). Geochemist's Workbench was used for the simulations (Bethke, 2008) along with a 500 bar thermodynamic database that includes mineral solid-solution chemistry (Pester et al., 2012). Thermodynamic data for Mg-hydroxy-sulfate-hydrate (MHSH) was also included (Janecky and Seyfried, 1983), and combined effects of anhydrite and MHSH precipitation were calibrated using additional experimental data (Bischoff and Rosenbauer, 1983; Bischoff and Seyfried, 1978). However, MHSH proved to be unstable in the presence of silicates during preliminary models and was ultimately suppressed for simplicity in the final calculations.

Two main groups of simulations were conducted at four different temperatures ranging from 250 to 400°C (Fig. S2.1). The first simulations use modern seawater and the others use average Cretaceous seawater, represented by NaCl balanced solutions with [Mg]:[Ca]:[SO_4] of 53:10:28 and 30:30:10, respectively (mmol/kg). In all scenarios, one kg of starting solution is heated to the initial temperature of interest (250-400°C), which causes the precipitation of anhydrite until either Ca or SO_4 is fully removed. The isothermal solution is then reacted with basalt by incrementally adding small amounts to the system. The bulk mineral assemblage of the basalt consists of: plagioclase (An75) : olivine (Fo80) : diopside : enstatite : hedenbergite : pyrrhotite, in the mass ratio 0.69 : 0.21 : 0.063 : 0.018 : 0.019 : 0.003 (pyrrhotite was added as an appropriate source of reduced sulfur).

The results of the simulations, along with data from modern hydrothermal vents, are plotted in Fig. S2.1. When seawater [Ca] < [SO_4], as in modern systems, a second phase of anhydrite formation occurs as seawater Mg is exchanged for basaltic Ca. The cumulative amount of anhydrite precipitated is shown as dashed red lines. The simulations show that all of the sulfate is removed before dissolved Ca begins to increase in the fluids, in agreement with the two stages of anhydrite precipitation in our Sr-isotope model.

After sulfate is removed and Mg has been fully replaced with basaltic Ca, the compositions of the fluids increasingly diverge with decreasing water/rock ratio (W/R < ~10), with differences depending largely on the phase equilibria for different temperatures. In both scenarios, the models predict that below ~350 °C, albitic plagioclase becomes increasingly stable with decreasing T, resulting in a small fraction of seawater Na being removed to accommodate additional dissolved Ca in the fluids. Above 350 °C, calcic plagioclase and amphibole are increasingly stable, drawing down Ca and increasing dissolved Na and Fe in the fluids (not shown). Generally, albitization drives [Ca] upwards at lower temperatures, and amphibole precipitation drives [Ca] downwards at higher temperatures, as corroborated by modern hydrothermal vent fluids (Fig. S2.1c). The dominant secondary silicates that form in all simulations are chlorite, tremolite, and secondary plagioclase solid solutions, along with small amounts of epidote when T < 400 °C.

Despite the variability at different temperatures, we note that the average [Ca] values are approximately the same as for average modern vent fluids (~30-35 mM) (Elderfield and Schultz, 1996; Von Damm et al., 1985), which represent an integration of many different fluid flow-paths and temperatures. Model results between 300 and 400°C using modern seawater (Fig. S2.1a) agree with the concentration range of dissolved [Ca] in hydrothermal fluids sampled from the Mid-Atlantic Ridge, Juan de Fuca Ridge, and the East Pacific Rise (Fig. S2.1c), when normalized to seawater chlorinity to account for the effects of fluid phase separation (Pester et al., 2015). Generally, at higher water/rock ratios the reaction path for Ca is nearly independent of T because the removal of seawater Mg to hydrous alteration minerals is thermodynamically favorable at all conditions.

When using Cretaceous seawater we notice two important differences (Fig. S2.1b), the first is that it comes into the system with much higher Ca (~20 mM) than modern seawater, which has not been titrated by prior anhydrite precipitation, and that the Ca concentration for all simulated temperatures is higher than for modern vents. This model serves to indicate that seawater calcium was more likely to persist through hydrothermal circulation at times of high seawater Ca/SO_4 and low Mg/Ca, with conservative paleoseawater estimates suggesting average vent fluids contained up to ~40% seawater calcium (e.g. Fig. 2.2), instead of ~ 0% as is suggested by δ^{44}Ca signatures in modern hydrothermal vents (Amini et al., 2008; Bach and Humphris, 1999; Pester et al., 2016). The simulation results in Fig. S2.1 should also encompass reactions with more ultramafic lithologies because models run with lower primary plagioclase fractions (not shown) exhibit less T-dependent variability beyond the Mg titration stage.

From the GWB simulations, we infer that the average composition of the fluids after full titration of seawater components is a good estimate of average modern high-temperature hydrothermal vent fluids when considering the natural range in compositions (Fig. S2.1c). In the modern ocean, the exit temperature of hydrothermal fluids is loosely correlated with the amount of dissolved $[\mathrm{Ca}]_{\mathrm{hyd}}$, likely due to phase equilibria at different temperatures. The average $[\mathrm{Sr}]_{\mathrm{hyd}}$ we use in our model (~110 μM) is from a compilation of published values for hydrothermal vent fluids corrected for phase separation (Fig. S2.4).

2.8.2. Charge-Balance Model

Following the logic put forward in the main text (shown schematically in Fig. S2.2), the losses and gains of Sr are tied to the losses and gains of Ca. We define the variables in equations [2.4, 2.5] as follows:

$$[\mathrm{Sr}]_{\mathrm{Anh1}} = R_{anh}\begin{bmatrix} [\mathrm{SO_4}]_{\mathrm{SW}} & \text{if } [\mathrm{Ca}]_{\mathrm{SW}} > [\mathrm{SO_4}]_{\mathrm{SW}} \\ [\mathrm{Ca}]_{\mathrm{SW}} & \text{if } [\mathrm{Ca}]_{\mathrm{SW}} < [\mathrm{SO_4}]_{\mathrm{SW}} \end{bmatrix} \qquad \text{[Eq. S2.1]}$$

The strontium lost during anhydrite-2 precipitation is a combination of seawater Sr ($[\mathrm{Sr}]_{\mathrm{anh2,sw}}$) and Sr gained from the basalts. The total amount of Ca released from basalt (counter-balanced by a loss of seawater Mg) and captured as anhydrite-2 is defined:

$$[\mathrm{Ca}]_{\mathrm{Anh2}} = \begin{bmatrix} 0 & \text{if } [\mathrm{Ca}]_{\mathrm{SW}} > [\mathrm{SO_4}]_{\mathrm{SW}} \\ \{[\mathrm{SO_4}]_{\mathrm{SW}} - [\mathrm{Ca}]_{\mathrm{SW}}\} & \text{if } [\mathrm{Ca}]_{\mathrm{SW}} < [\mathrm{SO_4}]_{\mathrm{SW}} \end{bmatrix} \qquad \text{[Eq. S2.2]}$$

The amount of basaltic and seawater Sr in the fluids after each step of anhydrite-2 precipitation is calculated iteratively in 1-mmol increments of Ca (Δ_{Ca}) until sulfate is fully removed, from n = 0 to n = $[Ca]_{Anh2}$, such that:

$$[Sr]'_{bslt}(n+1) = [Sr]'_{bslt}(n) + \Delta_{Ca}R_{bslt} - \Delta_{Ca}R_{anh}\left[\frac{[Sr]'_{bslt}(n) + R_{bslt}}{[Sr]'_{sw}(n)+[Sr]'_{bslt}(n)+R_{bslt}}\right] \qquad \text{[Eq. S2.3]}$$

$$[Sr]'_{sw}(n+1) = [Sr]'_{sw}(n) - \Delta_{Ca}R_{anh}\left[\frac{[Sr]'_{sw}(n)}{[Sr]'_{sw}(n)+[Sr]'_{bslt}(n)+R_{bslt}}\right] \qquad \text{[Eq. S2.4]}$$

Where $[Sr]'_{bslt}$ and $[Sr]'_{sw}$ are the amounts of basaltic and seawater Sr in the hydrothermal fluids after n steps of sulfate removal, respectively. $[Sr]'_{bslt}$ (n = 0) equals zero, and $[Sr]'_{sw}$ (n = 0) equals $[Sr]_{sw} - [Sr]_{anh1}$, which is the strontium left over after primary anhydrite precipitation.

Therefore, the amount of seawater Sr lost to anhydrite-2 is:

$$[Sr]_{anh2,sw} = [Sr]_{sw} - [Sr]_{anh1} - [Sr]'_{sw}(n = [Ca]_{Anh2}) \qquad \text{[Eq. S2.5]}$$

And the overall amount of basaltic Sr gained by the fluids after anhydrite-2 formation is:

$$[Sr]_{bslt1} = [Sr]'_{bslt}(n = [Ca]_{Anh2}) \qquad \text{[Eq. S2.6]}$$

The effects of anhydrite-2 formation on the seawater and basaltic [Sr] in the fluids are depicted in Fig. S2.3. After complete removal of seawater sulfate as anhydrite, the remaining seawater Mg then exchanges with basaltic Ca, releasing a proportional amount of basaltic Sr such that:

$$[Sr]_{bslt2} = R_{bslt}\{[Mg]_{SW} - [Ca]_{anh2}\} \qquad \text{[Eq. S2.7]}$$

Further exchange is required to arrive at the average Sr isotopic composition for modern vents. We define the high-temperature Ca,Sr exchange:

$$[Sr]_{exch} = [Ca]_{hyd}\theta_{exch}R_{bslt} \qquad \text{[Eq. S2.8]}$$

Where θ_{exch} is the fraction of total hydrothermal Ca that exchanges with basalt after the Mg-Ca charge balance has been satisfied. The value of θ_{exch} is calibrated from modern hydrothermal systems (θ_{exch} = 0.108) (*e.g.* ~11% of modern $[Ca]_{hyd}$ needs to exchange with basalt with stoichiometric Sr/Ca (R_{bslt}) to arrive at $^{87}Sr/^{86}Sr = 0.7037$).

Previous iterations of our final model, which included models using i) different Sr/Ca ratios for anhydrite-1 and anhydrite-2, ii) variations in the high-T Ca,Sr exchange factor (θ_{exch}), and iii) variable Sr/Ca according to various distribution coefficients (using GWB), yield the same results as our final model with only slight differences in the amplitude of the $^{87}Sr/^{86}Sr$ oscillations.

2.8.3. Comments on hydrothermal reaction rates

Ca,Sr exchange factor: Hydrothermal fluid compositions could be further changed if paleoseawater chemistry also induced differences in chemical reaction rates during hydrothermal circulation. The model presented in the main text does not incorporate any potential differences in seawater-basalt exchange rates due to paleoseawater chemistry. However, it is unlikely that there are no changes to the kinetics of the discussed chemical reactions due to differences in the composition of seawater, especially at lower temperatures.

Experimental studies of hydrothermal basalt alteration have shown that a large pH drop accompanies the precipitation of secondary Mg-OH minerals (Seyfried and Bischoff, 1981), and experimental and modeling work has shown that lower pH values can speed up basalt dissolution by several orders of magnitude (Gudbrandsson et al., 2011), with small effects still predicted to persist at high temperatures (Aradóttir et al., 2013). This implies that precipitation of Mg-OH minerals may serve to increase the exchange rates between seawater and basalt, and thus could have additional kinetic effects on the composition of hydrothermal fluids. A large pH drop especially accompanies the precipitation of MHSH phases (Bischoff and Seyfried, 1978; Haymon and Kastner, 1986; Janecky and Seyfried, 1983), which are likely to be the metastable precursors of anhydrite-2, and this effect may have been completely absent in Paleoseawater with [Ca] > [SO_4] (Figs. 2, S1, S2).

If the removal of dissolved Mg from the hydrothermal fluid as it circulates through the system is responsible for acidifying the fluid (Bischoff and Seyfried, 1978; Seyfried and Bischoff, 1981), then at times of low seawater [Mg], hydrothermal fluids might be less acidified and hence less reactive. Any slowing of the reaction between basalt and hydrothermal fluid would enhance the likelihood of seawater Sr and Ca persisting through the hydrothermal system and increase their presence in the fluid budget at the vents, which would increase the $^{87}Sr/^{86}Sr$ of exiting hydrothermal fluids.

A first-order attempt at exploring the potential dependence of seawater-basalt exchange rates on seawater Mg concentrations is made by scaling θ_{exch} with $[Mg]_{sw}$ according to:

$$\theta(t) = \theta(0)\left\{\frac{[Mg]_{sw}(t)}{[Mg]_{sw}(0)}\right\}^{m} \qquad \text{[Eq. S2.9]}$$

This formulation allows us to vary the fluid-basalt exchange to assess its effect on the results. Our base model in the main text is $m = 0$, and we evaluate the results for m up 3. In all of the cases where $m \neq 0$, this factor serves to subtly increase the amount of recycled seawater Sr in hydrothermal output fluids by decreasing the seawater-basalt exchange, but would have much greater effects if θ_{exch} (calculated to be ~0.108 for modern) was larger.

Dual porosity model: To explore possible changes in reaction rates from another point of view, we construct a steady state dual-porosity model for hydrothermal fluids based on previous work (DePaolo, 2006). The parameters are set such that modern seawater exits the system with average vent fluid $^{87}Sr/^{86}Sr$ compositions. This allows us to then explore the effects of changing [Sr] and reaction rates (Fig S5).

The dual-porosity model assumes steady state with no change in porosity (dissolution = precipitation rate), and represents flow through a fracture with chemical diffusion supplying basaltic components from the walls. The model applies well to hydrothermal Sr isotopic evolution in systems like MOR where circulation is dominated by fluid flow in fractures. The essential effect of fractures is that the extent of exchange depends on the amount of chemical communication between fractures and bulk matrix. The latter is determined by the ratio of diffusivity and the reaction rates in the inter-fracture rock matrix [parameter denoted as "R" by (DePaolo, 2006)].

The dual-porosity model constructed has parameters set so that emergent fluids have $^{87}Sr/^{86}Sr$ = 0.7037 when using modern seawater (other input parameters given in the figure caption). We then explore the effects of increasing [Sr] and reducing reaction rates in order to simulate potential differences resulting from changes in paleoseawater composition. The modern case (position “A” on Fig. S2.5) is calculated assuming the initial fluid [Sr] is ~35 μM due to Sr removal associated with earlier anhydrite precipitation, consistent with our previous charge-balance calculations. The parameters used then require that the reaction rate, R, be about 0.0003 yr^{-1} to match modern $^{87}Sr/^{86}Sr$ output. The units mean that 0.03% of the rock mass dissolves (and reprecipitates as secondary minerals) each year.

To evaluate the difference with paleoseawater, the model is modified so that the initial fluid has [Sr] of 285 μM in order to simulate higher seawater [Sr] and lower losses to anhydrite, as suggested by our Cretaceous charge-balance models. With higher levels of seawater [Sr] entering the reaction zone, the exiting fluid was calculated to increase to 55% seawater Sr, position “B” on figure S2.5, despite having the same reaction rate as the first simulation. When we additionally decreased the reaction rate by an arbitrary factor of three (0.0001 yr^{-1}), the $^{87}Sr/^{86}Sr$ increased to 71% SW Sr, position “C” on figure S2.5. Contours for constant seawater Sr fractions in the exiting hydrothermal fluids for various reaction rates and [Sr] concentrations remaining after sulfate removal are also shown.

The dual porosity model indicates that an arbitrary three-fold decrease in reaction rate relative to modern would result in a ~15-20% increase in seawater-derived Sr in the exiting fluids, with greater differences as seawater [Sr] increases (Fig. S2.5). From this model, we conclude that relatively small changes in reaction rates for hydrothermal exchange, associated with variable paleoseawater chemistry, would lead to fairly significant changes in the $^{87}Sr/^{86}Sr$ of hydrothermal fluids. However, reaction rate data for dissolution/precipitation of individual minerals and experimental work using modified seawater compositions will be necessary in order to construct a realistic model for MOR hydrothermal systems, which would ideally include reactive transport modeling and kinetic effects.

2.8.4. Supplementary figures

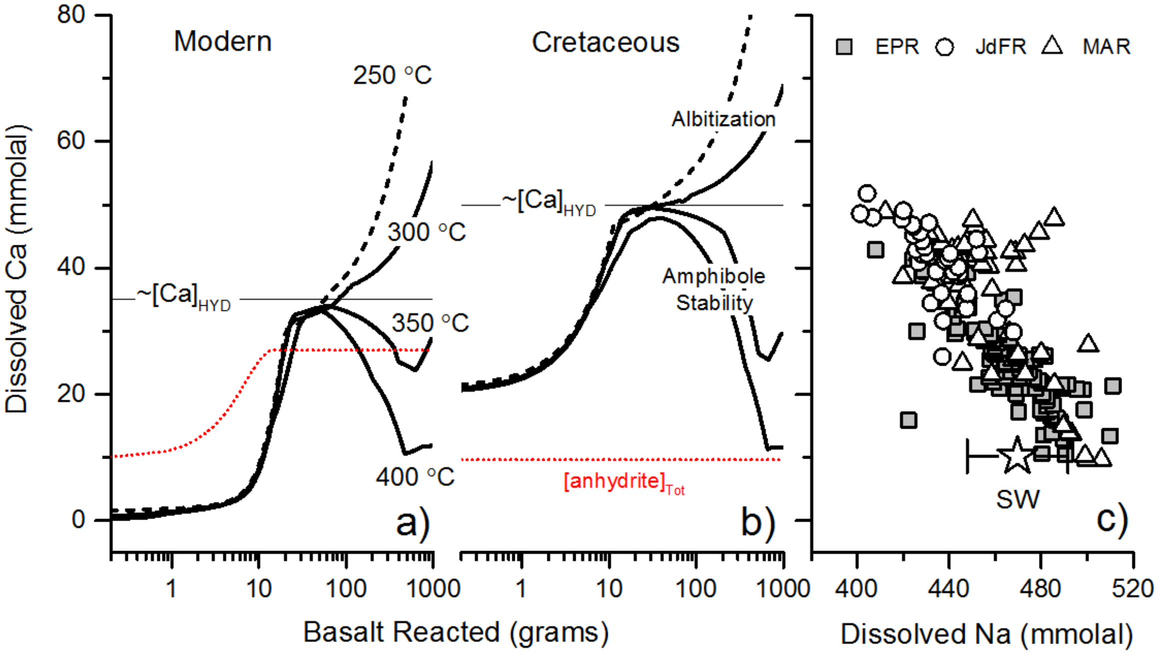

Fig. S2.1. Evolution of dissolved [Ca] in hydrothermal reaction-path models where 1 kg of basalt is incrementally added to 1 kg of (a) modern seawater and (b) estimated Cretaceous seawater. Individual curves represent independent isothermal simulations between 250 and 400 °C, cumulative milliequivalents of precipitated anhydrite are shown for reference (red dotted line, see text). 250 °C calculations (dashed) were truncated at fluid/rock = 2 (500 g basalt reacted). In (c) error on [Na] in seawater reference point (star) reflects general uncertainty in evaluating charge balance compensation with [Ca] in vent fluids due to the order of magnitude higher concentration. Vent fluid data are from various sources (Butterfield et al., 1997, 1990; Butterfield and Massoth, 1994; Campbell et al., 1988; Charlou et al., 2002, 2000, 1996; Edmond et al., 1995; Foustoukos et al., 2009; Foustoukos and Seyfried, 2007; Gallant and Von Damm, 2006; Grimaud et al., 1984; Kumagai et al., 2008; Michard et al., 1984; Pester et al., 2012, 2011, Seyfried et al., 2011, 2003, Von Damm et al., 1985, 2002, 1998, Von Damm, 2004, 2000).

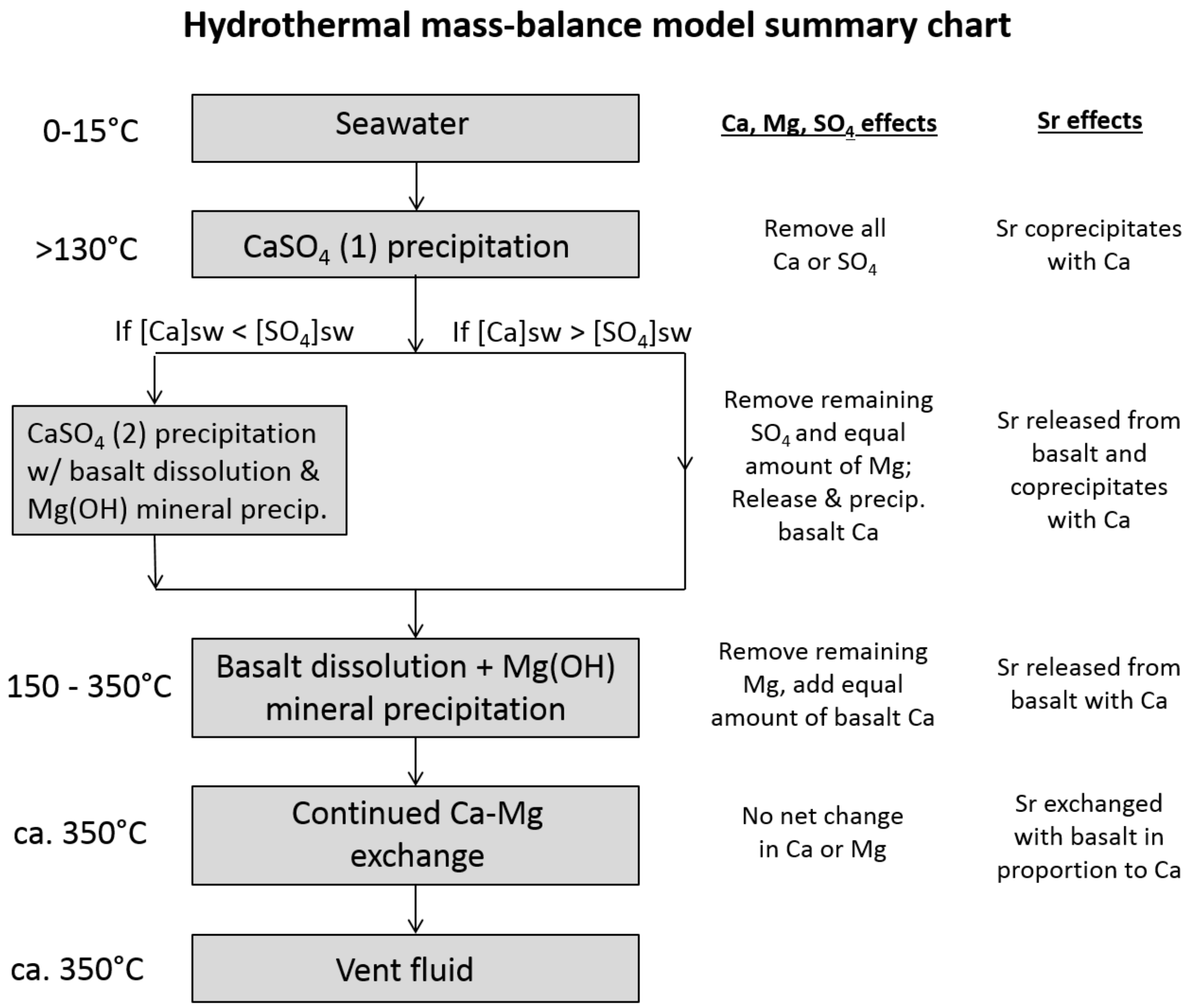

Fig. S2.2. Schematic for hydrothermal model, showing the four major steps discussed in the main text.

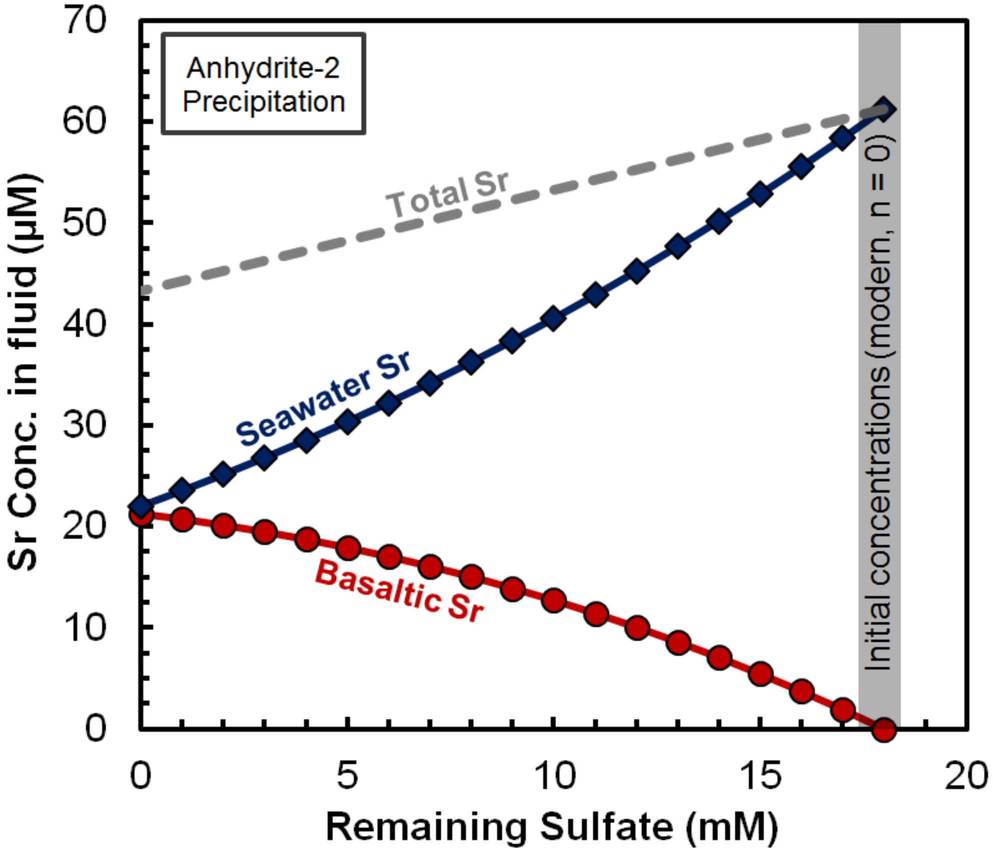

Fig. S2.3. Sr concentrations during precipitation of anhydrite-2 using modern seawater input values. Lines represent [Sr] in the evolving hydrothermal fluid: grey line is total [Sr], blue line is seawater [Sr], and red line is basaltic [Sr]. Initial Sr is equal to $[Sr]_{SW} - [Sr]_{anh1}$ (at n =0) and the number of steps (n) in the iterative calculation is equal to $[Ca]_{anh2}$, according to equations [S2.3] through [S2.6]; In the modern case, $[Ca]_{anh2} = 18$.

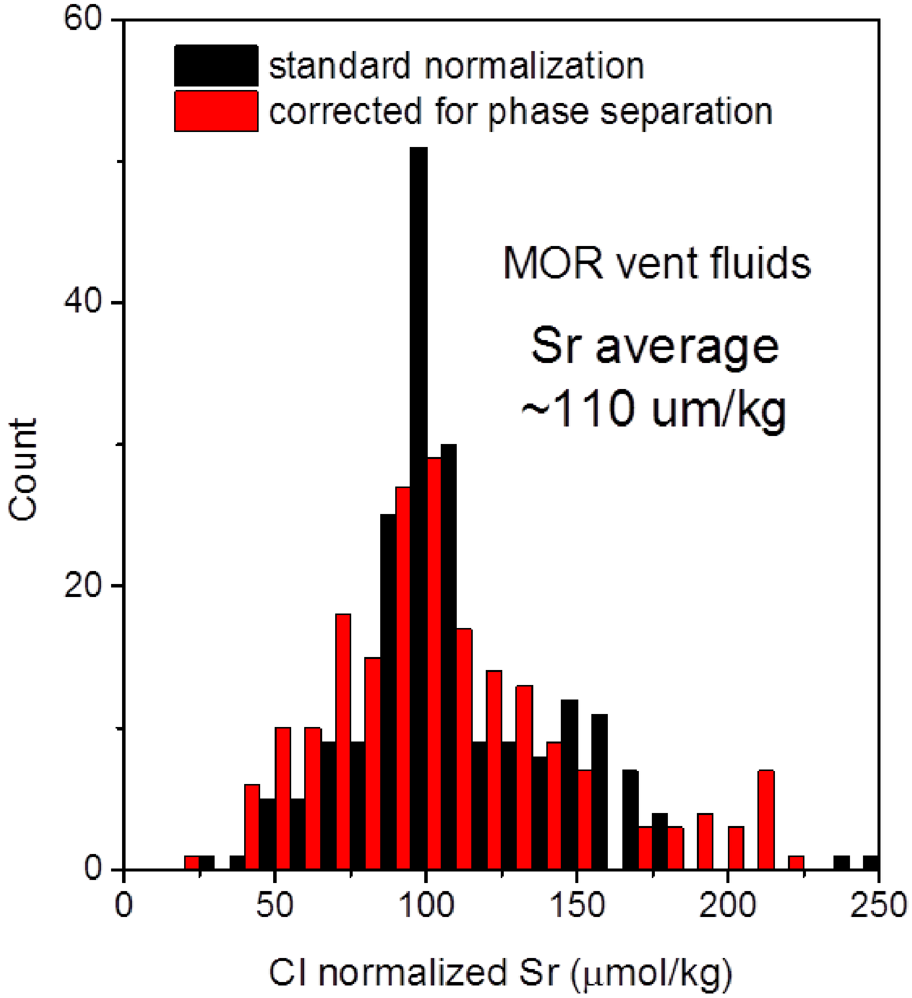

Fig. S2.4. Histogram of end-member [Sr] values in deep-sea hydrothermal fluids, normalized to seawater chlorinity ($[Cl]_{SW}$ = 548 mmol/kg). Standard normalization (black bars) and a normalization accounting for partitioning due to phase separation (Pester et al., 2015) (red bars) are both presented. Data are from various sources (Butterfield et al., 1997, 1994, 1990; Butterfield and Massoth, 1994; Campbell et al., 1988; Charlou et al., 2002, 2000, 1996; Edmond et al., 1995; Foustoukos et al., 2009; Foustoukos and Seyfried, 2007; Gallant and Von Damm, 2006; Grimaud et al., 1984; Kumagai et al., 2008; Michard et al., 1984; Pester et al., 2014, 2012, 2011; Reeves et al., 2011; Seyfried et al., 2011, 2003, Von Damm et al., 1985, 2002, 1998, Von Damm, 2004, 2000).

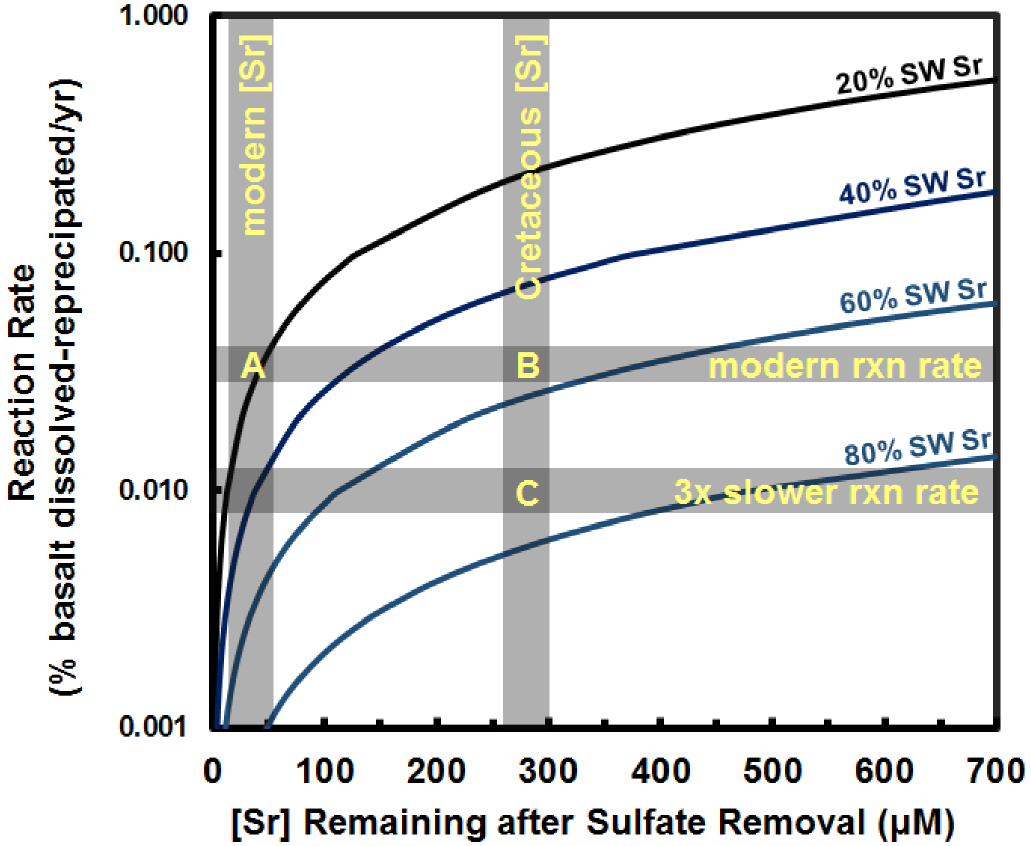

Fig. S2.5. Hydrothermal output $^{87}Sr/^{86}Sr$ compositions (as % seawater Sr, plotted as curves) as functions of reaction rate and seawater [Sr] remaining after full removal of seawater sulfate as anhydrite, calculated using a steady-state dual porosity model (DePaolo, 2006) described in the SI text. Vertical and horizontal bars demarcate modern [Sr], modern reaction rate (0.03% yr^{-1}), estimated Cretaceous [Sr], and an arbitrarily 3x slower reaction rate (0.01% yr^{-1}). At “A” exiting fluid has ~18% seawater Sr. At “B” exiting fluid has ~55% seawater Sr, and at “C” exiting fluid has 71% seawater Sr; these represent hydrothermal fluid $^{87}Sr/^{86}Sr$ of 0.7037, 0.7062, and 0.7073, respectively. Other parameters: fracture fluid velocity = 820 m/yr, fracture width = 5 cm, fracture spacing = 2 m, matrix porosity = 0.01.

Chapter 3

Radiogenic Ca isotopes confirm post-formation K depletion of lower crust

3.1. Overview

Heat flow studies suggest that the lower crust has low concentrations of heat-producing elements. This could be due to either (i) greater fractions of basaltic rock at depth or (ii) depletion of radioactive elements from rocks with more evolved (andesitic to granodioritic) compositions. However, seismic data suggest that lower crust is not predominantly basaltic, and previous studies (using Pb and Sr isotopes) have shown that lower-crustal rocks have experienced significant losses of U and Rb. This loss, however, is poorly constrained for K, which is inferred to be the most important source of radioactive heat on the early Earth. Our high-precision Ca isotope measurements on a suite of granulite-facies rocks and minerals from several localities show that significant losses of K (~60% to >95%) are associated with high-temperature metamorphism. These results support models whereby depletion of heat from the lower crust, and consequent stabilization of continental cratons in the Precambrian, are largely due to high-temperature metamorphic processes. The relative changes in whole-rock K/Ca suggest that 20-30% minimum (granitic) melt removal can explain the K depletions.

3.2. Introduction

Samples from the lower continental crust can be brought to the surface in two major ways, either (i) as coherent high-grade terranes, through tectonic processes, or (ii) as individual xenoliths, through deep-seated volcanism. Based on analysis of these samples it has been established that much of the lower continental crust was heated to granulite-facies conditions (> ~800 °C) and lost significant amounts of its original heat-producing element budget (Rudnick and Gao, 2014), yet it is uncertain whether this is a sufficient explanation for modern heat-flow data without invoking greater fractions of mafic crust at depth (Hacker et al., 2015).

Metamorphic heating results in the breakdown of primary hydrous mineral phases to anhydrous mineral assemblages. Typical reactions involve the transformation of amphibole and mica into feldspar, pyroxene, sillimanite/kyanite, and (at higher pressures) garnet. These transformations are typically accompanied by the generation of granitic liquids (rich in incompatible elements and containing dissolved H_2O) that are generally lost from the system, but found preserved as microscopic melt-inclusions (*e.g.* Bartoli *et al.*, 2016; Ferrero *et al.*, 2018; Stepanov *et al.*, 2016). There is also evidence that fluid loss in the absence of melt-generation could contribute to the geochemical changes, as suggested by the common observation of high Th/U in granulite-facies rocks (Rudnick and Gao, 2014). Generation and loss of melt, however, is viewed in the more recent literature as being the primary mechanism affecting granulite and ultrahigh temperature (UHT) rocks (*e.g.* Guernina and Sawyer, 2003; Kelsey and Hand, 2015; White and Powell, 2002). The lower U, Th, (and K) concentrations and higher-density of lower continental crust (Hacker et al., 2015; Rudnick and Gao, 2014) could therefore be attributed to the effects of melt loss during high-temperature metamorphism.

Previous work suggesting that U is lost from the lower crust has been facilitated by measurement of Pb isotopes and by comparisons with Th (Rudnick and Gao, 2014), which can also be lost during partial-melting at extreme conditions (Ewing et al., 2014; Stepanov et al., 2014). However, ancient K-loss during melting of lower crust is hard to constrain because there are few means to establish K content of the protoliths (Rudnick et al., 1985). Previous studies show that Rb is preferentially lost during granulite-facies metamorphism relative to Sr and K (Rudnick et al., 1985), and that there can also be K lost relative to Ca (Ewing et al., 2014; Stepanov et al., 2014). However, this argument has considerable uncertainty for K when the protoliths are unavailable for analysis, and the magnitude of K loss from lower crust remains poorly constrained. To address this problem, we use measurements of radiogenic ^{40}Ca in lower-crustal granulite-facies rocks and minerals. The K-Ca system is well-suited for this purpose because ^{40}K decays to ^{40}Ca (and ^{40}Ar, $t_{1/2}$ ~1.25 Gy), the two elements are separated from each other during partial melting, and the daughter product is generally more compatible than the parent (Marshall and DePaolo, 1989).

3.3. Samples and analytical procedures

We report radiogenic ^{40}Ca variations (ε_{Ca}) in granoblastic to porphyroblastic mafic, granitic, and pelitic whole-rock samples and mineral separates from four localities: the Napier Complex, Antarctica (NC); the Slave Province, Canada (SP); the Ivrea-Verbano Zone, Italy (IVZ); and the Lhasa Block, Tibet (Sumdo eclogite, SE). The rocks span a wide range of chemical compositions and metamorphic pressure and temperature conditions, including granulite/ultrahigh temperature (n = 17), amphibolite (n = 3), and eclogite facies (n=1), and range in age from Archean to Mesozoic (see Supplementary Information and Tables S3.1 through S3.4). The SE sample is not likely to have lost significant amounts of K and is included only for reference (Fig. 3.1). Ca isotopic compositions were measured by TIMS at the University of California, Berkeley, and are reported in epsilon notation relative to bulk-silicate Earth (BSE, see Supplementary Information, Table S3.5), according to equation (3.1).

$$\varepsilon_{Ca} = \left(\frac{\left[{}^{40}Ca / {}^{44}Ca \right]_{measured}}{\left[{}^{40}Ca / {}^{44}Ca \right]_{BSE}} - 1 \right) x\ 10^4 \qquad \text{(Eq. 3.1)}$$

3.4. ε_{Ca} in low-K metamorphic rocks and minerals

Garnet is an ideal mineral for ε_{Ca} analyses because it effectively excludes K, is easy to separate, and commonly contains substantial amounts of Ca. Given a clean mineral separation, any excess radiogenic Ca in garnet must be inherited from ^{40}K that decayed to ^{40}Ca in the *protolith*, prior to garnet formation. We find that clean garnet separates from our samples have ε_{Ca} ranging from 0 to +42 (Table S3.5). Higher ε_{Ca} values are found in garnets with lower grossular content [molar Ca/(Ca+Fe+Mg+Mn) < ~5%], from rocks with generally higher whole-rock peraluminosity [defined as molar $Al_2O_3/(CaO+Na_2O+K_2O)$ and denoted A/CNK (Fig. 3.1a)]. In mafic granulites, both garnet and low-K plagioclase separates (which were sampled in the absence of garnet), have a narrow ε_{Ca} range from 0 to +3 (Fig. 3.1b). Whole-rock and high-K feldspar separates were also measured (Fig. S3.1) in order to obtain rough K-Ca isochrons (Fig. S3.2), which are in general agreement with more precise dating methods for the various regions (Supplementary Information).

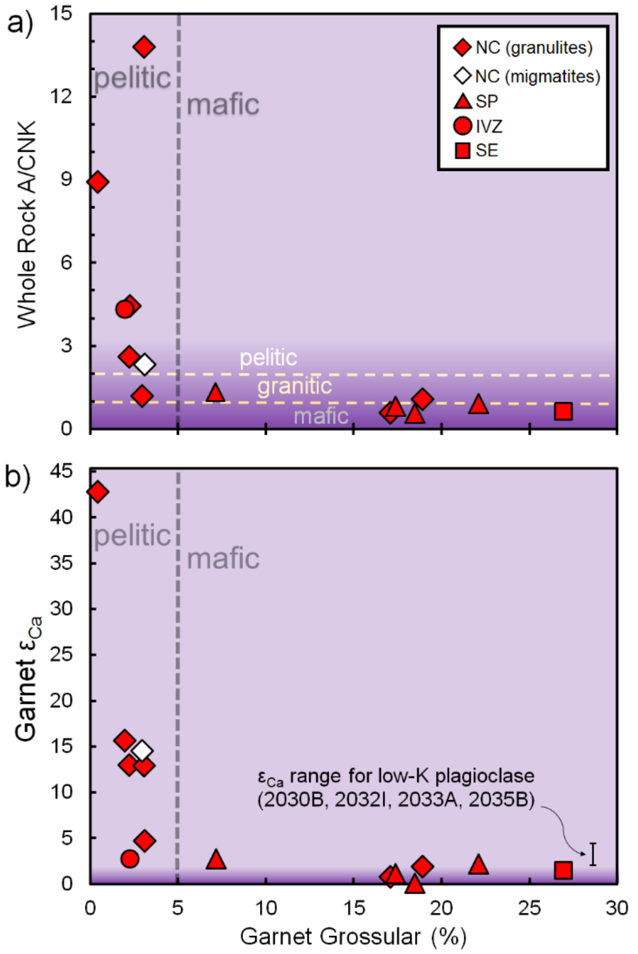

Fig. 3.1. Garnet grossular content versus **(a)** whole-rock peraluminosity index (A/CNK) and **(b)** garnet ε_{Ca} values (for samples containing garnet, n = 14). 2σ uncertainties (±1 for ε_{Ca}) are smaller than the symbols. Approximate mafic, granitic, and pelitic compositional zones are separated by dashed lines (Supplementary Information). Darker purple band in **(b)** represents Bulk-Silicate Earth ($\varepsilon_{Ca} = 0$) composition, corresponding to ^{40}Ca/^{44}Ca = 47.156 (Supplementary Information).

3.5. Protolith K/Ca estimates

Large depletions in K associated with metamorphism can be detected with our data on garnet mineral separates. Garnet and whole-rock measurements for NC sample 2040C, for example, have indistinguishable (yet highly elevated) ε_{Ca} values (+12.5, see Table S3.5) due to a nearly complete loss of K from the rock during metamorphism, resulting in a near-zero K/Ca similar to that of garnet. For other samples where K-loss is less extreme, protolith K/Ca values are evaluated from ε_{Ca} (garnet or low-K plagioclase/whole-rock samples, see Supplementary Information) and the time interval between protolith formation and granulite-facies metamorphism.

Using the metamorphic and protolith ages for each locality (Supplementary Information), we are able to estimate the protolith K/Ca values using equation (3.2), adapted from (Marshall and DePaolo, 1989).

$$[K/Ca]_{protolith} = \frac{\varepsilon_{Ca}(t_2) - \varepsilon_{Ca}(t_1)}{Q_{Ca}(e^{\lambda_K t_1} - e^{\lambda_K t_2})} \qquad \text{(Eq. 3.2)}$$

Where $\varepsilon_{Ca}(t_2)$ and $\varepsilon_{Ca}(t_1)$ are ε_{Ca} values at metamorphic age (t_2) and protolith age (t_1), respectively; λ_k is the total decay constant of ^{40}K (assumed 0.554 Gyr^{-1}), and Q_{Ca} (~1.0804) is a factor incorporating the branching ratio of ^{40}K decay and the abundances of ^{40}K, ^{44}Ca, and ^{40}Ca relative to BSE.

In Figure 3.2, we show the effect of protolith age uncertainty on the estimate for $[K/Ca]_{protolith}$ for our samples from the NC, based on equation (3.2). This equation provides a *minimum* constraint on $[K/Ca]_{protolith}$ values because of three assumptions implicit in our use of the equation: (i) the oldest protolith age estimates for the various localities, (ii) single-stage evolution from BSE [$\varepsilon_{Ca}(t_1) = 0$] to garnet ε_{Ca} values [$\varepsilon_{Ca}(t_2)$], and (iii) that garnets form out of the bulk protolith Ca pool at the time of metamorphism. Younger protolith ages, multiple stages for $[K/Ca]_{protolith}$ (e.g. increases driven by weathering/metasomatic processes), and/or partial loss of radiogenic Ca from K-bearing minerals prior to garnet formation (through earlier melting events), would all require higher $[K/Ca]_{protolith}$ to reach the same initial ε_{Ca} values at the time of metamorphism.

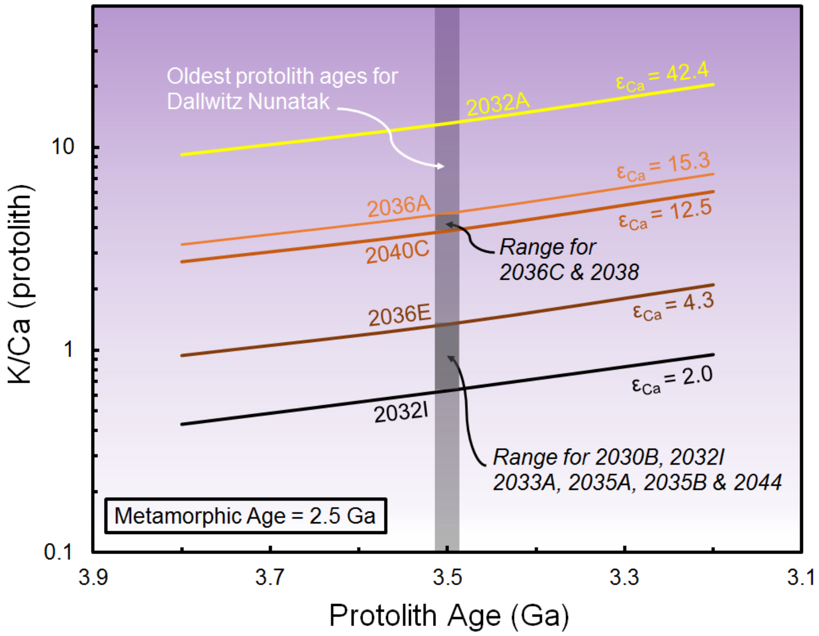

Fig. 3.2. Dependence of $[K/Ca]_{protolith}$ on protolith age for samples from Dallwitz Nunatak (NC, n = 12) based on equation (3.2). Curves are labeled by sample name and delineate constant values for initial ε_{Ca} at 2.5 Ga with varying protolith ages. Grey band demarcates oldest protolith age found at Dallwitz Nunatak, in the northern Napier Complex (see Supplementary Information).

3.6. Potassium loss during high-T metamorphism

Including data from the other localities, we find as expected that mafic samples have lower $[K/Ca]_{protolith}$ (< 1), and pelitic samples have higher $[K/Ca]_{protolith}$ ranging from 1 to ~13. Comparing these estimates with $[K/Ca]_{modern}$ in the whole rocks (Fig. 3.3), we are able to assess K-mobility during granulite metamorphism (see Figure S3.3 for data labels).

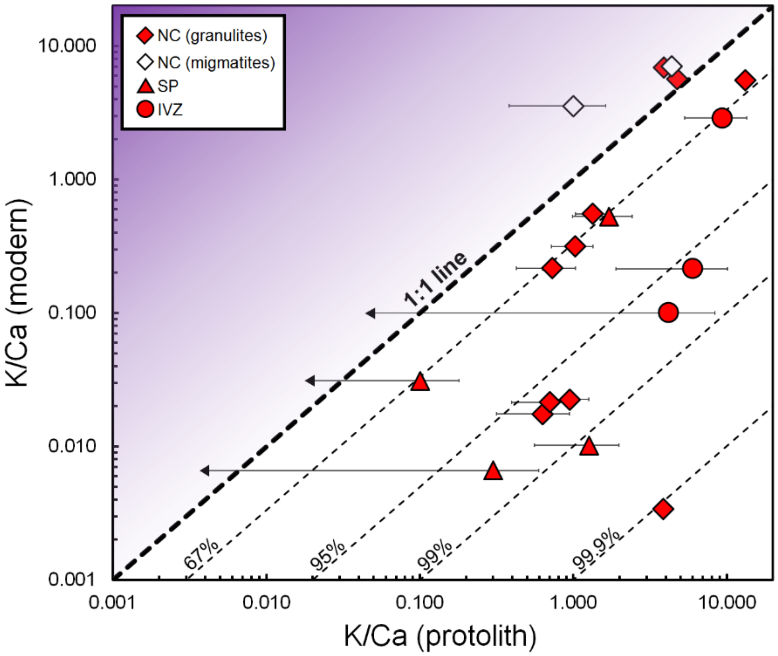

Fig. 3.3. Whole rock K/Ca (modern) versus K/Ca (protolith) based on ε_{Ca} [equation (3.2)]. NC granulite samples (n = 10), NC migmatites (n = 2), SP samples (n = 4), IVZ samples (n = 3). Contours indicate relative K-loss (in %) assuming constant Ca. Uncertainties in protolith K/Ca are calculated using equation (3.2), using our 2SD on ε_{Ca} (±1); arrow terminations represent samples within error of BSE. Protolith-metamorphic ages: 3.5-2.5 Ga (NC); 3.0-2.5 Ga (SP); and 0.6-0.3 Ga (IVZ) (see Supplementary Information). Uncertainties for modern K/Ca are < ~5%.

Our results indicate that most granulite samples have measured K/Ca that is substantially lower than that calculated for the protolith, indicating significant K-loss during metamorphism. The samples fall into 3 rough groups: one group has no K-loss, or a slight K enrichment, and the other groups cluster at 67% and 97%; one NC sample suggests greater than 99.9% K-loss (Fig. 3.3). Samples with younger ages and lower ε_{Ca} have larger uncertainties. Two pelitic granulites and migmatites from the NC have an apparent increase in K/Ca relative to their protolith compositions, which can potentially be explained by the presence of (externally-derived) captured melt. Our data suggest that granulite-facies samples with less than ~2 wt% modern whole-rock K_2O have generally lost K, and samples with > 2 wt% have generally gained K (relative to Ca, Figure S3.4). Although we are unaware of K-loss estimates for the NC and SP, our data agree with previous estimates for the IVZ, where granulite-facies samples have about 2/3 less K than their lower-temperature (amphibolite-facies) counterparts (Ewing et al., 2014). Our results are also in agreement with previous work high-lighting the metamorphic losses of heat-producing elements such as U/Th and Rb/Sr in the Napier Complex (*e.g.* DePaolo *et al.*, 1982; Kelsey and Hand, 2015).

3.7. Melt-loss modeling

Although there is still some debate as to whether or not granulites need externally-derived fluids in order to initiate melting (Aranovich et al., 2016; Clemens et al., 2016), the conclusion from melting experiments (Gao et al., 2016) and from trapped melt-inclusions in peritectic minerals (Bartoli et al., 2016; Ferrero et al., 2018; Stepanov et al., 2016) is that granulites are often associated with loss of granitic melt. Given that we can quantify relative K/Ca decreases, we are also able to place constraints on the amount of melt-loss required to form our samples by modeling the partitioning of K and Ca between melt and residual minerals.

To estimate K/Ca fractionation during partial melting, we use a modified non-modal batch melting model, where the bulk distribution coefficient for K (D_K) is a function of the mass fraction of remaining residual K-feldspar (the most significant K-bearing mineral at granulite-facies conditions), and the bulk distribution coefficient for Ca (D_{Ca}) is a function of the mass fraction of residual plagioclase + clinopyroxene (see Supplementary Information, Fig. S3.5).

3.8. Model results

Comparing our model estimates for $[K/Ca]_{solid}/[K/Ca]_o$ versus $[K_2O]_{solid}$ (at various values of F) to our ε_{Ca}-based $[K/Ca]_{mdrn}/[K/Ca]_{protolith}$ estimates and $[K_2O]_{mdrn}$ analyses for granulite-facies samples, and assuming that melt is completely lost from the system, we find that most of the samples are consistent with 20-30% melting, with the most extreme sample suggesting melt fractions of ~50% (Fig. 3.4). Although the distribution coefficients used in our model are currently rough estimates, varying K and Ca distribution coefficients over a range of likely values (Fig. S3.6) does not significantly change the results, which depend most significantly on $[K/Ca]_{protolith}$.

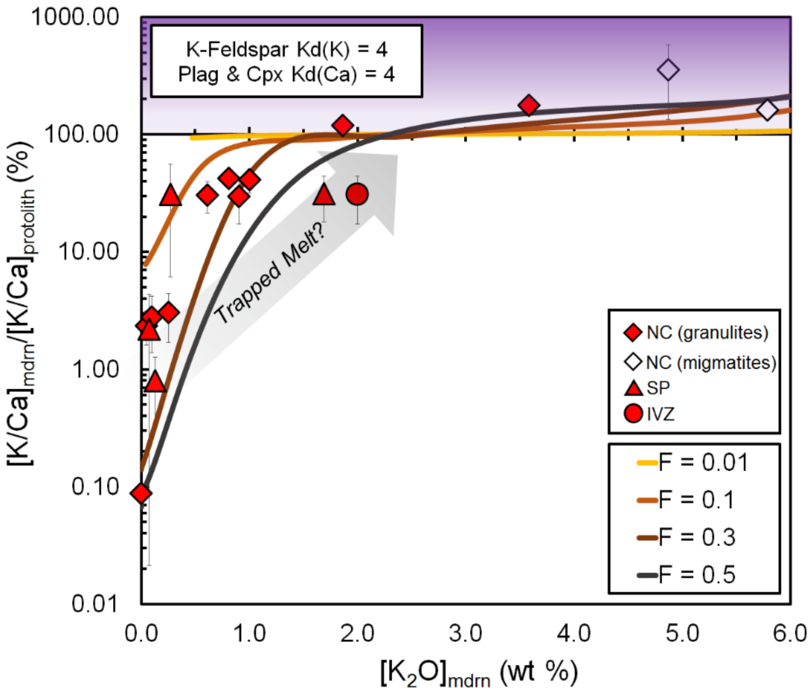

Fig. 3.4. ε_{Ca}–based $[K/Ca]_{mdrn}/[K/Ca]_{protolith}$ [equation (3.2)] versus measured $[K_2O]_{mdrn}$ (excluding amphibolite and eclogite samples). Predictions from our melting model [equations (S3.2 through S3.4)], for various starting compositions (same as in Figure S3.5) varying degree of partial melting (F) (colored lines). NC granulites (n = 10), NC migmatites (n = 2), SP samples (n = 4), IVZ sample (IV-16-24, n = 1). Vertical error bars calculated using equation (3.2), combining with those from XRF (< ~5% for K_2O/CaO); horizontal error bars are smaller than the symbols. Arrow shows effect of trapped melt on residual solids. Although the samples plotting above 100% are consistent with model-predictions for high K/Ca protoliths, petrographic evidence (see SM) suggests that these enrichments (based on minimum K/Ca estimates) are the probable result of (externally-derived) trapped melt.

The model results generally agree with other approaches for estimating melt production during granulite-facies metamorphism, including pseudosection analyses (Green et al., 2016; Palin et al., 2016; Redler et al., 2012; White and Powell, 2002; Yakymchuk and Brown, 2014) and other methods (Bartoli, 2017; Guernina and Sawyer, 2003). These estimates typically range from ~20-50% total melt depending on protolith compositions and P-T-time conditions.

3.9. Discussion and conclusions

Although our assumption of complete melt-segregation may be an overestimate, significant melt-loss is a common feature associated with granulite-facies terranes (*e.g.* Brown, 2002; Guernina and Sawyer, 2003), and a minimum of 50-70% of generated melt (assuming 40% total melt) must be lost in order to retain a high-temperature mineral assemblage (White and Powell, 2002). If melt is not fully lost from the system, our model requires greater total melt fractions in order to match $[K/Ca]_{mdrn}$ measured in the samples today. This suggests that our melting model (which uses minimum $[K/Ca]_{protolith}$ estimates and assumes total loss of melt), provides minimum estimates for total melt fractions.

Based on ε_{Ca} data, and assuming conservative protolith ages for each locality, we find that many lower-crustal samples from the Napier Complex, Ivrea-Verbano Zone, and the Slave Province have undergone significant amounts of K depletion, with relative K/Ca decreases ranging from ~60% to greater than 95%. These results confirm that K, which is inferred to be the most important heat-producing element in the Archean, is efficiently mobilized and removed from the lower crust during metamorphism. This observation implies that greater fractions of mafic rock in the lower crust are not necessary to explain modern heat-flow data, and supports crustal evolution models where continental stabilization is promoted through high–temperature metamorphism and depletion of radioactive elements from the lower crust.

3.10. Supplementary information

3.10.1. Sample descriptions and petrography

Granulite-facies metamorphism occurs when rocks are subjected to temperatures greater than about 800 °C. This condition of prolonged high temperature can occur in geologic settings ranging from short-duration heating events (< 20 My) in back-arc settings (Brown, 2007, 2006; Pownall et al., 2014), to regional-scale long-duration events (up to 100 My) in large hot orogenies (LHO) (Harley, 2016; Kelsey and Hand, 2015), as well as during rifting and extreme subduction of crust (Hermann and Rubatto, 2014). Details of past metamorphic settings are inferred using a combination of geochronology, thermobarometry, and pseudosection modeling, and mainly differ based on pressure-temperature-time (P-T-t) paths, which range from clockwise heating/pressurization with subsequent decompression (gradual to near isothermal) to heating followed by near isobaric cooling at depth (Harley, 2016).

Twelve ultrahigh-temperature (UHT) granulite samples were collected by E.S.G. in January 1978 on an east-west traverse of Dallwitz Nunatak, in the Archean Napier Complex (NC), Enderby Land, East Antarctica. Four lower crustal granulite xenoliths, provided by T.C., come from the Diavik Diamond Mine in the Lac-de-Gras region of Canada (Slave Province, SP). One ultrahigh-temperature (UHT) facies metapelite, along with two mafic amphibolites, come from the Ivrea-Verbano Zone (IVZ), collected by D.R. along a transect of increasing temperature. A fourth sample (IV-16-19) is determined to be a late-stage crustally-contaminated gabbro intrusion in the same area. A single sample of the Sumdo eclogite (SE) was collected by D.J.D. from the Lhasa Block, Tibet. The P-T-t paths for the three major locations vary from short-lived clockwise heating (up to UHT conditions) and exhumation in the IVZ (Ewing et al., 2013; Pape et al., 2016; Redler et al., 2012) with peak pressures up to ~1.2 GPa, to long-lived heating followed by isobaric cooling in the NC and SP at pressures ~1.0-1.3 GPa (Davis *et al.*, 2003; Harley, 2016; Mitchell and Harley, 2017, this study)

3.10.1.1. Antarctic samples (Napier Complex)

The NC exposed in Dallwitz Nunatak (formerly called Spot 945, which has coordinates 66° 57' S, 51° 30' E and is part of the Tula Mountains east of Amundsen Bay, Enderby Land) comprises a variety of rock types metamorphosed under UHT conditions, including mafic and pelitic granulites and subordinate migmatite units and granitic gneisses. Samples are numbered increasing from west to east, with samples 2033 and above collected northeast of the summit. According to PT estimates for the region, our samples are likely to have formed at ~1.0 GPa with peak temperatures of ~900 °C, followed by slow isobaric cooling (Harley, 2016; Mitchell and Harley, 2017). We describe the mineralogy and field relationships as follows:

2030B. Mafic layer in a pyroxene-plagioclase granulite. Dominantly orthopyroxene with minor plagioclase and clinopyroxene; granoblastic texture. Traces of secondary biotite. Opx and Cpx show lamellar exsolution, plagioclase has traces of antiperthitic exsolution.

2032A. Layered garnet-sapphirine-quartz metapelite, interbedded with mafic pyroxene granulite (2032I). Sapphirine grains are free of garnet inclusions. Sapphirine is overgrown by garnet, sillimanite, and cordierite. Hercynite and quartz are included in the sapphirine. Cordierite displays twinning; vermicular cordierite-quartz symplectites are fairly abundant. Rare orthopyroxene grains and secondary biotite are also present.

2032I. Equigranular mafic pyroxene granulite alternating with layers of metapelite (2032A). Dominantly orthopyroxene with minor plagioclase and clinopyroxene. Both clinopyroxene and orthopyroxene have lamellar structure. Minor secondary biotite.

2033A. Coarse-grained mafic pyroxene granulite. Dominantly plagioclase with subordinate orthopyroxene and clinopyroxene, granoblastic texture. Secondary olive-colored hornblende and biotite replacing pyroxenes also present. Minor antiperthitic exsolution.

2035A. Center of metamorphosed ultramafic dike. A coarse-grained biotite-pyroxene mafic rock showing lineation and foliation with dominant orthopyroxene, subordinate plagioclase, olivine, clinopyroxene & hornblende, and minor biotite with indistinct preferred orientation. Olivine appears relatively fresh. Pyroxenes exhibit lamellar exsolution. Minor hercynite and opaques (prob. magnetite) are intergrown. The dike is 1.7 m thick with a paler marginal zone 7-8 cm thick (2035B) and pinches out to the east. The lower contact is folded, and appears to be discordant, possibly because of transposition. Overall, the dike appears concordant with the gneissic layering.

2035B. Outer-edge of metamorphosed ultramafic dike. From pale-colored, 7-8 cm thick, marginal zone of mafic dike (2035A). Strong granoblastic texture, dominantly orthopyroxene with minor plagioclase and clinopyroxene. Minor hornblende and biotite are included within orthopyroxene, which has a lamellar structure. Plagioclase shows minor antiperthitic exsolution.

2036A. Rusty garnet quartzite unit, finely layered white and gray on centimeter scale. Interbedded with units represented by samples 2036C and 2036E. Dominated by quartz-cordierite vermicular intergrowths, subordinate garnet, K-feldspar, and well-aligned sillimanite. Minor euhedral sillimanite, rutile, and hercynite inclusions in garnet. Hercynite grains appear entrained in quartz-cordierite-K-feldspar regions (interpreted as trapped melt). K-feldspar contains minor perthitic exsolution.

2036C. Fine-grained, rusty garnet-sillimanite quartzite with melt veinlets. Dominantly quartz and cordierite with strongly perthitic K-feldspar (interpreted to be trapped melt) with significant amounts of garnet and sillimanite.

2036E. Coarse-grained, garnet-sillimanite quartzite. Dominantly garnet with subordinate quartz and plagioclase. Plagioclase has minor antiperthitic exsolution. Hercynite is included in garnet. Minor secondary biotite around garnet. Sillimanite lineation seems to be parallel to measured fold axes of the outcrop layers, also outlined by garnet and possible orthopyroxene.

2038. Leucocratic aplitic gneiss from migmatite unit. Dominantly quartz, K-feldspar with string perthite exsolution, and minor rutilated garnet and subordinate sillimanite. Garnet has inclusions of K-feldspar and quartz, along with minor amounts of ilmenite, rutile, monazite & zircon.

2040C. Garnet-pyroxene-biotite lens (about 1m across in a mafic layer**)**. Dominantly garnet and orthopyroxene, minor quartz and traces of secondary biotite rimming garnet. Granoblastic texture. Garnet has abundant rounded quartz inclusions. There is a single patch of possible cordierite + quartz "fingerprint" symplectite.

2044. Granitic gneiss collected from eastern-most part of outcrop. Dominantly K-feldspar with subordinate quartz and minor plagioclase and orthopyroxene with traces of skeletal garnet and secondary biotite. Feldspar is mesoperthitic, but locally grain margins free of lamellae, opaques have inclusions of spinel (hercynite). Minor alteration of Opx.

3.10.1.2. Diavik xenolith samples (Slave Province)

The four xenoliths in this study are from the A154N kimberlite pipe, Diavik Diamond Mine, NT, Canada. They represent pieces of the lower crust that have been transported to the surface much faster than those in high-grade terranes such as NC and IV. As a result of the emplacement processes, we do not have spatial information for the xenolith samples, which are likely to be from variable depths in the lower crust. We constrain their metamorphic conditions using traditional geothermobarometric techniques (TWEEQU software package) and microprobe data collected at the University of Alberta (Table S3.3) and find that they generally come from crustal depths of approximately 35-45 km (1.0-1.3 GPa), have uniform garnet compositions along transects, and yield (minimum) peak metamorphic temperatures between 760-870 °C. Although younger metamorphic events have been recorded in the Slave Province (Aulbach et al., 2010; Davis et al., 2003), two samples (including one that was not analyzed in this study, DDM20) have LA-ICP-MS metamorphic zircon Pb-Pb ages ranging from ~2.53 to ~2.58 Ga (analyzed at the University of Alberta) and our Fe-Mg exchange temperature-estimates (described for each sample) suggest that the samples were not reset after the major episode of granulite metamorphism in the Slave province *ca.* 2.5 Ga (Davis et al., 2003). The mineralogy and PT estimates are as follows:

DDM163. Coarse-grained mafic granulite. Dominantly clinopyroxene, clean labradorescent plagioclase, and euhedral garnet, with minor orthopyroxene exhibiting a generally granoblastic texture. Traces of hornblende rimming opaques (FeS_x) and rutile. Orthopyroxenes have lamellar structure. Garnet-clinopyroxene and garnet-orthopyroxene Fe-Mg exchange thermometry indicate temperatures of 760-840 °C. Given the susceptibility of Fe-Mg exchange thermometers to re-equilibration on slow cooling of granulite-facies rocks (*e.g.* Frost and Chacko, 1989), these temperatures should be regarded as minimum estimates of the peak metamorphic temperature experienced by this sample. Garnet-plagioclase-pyroxene-(quartz) barometry suggests maximum pressures of 1.1-1.3 GPa.

DDM303. Kyanite-garnet-plagioclase metapelite xenolith. Dominantly plagioclase and rutilated garnet, with abundant opaque grains of at least two varieties. Black-colored opaques surround garnets. Subordinate K-feldspar, orthopyroxene, and kyanite, along with veins of serpentine and chlorite which may have intruded from the kimberlite. K-feldspar is perthitic. Minerals in smaller proportions include rutile, secondary biotite (around opaque minerals), apatite, hercynite, monazite, zircon, magnetite, ilmenite, and pyrite. Garnet-orthopyroxene-plagioclase-(quartz) thermobarometry indicate a minimum temperature of 770 °C and maximum pressures of ~1.2 GPa (using kyanite reactions the pressure estimate is slightly higher, ~1.3 GPa). Two ~150 μm metamorphic zircon grains (containing inclusions of garnet) yielded a $^{207}Pb/^{206}Pb$ age of 2528 ± 8.6 Ma (n = 7) by LA-ICP-MS at the University of Alberta.

DDM309. Coarse-grained equigranular mafic xenolith. Composed of clean clinopyroxene, plagioclase, and euhedral garnet, along with minor amounts of clean orthopyroxene. Plagioclase shows very strong labradorescence. Pyrite and apatite are also present. Small amounts of secondary hornblende around mafic minerals. Strong granoblastic texture, no kimberlite intrusion appears to be present. Garnet-orthopyroxene and garnet-clinopyroxene Fe-Mg exchange thermometry yields minimum temperature estimates of 840-880 °C with garnet-plagioclase-pyroxene-(quartz) maximum pressures of 1.0 – 1.1 GPa.

DDM342. Coarse-grained anorthositic mafic xenolith**.** Composed dominantly (~80%) of very clean plagioclase separating subordinate garnet and small amounts of clinopyroxene, generally found in association with each other. Abundant string-perthite exsolution also present. Rutilated garnets and clinopyroxene grains appear slightly resorbed at margins. Celsian and chlorite present along fractures. Clinopyroxene rimmed by chlorite then celsian, potentially from kimberlite intrusion. Garnet-clinopyroxene-plagioclase-(quartz) thermobarometry gives a minimum temperature of 870 °C and maximum pressure of 1.3 GPa.

3.10.1.3. Ivrea-Verbano samples

The Ivrea-Verbano Zone contains packages of mafic and pelitic rocks that gradually increase in metamorphic grade from amphibolite to upper granulite/UHT facies (Redler et al., 2012). Four samples from Ivrea were collected by D.R. during the field season of 2016, along the main road in the Strona Valley. We have analyzed lower-temperature (amphibolite) mafic rocks from one end of the sequence (~700 °C), a UHT facies metapelite from the other end of the sequence (> 870 °C), and a crustally-contaminated garnet-bearing mafic intrusion (which is not thought to have lost-melt and is included only for reference in Fig. 3.1). Pressure and temperature conditions for samples that are part of the sequence can be deduced based on their locations compared to published isobars (0.6-1.0 GPa) and isotherms for the region, for which there is an inferred clockwise P-T-t path (Redler et al., 2012).

IV-16-09. A banded quartz-biotite-plagioclase schist with garnet porphyroblasts and minor sillimanite, chlorite, apatite, and K-feldspar. Main garnets contain inclusions of rounded quartz, FeS, and ilmenite. A small population of rare fine-grained REE-enriched garnets were also identified in a corner of the sample. The sample is from the low temperature part of the sequence when large garnet first appear in the metapelites (45°54'54" N, 08°13'35" E), past the K-feldspar (+ sillimanite)-in isograd (Redler et al., 2012). Temperature is estimated to be ~700-750 °C with pressures of ~0.6-0.9 GPa.

IV-16-19. Garnet-plagioclase amphibolite. Dominantly composed of hornblende with subordinate garnet and plagioclase. Garnet is highly fractured and rounded suggesting extensive post-crystallization deformation. Ilmenite grains are associated with hornblende and garnet. Plagioclase is strongly altered, possibly to microcrystalline epidote. Hornblende + quartz symplectites rim garnet. This sample is from the main lower crustal gabbro, with abundant crustal contamination (thus the garnet), which outcrops in the upper part of the valley at Campello Monti (45°56'05" N, 08°14'16" E). The contact between gabbro and the UHT metapelites is not exposed along the Val Strona road. Large-scale mapping suggests that the gabbro cross-cuts the regional UHT metamorphism. A better studied section in Val Sesia has a highly contaminated gabbro which probably intruded at 0.5-0.7 GPa (we are not aware of any direct estimate of P in the Campello mafic body). The original temperature of crystallization was likely around 1000-1200 °C (solidus for a gabbro), but because the gabbro was intruded into the hot lower crust, it is expected that it slowly cooled to amphibolite-facies. Many of the lower crustal gabbros in Ivrea are amphibole bearing, yet whether or not the amphibole itself is a primary product remains an open question.

IV-16-24 Garnet-K-feldspar-quartz metapelite. Dominated by K-feldspar and garnet, with subordinate quartz, cordierite, and sillimanite. Fairly abundant opaques (mostly ilmenite). K-feldspar is perthitic. Sillimanite, quartz, rutile, ilmenite, and minor monazite inclusions in garnet. Ilmenite found partially replacing rutile; cordierite-quartz symplectites replacing garnets. The sample is from the high temperature section of Val Mastallone (45°52'51" N, 08°10'21" E), where slivers of metapelites (septa) are found within the main gabbro body. Peak temperatures determined by thermodynamic modeling are > 870 °C and pressures > 0.95 GPa (Redler et al., 2012). Zr-in-rutile thermometry for the Val Mastallone septa indicates extreme T of 1020-1050 °C (Ewing et al., 2013; Pape et al., 2016).

IZ-408 (L&M). A banded amphibolite grade mafic rock displaying incipient melting, containing mainly amphibole and plagioclase. The ground mass is dominantly composed of equigranular hornblende showing weak preferred orientation, interspersed with quartz and plagioclase, and containing minor amounts of ilmenite, titanite (from ilmenite), muscovite, apatite, & magnetite. Quartz, epidote, and more albitic plagioclase are concentrated in the leucosomes along with traces of zircon, chalcopyrite, and calcite. A quartz-rich leucosome (IZ-408L) and typical melanosome ground-mass (IZ-408M) were separated for individual XRF and Ca-isotope analyses. The sample was collected from one of the large bodies of amphibolite within the metapelites and the locality is in between the K-feldspar-in and the biotite-out isograds (for the metapelites) near the locality of Rosarolo (temperatures ~800 °C at ~0.8 GPa) (Redler et al., 2012).

3.10.1.4. Sumdo Eclogite (Tibet)

The single eclogite sample analyzed in this study was collected in 2014 by D.J.D. from the Sumdo Group, Lhasa Block, Tibet, at a location of 29°52'22.9" N, 92°31'33.5" E, near the town of

Xianduogang, Gongbo’gyamda, Nyingchi. The sample is of Permian age (~275 Ma) from U-Pb dating of zircons (Weller et al., 2016; Yang et al., 2009).

14DLB39. Coarse-grained mafic eclogite. Dominantly composed of omphacite and garnet with subordinate quartz and minor yet significant amounts of large rutile and large rounded apatite grains (in equal abundance). Garnet is highly fractured and appears partially replaced by clinopyroxene with higher aegirine component than the main omphacite. Rutile is associated with garnet and also found as inclusions in garnet. Minor zircon inclusions also in garnet. PT estimates based on previous work suggest relatively high-T (~700 °C) and pressures of ~2.7 GPa (Weller et al., 2016; Yang et al., 2009).

3.10.2. Methods

We characterized the modal mineralogy (Table S3.1), bulk-rock chemical composition (Table S3.2), in-situ mineral compositions (Table S3.3), and mineral-separate compositions (Table S3.4) for each sample through optical and chemical image analysis methods, x-ray fluorescence (XRF) spectroscopy, electron probe micro-analysis (EPMA), inductively-coupled plasma optical-emission spectroscopy (ICP-OES) & isotope dilution thermal-ionization mass spectrometry (ID-TIMS), respectively. A ^{42}Ca-^{48}Ca double-spike method was used to determine [^{44}Ca] for the mineral separates used in isochron age calculations (Table S3.4). Unspiked calcium separates were measured for their Ca isotopic composition by TIMS at the University of California, Berkeley.

3.10.2.1. Analytical methods

Modal mineralogy: estimates were obtained through optical microscopy, combined with image analysis methods (using back-scattered electron maps and optical scans). BSE maps and thin-section X-ray maps (Fe, Mg, Si, Al, Ca) were used instead of optical scans for the SP xenoliths. All of the BSE maps were obtained using a 15 kV, 10 nA beam, with a fully-focused spot. The results of the modal mineral estimates are reported in Table S3.1.

Whole-rock compositions: For the NC samples, whole-rock chemistry was determined by X-Ray Fluorescence (XRF) at the University of California, Berkeley, using ~10 g aliquots of powdered bulk-rock prepared in a steel disk-mill, homogenized, and fused into disks. The IVZ and SE samples were sent to the Geoanalytical Laboratory at Washington State University (WSU), along with one SP xenolith (DDM309). For the majority of SP samples, whole-rock chemistry was reconstructed based on combining modal mineralogy with major mineral compositions. The reconstructed whole rock chemistry of DDM309 was compared to the XRF values. We found that intrusion of kimberlitic magma into the xenolith leads to a significantly higher Mg# than that derived from reconstructed whole-rock chemistry, but the K and Ca concentrations and K/Ca ratio are approximately the same; nevertheless, we use the reconstructed values for the SP samples in the figures and text. The whole-rock compositions, along with Mg#, A/CNK, and K/Ca values, are reported in Table S3.2.

In-situ mineral compositions: Mineral compositions were obtained using EPMA at the University of California, Davis (NC, IVZ, and SE samples) and at the University of Alberta (SP samples). Quantitative analyses were generally run at 15 kV (10 nA) with a 1-µm spot size, except for plagioclase which had a 10-µm spot size. The results of the microprobe analyses for garnet, plagioclase, and K-Feldspar, along with their calculated solid-solution compositions, are reported in Tables S3.3.

Mineral-separate compositions: Garnet and feldspar separates were obtained through manual mineral separation of whole-rocks crushed in a tungsten carbide impact-mortar and immersed in isopropyl alcohol. Fine tweezers, stereoscopic microscope, and both black and white weighing trays were used in order to select clean grains, which were subsequently dissolved in acid for the various analyses (following section). The various mineral separates ranged from ~10 to ~100 mg. Given availability, aliquots of the dissolved mineral separates and whole-rock powders were analyzed for Mg, Ca, Na, and K concentrations by ICP-OES at the University of California, Berkeley. For our isochron determinations, we analyzed mineral separates and whole rocks for their K and Ca concentrations by ID-TIMS, using a combined ^{41}K-^{43}Ca spike and calibrating to four USGS standards (AGV-2, DNC-1, GSP-2, & W2-A). Measurements of molar ^{44}Ca concentration for all of the isochron-related samples were performed using a ^{42}Ca-^{48}Ca double-spike technique generally used for measuring δ^{44}Ca at UC-Berkeley. This corrects for possible stable isotope fractionation in the samples. The purity of our dissolved mineral separates was verified by comparing the above analyses to those measured in-situ by EPMA. The results are reported in Table S3.4.

Ca isotope analyses: For ε_{Ca} analysis, ~10-100 mg of sample is weighed in screw-top Savillex beakers and dissolved using a 5:2:1 combination of concentrated hydrofluoric, 6N hydrochloric, and concentrated perchloric acid. After a minimum digestion period of one week at 130 °C, the samples are evaporated to dryness under flowing-N_2 in pot-stills. The dry samples are then redissolved in 3N nitric acid, from which aliquots are taken for the various TIMS and ICP-OES analyses. Difficulty dissolving certain samples is overcome by (i) dissolving fluorides in 6N hydrochloric acid, (ii) repeating the initial dissolution, and in extreme cases, (iii) placing the beakers in a heated ultrasonic bath (~60 °C) for extended periods of time.

Calcium is separated using established column-chemistry methods (Eichron DGA resin, Simon *et al.*, 2009) and several standards (USGS dolerites DNC-1 and W2a, and Ca isotope standard SRM915a) are run alongside the samples. After washing away matrix elements with 3N nitric acid, purified calcium is collected in acid-refluxed Savillex beakers using ultrapure water. The water is evaporated, and remaining solid is treated with a drop of concentrated nitric acid and 30% hydrogen peroxide, for a period of > 24 hours, in order to dissolve resin that may have come through the column. After the acid is evaporated, 3-5 μg of Ca is loaded onto out-gassed rhenium filaments in ~1 μL of 3M nitric and dried down. The dried aliquot is covered with ~1 μL of 40% phosphoric acid and heated on the filament for increased sample stability. Full coverage of the filament with phosphoric acid (as opposed to separate domains connected by stringers) is found to yield more consistent results, and a stereoscopic microscope is used to ensure enough H_3PO_4 is added to each filament.

The filaments are loaded into a ThermoFisher Scientific Triton TIMS analyzing ^{40}Ca, ^{42}Ca, ^{43}Ca, and ^{44}Ca. We use a double-filament method that takes ~3 hours per analysis. Current is slowly increased through the evaporation filament at 50 mA/min and through the ionization filament at 120 mA/min (up to a combined temperature of ~1410 C, ~3000 mA for most ionization filaments). When the evaporation filament reaches 1600 mA, the current is increased more slowly to ~1800 mA (at 10 mA/min) and the amplifier gains are re-calibrated during this period. Afterwards, we focus the beams and slowly increase current through the evaporation filament until there is ~18 volts for ^{40}Ca (typically at 1850-2200 mA). Peak-scans are performed prior to starting each measurement, which we use to correct for subtle changes in beam-alignment that can sometimes occur between samples. Generally, the ^{40}Ca signal slowly grows to ~25 V by the end of the acquisition, which consists of 10 blocks of 20 lines. Each line acquires Ca isotope data for ~10 seconds and ^{39}K data for ~1 second (always < 1 ppm compared to ^{40}Ca) and is followed by ~4 seconds of downtime. Each block is separated by an automated peak-centering and lens-focusing cycle.

3.10.2.2. Bulk silicate Earth (BSE) ^{40}Ca/^{44}Ca and ε_{Ca} uncertainty

We infer BSE to have ^{40}Ca/^{44}Ca = 47.156 ± 0.001 (2SE, n = 24) (at a corresponding ^{42}Ca/^{44}Ca = 0.31221), which is in accordance with our analyses of USGS dolerite standards W2a and DNC-1, modern hydrothermal vent fluids from Lost-City, and several mafic granulites from this study (Table S3.5). Other measurements of mafic-to-intermediate igneous rock standards (He et al., 2016; Mills et al., 2018; Schiller et al., 2012), and enstatite chondrites (Simon et al., 2009) corroborate this value, which is about ~1 epsilon unit lower than calcium isotope standard SRM915a [^{40}Ca/^{44}Ca = 47.163 ± 0.002 (2SE, n = 18), this study]. Our values of ^{40}Ca/^{44}Ca and ^{42}Ca/^{44}Ca, yield a value for ^{40}Ca/^{42}Ca of 151.039 ± 0.006 which compares favorably to the previously proposed value (Marshall and DePaolo, 1982) of 151.024 ± 0.016.

We have been able to distinguish the subtle differences in standard compositions through large numbers (n > ~10) of carefully repeated analyses, however, this is impractical for a large number of samples. We find that repeating a measurement twice provides adequate accuracy. The average difference between replicate ε_{Ca} analyses in this study (35 samples, excluding the standards) is ~0.8, which is skewed by a small number of samples with poor reproducibility (excluding five outliers, the average is ~0.6). However, due to drift in the machine over time, gradual cup passivation, and other sources of variability, we report a more-conservative uncertainty of ± 1 for ε_{Ca} in our figures and tables.

3.10.2.3. K-Ca isochrons

High-K whole rocks and feldspar separates, which were analyzed in order to build ^{40}K-^{40}Ca isochrons, have ε_{Ca} ranging from +4 to +75, with higher values generally found in older samples with higher K/Ca ratios (Figure S3.1). Incorporating [Ca] and [^{44}Ca] from double-spiked TIMS analyses and [K] from ID-TIMS or ICP-OES analyses (see Table S3.4), our measurements yield ages of 2.6 to 2.0 Ga (± 0.2 Ga, 2SD) with an average of 2.3 Ga for the NC (n = 4) and 0.4 ± 0.4 Ga (2SD) for the IVZ (n = 1) (Figure S3.2).

Although the isochrons have a maximum of three-points and are not reliable for accurate age determinations, the ages they provide are in general agreement with more precise dating methods for the Northern NC (~2.5 Ga) (Harley, 2016; Horie et al., 2012) suggesting closed-system evolution of ^{40}K-^{40}Ca in our samples after metamorphism. Oxygen isotope thermometry from the same region of the NC as our study (Farquhar et al., 1996) has also shown that garnet is particularly resistant to retrograde exchange, even during protracted reheating and deformation. Although metamorphic ages in the IVZ (~0.3 Ga) are in agreement with our results (Redler et al., 2012), our uncertainties are too large to rule out post-metamorphic K-Ca redistribution. The SP xenoliths and Sumdo eclogite were not used for K-Ca dating due to low whole-rock K/Ca values and possible effects of kimberlite-related metasomatism in the bulk xenoliths.

3.10.2.4. Protolith K/Ca calculations

The Antarctic samples in our study (NC) were collected from Dallwitz Nunatak, which has Sm-Nd and inherited zircon protolith ages up to ~3.5 Ga (DePaolo et al., 1982; Horie et al., 2012; Kelly and Harley, 2005; Kusiak et al., 2013) and a metamorphic age of ~2.5 Ga (Harley, 2016; Horie et al., 2012). Available data for lower crustal xenolith samples from the Slave province (from the same kimberlite as our samples) have Re-Os model ages ranging up to ~3.3 Ga (Aulbach et al., 2010) but most lower-crustal xenolihs have ~2.6 Ga protolith ages (Davis et al., 2003; Pehrsson et al., 2000). We use a conservative estimate of 3.0 Ga for our calculations. Metamorphic ages for the SP are also generally ~2.5 Ga (Davis et al., 2003). For the IVZ, Sm-Nd protolith ages range up to ~0.6 Ga (Voshage et al., 1987), and the oldest detrital zircon ages in metapelites range up to ~550 Ma, with numerous samples around 450 Ma (Kunz et al., 2018). We use a protolith age of 0.6 Ga to remain conservative in our K/Ca calculations. The IVZ metamorphic ages cluster around ~0.3 Ga (Ewing et al., 2013; Kunz et al., 2018; Vavra et al., 1996). The single sample from Tibet (SE) has a U-Pb zircon age of 0.27 Ga (Weller et al., 2016), but does not have garnet ε_{Ca} resolvable from BSE or available protolith age estimates. In our use of Equation 3.1 from the main text, we chose the oldest protolith age from each locality in order to generate minimum estimates for protolith K/Ca, but have not incorporated uncertainties in the protolith ages themselves.

The expression for calculating $[K/Ca]_{protolith}$, given ε_{Ca} values and protolith/metamorphic ages [equation (3.2) in the main text], incorporates the factor Q_{Ca}, modified from (Marshall and DePaolo, 1989). In our formulation, Q_{Ca} is equal to ~1.0804 defined:

$$Q_{Ca} = \frac{R_{\beta}[{}^{40}K(ab)/{}^{44}Ca(ab)] \cdot 10000}{({}^{40}Ca/{}^{44}Ca)_{BSE}} \qquad \text{(Eq. S3.1)}$$

Where R_{β} is the branching ratio for ^{40}K decay [$\lambda_{\beta-}/(\lambda_{\beta-}+\lambda_{EC})$, equal to 0.8952], $^{40}K(ab)$ is the modern isotopic abundance of ^{40}K relative to total K (0.000117) and $^{44}Ca(ab)$ is the isotopic abundance of ^{44}Ca relative to total Ca [equal to 0.020558, assuming $(^{40}Ca/^{44}Ca)_{BSE}$ is 47.156].

In order to calculate $[K/Ca]_{protolith}$ for samples where garnet was not available, we used low K/Ca plagioclase separates (verified by ICP-OES) to constrain initial ε_{Ca}. For sample 2044, we used whole rock K/Ca values and assumed an age of 2.5 ± 0.3 Ga in order to estimate initial ε_{Ca}. For sample IZ-408M and 2035A, the measured whole-rock K/Ca is low enough to assume ε_{Ca} is the same today as at the time of metamorphism (Tables S3.2 and S3.5). Although we analyzed garnet from IVZ sample IV-16-09 and SE sample 14DLB39, we excluded them from our models because the former is inferred to represent a crustally-contaminated gabbro intrusion into the IVZ and the latter is an eclogite (see sample descriptions).

3.10.2.5. Partial-melting model

In order to estimate melt-loss from our data, it is essential to constrain $[K/Ca]_{melt}$. The simplest approach for estimating $[K/Ca]_{melt}$ would be to assume that it is the same as for local granitic/migmatite samples (2038 & 2044, See Table S3.2), however, the modern [K/Ca] ratios of these two samples (which were probably generated at similar conditions) are quite different. Assuming similar ages, our ε_{Ca} measurements indicate that the two migmatites were likely derived from pre-cursor materials with very different $[K/Ca]_{protolith}$ (see Fig. 3.3). The initial ε_{Ca} of migmatite 2038 (measured in garnet) is ~14, whereas the initial ε_{Ca} of sample 2044 (calculated from whole-rock ε_{Ca} and $[K/Ca]_{modern}$, assuming an age of 2.5 ± 0.3 Ga) is only ~3. This suggests that migmatite 2038 came from melting of a high K/Ca pelitic protolith (similar to those of 2036A, 2036C, & 2040C), whereas 2044 came from melting of a lower K/Ca igneous protolith (similar to those of our meta-granitic/mafic samples). Therefore, it appears that $[K/Ca]_{protolith}$ exerts a strong control on $[K/Ca]_{melt}$, so assuming a single melt composition would not be realistic.

We therefore construct a non-modal batch melting model, where the distribution coefficients for K and Ca are a function of the weight fractions for their residual host minerals. For a standard batch melting model, the enrichment or depletion of an element in the liquid relative to the original solid is given by:

$$\frac{C_l}{C_o} = \frac{1}{\bar{D}_i(1-F)+F} \qquad \text{(Eq. S3.2)}$$

Where F is the melt fraction, C_l is the concentration of element *i* in the liquid, and C_o is the concentration of element *i* in the original rock. We assume that the bulk distribution coefficient for K is proportional to the modal abundance of K-feldspar, and hence decreases as K-feldspar is consumed (non-modal batch melting), until there is no K-feldspar left in the solid phase.

$$\bar{D}_K(F) = \begin{cases} K_d^{Kspar}\left[\frac{X_o^{Kspar}-F\theta_{Kspar}}{(1-F)}\right] & if \left[\frac{X_o^{Kspar}-F\theta_{Kspar}}{(1-F)}\right] > 0 \\ 0.0005 & if \left[\frac{X_o^{Kspar}-F\theta_{Kspar}}{(1-F)}\right] \leq 0 \end{cases} \qquad \text{(Eq. S3.3)}$$

Where $K_d(kspar)$ is the distribution coefficient for K-feldspar, $X_o(kspar)$ is the original weight fraction of K-feldspar in the rock, θ_{Kspar} is the fraction of K-feldspar component in the generated melt. We calculate the weight fraction of K-feldspar using $[K_2O]/13.5$ (wt%) (assuming a composition of Or80), and assume a K-feldspar-absent bulk D_K of 0.0005. The incorporation of biotite as another K source in the starting materials does not greatly affect our results given the similar K concentrations and distribution coefficients for the two minerals.

Similarly for calcium, but without the possibility of total exhaustion, we have:

$$\bar{D}_{Ca}(F) = K_d^{Plag}\frac{\left(X_o^{Plag}-F\theta_{Plag}\right)}{(1-F)} + K_d^{Cpx}\frac{\left(X_o^{Cpx}-F\theta_{Cpx}\right)}{(1-F)} \qquad \text{(Eq. S3.4)}$$

Where $K_d(plag)$ and $K_d(cpx)$ are the distribution coefficients for Ca in plagioclase and clinopyroxene, $X_o(plag)$ and $X_o(cpx)$ are the total weight percent of plagioclase and clinopyroxene in the rock, and θ_{Plag} and θ_{Cpx} are the fraction of plagioclase and clinopyroxene in the generated melt. Because they have similar distribution coefficients, we assume that plagioclase and clinopyroxene are present in equal abundance, and calculate their weight fractions as $[CaO]/15.8$ (wt%) (corresponding to fractions of 50% An70 + 50% Di70). The incorporation of amphibole as another Ca source in our models does not lead to significant differences in our results, given the assumptions inherent to our estimates of modal mineralogy and distribution coefficients.

A large database exists for melt-inclusions found in granulites (Bartoli et al., 2016), but information linking them to their host-rock compositions is not available, making distribution coefficients hard to determine from natural data. We use a compilation of anhydrous melting experiments at 900 ± 50 °C and at 1.0 ± 0.2 GPa, isolated from a larger compilation (Gao et al., 2016) based on a wide variety of starting materials [$(K/Ca)_{protolith}$ ranging from ~0.4 to ~31 (Table S3.6)]. Assuming a melt fraction (F) of ~0.2 to ~0.4 for the experiments at relevant PT conditions, $K_d(K)$ for K-feldspar is about ~4 and $K_d(Ca)$ for plagioclase & clinopyroxene is also ~4. Varying the *Kd*'s over likely ranges only slightly modifies our main results (Fig. S3.6a-h), which depend most significantly on $[K/Ca]_{protolith}$.

To estimate the amount of K-feldspar and plagioclase in average granulite melts (θ_{Kspar} and θ_{plag}), we use a compilation of ~600 melt-inclusion analyses from a wide range of granulite-facies rocks (Bartoli et al., 2016). From this compilation, the average orthoclase fraction in the melt is approx. ~0.28 and the average anorthite fraction is ~0.02. Assuming that these components are sourced from K-feldspar and plagioclase melting, this translates into 35% K-feldspar (θ_{Kspar} equals 0.35, assuming Or80) and ~2% plagioclase (θ_{plag} = ~0.02, assuming An70). In accordance with common Ab-An-Di phase diagrams, we set θ_{Cpx} to ½ of θ_{plag} (~0.01), however, we note that at high melt fractions, when nothing but clinopyroxene and plagioclase are left in the residue, $\theta_{plag} + \theta_{Cpx}$ must equal 1. This condition, however, is not reached by our starting compositions at values of $F <$ ~0.65. We also note that the behavior of Ca during melting is secondary to the effects of K when considering evolution of K/Ca as a function of F. Combining equations (S3.2) and (S3.3) and equations (S3.2) and (S3.4), and rearranging to solve for C_s/C_o (remembering $D_i = C_l/C_s$), we arrive at two expressions for the composition of residual solid at various degrees of partial melting (Fig. S3.5a,b). Taking the ratio of these two expressions, we arrive at our final model for the evolution of $[K/Ca]_{solid}/[K/Ca]_o$ during partial melting (Fig. S3.5c).

For the most common compositions, the bulk distribution coefficient for K generally decreases as a function of melt fraction (F), and the bulk distribution coefficient for Ca generally increases. However, rocks with high initial $[K/Ca]_{protolith}$ behave in the opposite fashion (Fig. S3.5). Although distribution coefficients for K in K-feldspar and for Ca in plagioclase and clinopyroxene are currently rough approximations, varying them over likely ranges only slightly modifies the results (Fig. S3.6), which depend most significantly on $[K/Ca]_{protolith}$.

Of the seventeen samples plotted in Figure 3.4 of the main text, two of our granulites fall to the right of our predicted whole rock $[K_2O]_{mdrn}$ values, which could potentially be a manifestation of incomplete melt segregation. Although it is difficult to calculate the amount of trapped melt required to explain the samples without assuming an arbitrary value for F, the general effect of melt trapping would be to shift data towards the upper right of Figure 3.4. Additional to melt-trapping, complexities may also arise from variations in the values for K_d(plag) and K_d(Kspar) during melting. Given the same protolith, the distribution coefficients for K and Ca also depend on temperature, pressure, and external fluids, and may change along the course of melting, with lower temperatures favoring higher $[K/Ca]_{melt}$ (Gao et al., 2016).

Although we cannot directly address the PT conditions of melting with our data, if a non-negligible amount of calcium is lost, our ε_{Ca} measurements suggest that melt-segregation probably occurred during/after the formation of garnet, otherwise large ε_{Ca} signatures would not be fully preserved. This would especially be the case for pelitic samples with low initial [CaO] — where Ca acts incompatibly during initial melting (see Fig. S3.5b). On the other hand, if only minor amounts of Ca are lost, this would preclude any statements addressing the timing of melt-loss, which can occur both before and after peak metamorphic pressure and temperature conditions (Yakymchuk and Brown, 2014). In spite of this uncertainty, our results are in general agreement with melt estimates from other studies, and ~90% of our samples appear to be consistent with our model predictions. Fractional melting models and hybrid-models where melt is removed from the system in batches of ~7% lead to higher melt-fraction estimates for our samples. In order to remain conservative in our minimum melt-loss estimates, and given the uncertainty in melt-loss dynamics, we chose to model our results with a non-modal batch-melting model. Many additional processes, however, have been shown to affect the composition of crustal melts, including entrainment of peritectic/residual minerals (García-Arias, 2018; Garcia-Arias and Stevens, 2017; Sawyer, 2014), diffusion of H_2O and K_2O (Nicoli et al., 2017), and disequilibrium melting (Madlakana and Stevens, 2018).

3.10.3. Supplementary figures and tables

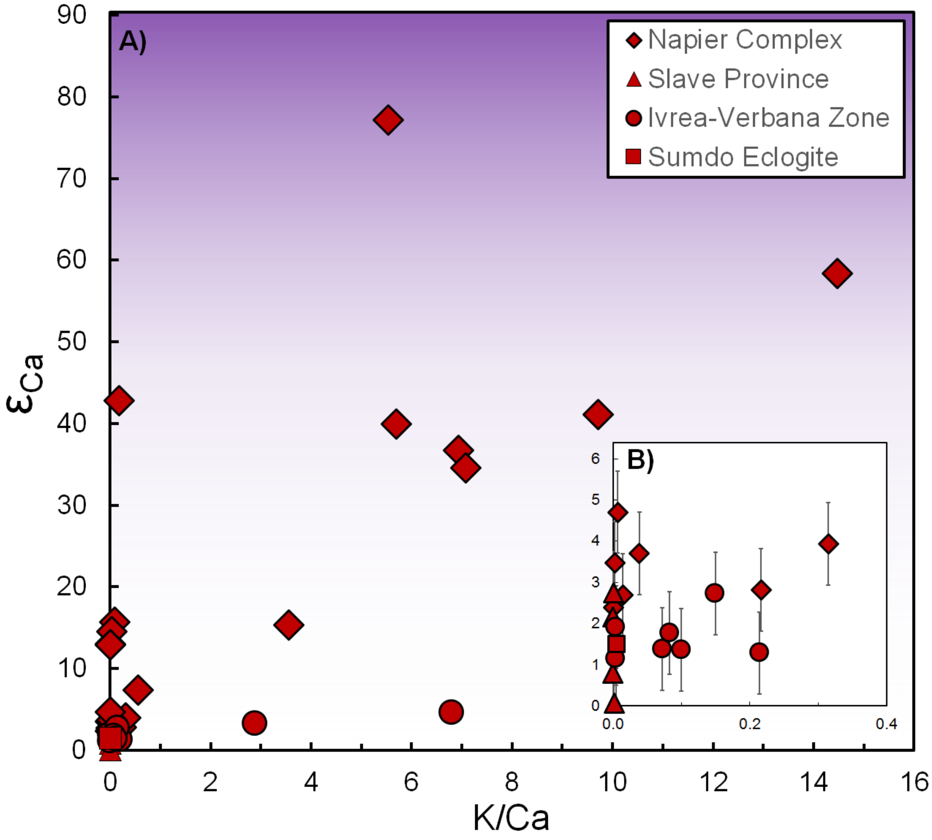

Fig. S3.1. (a). ε_{Ca} vs. modern K/Ca (measured by XRF, ICP-OES, or ID-TIMS) for all measured samples in this study (n = 35), differentiated by location as indicated in the legend. Inset **(b)** has the same axes as A, but is zoomed in to show the finer variability between samples. Horizontal error bars are smaller than the symbols, vertical error bars are ± 1 (see methods for discussion).

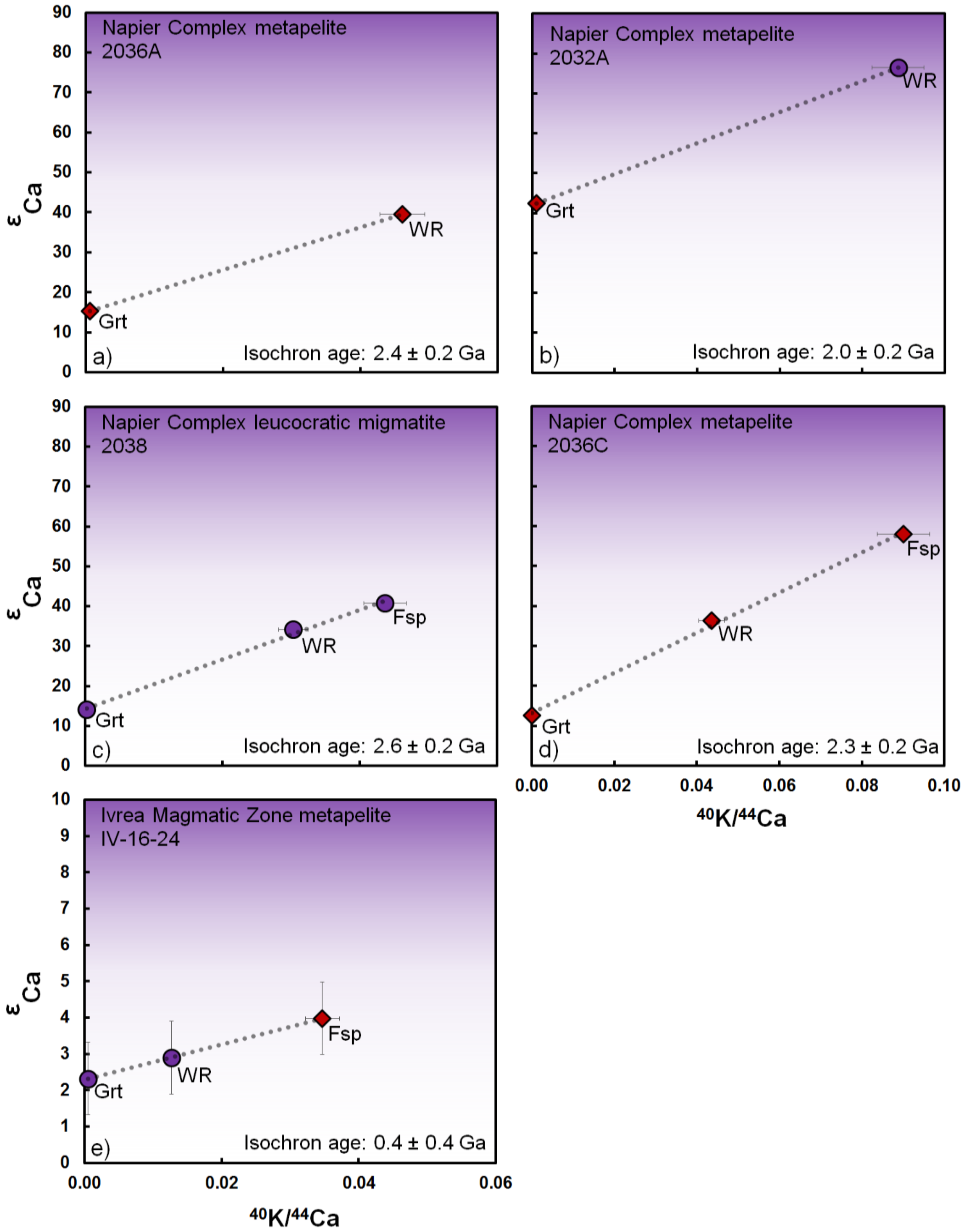

Fig. S3.2. ^{40}K-^{40}Ca isochrons for samples from the Napier Complex, Antarctica, and from the Ivrea-Verbano Zone, Italy. Potassium concentrations measured by ICP-OES (purple diamonds) or ID-TIMS (red diamonds), [^{44}Ca] concentrations calculated from double-spike TIMS analyses (Table S3.4).

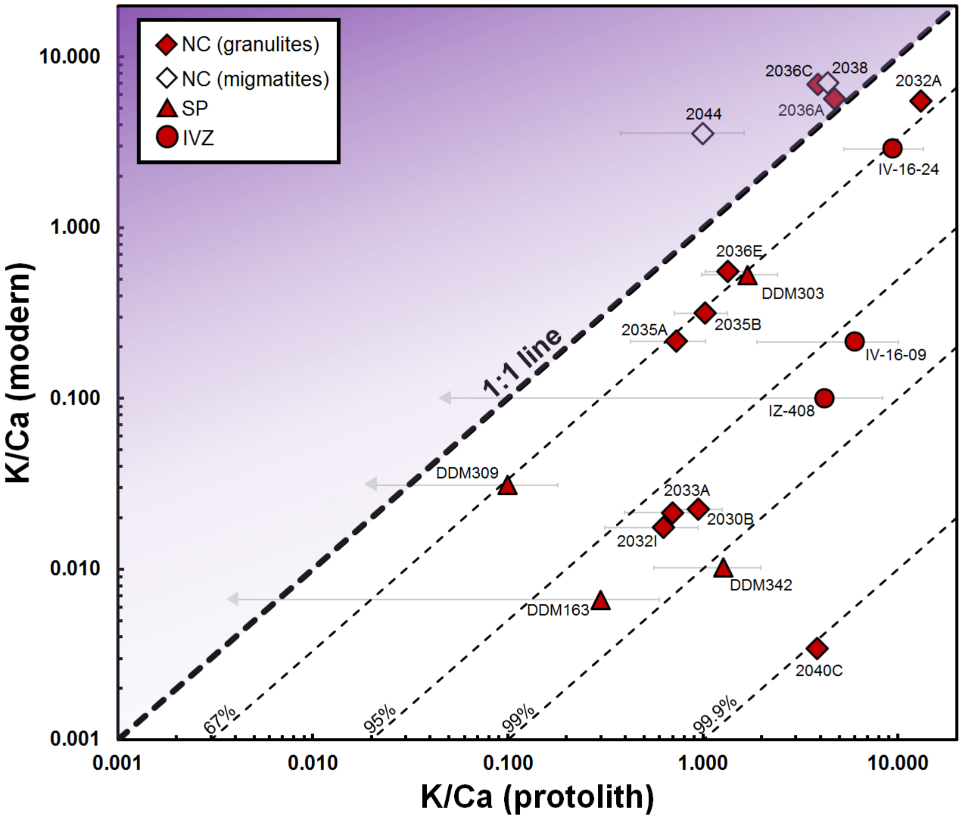

Fig. S3.3. Whole rock K/Ca measured in modern samples versus ε_{Ca}-based K/Ca estimates in protolith rocks [from equation (3.2)]. NC granulite samples (n = 10), NC migmatites (n = 2), SP samples (n = 4), IVZ samples (n = 3). Contours indicate relative K-loss (in %) assuming constant Ca. Uncertainties in protolith K/Ca are calculated using equation (3.2), taking into account ages for each sample and our 2SD on ε_{Ca} (±1); arrow terminations represent samples within error of BSE. Uncertainties for modern K/Ca (measured by XRF, < ~5%) are smaller than the symbols.

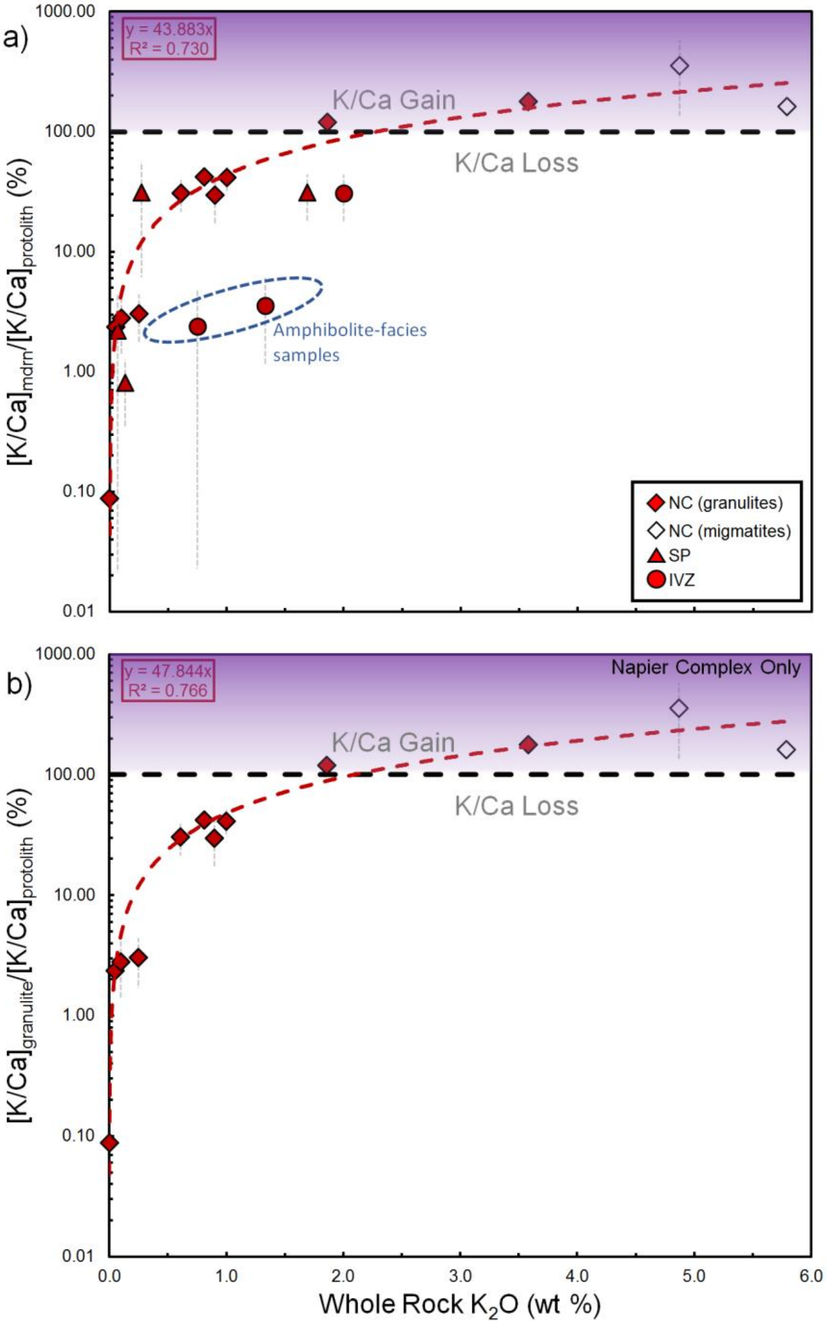

Fig. S3.4. Linear regressions of $[K/Ca]_{mdrn}/[K/Ca]_{protolith}$ vs. whole rock K_2O (wt%) for **(a)** all samples (excluding IV-16-19 and 14DLB39) and for **(b)** Napier Complex samples only. Symbols and uncertainties are the same as in Fig. 3.4 of the main text. NC granulite samples (n = 10), NC migmatite samples (n = 2), SP samples (n = 4), IVZ samples (n = 3). Regressions are forced through the origin.

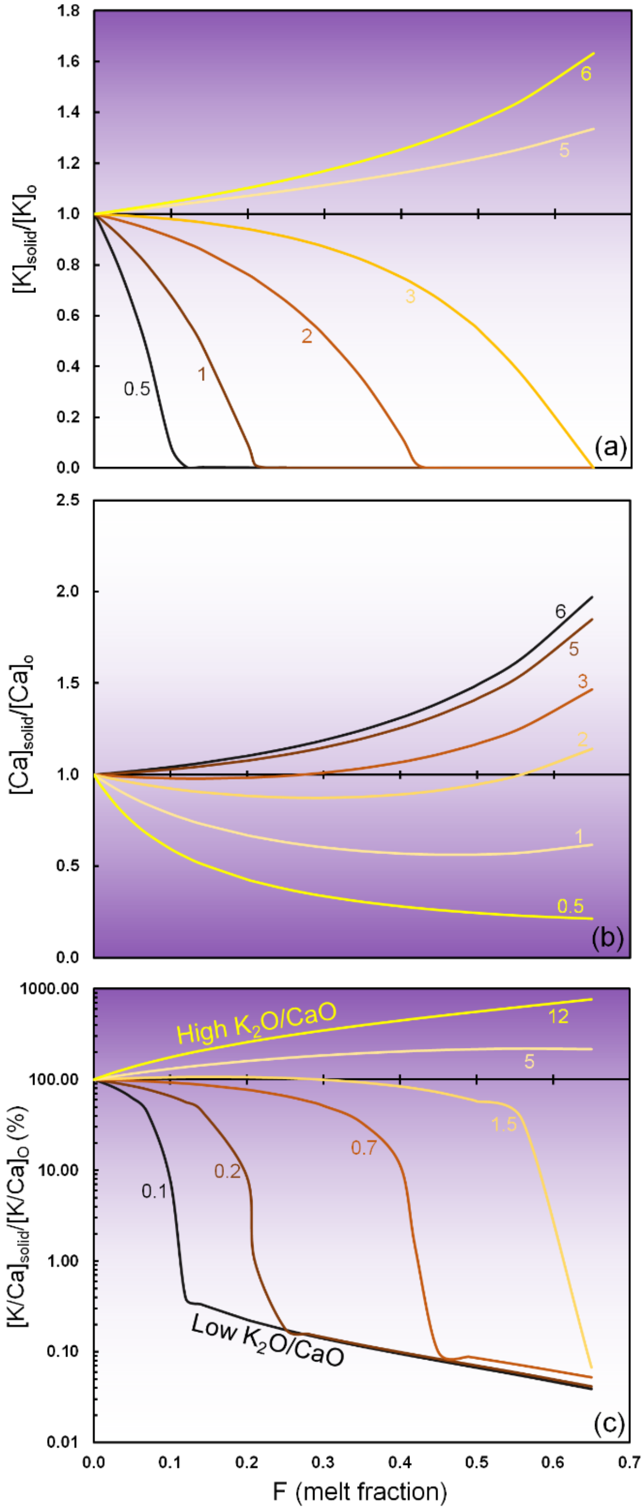

Fig. S3.5. Model calculations for **(a)** $[K]_{solid}/[K]_o$, **(b)** $[Ca]_{solid}/[Ca]_o$, and **(c)** $[K/Ca]_{solid}/[K/Ca]_o$ for different hypothetical protolith compositions, based on non-modal batch melting model [equations (S3.2) through (S3.4)]. In a) lines are labeled with starting whole-rock K_2O (wt%), in b) lines are labeled with starting CaO (wt%). In c), the lines are labeled with starting K_2O/CaO (wt/wt). Bulk D_K is a function of remaining K-feldspar, and bulk D_{Ca} is a function of remaining plagioclase + clinopyroxene (Methods). $K_d(K)$ for K-feldspar = 4 and $K_d(Ca)$ for plagioclase & clinopyroxene = 4.

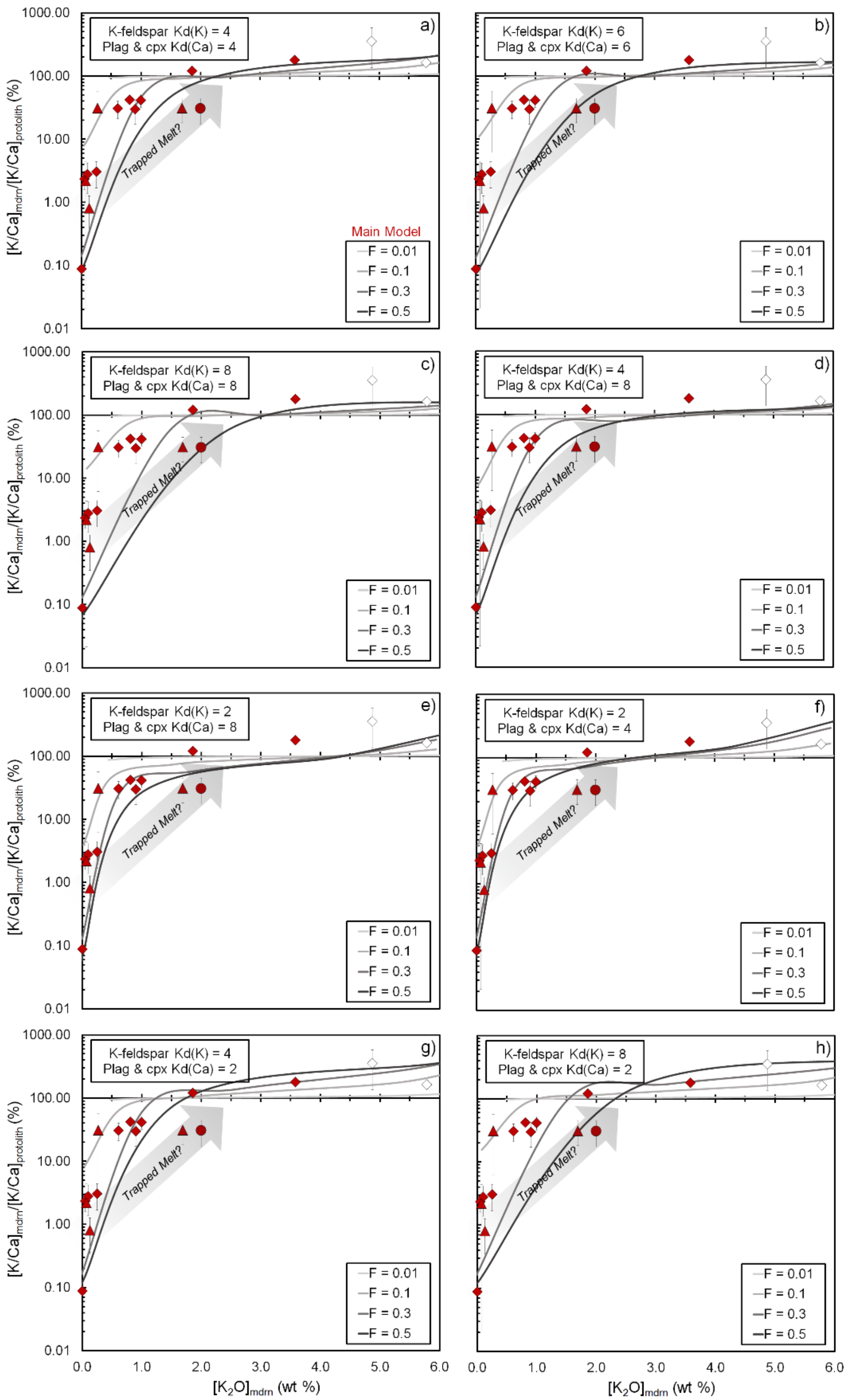

Fig. S3.6. Melting model results with different distribution coefficients, using equations (3.3-3.5) in the main text. In **(a-c)** we show the effects of increasing both *K$_d$(K)* and *K$_d$(Ca)* equally. In **(d,e)** we show the effects of decreasing *K$_d$(K))*, and in **(f-h)** the effects of increasing *K$_d$(K)* [relative to *K$_d$(Ca)*].

Table S3.1. Modal mineralogy estimates of analyzed samples (from optical, X-ray map, and BSE image analyses).

	2030B	**2032A**	**2032I**	**2033A**	**2035A**	**2035B**	**2036A**	**2036C**	**2036E**	**2038**	**2040C**
Plag	2	-	20	63	-	18	-	6	25	9	-
Cpx	9	-	11	14	8	1	-	-	-	-	-
Opx	89	1	68	23	58	80	-	-	-	-	60
Grt	-	22	-	-	-	-	21	25	36	4	30
Sil	-	6	-	-	-	-	7	11	1	1	-
Qtz	-	?	-	-	-	-	36	33	20	47	10
Crd	-	46	-	-	-	-	20	-	7	-	-
Spr	-	19	-	-	-	-	-	-	-	-	-
Ol	-	-	-	-	16	-	-	-	-	-	-
Hbl	-	-	-	-	14	-	-	-	-	-	-
Bt	1	-	-	-	3	1	-	-	4	-	-
Kspar*	-	6	-	-	-	-	14	25	7	39	-
Ap	-	-	0.6	-	-	-	0.2	-	-	-	-
Spl	-	-	-	-	-	-	1	-	-	-	-
Opqs	0.4	0.1	0.1	0.1	0.5	0.4	0.4	0.5	0.5	0.0	0.2
Rt	-	-	-	-	-	-	-	-	-	-	-

	2044	**DDM163**	**DDM303**	**DDM309**	**DDM342**	**IV1609**	**IV1619**	**IV1624**	**IZ408L**	**IZ408M**	**14DLB39**
Plag	16	26	65	52	81	45	20	-	21	41	-
Cpx	-	41	-	22	10	-	-	-	-	-	49
Opx	1	2	1	16	-	-	-	-	-	-	-
Grt	-	31	21	6	8	5	33	30	-	-	34
Sil	-	-	-	-	-	-	-	1	-	-	-
Qtz	42	-	-	-	-	37	-	7	75	-	13
Crd	-	-	-	-	-	-	-	4	-	-	-
Spr	-	-	-	-	-	-	-	-	-	-	-
Ol	-	-	-	-	-	-	-	-	-	-	-
Hbl	1	-	-	2	-	-	47	-	3	53	-
Bt	-	-	2	-	-	11	-	-	-	-	-
Kspar*	40	-	10	-	-	-	-	58	-	-	-
Ap	-	-	-	-	-	-	-	-	-	-	2
Spl	-	-	-	-	-	-	-	-	-	-	-
Opqs	0.0	0.2	1.0	1.8	0.2	1.0	0.8	0.9	0.1	6.1	-
Rt	-	-	-	-	-	-	-	-	-	-	1.7

**K-spar is dominantly perthitic*

Table S3.2. Whole-Rock Chemistry (by XRF or EPMA reconstruction*).

Sample	**2030B**	**2032A**	**2032I**	**2033A**	**2035A**	**2035B**	**2036A**	**2036C**
SiO_2	48.5	65.0	58.2	46.6	45.1	58.6	67.0	60.7
TiO_2	0.3	0.9	0.5	0.1	0.8	0.6	0.8	0.9
Al_2O_3	5.9	19.3	8.0	20.5	4.6	8.3	17.3	19.8
FeO	19.6	6.1	10.4	10.0	18.2	11.1	5.9	8.3
MgO	20.3	6.4	14.5	5.9	22.8	15.2	5.1	3.6
CaO	2.6	0.2	6.6	13.6	4.8	2.3	0.4	0.6
Na_2O	0.4	0.6	0.2	1.5	0.4	1.9	0.8	1.6
K_2O	0.05	0.81	0.10	0.25	0.90	0.61	1.86	3.58
MnO	0.3	0.1	0.2	0.2	0.3	0.2	0.1	0.1
Mg#	64.9	65.3	71.3	51.3	69.1	71.0	60.7	43.4
A/CNK	1.08	8.93	0.63	0.75	0.44	1.05	4.33	2.60
K/Ca	0.02	5.54	0.02	0.02	0.22	0.32	5.69	6.93

Sample	**2036E**	**2038**	**2040C**	**2044**	**DDM163***	**DDM303***	**DDM309**	**DDM309***
SiO_2	51.1	76.2	48.2	74.3	48.9	53.7	47.1	49.4
TiO_2	0.8	0.1	0.5	0.2	0.4	0.0	1.3	1.3
Al_2O_3	15.2	13.8	8.6	13.6	15.5	24.3	13.7	15.8
FeO	15.9	0.7	19.7	2.1	11.8	6.9	13.0	11.2
MgO	11.1	0.2	20.1	0.4	8.5	3.9	12.8	6.7
CaO	2.1	1.0	0.3	1.6	12.3	3.7	10.1	12.6
Na_2O	1.0	2.3	0.0	2.8	2.2	5.8	1.3	2.7
K_2O	1.00	5.79	0.004	4.87	0.07	1.69	0.27	0.21
MnO	0.2	0.0	0.2	0.0	0.2	0.1	0.2	0.2
Mg#	55.4	29.7	64.5	22.6	56.3	50.3	63.7	51.6
A/CNK	2.33	1.18	13.81	1.06	0.59	1.34	0.66	0.57
K/Ca	0.55	7.08	0.003	3.56	0.01	0.53	0.03	0.02

Sample	**DDM342***	**IV-16-09**	**IV-16-19**	**IV-16-24**	**IZ408-L**	**IZ408-M**	**14DLB39**
SiO_2	48.5	66.4	42.5	51.4	90.8	45.0	44.1
TiO_2	0.4	0.9	1.8	1.7	0.1	3.2	2.1
Al_2O_3	28.1	16.5	20.7	24.9	5.4	14.6	16.2
FeO	3.3	5.3	13.5	13.5	0.4	17.2	14.3
MgO	2.4	1.8	6.7	4.3	0.1	7.1	8.1
CaO	14.8	7.2	12.1	0.8	1.8	8.7	13.0
Na_2O	2.4	0.4	1.6	1.2	1.3	2.7	1.3
K_2O	0.13	1.33	0.75	2.00	0.13	0.75	0.06
MnO	0.0	0.1	0.2	0.2	0.0	0.3	0.2
Mg#	57.1	37.5	47.2	36.0	34.2	42.3	50.2
A/CNK	0.91	1.08	0.81	4.45	0.99	0.69	0.63
K/Ca	0.01	0.21	0.07	2.89	0.08	0.10	0.005

Table S3.3. Mineral Compositions analyzed by EPMA (in wt%).

	2030B	**2032A**	**2032I**	**2033A**	**2035A**	**2035B**	**2036A**	**2036C**	**2036E**	**2038**	**2040C**
Garnet											
SiO_2		40.6					40.6	39.6	40.8	38.4	40.3
TiO_2		0.03					0.06	0.04	0.06	0.05	0.02
Al_2O_3		23.1					22.6	22.7	23.1	22.0	22.3
FeO		22.9					23.3	24.0	21.7	30.5	23.6
MgO		13.6					13.6	13.0	13.5	7.3	12.9
CaO		0.2					0.7	0.8	1.2	1.1	1.2
Na_2O		-					< D.L.	0.01	0.005	-	0.003
K_2O		-					0.003	0.001	0.004	-	-
MnO		0.2					0.5	0.2	0.3	0.9	0.5
Cr_2O_3		-					-	-	-	0.004	-
Y_2O_3		-					-	-	-	-	-
Total		100.7					101.3	100.4	100.7	100.1	100.8
Alm %		48.1					47.1	48.1	45.5	66.7	48.0
Pyr %		51.0					49.8	49.1	50.6	28.4	47.9
Grs %		0.4					2.0	2.2	3.1	3.0	3.1
Spsr %		0.5					1.1	0.5	0.7	2.0	1.1
Plagioclase											
SiO_2	45.0		45.9	47.6		57.8		64.2	58.7	62.1	
TiO_2	-		0.01	-		0.02		0.01	0.03	-	
Al_2O_3	35.1		35.5	33.7		26.6		21.6	26.7	24.3	
Fe_2O_3	0.15		0.09	0.13		0.15		0.04	0.05	0.02	
CaO	18.1		18.1	16.4		8.0		3.1	8.1	4.8	
Na_2O	1.3		1.1	2.1		6.7		7.9	6.3	8.6	
K_2O	0.05		0.02	0.20		0.26		2.22	0.31	0.26	
Total	99.6		100.8	100.0		99.4		99.0	100.2	100.1	
An %	88.4		89.8	80.0		39.2		15.4	40.7	23.3	
Ab %	11.3		10.1	18.8		59.2		71.3	57.5	75.2	
Orth %	0.3		0.1	1.2		1.5		13.3	1.8	1.5	
K-feldspar											
SiO_2							63.7	64.2		64.1	
TiO_2							-	0.04		-	
Al_2O_3							19.0	19.1		19.1	
Fe_2O_3							0.03	0.01		0.01	
CaO							0.26	0.31		0.05	
Na_2O							2.0	2.4		1.0	
K_2O							13.9	13.1		15.4	
Total							98.9	99.1		99.7	
An %							1.2	1.6		0.3	
Ab %							17.7	21.3		9.1	
Orth %							81.1	77.1		90.7	

Table S3.3 (continued). Mineral Compositions analyzed by EPMA (in wt%).

	2044	**DDM163**	**DDM303**	**DDM309**	**DDM342**	**IV-16-09**	**IV-16-19**	**IV-16-24**	**IZ408-L**	**IZ408-M**	**14DLB39**
Garnet											
SiO_2		39.6	40.3	38.7	39.8	38.0	39.1	39.3			39.8
TiO_2		0.13	0.02	0.16	0.13	0.02	0.10	0.02			0.08
Al_2O_3		22.0	22.7	21.8	22.2	21.4	21.2	21.7			21.7
FeO		23.6	22.5	26.9	21.3	29.9	24.3	28.6			21.7
MgO		8.8	12.3	6.0	8.9	3.2	7.7	9.3			6.9
CaO		6.3	2.7	6.7	8.2	6.7	6.5	0.8			9.9
Na_2O		0.02	0.04	0.02	0.02	-	-	-			-
K_2O		< D.L.	< D.L.	0.01	< D.L.	-	-	0.004			0.01
MnO		0.5	0.3	0.8	0.4	1.0	1.0	0.4			0.4
Cr_2O_3		-	-	-	-	0.01	0.01	0.04			0.002
Y_2O_3		-	-	-	-	-	0.01	0.01			0.02
Total		101.0	100.8	101.2	101.0	100.2	99.8	100.2			100.5
Alm %		49.0	46.8	56.7	44.0	66.1	51.2	61.5			46.0
Pyr %		32.9	45.5	23.1	33.1	12.7	29.1	35.5			26.2
Grs %		17.1	7.2	18.5	22.1	18.9	17.4	2.3			26.9
Spsr %		1.1	0.6	1.8	0.8	2.3	2.1	0.8			0.9
Plagioclase											
SiO_2	61.4	60.3	63.0	55.3	50.1	45.2	48.8		66.2	56.2	
TiO_2	-	-	-	0.01	-	-	-		-	-	
Al_2O_3	24.4	26.0	23.8	28.1	32.8	35.8	33.0		21.4	28.2	
Fe_2O_3	0.17	0.03	0.03	0.07	0.06	0.03	0.38		0.17	0.09	
CaO	5.2	7.1	4.5	10.1	14.7	18.2	14.6		1.4	9.2	
Na_2O	8.0	7.5	8.9	5.5	3.0	1.1	2.9		10.6	6.1	
K_2O	0.77	0.33	0.35	0.34	0.17	0.01	0.16		0.25	0.09	
Total	99.9	101.1	100.6	99.5	100.8	100.4	99.8		100.0	100.0	
An %	25.3	33.5	21.4	49.3	72.5	90.0	72.8		6.5	45.1	
Ab %	70.2	64.6	76.6	48.7	26.5	10.0	26.3		92.1	54.3	
Orth %	4.5	1.9	2.0	2.0	1.0	0.1	0.9		1.4	0.5	
K-feldspar											
SiO_2	63.8							61.9			
TiO_2	-							-			
Al_2O_3	19.0							18.9			
Fe_2O_3	0.03							0.10			
CaO	0.11							0.16			
Na_2O	1.3							1.9			
K_2O	14.7							14.1			
Total	99.1							97.0			
An %	0.6							0.8			
Ab %	12.1							16.7			
Orth %	87.3							82.5			

Table S3.4. Mineral-separate compositions (by ICP-OES, double-spike†, and mixed-spike TIMS‡).

	2032A	2032I	2035A	2035B	2036A	2036C	2038
Garnet Separates							
Ca (wt%)	0.09				0.49	0.51	0.70
K (wt%)	0.02				0.05	0.003	0.02
MgO (wt%)*	9.9				13.5	11.7	7.3
Na_2O (wt%)*	0.01				0.003	<D.L.	0.004
K/Ca (mol/mol)	0.18				0.09	0.01	0.03
Ca (wt%)†	0.11				0.54	0.58	0.70
^{44}Ca (mol)†	5.5E-05				2.8E-04	3.0E-04	3.6E-04
Ca (wt%)‡	-				-	-	0.65
K (wt%)‡	-				-	-	0.03
Feldspar Separates							
Ca (wt%)		11.41		3.49		0.49	0.89
K (wt%)		0.27		0.55		8.21	8.65
MgO (wt%)*		1.3		1.5		<D.L.	0.02
Na_2O (wt%)*		1.0		4.7		3.2	3.6
K/Ca (mol/mol)		0.02		0.16		17.1	10.0
Ca (wt%)†		12.72		3.99		0.68	0.88
^{44}Ca (mol)†		6.5E-03		2.1E-03		3.5E-04	4.5E-04
Ca (wt%)‡		-		-		-	0.76
K (wt%)‡		-		-		-	6.67
Whole Rocks							
Ca (wt%)	-	4.99	3.12	1.32	0.16	0.30	0.73
K (wt%)	-	0.08	0.77	0.46	1.39	2.48	5.38
MgO (wt%)*	-	15.4	17.3	13.4	4.6	3.5	0.2
Na_2O (wt%)*	-	0.2	0.5	1.9	0.3	1.0	2.6
K/Ca (mol/mol)	-	0.02	0.25	0.4	8.8	8.4	7.6
Ca (wt%)†	0.035	4.71	3.48	1.54	0.18	0.33	0.69
^{44}Ca (mol)†	1.8E-05	2.4E-03	1.8E-03	8.0E-04	9.0E-05	1.7E-04	3.5E-04
Ca (wt%)‡	0.035	-	-	-	0.063	-	0.56
K (wt%)‡	0.539	-	-	-	0.49	-	3.62

†measurement using ^{42}Ca-^{48}Ca double spike (TIMS); ‡measurement using ^{41}K-^{43}Ca mixed-spike (ID-TIMS),
*value converted to oxide (wt%) for easier comparison to other analyses.

Table S3.4 (continued). Mineral-separate compositions (by ICP-OES, double-spike†, and mixed-spike TIMS‡).

	2044	DDM303	IV-16-09	IV-16-24	IZ408-L	IZ408-M	14DLB39
Garnet Separates							
Ca (wt%)		1.73		0.47			7.72
K (wt%)		<D.L.		0.08			0.01
MgO (wt%)*		13.9		8.2			7.4
Na$_2$O (wt%)*		0.03		0.03			0.17
K/Ca (mol/mol)		-		0.15			0.001
Ca (wt%)†		1.70		0.54			7.22
^{44}Ca (mol)†		8.7E-04		2.8E-04			3.7E-03
Ca (wt%)‡		-		0.37			-
K (wt%)‡		-		0.05			-
Feldspar Separates							
Ca (wt%)		2.66		0.56			
K (wt%)		0.65		3.76			
MgO (wt%)*		1.5		0.1			
Na$_2$O (wt%)*		6.8		3.3			
K/Ca (mol/mol)		0.25		6.8			
Ca (wt%)†		3.01		0.63			
^{44}Ca (mol)†		1.5E-03		3.2E-04			
Whole Rocks							
Ca (wt%)	1.17		5.78	0.62	1.33	6.94	9.72
K (wt%)	4.11		1.26	1.68	0.10	0.62	0.03
MgO (wt%)*	0.3		2.2	5.0	0.1	8.4	9.1
Na$_2$O (wt%)*	3.0		0.4	1.2	1.3	2.7	1.4
K/Ca (mol/mol)	3.6		0.22	2.8	0.08	0.09	0.003
Ca (wt%)†	1.17		5.42	0.60	1.29	6.36	-
^{44}Ca (mol)†	6.0E-04		2.8E-03	3.1E-04	6.6E-04	3.3E-03	-
Ca (wt%)‡	1.22		-	0.53	-	-	-
K (wt%)‡	4.10		-	1.32	-	-	-

†measurement using ^{42}Ca-^{48}Ca double spike (TIMS); ‡measurement using ^{41}K-^{43}Ca mixed-spike (ID-TIMS),
*value converted to oxide (wt%) for easier comparison to other analyses.

Table S3.5. ε_{Ca} of analyzed samples and standards.

Sample	Type	Notes	$^{40}Ca/^{44}Ca$	SE	ε_{Ca}	Sample	Type	Notes	$^{40}Ca/^{44}Ca$	SE	ε_{Ca}
SRM915a	WR	NC	47.161	0.001	1.0	**Lost-City**	Vent BH2	C	47.163	0.001	1.4
	WR	NC	47.161	0.006	1.1		Vent BH2	C	47.157	0.001	0.3
	WR	NC	47.161	0.001	1.0		Vent BH2	C	47.155	0.001	-0.2
	WR	C	47.164	0.001	1.6		Vent BH2	C	47.150	0.001	-1.3
	WR	NC	47.165	0.001	1.9		Vent BH2	C	47.153	0.001	-0.6
	WR	C	47.157	0.001	0.1		Vent BH2	C	47.157	0.001	0.1
	WR	C	47.165	0.001	2.0		Vent BH2	NC	47.155	0.001	-0.2
	WR	NC	47.161	0.001	1.1			**Average**	**47.156**	-	**-0.1**
	WR	NC	47.165	0.002	1.9			**2SE**	0.003	-	0.6
	WR	C	47.166	0.001	2.2						
	WR	NC	47.162	0.001	1.2	**DNC-1**	WR	C	47.150	0.001	-1.3
	WR	C	47.156	0.002	0.1		WR	C	47.155	0.001	-0.3
	WR	NC	47.168	0.001	2.6		WR	C	47.152	0.001	-0.9
	WR	C	47.168	0.001	2.6		WR	C	47.160	0.001	0.9
	WR	NC	47.159	0.001	0.7		WR	C	47.157	0.001	0.1
	WR	NC	47.162	0.001	1.2		WR	C	47.159	0.001	0.6
	WR	NC	47.166	0.001	2.1		WR	C	47.159	0.001	0.5
	WR	NC	47.166	0.001	2.1		WR	C	47.158	0.001	0.3
		Average	**47.163**	-	**1.5**		WR	C	47.160	0.001	0.8
		2SE	0.002	-	0.4			**Average**	**47.156**	-	**0.0**
								2SE	0.003	-	0.6
W2A	WR	C	47.152	0.001	-0.8						
	WR	C	47.154	0.001	-0.3						
	WR	C	47.157	0.002	0.2						
	WR	C	47.156	0.001	0.0	**BSE***	*(n = 24)*	**Average**	**47.156**	**-**	**0.0**
	WR	C	47.149	0.001	-1.4			**2SE**	0.001	-	0.3
	WR	C	47.162	0.001	1.2						
	WR	C	47.155	0.001	-0.1						
	WR	C	47.157	0.002	0.1						
		Average	**47.155**	-	**-0.1**						
		2SE	0.003	-	0.5						

Table S3.5. (continued) ε_{Ca} of analyzed samples and standards.

Sample	Type	Aliquot	^{40}Ca/^{44}Ca	SE	ε_{Ca}	
2030B	plag	A	47.173	0.001	3.6	
	plag	B	47.168	0.001	2.6	**3.1**
2032A	WR	A	47.514	0.002	76.0	
	WR	B	47.515	0.002	76.1	
	WR	C	47.520	0.002	77.3	
	WR	D	47.518	0.003	76.7	
	WR-2	A	47.523	0.001	77.8	**76.8**
	grt	A	47.356	0.001	42.4	
	grt	B	47.356	0.001	42.4	**42.4**
2032I	plag	A	47.165	0.001	1.9	
	plag	B	47.166	0.001	2.1	**2.0**
2033A	plag	A	47.172	0.001	3.4	
	plag	B	47.161	0.002	1.2	**2.3**
2035A	WR	A	47.163	0.001	1.5	
	WR	B	47.172	0.001	3.4	**2.4**
2035B	WR	A	47.175	0.001	3.9	
	WR	B	47.171	0.001	3.1	**3.5**
	plag	A	47.169	0.001	2.9	
	plag	B	47.174	0.001	3.8	**3.3**
2036A	WR	A	47.344	0.001	39.8	
	WR	B	47.341	0.001	39.3	**39.6**
	grt	A	47.217	0.001	13.0	
	grt	B	47.231	0.001	16.0	
	grt	C	47.231	0.001	15.9	
	grt	D	47.233	0.001	16.3	**15.3**
2036C	WR	A	47.329	0.001	36.8	
	WR	B	47.321	0.001	35.1	
	WR	C	47.331	0.001	37.1	**36.3**
	Kspar	A	47.427	0.001	57.4	
	Kspar	B	47.432	0.001	58.5	**58.0**
	grt	A	47.215	0.001	12.4	
	grt	B	47.216	0.001	12.8	**12.6**
2036E	WR	A	47.184	0.001	5.8	
	WR	B	47.187	0.001	6.6	
	WR	C	47.196	0.001	8.4	**6.9**
	grt	A	47.177	0.001	4.4	
	grt	B	47.176	0.001	4.2	**4.3**
2038	WR	A	47.312	0.001	33.1	
	WR	B	47.321	0.001	35.0	
	WR	C	47.318	0.001	34.3	**34.1**
	Kspar	A	47.345	0.001	40.2	
	Kspar	B	47.350	0.001	41.2	**40.7**
	grt	A	47.222	0.001	14.0	
	grt	B	47.225	0.001	14.7	
	grt	C	47.220	0.001	13.7	**14.1**
2040C	WR	A	47.215	0.001	12.5	
	WR	B	47.215	0.001	12.5	**12.5**
	grt	A	47.213	0.001	12.1	
	grt	B	47.217	0.001	12.9	**12.5**
2044	WR	A	47.225	0.001	14.5	
	WR	B	47.228	0.001	15.3	**14.9**
DDM163	grt	A	47.161	0.001	1.1	
	grt	B	47.155	0.001	-0.2	
	grt	C	47.158	0.002	0.3	**0.4**
DDM303	grt	A	47.167	0.001	2.4	
	grt	B	47.167	0.002	2.3	**2.4**
DDM309	grt	A	47.153	0.001	-0.6	
	grt	B	47.157	0.001	0.3	
	grt	C	47.153	0.001	-0.6	**-0.3**
DDM342	grt	A	47.163	0.003	1.5	
	grt	B	47.165	0.001	2.0	**1.8**
IV-16-09	WR	A	47.157	0.001	0.3	
	WR	B	47.163	0.001	1.5	**0.9**
	grt	A	47.164	0.002	1.6	
	grt	B	47.163	0.001	1.4	**1.5**
IV-16-19	WR	A	47.162	0.001	1.2	
	WR	B	47.160	0.001	0.8	**1.0**
	grt	A	47.160	0.002	0.9	
	grt	B	47.159	0.002	0.6	**0.7**
IV-16-24	WR	A	47.172	0.001	3.4	
	WR	B	47.167	0.001	2.4	**2.9**
	grt	A	47.170	0.001	2.9	
	grt	B	47.164	0.001	1.7	**2.3**
	Kspar	A	47.173	0.003	3.5	
	Kspar	B	47.171	0.001	3.1	
	Kspar	C	47.181	0.003	5.3	**4.2**
IZ408-L	WR	A	47.161	0.001	1.0	
	WR	B	47.164	0.001	1.8	**1.4**
IZ408-M	WR	A	47.164	0.002	1.7	
	WR	B	47.157	0.001	0.3	**1.0**
14DLB39	grt	A	47.162	0.001	1.3	
	grt	B	47.160	0.002	0.9	**1.1**

note: ε_{Ca} Values are normalized to BSE (^{40}Ca/^{44}Ca = 47.156)

Table S3.6. Selected results from anhydrous melting experiments at ~900 °C and ~1.0 GPa with various starting materials, taken from (Gao et al., 2016); (Castro et al., 2000, 1999; Patiño Douce and Beard, 1995; Pickering and Johnston, 1998; Rapp et al., 1991; Skjerlie et al., 1993; Skjerlie and Johnston, 1996, 1993, 1992; Watkins et al., 2007).

	P	TMP	TMG	BG	T	T	T	BT	HT	HT	MV	OPH	QA
T (°C)	900	900	900	900	900	900	875	875	875	875	900	900	900
P (kbar)	10	10	10	10	10	10	10	10	10	11	10	8	10
Starting Compositions													
SiO_2	57.36	77.14	69.10	67.02	68.30	67.05	68.26	70.12	68.98	68.98	59.03	51.19	60.40
TiO_2	1.26	0.50	0.52	0.41	0.50	0.48	0.52	0.29	0.35	0.35	1.12	1.18	1.70
Al_2O_3	23.24	11.20	15.20	16.98	14.90	15.19	14.89	16.18	16.07	16.07	15.12	16.62	11.30
FeO (T)	8.59	3.39	3.77	-	4.70	3.84	4.67	2.07	2.54	2.54	13.00	11.32	7.90
MnO	0.17	-	0.04	0.04	0.10	0.04	0.06	0.02	0.03	0.03	0.16	0.23	0.20
MgO	2.72	1.23	1.51	0.60	1.70	1.88	1.73	0.77	1.00	1.00	2.48	6.59	6.70
CaO	0.40	0.75	1.28	3.18	2.90	2.56	2.93	2.69	3.77	3.77	5.31	5.49	7.60
Na_2O	0.48	1.42	3.06	4.09	4.50	4.83	4.47	5.31	5.29	5.29	3.28	4.33	1.90
K_2O	3.63	2.44	3.81	3.62	2.10	1.85	2.05	1.81	1.53	1.53	1.64	0.82	0.70
P_2O_5	-	-	-	0.20	0.20	0.13	0.15	-	-	-	0.20	-	-
K/Ca	**10.54**	**3.78**	**3.46**	**1.32**	**0.84**	**0.84**	**0.81**	**0.78**	**0.47**	**0.47**	**0.36**	**0.17**	**0.11**
A/CNK	**4.27**	**1.77**	**1.32**	**1.03**	**1.00**	**1.04**	**1.00**	**1.04**	**0.93**	**0.93**	**0.90**	**0.92**	**0.64**
Mg#	**36.08**	**39.27**	**41.66**	**-**	**39.20**	**46.60**	**39.77**	**39.87**	**41.24**	**41.24**	**25.38**	**50.93**	**60.19**
Melt Compositions													
SiO_2	75.35	74.13	74.11	73.59	73.48	73.42	74.27	76.00	76.29	75.62	74.65	64.52	76.22
TiO_2	0.22	0.20	0.17	0.33	0.10	0.07	0.07	0.10	0.19	0.16	0.22	0.47	0.34
Al_2O_3	14.18	15.55	15.90	14.80	14.88	14.89	15.26	13.92	13.45	13.47	15.17	19.62	14.92
FeO (T)	1.70	1.39	1.41	1.26	1.26	1.24	1.25	1.58	1.59	1.51	2.03	4.45	2.01
MnO	0.03	<D.L.	0.07	0.03	<D.L.	0.04	0.03	0.04	0.08	0.15	0.02	<D.L.	0.06
MgO	0.43	0.28	0.22	0.13	0.10	0.13	0.13	0.18	0.17	0.35	0.20	1.24	0.50
CaO	0.24	0.83	0.70	0.93	1.05	1.03	1.16	1.43	1.19	1.42	1.66	3.15	2.81
Na_2O	1.36	2.13	3.49	4.20	4.61	4.67	3.89	3.32	2.91	3.23	1.92	5.35	0.95
K_2O	6.38	5.23	3.93	4.73	4.51	4.49	3.89	3.44	4.13	4.11	4.05	1.20	2.17
P_2O_5	0.11	0.24	-	-	-	0.03	0.03	-	-	-	0.07	-	-
K/Ca	**30.60**	**7.29**	**6.52**	**5.91**	**4.99**	**5.08**	**3.89**	**2.78**	**4.03**	**3.37**	**2.83**	**0.44**	**0.90**
A/CNK	**1.48**	**1.46**	**1.41**	**1.08**	**1.04**	**1.03**	**1.20**	**1.18**	**1.18**	**1.09**	**1.44**	**1.24**	**1.65**
Mg#	**31.22**	**26.72**	**21.76**	**15.53**	**12.93**	**15.34**	**15.34**	**16.56**	**15.68**	**29.07**	**14.94**	**33.24**	**30.72**

Chapter 4

Kinetic and equilibrium Ca isotope effects in high-T rocks and minerals

4.1. Overview

Calcium isotope fractionation at high temperatures can result in δ^{44}Ca variations significantly larger than at surface conditions. Ca diffusion in experimental silicate melts, for example, can lead to very large kinetic Ca isotope effects (δ^{44}Ca shifts up to ~10‰), while studies of natural igneous samples suggest that equilibrium Ca isotope effects dominate (δ^{44}Ca shifts $\leq$ ~1‰) and can be used for geothermometry. However, kinetic Ca isotope effects, which can potentially obfuscate equilibrium signatures, have not been sufficiently explored in natural samples, and current silicate-mineral equilibrium predictions only exist for pyroxene minerals. Here, we present Ca isotope data (δ^{44}Ca and $\mu^{48/44}$Ca) for a suite of high-temperature metamorphic rocks and minerals, as well as density-functional theory (DFT) estimates of equilibrium Ca isotope fractionation factors for plagioclase, garnet, clinopyroxene, orthopyroxene, olivine, and apatite. At upper-granulite facies temperature conditions (T $\geq$ ~900°C), the largest predicted equilibrium fractionations are ~0.8‰, however, we find larger δ^{44}Ca variations in both whole-rocks (which span a δ^{44}Ca range of ~4‰) and individual minerals (which span a range of ~8‰). We also find large variations in the Ca isotope fractionations between mineral pairs (*e.g.* Δ^{44}Ca$_{grt\text{-}plag}$ varies from -1.5 to +1.5 ‰), which deviate further from predicted equilibrium values with increasing whole-rock Mg#, plagioclase anorthite content, orthopyroxene Ca/Mg, and garnet Mg#. We show that these dominantly kinetic fractionations can be distinguished from equilibrium fractionations through precise measurement of $\mu^{48/44}$Ca, by exploiting the slopes in triple-isotope space, and introduce a new variable (Δ^{48}Ca') which quantifies deviations from Ca-isotope equilibrium. Finally, we use available geochronological constraints and numerical modeling to demonstrate that observed kinetic isotope fractionations (up to ~3 ‰) between adjacent high [Ca] and low [Ca] rocks are most consistent with diffusion rates of ~10^{-10} – 10^{-7} m^2/yr, consistent with Ca transport via volume- and grain-boundary diffusion during lower-crustal metamorphism, where ^{44}Ca diffuses up to ~1% slower than ^{40}Ca ($D_{44}/D_{40} \approx 0.99$). This study confirms that kinetic Ca isotope effects are abundant in nature and commonly overwrite comparatively small equilibrium effects, even at very high temperatures and even when traditional techniques (such as Fe-Mg exchange and Ca-in-Opx thermometry) suggest the establishment of chemical equilibrium. Our results imply that δ^{44}Ca measurements cannot be used for geothermometry or as a tracer of carbonate recycling into the mantle, without first taking into consideration kinetic fractionation processes.

4.2. Introduction

Over the last two decades, precise stable Ca isotope measurements in high-temperature rocks and minerals have started to yield important constraints on solid-Earth processes (*e.g.* DePaolo, 2004;

Schiller et al., 2016). Recent studies have dominantly focused on δ^{44}Ca [defined $(^{44}\text{Ca}/^{40}\text{Ca})_{\text{sample}}/(^{44}\text{Ca}/^{40}\text{Ca})_{\text{standard}} - 1$] variations in mantle xenoliths and bulk lavas (Amini et al., 2009; Chen et al., 2018; Huang et al., 2011; S. Huang et al., 2010; Kang et al., 2017, 2016; Liu et al., 2017; Zhao et al., 2017), as well as *ab-initio* predictions for Ca isotope equilibrium fractionation factors between clinopyroxene and orthopyroxene at various temperatures (Feng et al., 2014; Wang et al., 2017). Results from these studies have been used to suggest that equilibrium Ca isotope fractionation between minerals, which depends mainly on the strength and coordination of Ca-O bonds in various mineral structures, can be used for isotopic thermometry. Several studies also use trends in δ^{44}Ca values for estimating fractions of recycled carbonate in mantle xenoliths and ocean island basalts (*e.g.* Chen et al., 2018; Huang et al., 2011; S. Huang et al., 2010; Kang et al., 2017, 2016; Liu et al., 2017).

The applicability of equilibrium predictions to natural samples, however, needs to be evaluated in the context of potential kinetic fractionations that could affect inter-mineral fractionation, $\Delta^{44}\text{Ca}_{\text{A-B}}$, which is defined as $\delta^{44}\text{Ca}_{\text{A}}$- $\delta^{44}\text{Ca}_{\text{B}}$ for minerals A and B. For example, Rayleigh-fractionation models applied to carbonate precipitation from mantle fluids have been invoked to explain positive δ^{44}Ca shifts in xenolith samples (Kang et al., 2017) (as opposed to negative shifts interpreted as direct carbonate incorporation in the other mentioned studies). One other study identified small, probably kinetic, effects in δ^{44}Ca and δ^{57}Fe mantle olivine (Zhao et al., 2017). Other than these two studies, kinetic Ca isotope fractionation at high temperatures has remained largely unexplored.

Kinetic effects at high-temperatures have been studied in the laboratory, however, and a large-body of experimental work has shown that Ca diffusion in molten silicates can result in much larger Ca isotope fractionations than have been documented so far in natural rocks and minerals (Watkins et al., 2017). Due to the large mass differences between isotopes of calcium (up to ~20% for ^{48}Ca *vs.* ^{40}Ca), there are large differences in the average speed for different isotopic species at a given kinetic energy, resulting in separation of isotopes during diffusive transport. In general, the diffusivity of ^{44}Ca relative to ^{40}Ca (D_{44}/D_{40}, equal to the square-root of the inverse mass ratio raised to an empirically-derived exponent) depends most significantly on diffusion medium (Richter et al., 1999). Large δ^{44}Ca effects (up to ~10‰) have been documented for Ca isotopes undergoing simple chemical diffusion (*e.g.* Richter et al., 2009, 2003, 1999, Watkins et al., 2014, 2011, 2009), thermal (Soret) diffusion (F. Huang et al., 2010; Richter et al., 2009), and isotopic self-diffusion in silicate liquids (Watkins et al., 2014), yet these effects remain underexplored in nature [see (Chopra et al., 2012) for an example using Mg isotopes]. However, Ca diffusion in solid minerals (*i.e.,* 'volume diffusion') and along grain-boundaries, applicable to a majority of metamorphic settings, are many orders of magnitude slower than in silicate liquids (Dohmen and Milke, 2010), and several orders of magnitude slower than Fe and Mg diffusion in analogous processes (Grant, 1988; Hudgins et al., 2011; Vielzeuf et al., 2007). Due to the time-scales required, Ca isotope fractionation during grain-boundary and volume-diffusion are much more difficult to evaluate experimentally.

In order to begin addressing the many open questions regarding Ca isotope fractionation in high-temperature rocks and minerals, and to gain insight into Ca isotope fractionation during lower-crustal metamorphic processes, we compare equilibrium estimates from density-functional theory

(DFT) to Ca isotope measurements in high-temperature metamorphic mineral-separates and whole-rocks from various locations.

4.3. Samples and methods

We report δ^{44}Ca measurements, corrected for radiogenic ^{40}Ca excesses [as reported in (Antonelli et al., 2018), see Fig. S4.1], along with bulk-rock and mineral chemical compositions for twenty-one whole-rock samples and their major minerals (including plagioclase, K-feldspar, garnet, clinopyroxene, orthopyroxene, hornblende, and apatite) from four different localities. The modal mineralogies, whole-rock compositions, in-situ mineral compositions, and mineral separate compositions are reported in Tables S4.1 to S4.4. The measured δ^{44}Ca for samples and standards are reported in Tables S4.5 and S4.6, respectively.

We also present multiple Ca isotope results, including μ^{48}Ca [defined as $(^{48}\text{Ca}/^{44}\text{Ca})_{\text{sample}}/(^{48}\text{Ca}/^{44}\text{Ca})_{\text{standard}} - 1$] for a select group of whole-rocks and mineral separates (including plagioclase, garnet, and orthopyroxene) measured by MC-ICP-MS (Table S4.7), DFT estimates for equilibrium fractionation in a variety of minerals with variable solid-solution compositions (including plagioclase, garnet, clinopyroxene, orthopyroxene, olivine, apatite, and several others) and numerical modelling results for diffusive Ca isotope fractionation in metamorphic whole-rocks (see Supplementary Materials, SM, for details).

The samples in this study are dominantly granulite and ultrahigh temperature (UHT) granulite-facies rocks with granoblastic to porphyroblastic textures (n = 17), but also include several amphibolites (n = 3) and a single eclogite [the same samples as studied in (Antonelli et al., 2018)]. Twelve granulite samples come from the northern part of the Napier Complex (NC), Antarctica; four lower-crustal granulite-facies xenoliths come from the Diavik Diamond Mine, Slave Province (SP), Canada; four amphibolite to granulite-facies samples come from the Ivrea-Verbano Zone (IVZ), Italy; and the eclogite sample (Sumdo Eclogite, SE) comes from the Lhasa Province, Tibet. Petrographic descriptions for the samples, along with previous work highlighting geochronologic and thermobarometric constraints for the various localities, are available in the Supplementary Information of (Antonelli et al., 2018).

4.4. Results

4.4.1. Predicted equilibrium fractionations

The results of our DFT predictions, in the form of reduced partition function ratios (RPFR, 1000lnβ), and comparisons between different calculation methods are tabulated in Table 4.1. We find that equilibrium δ^{44}Ca signatures are expected to increase in the general order: plagioclase < apatite < clinopyroxene < orthopyroxene ≤ garnet < olivine. We also confirm the previously proposed relationship (*e.g.* Feng et al., 2014; S. Huang et al., 2010; Magna et al., 2015; Wang et al., 2017) between 1000lnβ and Ca-O bond lengths (and coordination) in the studied minerals, where minerals with shorter bonds favor the heavy isotope (Fig. 4.1). Although minerals with eight-fold coordination (*e.g.* clinopyroxene & garnet) generally have longer Ca-O bond lengths than minerals with six-fold coordination (*e.g.* orthopyroxene & olivine, Table S4.8), they are predicted to have heavier δ^{44}Ca at a given bond-length. However, some of the more complex structures have extra Ca-O bonds with different lengths than the others, as tabulated in Table S4.8, and it is not always straightforward to disentangle coordination and average bond length for these irregular sites.

Our calculated equilibrium Δ^{44}Ca values between orthopyroxene and clinopyroxene are in general agreement with published values (Feng et al., 2014; Wang et al., 2017), and confirm that decreasing Ca/Mg in enstatite from 1/16 to 1/32 leads to increasing RPFRs, and that further decreases (to 1/64) do not lead to significantly larger effects. Our models, however, show less sensitivity to Ca isotope fractionation due to Ca dilution effects in enstatite than reported in previous studies (Feng et al., 2014; Wang et al., 2017).

Table 4.1. Calculated reduced partition-function ratios (1000ln$^{44/40}\beta$) from DFT modeling.

		Reduced partition function ratios, 1000•ln($^{44/40}\beta$)					
		Phonon-based (PBE*)		Force-constants (PBE*)		Force-constants (LDA)	
		298.15 K	1000 K	298.15 K	1000 K	298.15 K	1000 K
Diopside	-	14.26	**1.32**	13.77	1.23	14.61	1.31
	Doubled c	-	-	14.26	1.28	-	-
	Full C2/c cell, 2c	-	-	14.65	1.31	-	-
Enstatite	Ca:Mg = 1:15	-	-	19.20	1.72	-	-
	Ca:Mg = 1:15, 2c	-	-	19.28	1.73	-	-
	Ca:Mg = 1:31, 2c	-	-	20.50	1.84	-	-
	Ca:Mg = 1:63, quad cell	-	-	20.58	**1.85**	-	-
Forsterite	Ca:Mg = 1:7, M2 sub	-	-	20.30	1.82	-	-
	Ca:Mg = 1:15, 2a	-	-	23.35	2.10	-	-
	Ca:Mg = 1:31, 2a & c	-	-	23.11	**2.08**	-	-
	Ca:Mg = 1:63, 4a & 2c	-	-	23.48	2.11	-	-
Garnet	Grossular	18.63	**1.74**	19.39	1.74	20.09	1.80
	Ca:Mg = 1:11 (pyr)	-	-	22.32	2.00	-	-
	Ca:Mg = 1:23 (pyr, FC)	-	-	22.60	**2.03**	-	-
	Ca:Fe = 1:11 (alm, FM)	-	-	20.60	**1.85**	-	-
	Ca:Mn = 1:11 (sps, FM)	-	-	20.43	**1.83**	-	-
Plagioclase	Anorthite	11.41	**1.06**	12.06	1.08	14.06	1.26
	An50 (v1)	**-**	**-**	10.93	**0.98**	-	-
	An50 (v2)	**-**	**-**	11.53	1.03	-	-
	An50 (v3)	**-**	**-**	11.27	1.01	-	-
Apatite	Fluorapatite	13.10	1.21	-	-	-	-
Lime	(CaO)	16.43	1.51	-	-	-	-
Fluorite	(CaF_2)	14.69	1.34	-	-	-	-

*Assumed scale-factor of 1.06, LDA are unscaled. Preferred values are in bold. '2c' – doubled c axis, '2a' – doubled a axis, '4a' – quadrupled a axis; 'FC' – full cubic cell, 'FM' – Ferromagnetic; 'v1' through 'v3' are using ab-initio constraints obtained from (Kaercher et al., 2014).

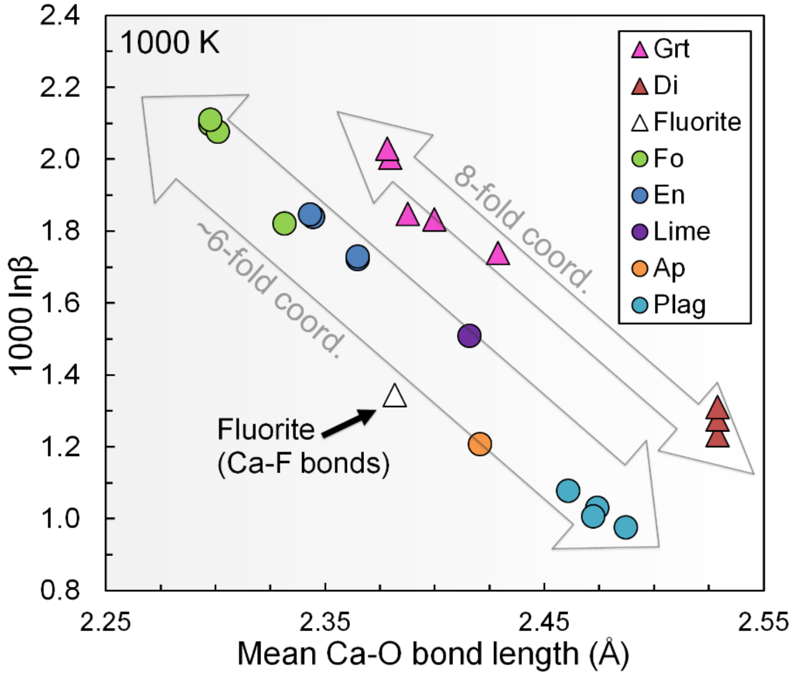

Fig. 4.1. Reduced partition-function ratios for ^{44}Ca/^{40}Ca (1000lnβ) *vs.* mean Ca-O bond lengths from our DFT simulations (n=23). Bond lengths and coordination are tabulated in Table S4.8. Triangles and circles represent minerals with ~eight-fold and ~six-fold coordination, respectively.

Applying the same exercise to forsterite and pyrope with various Ca/Mg (ranging from 1/8 to 1/64, and 1/12 to 1/24, respectively) we find that dilution does not significantly affect results for olivine or garnet. We do find, however, a small yet potentially measurable difference in the predicted equilibrium Ca isotopic compositions for anorthite and labradorite (An50), for all three labradorite structures used in our simulations (Kaercher et al., 2014) (Table 4.1). We find that labradorite has the lowest 1000lnβ values of all our results and is predicted to be the lightest at equilibrium conditions. The fluorite structure (CaF_2) leads to similar results as diopside, while fluorapatite [$Ca_5(PO_4)_3F$] lies between anorthite and fluorite, and lime (CaO) is predicted to have slightly heavier δ^{44}Ca than fluorite.

Assuming that the temperature dependence of 1000 lnβ values can be well represented at high temperature by the equation [$1000\ln\beta(T) = 1000\ln\beta(1000\ K) \times (10^6/T^2)$, where temperature is in Kelvin], we find that equilibrium Ca isotope fractionations between minerals do not exceed ~0.8‰ at temperatures relevant to the samples in our study (greater than ~800-900°C, Fig. 4.2). Fractionation factors (1000lnα), which represent the prediction for Δ^{44}Ca between minerals, can be approximated visually from Fig. 4.2 (using $1000\ln\beta_a - 1000\ln\beta_b$), but are calculated for our purposes using $\alpha_{a\text{-}b} = \beta_a/\beta_b$. Note that the fractionation factor between two phases, a and b, is the ratio of their β values ($\alpha_{a\text{-}b} = \beta_a/\beta_b$) at a given temperature, and that $\Delta^{44}Ca_{a\text{-}b} \approx 1000\ln\alpha_{a\text{-}b} = 1000\ln\beta_a - 1000\ln\beta_b$.

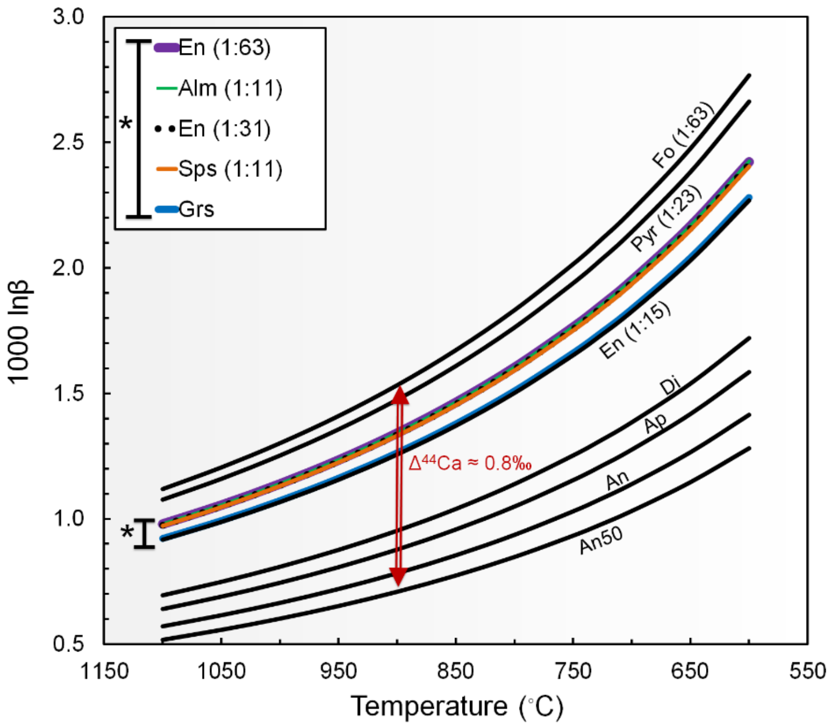

Fig. 4.2. Predicted temperature-variations for DFT-based ^{44}Ca/^{40}Ca reduced partition-function ratios (1000lnβ) in the studied silicate mineral structures. Lines are labeled by mineral-type and include (Ca:Mg), (Ca:Fe), or (Ca:Mn), as applicable to the various species. Expanded legend (*) indicates the order of results with similar RPFRs in the region indicated by the asterisk. Double-headed red arrow represents the approximate range in Δ^{44}Ca$_{A\text{-}B}$ predicted at 900 °C. Fo = forsterite, Pyr = pyrope, En = enstatite, Alm = almandine, Sps = spessartine, Grs = grossular, Di = diopside, Ap = fluorapatite, An = anorthite, An50 = labradorite. Fractionation factors (1000ln$\alpha_{A\text{-}B}$) and inter-mineral fractionations (Δ^{44}Ca$_{A\text{-}B}$) are ≈1000lnβ_A-1000lnβ_B.

4.4.2. Bulk-rock and mineral δ^{44}Ca variations

The δ^{44}Ca values of whole-rocks and minerals analyzed in the present study, corrected for radiogenic ingrowth of ^{40}Ca, are displayed in Fig. 4.3. We find that mafic rocks generally have more restricted whole-rock compositions compared to metapelites, and that minerals other than clinopyroxene exhibit large ranges in δ^{44}Ca (greater than ~3‰). Orthopyroxene, and in a few instances, feldspar and garnet, are found to be the most ^{44}Ca-enriched mineral phases, whereas clinopyroxene and hornblende are most similar to bulk-silicate Earth (BSE) and garnet and K-feldspar are the most ^{44}Ca depleted. Our results are in general agreement with previous δ^{44}Ca measurements in granitic minerals from a single whole-rock sample (Ryu et al., 2011). Given that our orthopyroxene separates were not completely pure, we used unmixing calculations to estimate the isotopic composition of pure orthopyroxene (Opx*, see SM and Fig. S4.2 for details). The single analyzed apatite separate was found to be the most ^{44}Ca-depleted mineral phase in our eclogite sample. We show our δ^{44}Ca results, organized by whole-rock sample, in Fig. S4.3.

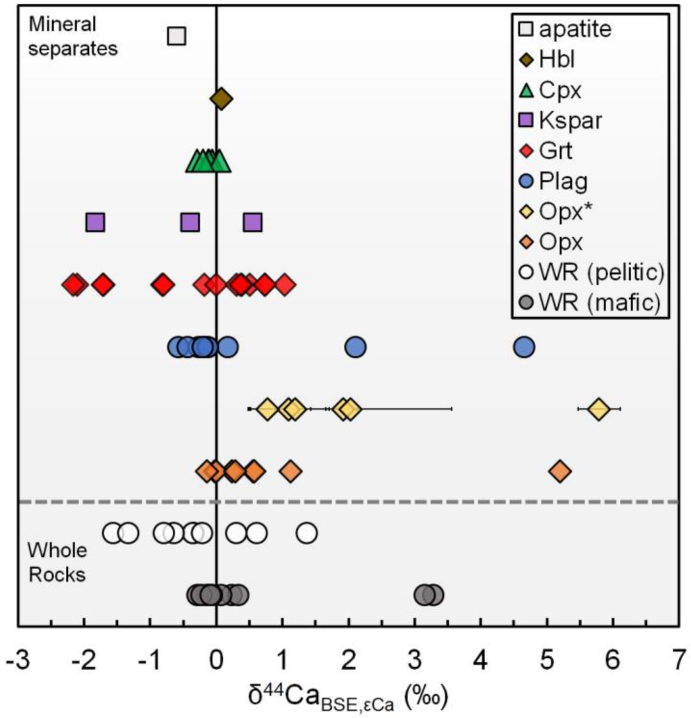

Fig. 4.3. Plot of δ^{44}Ca for the various mineral separates and whole-rocks analyzed in this study (n=66). Mafic (n=12) and pelitic (n=10) whole-rocks, orthopyroxene (n=9), pure-orthopyroxene (Opx*, n=6), plagioclase (n=10), garnet (n=14), K-feldspar (n=3), clinopyroxene (n=6), hornblende (n=1), and apatite (n=1). 2SD error bars on most measurements (< ±0.14‰) are smaller than the symbols, except for Opx*, where uncertainties range from ±0.2 to ±1.5‰ (with an average of ±0.5‰), depending on the unmixing parameters (See Fig. S4.2). Data are relative to bulk-silicate Earth (BSE).

Comparing our results with whole-rock chemical compositions, we find that mafic and pelitic samples with the lowest CaO and highest Mg# [defined as molar MgO/(MgO+FeO), using FeO_{total}] have the highest variability in bulk-rock δ^{44}Ca (Fig. 4.4). Interlayered whole-rocks (connected by colored arrows in Fig. 4.4) are found to exhibit the largest whole-rock δ^{44}Ca fractionations. Minerals from within the analyzed whole rocks generally show increasing δ^{44}Ca with increasing whole-rock Mg# and decreasing whole-rock and mineral CaO (wt%) (Fig. S4.4). As discussed further below, these patterns in whole rock chemistry and Ca isotopic composition can be explained by diffusive transport of Ca between high-Ca and low-Ca zones in the layered gneisses of the Napier complex.

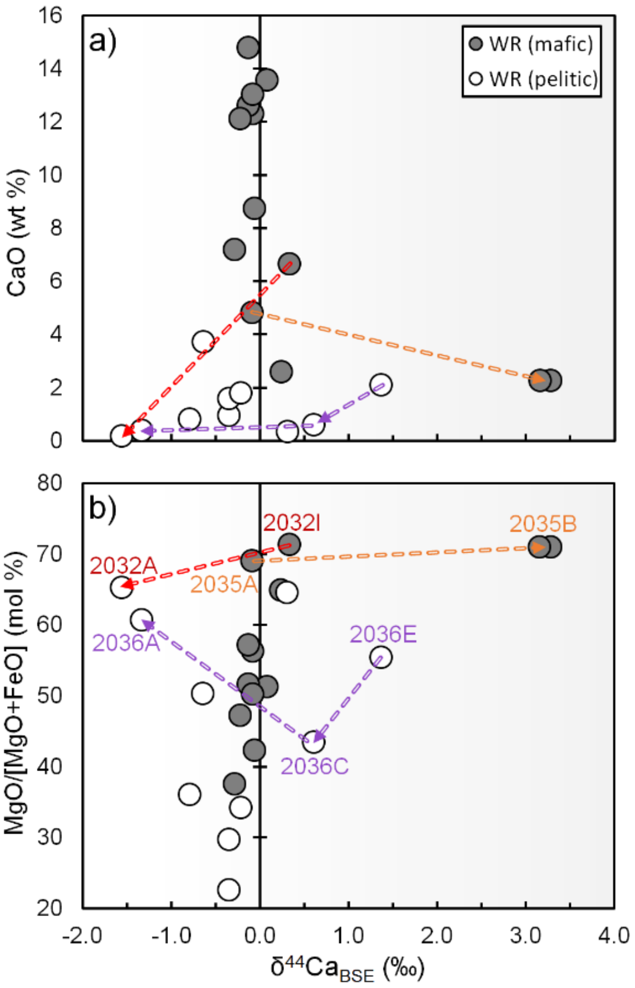

Fig. 4.4a,b. Plots of radiogenic-corrected whole-rock δ^{44}Ca versus **(a)** whole-rock CaO (wt%) and **(b)** whole-rock Mg# [molar MgO/(MgO+FeO)]. Colored arrows point in the direction of decreasing CaO between whole-rock samples collected from units with shared interfaces; 2035A-2035B (orange arrow), 2032A-2032I (red arrow), 2036A-2036C-2036E (purple arrows). Error bars are smaller than the symbols.

4.4.3. Inter-mineral δ^{44}Ca variations (Δ^{44}Ca)

Many of our samples have inter-mineral Δ^{44}Ca fractionations significantly different from equilibrium predictions (Fig. 4.5a-f). Within a single sample, δ^{44}Ca differences (Δ^{44}Ca) between minerals can be as large as ~2‰, exceeding the range that we predict at temperatures relevant to our samples (Fig. 4.2). Differences in δ^{44}Ca between whole-rocks and their constituent minerals can also exceed 2‰, and certain samples [*e.g.* 2035B (δ^{44}Ca = 3.3‰), consisting of ~80% orthopyroxene (measured δ^{44}Ca = +5.2‰) and ~15% plagioclase (δ^{44}Ca = +4.66‰)] suggest that unidentified minor phases can have highly-fractionated δ^{44}Ca. The modal mineralogy, however, was estimated from a single thin-section and it is likely that our estimates (which have a large influence on the predicted δ^{44}Ca of unidentified minerals) for orthopyroxene and plagioclase are slightly high. Mass balance for the rock can be achieved using reasonable values for clinopyroxene (*i.e.*, similar to BSE) if the modal mineralogy is assumed to contain slightly higher clinopyroxene (*e.g.* ~5%) and slightly lower plagioclase (*e.g.* ~12%) than estimated for the thin section in Table S4.1.

At granulite-facies temperatures (~800-900 °C), $\Delta^{44}Ca_{grt\text{-}cpx}$ and $\Delta^{44}Ca_{grt\text{-}fsp}$ are expected to be positive and in the range of 0.3-0.6‰ and 0.5-0.9‰, respectively (depending on the compositions of garnet and feldspar), but are observed to vary between -1.5 and +1.5‰. At the same temperatures, fractionation between low-Ca orthopyroxene and plagioclase is expected to be in the range ~0.6 to 0.8‰, but $\Delta^{44}Ca_{opx\text{-}fsp}$ in our samples range from 0.2 to ~2.0‰. Analogously, $\Delta^{44}Ca_{opx\text{-}cpx}$ equilibrium should be approximately +0.3 to +0.5‰, but measured values can exceed ~1‰. $\Delta^{44}Ca_{grt\text{-}opx}$ values (predicted values of -0.1 to +0.2‰) are observed to range between -1.6 and +0.3‰.

As shown in Fig. 4.5a-f, garnet-mineral and orthopyroxene-mineral $\Delta^{44}Ca$ deviate further from predicted equilibrium values with increasing values for several whole-rock and mineral-composition proxies. Garnet fractionations ($\Delta^{44}Ca_{grt\text{-}fsp}$, $\Delta^{44}Ca_{grt\text{-}cpx}$, $\Delta^{44}Ca_{grt\text{-}opx}$, & $\Delta^{44}Ca_{grt\text{-}wr}$) grow increasingly negative with increasing whole-rock Mg# and garnet Mg# (Fig. 4.5a,b), and orthopyroxene-mineral fractionations grow increasingly positive with increasing whole-rock Mg#, feldspar anorthite content, orthopyroxene Ca/Mg, and modal orthopyroxene content (Fig. 4.5c-f).

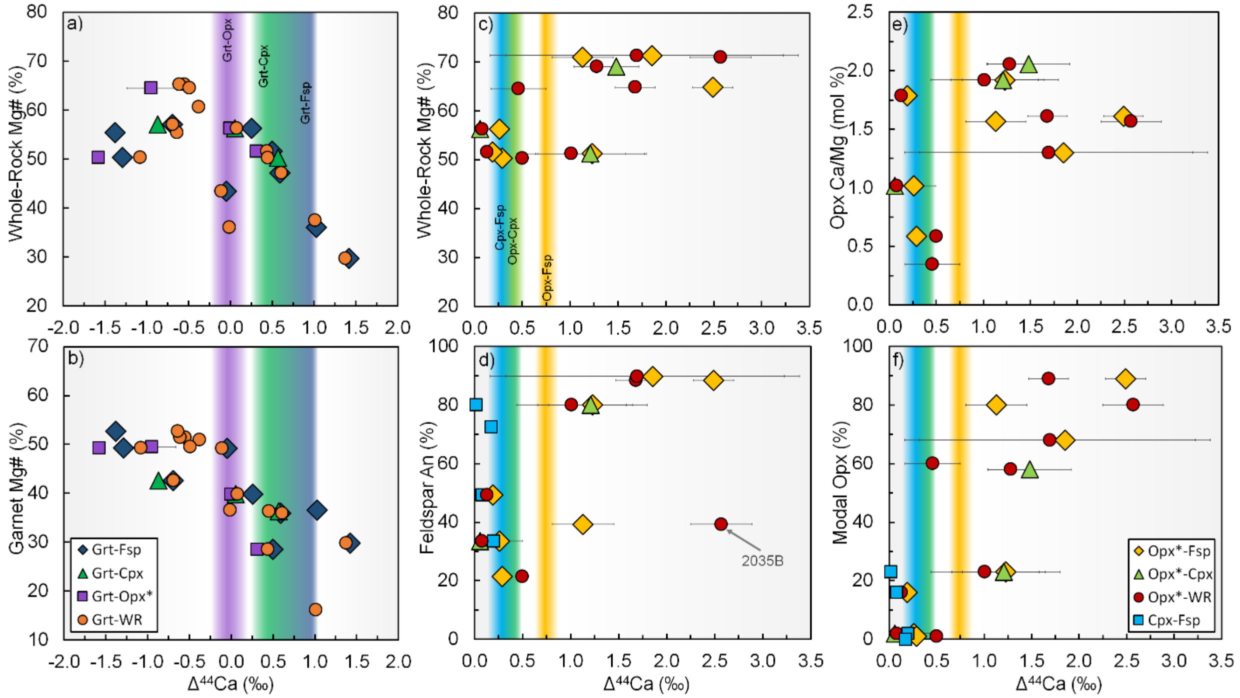

Fig. 4.5a-f. Plots of mineral $\Delta^{44}Ca$ versus various whole-rock and mineral compositions. Garnet-mineral and garnet-whole rock $\Delta^{44}Ca$ versus **(a)** whole rock Mg# and **(b)** garnet Mg#. Orthopyroxene-mineral and orthopyroxene-whole rock $\Delta^{44}Ca$ versus **(c)** whole-rock Mg#, **(d)** feldspar anorthite content, **(e)** Ca/Mg of orthopyroxene, and **(f)** modal orthopyroxene content. Panels (d) and (f) also include measurements of $\Delta^{44}Ca_{cpx\text{-}fsp}$. For non-orthopyroxene mineral-pairs, error bars are smaller than the symbols, for data including Opx*, uncertainties range from 0.2 to 1.5‰, varying with unmixing parameters (Fig. S4.2). Colored bands indicate predicted equilibrium values at 800-900 °C: Grt-Opx (purple), Grt-Cpx (green), Grt-Fsp (blue), Opx-Fsp (yellow), Opx-Cpx (pale green), and Cpx-Fsp (cyan). Larger Font for colored bands.

Based on single analyses, $\Delta^{44}Ca_{hbl\text{-}plag}$ (+0.28‰) is similar to $\Delta^{44}Ca_{cpx\text{-}plag}$ in other rocks, and $\Delta^{44}Ca_{cpx\text{-}ap}$ is slightly higher (+0.41‰, suggesting disequilibrium when compared to DFT). No trends between $\Delta^{44}Ca_{cpx\text{-}plag}$ and whole-rock or mineral compositions are clearly distinguishable. Half of the measured $\Delta^{44}Ca_{cpx\text{-}plag}$ values are similar to equilibrium predictions (+0.2 to +0.3‰), and the other half have slightly smaller $\Delta^{44}Ca_{cpx\text{-}plag}$ (0.0 to +0.1‰) that may suggest temperatures higher than ~900°C, assuming equilibrium. However, without further constraints it is hard to distinguish whether these values represent equilibrium at different temperatures or whether they result from small kinetic effects.

4.4.4. Δ^{48}Ca' and deviations from Ca-isotope equilibrium

Although previously untested, a possibility exists for distinguishing kinetic from equilibrium fractionation by measuring ^{48}Ca/^{44}Ca. Given sufficient precision, this can be achieved by exploiting the slopes between samples in triple-isotope space (*e.g.* ^{48}Ca/^{44}Ca *vs.* ^{42}Ca/^{44}Ca). The approach exploits differences in the kinetic-limit and equilibrium-limit for mass-dependence during stable-isotope fractionation (*e.g.* Young et al., 2002), and similar approaches have been used to distinguish kinetic from equilibrium effects in isotopic measurements of Fe (McCoy-West et al., 2018) and Mg (Olsen et al., 2013; Young and Galy, 2004). For Ca isotopes, this difference can be manifested using any two of the five total isotope ratios. Due to their relatively high abundances, we use μ^{48}Ca/μ^{42}Ca to evaluate slopes in triple isotope space.

The equilibrium-limit, describing a μ^{48}Ca/μ^{42}Ca slope of -1.751, is defined by the relationship $[(1/m_1)-(1/m_3)] \div [(1/m_1)-(1/m_2)]$, where m_1,m_2, & m_3 are the masses of ^{44}Ca, ^{42}Ca, and ^{48}Ca, respectively (Young et al., 2002); the kinetic limit is described by $\ln(m_1/m_3)/\ln(m_1/m_2)$, and results in a slope of -1.872. The difference in these slopes leads to a difference of ~200 ppm (~0.2‰) in μ^{48}Ca between equilibrium and kinetic fractionation, at a corresponding δ^{44}Ca fractionation of ~3‰. Using the method of (Schiller et al., 2012) and ^{44}Ca signals of ~10-30 V, however, the precision of our MC-ICP-MS measurements is sufficient to distinguish between equilibrium and kinetic μ^{48}Ca fractionations for corresponding δ^{44}Ca fractionations as small as ~0.5‰ (see SM).

Similar to notation for other elements with triple-isotope systems, we propose a new variable (Δ^{48}Ca') in order to easily quantify deviations from Ca-isotope equilibrium. This variable corresponds to excesses or deficits in μ^{48}Ca from predicted equilibrium values at a given μ^{42}Ca [defined $(^{42}Ca/^{44}Ca)_{sample}/(^{42}Ca/^{44}Ca)_{standard} - 1$], and can be reported as:

$$\Delta^{48}Ca' = \mu^{48}Ca_{measured} - \mu^{48}Ca_{predicted} \quad \text{(Eq. 4.1)}$$

$$\Delta^{48}Ca' = \mu^{48}Ca_{measured} - [(\mu^{42}Ca_{measured} + 1)^{-1.751} - 1] \quad \text{(Eq. 4.2)}$$

In order to test whether dominantly-kinetic *vs.* dominantly-equilibrium Ca isotope fractionation can be successfully identified using Δ^{48}Ca', we start by analyzing two igneous end-member samples, that are unrelated to the study at hand, but that are further explored in upcoming work. The first sample, in which fractionations are dominantly kinetic in origin, comes from experimental plagioclase phenocryst growth in a simplified tonalite melt. In this sample, the δ^{44}Ca difference between plagioclase separates and glass (Δ^{44}Ca) exceeds 2‰ (Table S4.7). The second end-member sample, a cumulate gabbro from the Stillwater igneous complex, Montana, where orthopyroxene and plagioclase separates have Δ^{44}Ca$_{opx-fsp}$ of ~0.7‰, represents slow-crystallization at magmatic temperatures over probably hundreds to thousands of years.

We find that the end-member samples have clearly distinguishable Δ^{48}Ca' (Fig. 4.6), with μ^{48}Ca/ μ^{42}Ca slopes closely matching the equilibrium- and kinetic-limits described above. The experimental sample shows a strong depletion in Δ^{48}Ca'$_{plag}$ [-153 ± 15 ppm (2SE)] relative to Δ^{48}Ca'$_{glass}$ [-15 ± 17 ppm (2SE)], and the Stillwater orthopyroxene and plagioclase separates have Δ^{48}Ca' values indistinguishable from each other [30 ± 8 ppm and 24 ± 9 ppm (2SE), respectively].

Given this promising result, we analyze several contrasting samples from our dataset in order to establish whether (i) Δ^{44}Ca values significantly-different from our DFT predictions (*e.g.* negative $\Delta^{44}Ca_{grt-plag}$) truly represent kinetic effects, and whether (ii) Δ^{44}Ca values in apparent agreement with our DFT predictions are corroborated by equilibrium Δ^{48}Ca' values between minerals (≈ 0).

We analyze garnet-feldspar pairs from two whole-rock samples, and find that (i) negative $\Delta^{44}Ca_{grt-plag}$ (-1.6‰, DDM303) is accompanied by a large Δ^{48}Ca' depletion, and that (ii) positive $\Delta^{44}Ca_{grt-plag}$ (+0.6‰, IV-16-19) is not accompanied by measureable Δ^{48}Ca' fractionation (Fig. 4.6). This suggests that our DFT predictions for garnet and plagioclase are approximately correct and that deviations from these values are the result of kinetic processes.

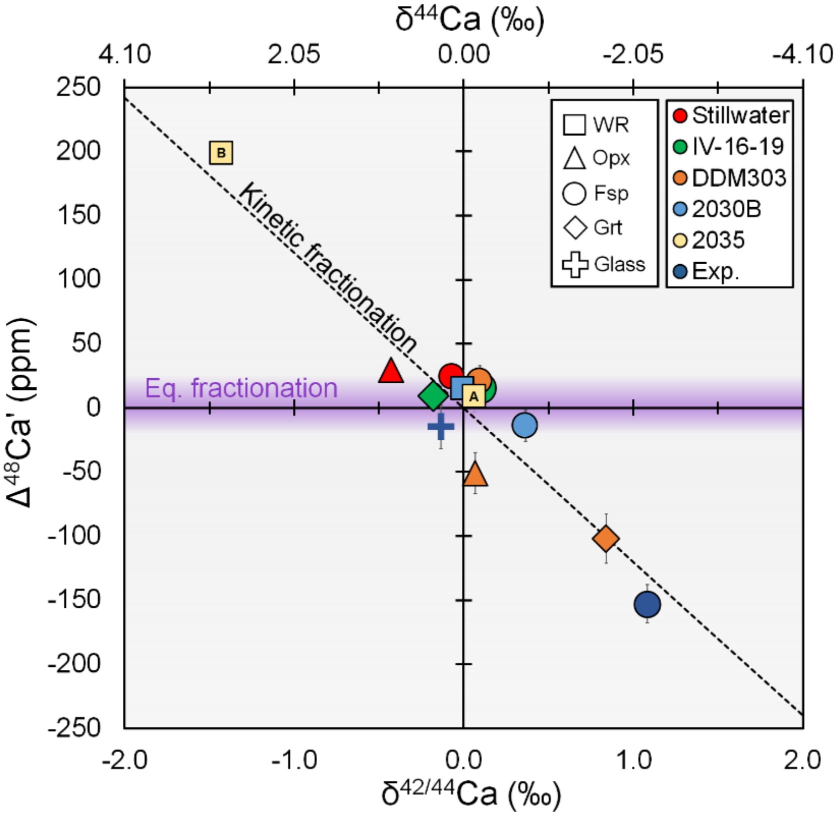

Fig. 4.6. Plot of Δ^{48}Ca' vs. $\delta^{42/44}$Ca for select samples and for kinetic and equilibrium end-members, measured by MC-ICP-MS. Equivalent δ^{44}Ca values [converted using a factor of -2.05 (Fantle and Tipper, 2014)] are also included for reference. All data are relative to SRM915b, which is ≈BSE (Schiller et al., 2012).

In a similar fashion, the large δ^{44}Ca difference between whole-rock samples from the center (2035A, -0.2‰) and edge (2035B, +3.0‰) of a metamorphosed ultramafic dike, is accompanied by a strong Δ^{48}Ca' enrichment [+199 ± 8 ppm in 2035B *vs.* +9 ± 12 ppm (2SE) in 2035A], which is in good agreement with the predicted kinetic slope for $\mu^{48}Ca/\mu^{42}Ca$ (Fig. 4.6). In concert with our experimental phenocryst constraints, this serves to re-inforce the applicability of the kinetic-limit for mass-dependence during diffusion ($\mu^{48}Ca/\mu^{42}Ca = -1.872$), for both positive and negative kinetic fractionations in significantly different high-T systems.

We also confirm that the largest measured $\Delta^{44}Ca_{opx-plag}$ value (sample 2030B) indeed represents kinetic enrichment (Fig. 4.6, see SM for details). In sum, these novel constraints suggest that our

DFT calculations are approximately correct, and that the large deviations we observe from predicted values are the manifestation of various kinetic processes affecting both whole-rock and inter-mineral Ca isotope variability.

4.4.5. Whole-rock δ^{44}Ca variations and diffusion modeling

Given that the large whole-rock δ^{44}Ca variations we observe are dominantly of kinetic origin, and that they are found to vary most dramatically when coming from units with shared interfaces, it is likely that they result from isotopic fractionation during diffusion of Ca. Paired with geochronological constraints for the duration of metamorphism in the Napier Complex (NC) [~100 Myr (*e.g.* Harley, 2016)], δ^{44}Ca in adjacent high-Ca and low-Ca samples (colored arrows in Fig. 4.4), can be used to gain information on diffusion rates and mechanisms attending long-lived high-temperature metamorphism in lower-crustal settings.

In order to successfully model Ca diffusion between whole-rock units with different bulk-compositions, without assuming a single diffusivity for all of the considered layers, we use a Python-based finite-difference diffusion model with a time-stepping grid, based on the method described in (Langtangen and Linge, 2017) for diffusion in heterogeneous media. The model has tunable input parameters for each layer, including (i) Ca concentration (wt%), (ii) Ca diffusivity (m^2/yr), and (iii) isotopic fractionation factor (D_{44}/D_{40}), and runs for any pre-specified amount of time (details in SM).

Using a country-rock Ca content, $[Ca]_{CR}$, of 0.5 wt% (the average for quartzites in our study), and an initial dike Ca content, $[Ca]_{Dk}$, of 3.5 wt%, we find that diffusivities (D_{Dk}) of ~10^{-10} m^2/yr with $D_{CR}/D_{Dk} > \sim 10^3$ and D_{44}/D_{40} ~0.990 ± 0.002 are required to explain our results for metabasic dike samples 2035A and 2035B (Fig. 4.7a). For these simulations, a Ca diffusivity ratio in the country rock relative to the dike (D_{CR}/D_{Dk}) lower than ~10^3 inhibits sufficient diffusion from taking place in the required time, while higher dike diffusivities (*e.g.* 10^{-9} m^2/yr) overstep the conditions represented by our samples after ~30 Myr (Figs. 4.7b and S4.5), even with lower D_{CR}/D_{Dk}. There are several reasons to believe that pelitic rocks would have higher effective Ca diffusivities, compared to mafic rocks, which are discussed in the following section.

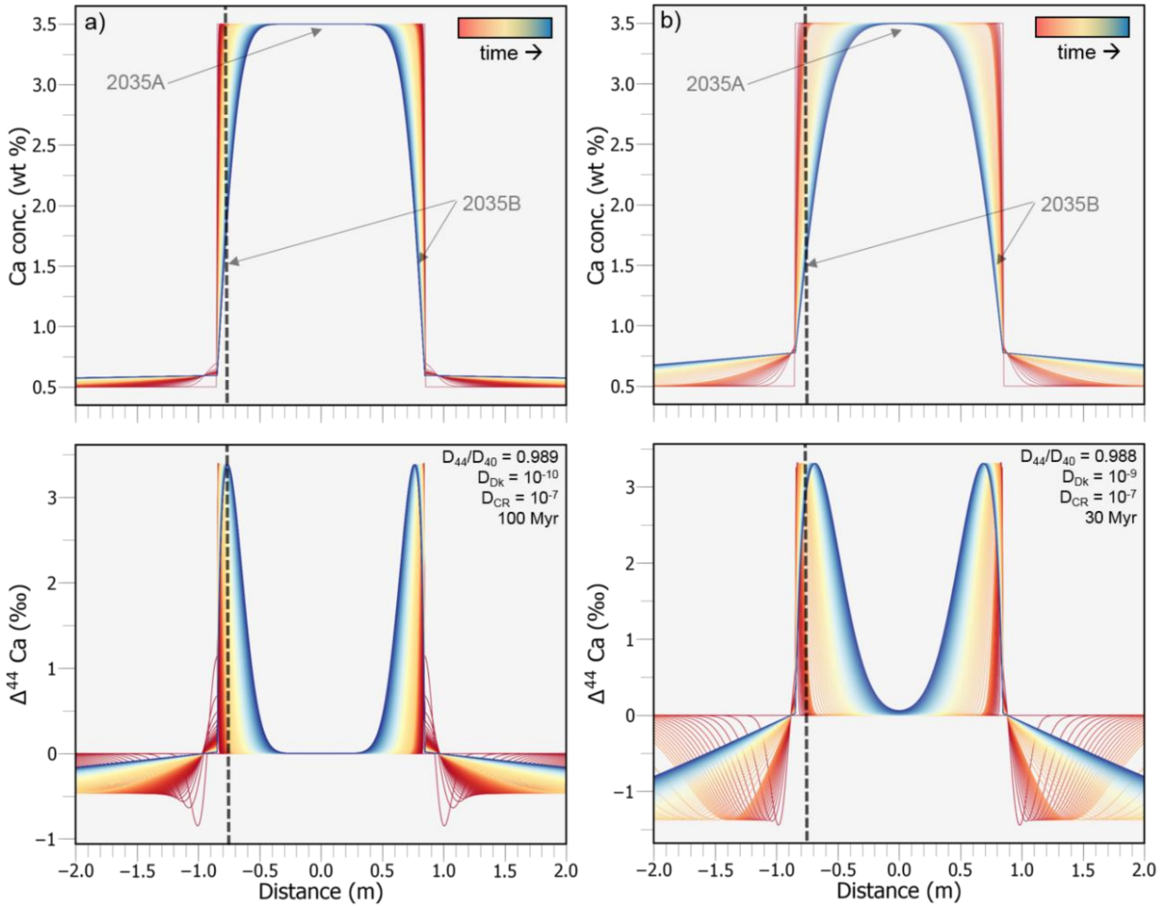

Fig. 4.7a,b. Numerical diffusion model results for spatial-variations in Ca concentration and change in δ^{44}Ca (Δ^{44}Ca) over time, showing the effect of variable dike diffusivities, as relevant to the center (2035A, δ^{44}Ca = -0.09‰) and edge (2035B, δ^{44}Ca = +3.22‰) of our metabasic dike samples from the Napier Complex. Dike (Dk) width is 1.7 m with initial [Ca] = 3.5 wt%; quartzitic country-rock (CR) has initial [Ca] = 0.5 wt%. In **(a)** dike diffusivity (D_{Dk}) is 10^{-10} m^2/yr and $D_{CR}/D_{Dk} = 10^3$, in **(b)** D_{Dk} is 10^{-9}m^2/yr and $D_{CR}/D_{Dk} = 10^2$. Other parameters are listed in the figure. Dashed lines indicate the approximate location of sample 2035B. Diffusivities are in m^2/yr.

We demonstrate that Ca diffusivities similar to the ultramafic dike samples, ~10^{-10} m^2/yr (Fig. 4.8a), are also required to match the signatures of interlayered samples 2032A-2032I in 100 Myr. In this case, however, D_{CR}/D_{Dk} must be lower than 1 in order to not get overly-high [Ca] in the pelites ("country-rock" in this case). Diffusivities lower than ~10^{-10} m^2/yr for D_{Dk} (mafic layers) do not generate low-enough [Ca], while higher values for D_{Dk} (*e.g.* 10^{-9} m^2/yr) exceed our constraints in just ~10 Myr. Another significant difference from the ultramafic-dike is that these samples require changes in D_{44}/D_{40} across the layers, and that the fractionation factors are much smaller, with D_{44}/D_{40} ~0.996 in the mafic layers and little to no fractionation required in the pelitic layers (*e.g.* D_{44}/D_{40} ~0.9995). We find that diffusivities of ~$7 \cdot 10^{-10}$, ~$2 \cdot 10^{-8}$, and $4 \cdot 10^{-8}$ m^2/yr for units 2036E, 2036C, and 2036A, respectively, accompanied by fractionation factors (D_{44}/D_{40}) of 0.9975, 0.995, and 0.998 (Fig. 4.8b) best explain our observations in 100 Myr. These samples, however, are much more poorly-constrained in terms of their relative locations within the diffusion profiles, and we intend the modeling to be mainly illustrative of complex spatial evolution for Δ^{44}Ca in multi-layered systems over time.

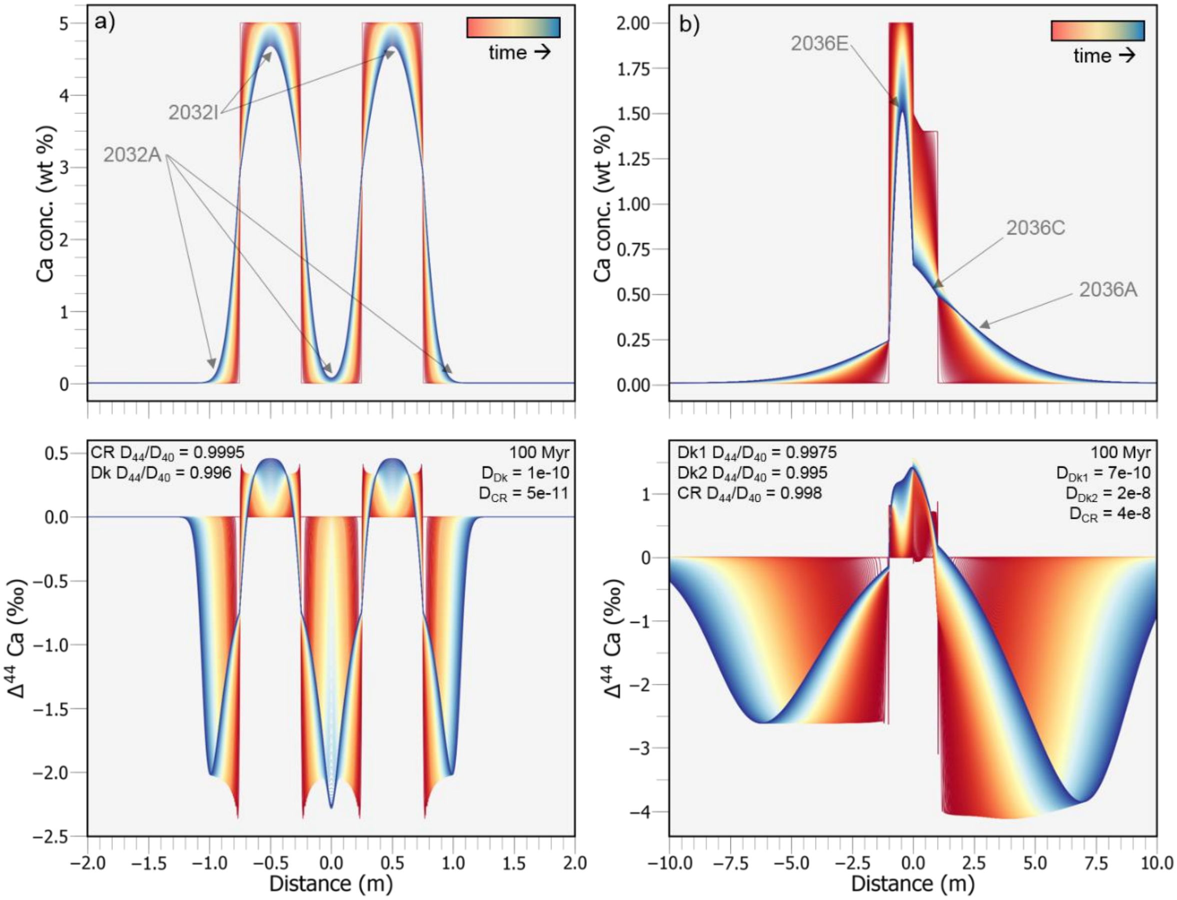

Fig. 4.8a,b. Numerical diffusion model results for spatial-variations in Ca concentration and Δ^{44}Ca over time. In **(a)**, which represents interlayered mafic-pelitic samples 2032I (δ^{44}Ca = +0.34‰) & 2032A (δ^{44}Ca = -1.56‰), initial mafic [Ca] = 5 wt%, initial pelitic (country rock) [Ca] = 0.01 wt%. In **(b)**, which roughly represents adjacent quartzite samples 2036E ('Dk1', δ^{44}Ca = +1.37‰), 2036C ('Dk2', δ^{44}Ca = +0.61‰), and 2036A ('CR', δ^{44}Ca = -1.33‰). Initial 2036E [Ca] = 2 wt%, initial 2036C [Ca] = 1.4 wt%, and 2036A [Ca] = 0.01 wt%. Other parameters are listed in the figure. Diffusivities are in m^2/yr.

4.5. Discussion

4.5.1. Implications for diffusion

Based on our diffusion models, we find that effective Ca diffusivities in the UHT granulites of the Napier Complex, a metamorphic terrane that represents slow-cooling over ~100 Myr at lower-crustal depths (Harley, 2016), are likely to range from ~10^{-7} to ~10^{-10} m^2/yr. Generally, our models require lower Ca diffusivities in mafic units (~10^{-10} m^2/yr) compared to pelitic units ($5 \cdot 10^{-11}$ to 10^{-7} m^2/yr), though they are relatively less well-constrained. Effective diffusivity in polycrystalline materials, generally increases with decreasing grain-size (increasing grain-boundary density) and with increasing [Ca] in the grain boundaries (GB) *vs.* in the solids ($[Ca]_{GB}/[Ca]_{solid}$) (Dohmen and Milke, 2010), both of which are likely to be higher in our metapelitic samples. In addition, pelitic and felsic units generally have lower liquidus temperatures, compared to mafic units, and are more likely to contain higher melt fractions at a given temperature, which may also serve to enhance Ca diffusivity in these units.

We find that our estimates compare favorably to experimental and natural estimates for Ca diffusion in solids (*aka*. volume-diffusion) and via grain-boundaries. For most elements and minerals, grain-boundary diffusion is 10^4-10^6 times faster than volume-diffusion (*e.g.* Dohmen and Milke, 2010). Experimental volume-diffusion rates for Ca in feldspar (An93, at ~900 °C) are ~$10^{-10.5}$ m^2/yr, while grain boundary diffusivities are several orders of magnitude larger ~$10^{-7.5}$ m^2/yr (Farver and Yund, 1995; LaTourrette et al., 1996), which is corroborated by natural samples, where Ca diffuses 3-4 orders of magnitude faster along grain-boundaries than within garnet (which is 2-3 orders of magnitude slower than in plagioclase) (Keller et al., 2008). Other experimental studies find an effective diffusivity of ~$10^{-8.5}$ m^2/yr in albite (Giletti, 1994), which is likely to be from a combination of grain-boundary and volume-diffusion. These observations suggest that Ca diffusivities in our mafic units (~10^{-10} m^2/yr) are most consistent with volume-diffusion, while Ca diffusivity in pelitic units (up to 10^{-7} m^2/yr) are more consistent with grain-boundary diffusion, as a likely result of higher $[Ca]_{GB}/[Ca]_{solid}$, lower grain-sizes, and/or higher volatile contents.

The D_{44}/D_{40} ratios required by our models range from ~0.990 to ~0.999 with generally lower values (0.990 and 0.996) in mafic units, and higher values in pelitic units (which can be as high as ~1 in some cases). Although the isotopic diffusivities of Ca have not yet been investigated in partially-solid or fully-solid systems, D_{44}/D_{40} values in experimental silicate liquids are observed to range from ~0.980 to ~0.997 (*e.g.* Watkins et al., 2017). In magmatic systems, where Ca diffusivity is much faster than in our models (~10^{-4} to 10^{-3} m^2/yr), diffusive Ca isotopic fractionation increases with magma viscosities, and there is a good positive correlation between $SiO_2 + Al_2O_3$ and D_{44}/D_{40} (Watkins et al., 2017); in basaltic melts ($SiO_2+Al_2O_3$ = ~50 wt%) D_{44}/D_{40} is ~0.997, progressing to ~0.980 in rhyolitic melts ($SiO_2+Al_2O_3$ = ~85 wt%).

The diffusivities required by our models, however, are much slower than in silicate melts. Thus, the Ca isotopic fractionations we observe are likely to represent sub-solidus processes. Within silicate melts, Ca may diffuse as an individual species or as a monomer with the approximate mass of plagioclase (Watkins et al., 2014), but it is uncertain what species are applicable to grain-boundary diffusion. Taken at face-value, however, the more-extreme D_{44}/D_{40} values required by our models (~0.990) are the same as estimated for a dacitic melt ($SiO_2 + Al_2O_3$ = 70 wt%), and the values closer to unity (~0.999) might indicate the presence of much lower-viscosity fluids during grain-boundary diffusion (*e.g.* Bourg et al., 2010; Richter et al., 2006).

4.5.2. Implications for Ca isotope thermometry

Based on our Δ^{44}Ca and Δ^{48}Ca' measurements, many of our inter-mineral samples are indicative of disequilibrium Ca isotope fractionation and cannot be reliably used for Ca isotope geothermometry. Excluding the samples with obvious disequilibrium Δ^{44}Ca (details in SM), we use our DFT results to calculate 1000lnα values (equivalent to Δ^{44}Ca) for mineral-pairs at various temperatures and compare them to our Ca isotope measurements. Given that Ca diffusion in minerals is several orders of magnitude slower than Fe-Mg exchange (Carlson, 2006, 2002; Hudgins et al., 2011; Vielzeuf et al., 2007), and therefore has higher closure temperatures (*e.g.* Hudgins et al., 2011 and references therein), it is expected that Δ^{44}Ca temperatures will be slightly higher than traditional Fe-Mg exchange temperatures. We find, however, that most of our samples give unreliable temperatures (described in SM, and tabulated in Table S4.9), even after removing those in obvious disequilibrium.

Ca-in-opx temperatures in our samples, although not specifically developed for application to granulites (Brey and Kohler, 1990), appear to be more reliable than our Δ^{44}Ca based estimates in mafic samples, agreeing with other temperature estimates for the various samples and localities (Table S4.9). This suggests that calcium concentrations in Opx can be approximately at equilibrium, but still retain a large degree of isotopic disequilibrium (*e.g.* sample 2030B has Ca-in-Opx temperature of 899°C but $\Delta^{44}Ca_{opx\text{-}plag}$ >1.66‰). Samples DDM303 and DDM342, which have obvious kinetic $\Delta^{44}Ca_{grt\text{-}fsp}$ (~ -1‰), are also approximately in Fe-Mg equilibrium (Table S4.9).

All in all, it appears that only ~5 of our samples give Δ^{44}Ca-based temperatures that are approximately in the correct range, suggesting that even samples with near-equilibrium chemical compositions can be affected by disequilibrium isotopic effects during metamorphism. Our dataset was obtained dominantly from granulite-facies samples, and only a few lower-grade metamorphic rocks. However, the available data suggest that Ca isotope thermometry in these lower-grade samples yields better results than in granulites (Table S4.9).

4.5.3. Implications for magmatic differentiation

Given that plagioclase represents the isotopically lightest silicate phase at equilibrium, enrichment of plagioclase in the melt (*e.g.* during partial-melting) would lead to negative $\Delta^{44}Ca_{melt\text{-}residue}$, if occurring at equilibrium. This could help explain the rough trends observed in igneous rocks, where more evolved melts may have slightly lower δ^{44}Ca (Amini et al., 2009; Schiller et al., 2016). An incipiently-melted amphibolite from the Ivrea-Verbano Zone (IZ408), seems to indicate that there may be a negative δ^{44}Ca shift between melt (leucosome, -0.22‰) and residue (melanosome, -0.06‰). The melt phase from this sample has essentially the same δ^{44}Ca as measured in feldspathic dikes from the NC (2038 and 2044, both -0.35‰). Garnet fractionation in magma sources has also been suggested to potentially explain δ^{44}Ca *vs.* REE trends in mafic whole-rocks (Kang et al., 2017), which we find to be in agreement with our DFT estimates for the four major garnet species (combined with our observations suggesting that magmatic garnet crystallization tends to occur closer to equilibrium than in metamorphic rocks).

Models for kinetic isotope fractionation during crystallization depend most significantly on (i) the distribution coefficients for Ca in various minerals *vs.* in the melt and (ii) the crystal growth rates relative to Ca diffusion rates in the magma (Watkins et al., 2017; Watson and Müller, 2009). Generally, crystals with larger growth rates are expected to have larger kinetic deviations from equilibrium, which we confirm based on our Δ^{44}Ca and Δ^{48}Ca' measurements in a fast-cooled experimental tonalite sample (Fig. 4.6).

Slower crystallization rates are expected to result in isotopic fractionations closer to predicted equilibrium values (Watson and Müller, 2009), which we confirm by measuring equilibrium Δ^{48}Ca' in slow-cooled mineral-separates from a cumulate gabbro sample (Stillwater Complex, Montana, Fig. 4.6, Table S4.7). A recent study of crystallization in a Hawaiian magma chamber suggests that slow crystallization of plagioclase + clinopyroxene, however, does not lead to significant mineral-melt Δ^{44}Ca fractionation (Zhang et al., 2018).

4.5.4. Mineral disequilibria and possible paragenetic constraints

Although most of our samples cannot be used for thermometry, the various kinetic effects contain information regarding mineral growth/paragenesis during high-T metamorphism. The triple-isotope slopes between mineral separates from these samples are approximately the same as measured for whole-rocks and for the fast-cooled experimental glass-plagioclase separates (Fig. 4.6), which suggests that diffusive processes are responsible for both whole-rock and inter-mineral disequilibria.

Based on the trends in Fig. 4.4, it appears that many garnet and orthopyroxene Δ^{44}Ca measurements deviate progressively further from our DFT predictions in a systematic fashion. Specifically, the deviations increase with increasing whole-rock and garnet Mg#, feldspar An content, Ca/Mg of orthopyroxene, and modal orthopyroxene content. Interestingly, all of these parameters tend to get larger in higher-temperature rocks. Thus, unlike equilibrium fractionation effects, which generally decrease with increasing temperature, increasing temperatures may play a role in variably activating diffusion pathways for Ca in different minerals and/or along grain-boundaries. Activation energies for grain-boundary diffusion are generally 40-60% lower than those required for volume diffusion (Dohmen and Milke, 2010), potentially implying that the activation of volume-diffusion at higher temperatures may be responsible for greater Ca isotope fractionations with increasing temperatures. Changes in temperature also affect the composition and assemblage of stable metamorphic phases.

In typical mafic composition rocks, the high-temperature side of granulite-facies mineral reactions generally include plagioclase + orthopyroxene + clinopyroxene ± garnet (Turner, 1981). High-temperature pelitic and semi-pelitic composition rocks may contain plagioclase + garnet ± orthopyroxene ± sillimante/kyanite assemblages, but in high-Mg pelites (such as 2032A) can also include sapphirine (*e.g.* Spear and Spear, 1993). Many metamorphic reactions in both bulk compositions have garnet on the higher-pressure side and orthopyroxene and plagioclase on the lower-pressure, higher-temperature side. As such, different pressure-temperature-time (P-T-t) paths and their associated reaction histories may influence inter-mineral Δ^{44}Ca fractionations and whether kinetic or equilibrium processes control Ca isotope partitioning.

4.5.4.1. Garnet Δ^{44}Ca disequilibria

In the NC samples, garnet grains contain inclusions of various high-temperature minerals and appear to have generally formed during isobaric cooling (*e.g.* ‘retrograde garnet growth’), which is consistent with the inferred P-T-t paths for the region (*e.g.* Harley, 2016). Growing garnet grains would thus have to incorporate Ca originally-sourced from other minerals, which could be subjected to isotopic fractionation during diffusion along grain boundaries and/or through minerals. All but one of our garnet-bearing samples from the Napier Complex have negative $\Delta^{44}\mathrm{Ca}_{\mathrm{grt\text{-}fsp}}$ and/or $\Delta^{44}\mathrm{Ca}_{\mathrm{grt\text{-}WR}}$ (discussed in SM). Slave Province xenoliths have variable $\Delta^{44}\mathrm{Ca}_{\mathrm{grt\text{-}fsp}}$ which range from strongly negative to slightly positive and are also consistent with isobaric cooling pathways [Supplementary Information of (Antonelli et al., 2018)]. We also note that only samples with low modal clinopyroxene (< ~10%) have large positive and negative $\Delta^{44}\mathrm{Ca}_{\mathrm{grt\text{-}mineral}}$ values (Fig. S4.6).

These observations suggest that retrograde transformation of clinopyroxene (+ plagioclase) to garnet does not lead to significant disequilibrium $\Delta^{44}\mathrm{Ca}_{\mathrm{grt\text{-}mineral}}$, but that transformation of orthopyroxene (or sapphirine) and plagioclase to garnet is accompanied by larger disequilibrium effects. This suggests that Ca diffusion length-scales and accompanying isotopic fractionations increase as Ca becomes locally depleted, or that garnet sourced from clinopyroxene is not subjected to significant Ca isotope kinetic effects. In a general sense, isotopic fractionation during retrograde garnet growth could happen during (i) Ca diffusion out of other minerals, (ii) transport of Ca towards growing garnet porphyroblasts, and/or (iii) attachment or removal, respectively, of Ca from growing garnet or resorbing mineral surfaces.

All three garnet-bearing samples from the Ivrea-Verbano zone, which has a clockwise PTt path (*e.g.* Redler et al., 2012), are likely to represent prograde garnet growth during metamorphism (excluding IV-16-19) and have positive $\Delta^{44}Ca_{grt\text{-}fsp}$. Sample IV-16-19, which was shown to contain equilibrium $\Delta^{48}Ca'$ signatures and reasonable equilibrium $\Delta^{44}Ca_{grt\text{-}fsp}$ temperatures (800-1000 °C), represents magmatic garnet formation in a crustally-contaminated late-stage lower-crustal gabbro intrusion, as opposed to prograde metamorphism (See Supplementary Information). The Ca isotope differences between the contrasting garnet formation pathways are potential manifestations of diffusion limitation during retrograde growth, because prograde garnet formation is attended by fluids, whereas volatiles have been mostly lost from the system prior to retrograde garnet formation, which may lead to decreased grain-boundary Ca diffusivities.

In sum, our observations suggest that magmatic garnet formation may occur close to equilibrium in igneous rocks, whereas garnet formation in high-grade metamorphic rocks depends on the PTt paths, where retrograde garnet formation leads to large negative kinetic effects and prograde garnet formation occurs closer to equilibrium. Our data also suggest that resorption of garnet in partial melts (as evidenced by NC sample 2038, SM) potentially leads to large positive $\Delta^{44}Ca_{grt\text{-}fsp}$, similar to the interpretation for disequilibrium Fe isotope fractionation in xenocrystic olivines (McCoy-West et al., 2018)..

4.5.4.2. Orthopyroxene Δ^{44}Ca disequilibria

Large disequilibrium $\Delta^{44}Ca_{opx\text{-}mineral}$, like large disequilibrium $\Delta^{44}Ca_{grt\text{-}mineral}$ values, are limited to rocks with not only low modal clinopyroxene (< ~15%), but also low feldspar (<20%), and no apparent garnet (Fig. S4.6). Correspondingly, we find that rocks with greater modal orthopyroxene generally have $\Delta^{44}Ca_{opx\text{-}mineral}$ further from equilibrium (Fig. 4.4f), along with other proxies consistent with increasing temperatures (Fig. 4.4c-e). This suggests that large positive orthopyroxene Ca isotope fractionations occur at high-temperatures when Ca is generally sparse in the rocks, implying that (i) large positive $\Delta^{44}Ca_{opx\text{-}mineral}$ could be limited to samples where Ca has to be sourced from minerals with low [Ca] (*e.g.* albitic plagioclase or K-feldspar) and/or that (ii) new pathways for loss of light Ca isotopes from orthopyroxene (relative to other mineral phases) are activated with increasing metamorphic temperatures.

Although Ca concentration gradients do not generally favor of outward diffusion from orthopyroxene, Fe and Mg, which are strongly concentrated in opx, may serve to carry Ca outwards and lead to enhanced isotopic fractionation. In olivine, Mg and Fe have been shown to diffuse 4-6 times faster than Ca during high-T metamorphism (corona-formation), and can serve to carry Ca (even up its own concentration gradients) (Grant, 1988). Other studies have also shown that Fe and Mg diffusivities are orders of magnitude faster than Ca diffusion in olivine, clinopyroxene, and orthopyroxene (Hudgins et al., 2011), which may be one of the reasons that samples with Fe-Mg exchange temperatures in apparent equilibrium can still have disequilibrium Δ^{44}Ca (Table S4.9).

Ca could also be driven out of orthopyroxene during cooling, as it becomes less compatible with decreasing temperatures (Brey and Kohler, 1990). Our Ca-in-Opx temperature estimates, based on the thermometer of (Brey and Kohler, 1990), appear to reflect equilibrium [Ca] concentrations in orthopyroxene at appropriate temperatures (except in 2040C, Table S4.9), yet we show that these samples can still contain excessively high or excessively low $\Delta^{44}Ca_{opx\text{-}mineral}$ values. This implies that Ca in orthopyroxene can be in isotopic disequilibrium while simultaneously reflecting Ca chemical equilibrium, which in turn suggests that either (i) isotopic rate differences (D_{44}/D_{40}) are high relative to Ca diffusivities (otherwise diffusive fractionation in grain-boundary fluids or in mineral grains would be accompanied by depletions in [Ca]), or that (ii) the effects are due to isotopic rate differences during attachment/detachment at the crystal surfaces [‘surface-kinetic effects’ (*e.g.* DePaolo, 2011)] which are currently unexplored in silicates. On the other hand, several samples with $\Delta^{44}Ca_{opx\text{-}mineral}$ too small to be explained by equilibrium at relevant temperatures could be a manifestation of the same processes envisaged for large negative $\Delta^{44}Ca_{grt\text{-}mineral}$ (*e.g.* fractionation during diffusion towards growing minerals) but would suggest fractionation during prograde as opposed to retrograde metamorphism, due to the increasing stability of Opx with increasing temperatures.

4.6. Conclusions

Using TIMS to measure radiogenic-corrected $\delta^{44}Ca$ values in a large number of high-temperature metamorphic whole-rocks and mineral separates (including amphibolite-facies, granulite-facies, UHT, and eclogite-facies samples) from various localities, and comparing them to $\mu^{48/44}Ca$ and $\mu^{42/44}Ca$ measurements by MC-ICP-MS, ab-initio predictions from DFT, and numerical diffusion models, we have demonstrated that:

(1) At temperatures greater than ~800°C, equilibrium $\Delta^{44}Ca$ fractionations do not exceed ~1‰, and $\delta^{44}Ca$ values are expected to decrease in the general order: olivine > garnet ≥ orthopyroxene > clinopyroxene > apatite > plagioclase. At ~900°C, average analytical uncertainties in measured $\delta^{44}Ca$ values in minerals and, in turn, inter-mineral $\Delta^{44}Ca$ fractionations translate into isotopic temperature uncertainties of ~ ±50°C for Opx-Plag, ~ ±100°C for Opx-Cpx, and larger for minerals with smaller predicted $\Delta^{44}Ca$ (*e.g.* Cpx-Plag, ~ ±250°C). The best mineral pairs for mantle thermometry, assuming equilibrium, would thus be olivine-plagioclase and/or olivine-clinopyroxene.

(2) Variations in whole-rock and mineral $\delta^{44}Ca$ values in high-temperature metamorphic samples are found to span a large range of ~4‰ and ~8‰, respectively. $\Delta^{44}Ca$ between adjacent whole-rock samples can exceed 3‰, and inter-mineral fractionations (*e.g.* $\Delta^{44}Ca_{grt\text{-}fsp}$) are observed to vary by a similar amount. We find that inter-mineral $\Delta^{44}Ca$ fractionations deviate progressively further from predicted equilibrium values in conjunction with chemical and mineralogical parameters traditionally associated with increasing temperatures (*e.g.* Mg#, feldspar anorthite content, & Opx Ca/Mg), and when the samples generally contain low modal clinopyroxene fractions (< ~15%). Only a small percentage of our samples have Ca-isotope signatures that agree with our equilibrium predictions at relevant temperatures.

(3) Kinetic and equilibrium Ca isotope fractionations greater than ~0.5‰ can be distinguished through quantification of $\Delta^{48}Ca'$, which corresponds to $\mu^{48/44}Ca$ deviations from predicted equilibrium values in triple-isotope space. We show that the largest positive and negative $\Delta^{44}Ca$ fractionations in our data set (including whole-rocks, Grt-Plag, and Opx-Plag pairs), along with plagioclase crystallization in a fast-cooled experimental tonalite, are consistent with (non-zero) $\Delta^{48}Ca'$ values for kinetic-fractionation, generally falling along the slope predicted by the kinetic-limit for mass-dependent fractionation (Young et al., 2002). Samples from a

slowly-crystalized cumulate gabbro sample (Stillwater-complex), along with garnet and feldspar separates from the metamorphic sample which best-corroborates our DFT predictions, were found to have equilibrium Δ^{48}Ca’ values (≈ 0).

(4) The Ca diffusivities required to model our data (10^{-10} to 10^{-7} m^2/yr) are much slower than in silicate liquids (Watkins et al., 2017), but are consistent with estimates for slow Ca diffusion within minerals (volume-diffusion) and faster Ca diffusion via grain boundary fluids (*e.g.* Dohmen and Milke, 2010). The required isotopic rate differences for Ca diffusion (D_{44}/D_{40}) range from ~0.990 (within the range observed for dacitic silicate liquids) to ~0.9995 (which is more similar to fractionation in aqueous media) (Watkins et al., 2017). Although poorly constrained, D_{44}/D_{40} appears to be generally lower in mafic units and higher (closer to unity) in pelitic units.

(5) Inter-mineral Δ^{44}Ca disequilibria are likely to be related to variations in mineral paragenesis along different PTt paths for various samples/localities. Our data suggest that retrograde garnet formation (*e.g.* during slow isobaric cooling from high-temperatures) leads to negative disequilibrium $\Delta^{44}Ca_{grt\text{-}mineral}$ values, which is likely a result of diffusive limitations and associated kinetic isotope fractionations during garnet growth. Magmatic and prograde garnet formation, on the other hand, appear to occur closer to equilibrium. Large positive $\Delta^{44}Ca_{grt\text{-}mineral}$ values (observed in a single feldspathic dike sample from the Napier Complex) may be the result of outward Ca diffusion (aided by Fe and Mg diffusion) from garnet entrained in partial-melts.

(6) Kinetic Ca isotope effects affecting orthopyroxene are capable of generating $\Delta^{44}Ca_{opx\text{-}mineral}$ both much higher and much lower than equilibrium values predicted by our DFT models at relevant temperatures, but they are not as easily linked to various paragenetic processes. Both Fe-Mg exchange and Ca-in-Opx thermometry yield temperatures in agreement with previous work for the different regions, even for samples with obvious disequilibrium $\Delta^{44}Ca_{opx\text{-}mineral}$ values. Thus, Ca, Fe, and Mg concentrations in orthopyroxene can be in approximate chemical equilibrium, but Ca isotopic compositions (including Δ^{48}Ca’) can still be significantly out of equilibrium. This implies that the relevant processes have relatively large isotopic rate differences (D_{44}/D_{40}) relative to their Ca diffusivities. As such, disequilibrium orthopyroxene signatures are not likely to be generated by isotopic fractionation during Ca diffusion from far-field sources, and may instead result from isotopic fractionation during nearby volume diffusion and/or during attachment/detachment at mineral surfaces.

In summary, we have shown that kinetic Ca isotope effects are abundant in nature, even at very high-temperatures. Disentangling equilibrium effects from kinetic effects, and understanding the various mechanisms/pathways responsible for Ca isotopic disequilibria in nature, however, would be further enhanced by similar studies focused on higher-resolution sampling, and/or by development of in-situ δ^{44}Ca analysis techniques. Although disequilibrium effects may be more pervasive in metamorphic rocks than in igneous rocks (*e.g.* due to the higher associated viscosities and/or longer time-scales), we have shown that a large degree of caution should be taken when assuming Ca isotope equilibrium (*e.g.* for Ca isotope thermometry), or if using stable Ca isotope variations to trace complicated multi-step processes, such as carbonate recycling in the mantle.

4.7. Supplementary information

4.7.1. Analytical methods

4.7.1.1. Bulk-rock and mineral characterization

The samples in this study are the same as studied in (Antonelli et al., 2018), and the reader is referred there for petrographic descriptions of the samples in this study. Modal mineralogies for the various samples (Table S4.1) were determined using petrographic microscope combined with BSE and X-ray image analysis methods. Whole rock chemical compositions (Table S4.2) for the majority of NC samples were determined by XRF at the University of California, Berkeley. IVZ and SE samples were sent to Washington State Geoanalytical Laboratory for XRF analysis, while SP xenoliths had their bulk-rock chemistries reconstructed according to EPMA mineral analyses and modal mineralogies determined from X-ray map image analyses, in order to avoid contamination by kimberlite materials. In-situ chemical compositions for major minerals were determined by EPMA (Table S4.3) at the University of California, Davis (NC, IVZ, and SE samples), and at the University of Alberta (SP samples). Mineral separates were obtained by lightly crushing samples and picking grains immersed in isopropyl alcohol, using a binocular microscope and fine tweezers. After dissolution (next section) and given availability, an aliquot of each dissolved sample was analyzed for its major cation concentrations by ICP-OES at the University of California, Berkeley (Table S4.4), in order to determine the purity of mineral separates and the potential identity of contaminating phases in low-Ca mineral separates such as orthopyroxene. Our double-spike TIMS analyses also give us constraints on Ca concentrations in each sample, with uncertainties generally better than ~2%.

4.7.1.2. ^{40}Ca/^{44}Ca and δ^{44}Ca measurements

Spiked and unspiked Ca isotope measurements were performed by TIMS at the University of California, Berkeley. Powdered whole-rock and mineral-separate samples (~10-100 mg) were combined with concentrated hydrofluoric, perchloric, and 6M hydrochloric acid in Savillex beakers and refluxed at ~130 °C for a minimum period of one week, after which the samples were evaporated to dryness and re-dissolved in 3M nitric acid. Aliquots of fully dissolved sample were then taken for the various analyses, including the previously described ICP-OES analyses and Ca isotope measurement by MC-ICP-MS (section 1.4). Unspiked sample aliquots and ^{42}Ca-^{48}Ca double-spiked aliquots (containing ~30 μg Ca) from each sample were run through column chemistry using Eichrom DGA resin (Simon et al., 2009) to separate Ca from matrix elements, and several standards (including SRM915a, USGS standards W2a and DNC-1, and an internal dunite standard) were processed alongside the samples.

Spiked and unspiked Ca isotope separates were loaded onto rhenium filaments and placed into a Thermofinnigan Triton TIMS for Ca isotopic analysis. Each sample was measured a minimum of two times. The unspiked Ca isotope measurements, which are described in (Antonelli et al., 2018), were used to correct for radiogenic excesses in ^{40}Ca/^{44}Ca of certain samples (as schematically described in Fig. S4.1), including inherited radiogenic Ca in low-K/Ca minerals. As such, the TIMS-based δ^{44}Ca values reported in this study (Table S4.5) have been corrected for radiogenic ^{40}Ca and are essentially the same as would be measured by ICP-MS, where ^{40}Ca is not directly measured and ^{44}Ca/^{42}Ca values are converted to δ^{44}Ca using a slope of 2.05 (Fantle and Tipper, 2014).

Based on repeated standard analyses and the average δ^{44}Ca difference between duplicate measurements (Tables S4.5, S4.6), we estimate an uncertainty of ±0.1‰ for uncorrected δ^{44}Ca values. The long-term 2SD uncertainty for unspiked ^{40}Ca/^{44}Ca analyses (Antonelli et al., 2018) are also ~0.1‰ (ε_{Ca} uncertainty of ± 1), thus, radiogenic-corrected $\delta^{44}Ca$ values are reported in the figures and tables with a combined 2SD uncertainty of ± 0.14‰. The observations from (Antonelli et al., 2018) suggest that the BSE value for $^{40}Ca/^{44}Ca$ might be closer to 47.156 instead of 47.162, which would lead to a negative shift of ~0.13‰ for all of the $\delta^{44}Ca$ values reported in this study, but still requires further verification.

4.7.1.3. $\delta^{44}Ca$ unmixing calculations for orthopyroxene

Although a great deal of care was taken in separating the various minerals, it is clear from the ICP-OES and TIMS measurements that Ca concentrations in the orthopyroxene separates are higher than their in-situ averages. This suggests that significant fractions (*e.g.* >50%) of the Ca analyzed in orthopyroxene separates were actually Ca from other minerals, in spite of the generally distinguishable $\delta^{44}Ca$ values. In order to estimate the $\delta^{44}Ca$ composition of pure-orthopyroxene in our samples, we used petrographic constraints and the major cation concentrations measured in mineral separates to identify probable sources of contamination. Out of the nine opx separates analyzed, three had $\Delta^{44}Ca_{opx\text{-}min}$ too small or [Ca] that was too large for successful unmixing estimates.

We determined that contaminant phases in our orthopyroxene separates were most often clinopyroxene (from Mg excesses in the separates, relative to EPMA data), and more rarely garnet (from petrographic constraints) and plagioclase (from Na excess). We then used Ca concentrations and $\delta^{44}Ca$ values, measured separately in the contaminating-minerals and in the orthopyroxene separates, to estimate the $\delta^{44}Ca$ compositions of pure orthopyroxene, assuming pure-Opx Ca concentrations measured in-situ by EPMA (Fig. S4.2). The uncertainties for pure-opx estimates (Opx* in the main text) were calculated using uncertainties for our $\delta^{44}Ca$ (± 0.1‰) and the [Ca] (wt%) difference between measured orthopyroxene separates and pure in-situ orthopyroxene (Fig. S4.2).

Although some samples are relatively well-constrained (*e.g.* 2030B, 2035A) our assumption of two-component mixing in orthopyroxene-separates may be an over-simplification. Additionally, two of the samples (2030B and 2032I) that have separates most-consistent with contamination by clinopyroxene did not have high-enough quantities to separate and analyze independently.

Based on several other samples and our equilibrium estimates, we assume for these samples that $\Delta^{44}Ca_{cpx\text{-}plag} = +0.3‰$. In 2030B, using this estimate for the unmixing calculations leads to similar results ($\delta^{44}Ca_{pure\text{-}opx} = 1.88 \pm 0.21‰$) from those using whole-rock (1.80 ± 0.25‰) and plagioclase (2.08 ± 0.21‰) (Fig. S4.2a-c). In 2032I, which has a relatively unclean orthopyroxene separation, this estimate leads to a result for pure-opx $\delta^{44}Ca$ (+2.0 ± 1.5‰) that is more like the others than with plagioclase-unmixing (+4.3 ± 1.5‰) (Fig. S4.2d,e), but this sample still remains the most poorly constrained.

The sample with the second-lowest Ca concentration (2040C), which consists of ~60% orthopyroxene, ~30% garnet, and ~10% quartz, also leads to difficulties for our unmixing estimates. We find that garnet separates from 2040C (~0.8 wt% Ca, $\delta^{44}Ca = -0.18‰$) have $\delta^{44}Ca$ significantly lower than the whole-rock (~0.3 wt%, $\delta^{44}Ca = +0.31‰$), yet attempts at isolating this positive component in orthopyroxene were unsuccessful (Table S4.5). Pure-orthopyroxene in this sample has ~0.08 wt% Ca (from EPMA), which is 10x less than in garnet. Our orthopyroxene separates, however, have 0.11 wt% Ca, with $\delta^{44}Ca$ composition (-0.02‰) that cannot be used to explain the whole-rock composition. Looking at thin sections of the sample, we observe that very small garnet grains disseminated throughout the orthopyroxene, and may be dominating the [Ca] budget (and isotopic composition) of our separates. We thus estimate the composition of pure-opx (δ^{44}Ca = +0.77 ± 0.29‰) using the measured δ^{44}Ca and [Ca] of garnet and whole-rock (Fig. S4.2i).

Although it is perplexing that our orthopyroxene separates for 2040C have similar δ^{44}Ca to those of garnet, it is unlikely that minerals other than opx are contributing to the total Ca budget of the rock. A potential explanation is that the whole-rock sample, which was finely-powdered and homogenized from >10g of material, may contain patches of higher-purity orthopyroxene than that which we used for opx-separation. Although none of our conclusions depend exclusively on this sample, it could also be the case that our measured values are correct and that orthopyroxene in the separate (in close proximity to analyzed garnet separates) has equilibrated with neighboring garnet, and orthopyroxene in the rest of the rock (as analyzed in the powdered whole-rock) has not.

4.7.1.4. $\mu^{48/44}$Ca and multiple Ca-isotope measurements

Aliquots of the same dissolved mineral and whole-rock separates measured by TIMS were dried down and sent to the Center for Star and Planet Formation (Natural History Museum of Denmark, University of Copenhagen) for Ca isotope measurement using a ThermoFisher Neptune MC-ICP-MS. After re-dissolving the samples, calcium was separated using the methods described in (Schiller et al., 2012), which involves a four-step purification procedure sequentially using (i) Eichrom Sr-spec resin, (ii) AG1-X4 200-400 mesh resin, (iii) TODGA resin, and (iv) BioRad AG50W-X8 200-400 mesh resin; resulting in very-low Sr/Ca and Ti/Ca in the purified calcium separates. The measurement procedures and data-reduction schemes, including uncertainty calculations, are also the same as in (Schiller et al., 2012), and the reader is referred there for further details. The data, along with the intensity of ^{44}Ca signals (in V) and number of repeat analyses, are reported in ppm deviations (μ-notation) from SRM915b (Table S4.7), which is indistinguishable from average terrestrial mafic rock standards (~BSE) for ^{42}Ca/^{44}Ca, ^{43}Ca/^{44}Ca, ^{46}Ca/^{44}Ca, and ^{48}Ca/^{44}Ca, and has the same ^{40}Ca/^{44}Ca as SRM915a (Schiller et al., 2012).

4.7.2. Density-functional theory (DFT) estimates

Equilibrium Ca isotope fractionations between various silicate minerals were estimated by first-principles lattice dynamics simulations at the University of California, Los Angeles, with methods similar to those in (Widanagamage et al., 2014). Models of olivine (forsterite), garnet (pyrope, almandine, grossular, spessartine), orthopyroxene (enstatite), clinopyroxene (diopside), plagioclase (anorthite and labradorite), fluorapatite [$Ca_5(PO_4)_3F$], lime (CaO), and fluorite (CaF_2) were constructed using the plane-wave density functional theory package Quantum Espresso (Giannozzi et al., 2009) and pseudopotentials from version 1.5 of the GBRV library [http://www.physics.rutgers.edu/gbrv, (Garrity et al., 2014)]. In some structures, fractionation factors were calculated according to the method of (Schauble et al., 2006), where phonon frequencies for ^{40}Ca and ^{44}Ca-substituted crystals were calculated at non-zero phonon wave vectors and used to estimate reduced partition functions ratios (Urey, 1946). Reduced partition functions ratios for more complex structures were estimated from force constants and determined by numerical differentiation of the energies of perturbed structures in which a Ca atom is slightly displaced from its equilibrium position in three orthogonal directions (Bigeleisen and Mayer, 1947; Moynier et al., 2011; Schauble, 2011; Widanagamage et al., 2014).

As in previous work by (Griffith et al., 2008; Widanagamage et al., 2014) the structures of non-Ca minerals were constructed for pure end-members, and then a Ca atom was swapped into the cell (or supercell). The resulting strained structure was then allowed to relax to a minimum-energy configuration. More dilute solid solutions were modeled using single Ca-atom substitutions into super-cells of the enstatite (Ca:Mg of 1:15, 1:31, and 1:63), olivine (1:7, 1:15, 1:31, and 1:63), and pyrope [1:11 (primitive, 80-atom unit cell) and 1:23 (conventional 160-atom unit cell)] structures. Labradorite (An50) was modeled using the structure proposed by (Kaercher et al., 2014). Almandine and spessartine models assume ferromagnetic ordering of unpaired Fe^{2+} and Mn^{2+} electrons, respectively. Test calculations with a more complicated magnetic arrangement in almandine, however, resulted in little change to the overall crystal structure, suggesting that magnetic ordering does not have very significant effects (as one might expect for species that are paramagnetic at geochemically relevant temperatures).

Our preferred estimates (bold values in Table 4.1 of the main text) use a gradient-corrected density functional [PBE; (Perdew et al., 1996)], which has been used in several previous studies (Griffith et al., 2008; Méheut et al., 2007; Schauble et al., 2006; Widanagamage et al., 2014). A vibrational frequency scale-factor of 1.06 is assumed for all models using the PBE functional, based on comparison with phonon frequencies measured at high-symmetry wave vectors in lime and fluorite (Elcombe and Pryor, 1970; Saunderson and Peckham, 1971). Force constants calculated by displacing Ca-atoms are scaled by the square of this factor (1.1236). As a test, models based on a simpler unscaled density functional (LDA) were calculated for select structures; these lead to similar results.

4.7.3. $\mu^{48/44}$Ca and Δ^{48}Ca' results

The experimental tonalite sample, described in upcoming work, was analyzed to confirm Δ^{48}Ca' effects for kinetic Ca fractionation (during formation of plagioclase phenocrysts). The sample was held at 1200°C and 200 MPa for 24 hrs, isobarically cooled to 550°C in ~10 minutes (at 60°C/min), and then brought down to room temperature/pressure in ~15 hours (at ~0.6°C/min & ~13 MPa/min), as part of an unrelated project at ETH-Zurich. As described in the main text, we find that this sample is characterized by strongly kinetic (non-zero) Δ^{48}Ca' fractionation.

Through Δ^{48}Ca' analyses in 2030B and DDM303, we have shown that large opx-fsp, grt-opx, and grt-fsp inter-mineral Δ^{44}Ca values are consistent with kinetic fractionation. Unfortunately, we had no remaining orthopyroxene separates from 2030B after completion of the various TIMS and ICP-OES analyses. Instead, we compare measurements of plagioclase separates from (δ^{44}Ca = -0.57‰) to those of the whole-rock powder (δ^{44}Ca = +0.24‰), where orthopyroxene comprises ~15% of the Ca budget. We find that the plagioclase sample [Δ^{48}Ca' = -14 ± 12 ppm (2SE)] and the whole-rock sample [Δ^{48}Ca' = +15 ± 14 ppm (2SE)] are indeed resolvable from each other, which suggests that large $\Delta^{44}Ca_{opx\text{-}plag}$ values are consistent with kinetic isotope fractionation. The μ^{48}Ca/μ^{42}Ca slope between plagioclase and whole-rock, though more-poorly resolved than for larger fractionations, appears to be slightly shallower (*e.g.* more equilibrium-like) than the kinetic-limit (Fig. 4.6), which may potentially indicate an influence from both processes. These observations suggest that Δ^{48}Ca' variations, along with unrealistic inter-mineral Δ^{44}Ca temperature-estimates, can be used to confidently identify kinetic Ca isotope effects in nature.

Interestingly, both the equilibrium end-member sample (Stillwater) and IV-16-19 sample, have slightly non-zero Δ^{48}Ca' offset from BSE, but equal to each other, which may be from inherited kinetic effects prior to subsequent equilibration between mineral phases.

4.7.4. Numerical diffusion modeling

Diffusive Ca isotope fractionation in heterogeneous media (*e.g.* between adjacent whole-rock layers with variable diffusivities) can be successfully modeled using numerical methods (Langtangen and Linge, 2017) by discretizing the following general equation:

$$\frac{\partial C(x,t)}{\partial t} = \frac{\partial}{\partial x}\left(\alpha(x)\frac{\partial C}{\partial x}\right) \qquad \text{(Eq. S4.1)}$$

Where C(x,t) is the Ca concentration at a given position and time, t is time, and α(x) is the Ca diffusivity in the various units (which thus depends on position). In order to apply this method to diffusive isotope fractionation, we run the simulation once for each isotope (with diffusivities modified by D_{44}/D_{40} for ^{44}Ca) and take the ratio of the solutions at each location over time. We used a total length of 30m (discretized into 3000 grid-points) in order to avoid edge effects. We use an upper-limit of 100 Myr for the duration of Ca diffusion in our models, in accordance with several thermochronological estimates for the NC, including Pb-Pb zircon analyses paired with coeval thermometric proxies [*e.g.* Ti-in-zircon thermometry (Mitchell and Harley, 2017)], which suggest that ultrahigh temperatures prevailed for very-long time periods (up to ~100 Myr) (Harley, 2016).

We focus on modeling the results of whole-rock sample pairs with adequate spatial-constraints from the field. The samples with the most precise spatial constraints (metabasic dike samples 2035A & 2035B, Fig. 4.7 in the main text), provide the most robust estimates for Ca diffusion at lower-crustal conditions. We also include rough models for diffusive Ca fractionation in intercalated (~0.5 m) layers of Ca-rich metabasic whole-rocks (2032I) and Ca-deficient garnet-sapphirine-cordierite metapelites (2032A), and a hypothetical model for diffusion in adjacent feldspathic-to-cordieritic garnet quartzite units, 2036A, 2036C, & 2036E (Fig. 4.8a,b in the main text), for which the layer-spacing is essentially unknown (*e.g.* ~1 to >10 m).

Exploring the parameter space we find that, along with [Ca] differences, larger differences in Ca diffusivity between simulated layers generally lead to significant differences in the resulting Ca fractionations. All else being equal, increasing Ca diffusivity in the surrounding media relative to the diffusion-source generally increases the degree of δ^{44}Ca enrichment in the source, along with the extent of Ca diffusion into the surroundings, but decreases the magnitude of δ^{44}Ca fractionation in the surroundings.

Due to large uncertainties, we did not include the potential effects stemming from temperature-gradients (F. Huang et al., 2010; Richter et al., 2009) or isotopic-gradients (Watkins et al., 2014) in our models. Isotopic self-diffusion, however, would serve to counter-act the fractionations generated by chemical diffusion, which suggests that our models provide minimum estimates for D_{44}/D_{40}, assuming no temperature variations across the analyzed length-scales. Given that the NC represents metamorphism in a large-hot orogeny (LHO) (Harley, 2016), it is not likely that there were significant temperature variations on the scale of our sample locality (Dallwitz Nunatak, Napier Complex).

The edge of our mafic dike (2035B) indicates an increase in δ^{44}Ca (~3‰, relative to the center, 2035A) with decreasing CaO (orange arrow in Fig. 4.4), consistent with outward diffusion of Ca into country rock, while the other samples (red and purple arrows in Fig. 4.4) have decreasing δ^{44}Ca with decreasing CaO, which can be interpreted as diffusion couples [where light isotopes are depleted in residual (high-Ca) units and diffusively enriched in adjacent low-Ca units].

4.7.4.1. Metabasic dike samples

We first explore the large fractionation observed between whole-rock samples 2035A & 2035B, which represent the largest measured Δ^{44}Ca in our dataset (> 3‰). These samples were collected from the center (2035A) and edge (2035B) of a ~1.7 m thick mafic dike intruded into quartzitic country rock (not sampled, but likely similar to analyzed quartzites from the same area). The dike has a ~8 cm thick, paler-colored, opx-rich marginal zone, from which we collected sample 2035B. It is quite clear from the geologic context, geochemical observations, magnitude of Δ^{44}Ca, and non-equilibrium Δ^{48}Ca' values (Fig. 4.6), that the differences between these two samples result from diffusion between the dike and country-rock.

There are several observations that we can use as constraints for our model. Firstly, 2035A still contains a large portion of hydrous minerals (*e.g.* ~14% Hbl, ~4% Bt) and primary magmatic minerals (*e.g.* ~16% relatively fresh olivine, 8% Cpx) and only traces of plagioclase, while 2035B has no hydrous minerals, no olivine, and little Cpx (~1%), and is dominantly composed of Opx (~78%) and An39 plagioclase (18%), both with extremely-high δ^{44}Ca values (the highest in Fig. 4.3). Secondly, the edge of the dike has high δ^{44}Ca compared to the center, which, in conjunction with the mineralogy, implies that diffusion has not affected the center of the dike (the center of the dike would become more positive than the edges if diffusion was allowed to proceed longer). Thus, the measured composition of 2035A (similar to BSE, δ^{44}Ca = -0.09‰, ~3.5 wt% Ca) is likely to be the initial composition in the dike before metamorphism, which we assume to be initially constant from the middle to the edges. The measured composition of 2035B (δ^{44}Ca = +3.22‰, ~1.5 wt%) is the composition in the edge-most ~10 cm of the dike after diffusion has stopped.

Using a country-rock $[\mathrm{Ca}]_{\mathrm{CR}}$ of 0.5 wt% (the average for quartzites in our study), and an initial dike $[\mathrm{Ca}]_{\mathrm{Dk}}$ of 3.5 wt%, and assuming a total diffusion time of 100 Myr, we find that diffusivities (D_{Dk}) of ~10^{-10} m^2/yr with $D_{\mathrm{CR}}/D_{\mathrm{Dk}}$ > ~10^3 and D_{44}/D_{40} ~0.990 are required to explain our results (Fig. 4.7a). For these simulations, ratios for the diffusivity of Ca in the country rock relative to the dike ($D_{\mathrm{CR}}/D_{\mathrm{Dk}}$) lower than ~$10^3$ inhibit sufficient diffusion from taking place in the required time.

Higher dike diffusivities (*e.g.* D_{Dk} of 10^{-9} m^2/yr, Fig. 4.7b), on the other hand, do not require as large diffusivity contrasts between the country-rock and dike, but overstep the conditions captured by our samples after ~30 Myr (see Fig. S4.6). In these simulations, a lower minimum $D_{\mathrm{CR}}/D_{\mathrm{Dk}}$ of only ~10^2 is required to generate a sufficient [Ca] depletion in the edge of the dike, without affecting [Ca] and δ^{44}Ca in the center in 30 Myr, but given the thermochronological constraints it is suggested that dike diffusivities of 10^{-9} m^2/yr are too high. Regardless of the specific diffusivities, our simulations require D_{44}/D_{40} values similar to ~0.990 ± 0.002 in order to match observations.

4.7.4.2. Interlayered pelitic and mafic-pelitic units

Sample 2032A was collected from a layered garnet-sapphirine-quartz metapelite, found alternating with orthopyroxene-rich mafic granulites (2032I) in layers of variable thickness, ranging from <10 cm to ~50 cm. Sample 2032I (δ^{44}Ca = +0.34‰, ~4.7 wt% Ca) is dominantly orthopyroxene (~70%) with minor plagioclase (An90, 20%) and clinopyroxene (10%), with no identifiable hydrous or primary igneous minerals. Both the clinopyroxene and orthopyroxene show strong exsolution lamellae, suggestive of slow cooling. Sample 2032A (δ^{44}Ca = -1.56‰, ~0.04 wt% Ca) is dominantly cordierite + quartz (~46%) with significant sapphirine (~19%) overgrown by garnet (~22%) that contains the lowest measured grossular content of all our garnet samples (0.4% Grs, equivalent to ~0.16 wt% Ca), but still represents a dominant fraction of the whole-rock Ca budget (with ~6% modal perthitic K-feldspar as the other source). The textural relationships suggest that garnet formation post-dates the other minerals, implying retrograde garnet growth during slow isobaric cooling at lower-crustal pressures.

For our simulations, we start by setting up a 0.5m-thick pelitic unit between two 0.5m layers of mafic rock (which is approximately correct for where the samples were collected), surrounded by ~30m of pelitic rock. We assume a starting compositions of 5 wt% Ca for the mafic layers and 0.01 wt% Ca in the pelitic layers. Although there is probably some variation between the δ^{44}Ca compositions of the mafic and pelitic starting materials, they are likely to be second-order compared to the effects caused by diffusion and would be an additional uncertainty if estimated, we therefore assume that the starting δ^{44}Ca of all the layers are the same.

We demonstrate that Ca diffusivities similar to the mafic dike samples, ~10^{-10} m^2/yr (Fig. 4.8a), are required to match the signatures of samples 2032A-2032I in 100 Myr. In this case, however, D_{CR}/D_{Dk} must be lower than 1 (*e.g.* ~0.5, in this case D_{CR} refers to the pelite layers and D_{Dk} refers to the mafic layers) in order to not get overly-high [Ca] in the pelites. Diffusivities lower than ~10^{-10} m^2/yr for D_{Dk} do not generate low-enough [Ca] in the mafic layers, while higher values for D_{Dk} (*e.g.* 10^{-9} m^2/yr) exceed our constraints in just ~10 Myr. Another significant difference from the mafic-dike example is that these samples require changes in D_{44}/D_{40} across the layers, and that the fractionation factors are much smaller, with D_{44}/D_{40} ~0.996 in the mafic layers and little to no fractionation required in the pelitic layers (*e.g.* D_{44}/D_{40} ~0.9995).

For the three adjacent pelitic units, which have unconstrained thicknesses, we assume two adjacent 1m thick layers representing starting materials for 2036E and 2036C, surrounded by low [Ca] country-rock representing 2036A. From the measurements, we can infer that 2036E (δ^{44}Ca = +1.37‰, ~1.5 wt% Ca) was depleted in light isotopes, 2036C (δ^{44}Ca = +0.61‰, ~0.4 wt% Ca) to a lesser amount, and 2036A (δ^{44}Ca = -1.33‰, ~0.3 wt% Ca) was enriched in light isotopes. This suggests that the starting materials for 2036E and 2036C had higher Ca than measured today, and that those of 2036A had lower [Ca] than measured today.

We assume initial concentrations of 2, 1.5, and 0.01 wt% Ca for the starting materials. We assume that the region to the left of 2036E has low Ca the same as 2036A, but the results are substantially different if a higher-Ca unit (*e.g.* similar to 2036C) is on the other side, or if the units have different thicknesses. For our specific model conditions, we find that diffusivities of ~7×10^{-10}, ~2×10^{-8}, and 4×10^{-8} m^2/yr for units 2036E, 2036C, and 2036A, respectively, accompanied by fractionation factors (D_{44}/D_{40}) of 0.9975, 0.995, and 0.998 (Fig. 4.8b) best explain our results in 100 Myr. These samples, however, are much more poorly-constrained in terms of their relative locations within the diffusion profiles, and we intend the modeling to be mainly illustrative of the complex spatial evolution of Δ^{44}Ca in multi-layered systems.

Together, the higher diffusivities and smaller isotopic rate differences required to model Ca isotope data in pelitic units are generally consistent with expectations, where smaller grain sizes, higher

$[Ca]_{gb}/[Ca]_{solid}$, and larger volatile budgets in pelitic units would lead to higher effective diffusivities (and to generally lower viscosities in grain-boundary fluids). All of our models, however, would be greatly enhanced by more-detailed spatial information and higher-resolution sampling.

4.7.5. Thermometry and inter-mineral Δ^{44}Ca variations

4.7.5.1. Temperature estimates

With a few exceptions, we have shown that Ca isotope analyses in higher-grade metamorphic rocks do not appear to be generally useful for thermometry. However, one sample measured by MC-ICP-MS (IV-16-19), approximately agrees with our DFT estimates and has Δ^{48}Ca' values indicative of equilibrium (Fig. 4.6). Although, we were not able to measure Δ^{48}Ca' in all of the samples, several other samples have Δ^{44}Ca values consistent with equilibrium. Excluding six samples with significantly negative $\Delta^{44}Ca_{grt\text{-}fsp}$ and $\Delta^{44}Ca_{grt\text{-}WR}$ (2032A, 2036A, 2036C, 2036E, DDM303, & DDM342), along with two samples where direct measurements suggest $\Delta^{44}Cao_{px\text{-}fsp}$ or $\Delta^{44}Ca_{opx\text{-}cpx}$ exceed ~1‰ (2030B & 2035A), we are left with 10 samples where inter-mineral Δ^{44}Ca measurements may potentially reflect equilibrium conditions (2033A, 2035B, 2038, DDM163, DDM309, IV-16-09, IV-16-19, IV-16-24, & 14DLB39), and three samples without multiple mineral separates (2044, IV-16-09, & IZ408).

For temperatures above 900°C, Δ^{44}Ca uncertainties of ±0.1‰ lead to temperature uncertainties generally smaller than ± ~50°C for the most-precise thermometers (Opx-Fsp, Pyr/Alm-Fsp, Ol-Fsp, & Ol-Cpx), and better than ± ~75°C (Grs/Sps-Fsp & Pyr-Cpx) and ± ~100°C (Opx-Cpx, Alm/Sps-Cpx, & Ap-Grs) for the second and third most-precise thermometers. Oher mineral pairs, however, do not give results better than ± ~200°C when applied at temperatures > 900°C, and many have unresolvable isotopic compositions at these temperatures (see Fig. 4.2). Additional uncertainty comes from the large range for garnet RPFRs, and uncertainty in the properties of solid-solutions involving all four end-members.

The temperature estimates that agree with previous work come from (i) Opx-Cpx (2033A, ~950 ± 100 °C), (ii) Cpx-Fsp (DDM163, ~800 ± 225 °C), (iii) two Grt-Cpx (14DLB39, 600-850 °C; DDM309, 760-1025 °C), and (iv) two Grt-Fsp pairs (DDM309, 850-1100 °C; IV-16-19, 800-1000 °C). Our single eclogite-facies sample has $\Delta^{44}Ca_{grt\text{-}cpx}$ (650-850 °C) and $\Delta^{44}Ca_{grt\text{-}ap}$ (475-640 °C) that agree with other temperature proxies [~700°C, (Weller et al., 2016)] and also suggest Ca isotopic equilibrium.

Samples 2032I, 2033A, DDM163, and DDM309, on the other hand, give unreasonably high $\Delta^{44}Ca_{opx\text{-}fsp}$ temperatures (1150 to > 1500 °C), suggesting that they are not at Ca isotope equilibrium, despite having Fe-Mg and Ca-in-opx exchange temperatures similar to ~850°C (Table S4.9). In sample 2040C, the measured $\Delta^{44}Ca_{opx\text{-}grt}$ is too positive, and can only be modeled by fractionation with pure-grossular garnet at unrealistically low temperatures (~500°C). Garnet in 2040C, however, is 96% Alm + Pyr, which are predicted to be equal to or heavier than orthopyroxene at equilibrium. Garnet-feldspar temperatures are unreasonably low in samples 2038 (~500°C) and IV-16-24 (650-725 °C) and unreasonably high in DDM163 (> 1400°C).

Orthopyroxene (δ^{44}Ca = +5.20‰) and feldspar (δ^{44}Ca = +4.66‰) separates from sample 2035B are in approximate agreement with our DFT estimates at ~1000 ± 75 °C, suggesting approximate equilibrium, yet the bulk-rock composition (+3.22‰) is strongly kinetically-controlled, while

$\Delta^{44}Ca_{opx-cpx}$ from the middle of the dike (2035A) has a measured value that exceeds our DFT predictions (+0.87‰, equivalent to ~500 ± 50 °C, unmixed value 1.61 ± 0.28‰). Given that these samples were metamorphosed ~1m apart, it is unlikely that they represent different metamorphic temperatures, so the high $\Delta^{44}Ca_{opx-cpx}$ in the middle of the dike (2035A) is likely to be the result of inter-mineral kinetic effects that are not apparent in the edge of the dike (2035B) without applying our unmixing calculations for orthopyroxene. Our unmixing estimates lead to a $\Delta^{44}Ca_{opx-fsp}$ of +1.13 ± 0.34‰, which translates into low temperatures ~600 ± 125 °C, if assuming equilibrium.

4.7.5.2. Δ^{44}Ca disequilibria

Kinetic effects between minerals are the probable result of inter-mineral variations in either (i) Ca diffusion out of minerals (*e.g.* different activation energies, diffusion-rates, or D_{44}/D_{40}, relevant to volume-diffusion), (ii) Ca availability during mineral growth (*e.g.* the length-scale for diffusion) and the medium through which Ca must diffuse to reach the growing mineral surfaces (*e.g.* solid minerals *vs.* grain-boundary fluids or silicate liquids), and/or (iii) surface kinetic effects (*e.g.* from isotopic rate differences during attachment/detachment of Ca at mineral surfaces).

Ca has been shown to diffuse two orders of magnitude faster in plagioclase than in garnet (Keller et al., 2008), which may contribute to the larger disequilibrium effects we observe. Volume-diffusion for Ca in garnet (predicted to be ~3×10^{-10} to 3×10^{-17} m^2/yr), is also found to depend on oxygen fugacity (Carlson, 2006), likely due to coupling with Fe diffusion, which is redox-sensitive.

In the Napier Complex and Slave Province, it is inferred that samples were heated to granulite/ultra-high temperatures (> 800-900 °C) for long time periods, and then slowly cooled isobarically ("counter-clockwise") back-down to lower-crustal temperatures (Harley, 2016). PTt evolution in the Ivrea-Verbano zone (up to ~UHT conditions), however, is consistent with a clockwise PTt path (Redler et al., 2012).

Thus, the dominantly negative $\Delta^{44}Ca_{grt-fsp}$ and $\Delta^{44}Ca_{grt-WR}$ we observe in the NC samples may be the result of diffusive limitations during retrograde garnet growth. Retrograde garnet growth is most obvious in sample 2032A, where garnet occurs as small stringers over-growing high-temperature sapphirine (the only Ca-source in the rock besides garnet is K-Feldspar). In 2036A, 2036C, and 2036E, garnet is also found to host inclusions of higher-temperature minerals, such as globular hercynite and sillimanite, consistent with retrograde garnet growth. In 2040C, garnet hosts large rounded orthopyroxene inclusions, and orthopyroxene grains are found to be rimmed by small garnet stringers.

The other samples with significantly negative $\Delta^{44}Ca_{grt-fsp}$ are two lower-crustal xenoliths from the Slave Craton (DDM303 and DDM342). Sample DDM342 is essentially an anorthosite, dominantly composed of An72 plagioclase, with smaller amounts of garnet (22% grossular), and minor clinopyroxene, yet still has significantly negative $\Delta^{44}Ca_{grt-mineral}$ values. In this sample, euhedral to subhedral garnet crystals often contain small-inclusions of globular clinopyroxene, also consistent with retrograde garnet growth. This sample strongly illustrates that the length-scales for diffusive Ca isotope fractionation do not have to be large, and potentially that diffusion is occurring via solids and not via grain-boundaries. In DDM303, garnet appears highly-rounded and is replaced at the margins by K-feldspar (potentially during interactions with by kimberlite host magma), yet we also find rare inclusions of Fe-oxides.

Only on sample had excessively high garnet-feldspar $\Delta^{44}Ca$ (2038), leading to unrealistically low $\Delta^{44}Ca_{grt\text{-}fsp}$ temperatures of 500-550 °C if assuming equilibrium. This suggests that garnet in 2038 was affected by a different set of kinetic effects that led to fractionation in the opposite direction, compared to other garnet-bearing samples. This sample differs from the others in that it represents a feldspathic migmatite dike, and probably contained much larger fractions of partial-melt. In this sample, irregular-shaped rounded garnet grains contain inclusions of rounded-to-circular quartz + mesoperthite (not present in our other NC samples), and are slightly replaced at the margins by the same assemblage, potentially indicating garnet dissolution during prograde heating. The isotopic difference could thus potentially be explained through a loss of light Ca isotopes from pre-existing/ xenocrystic garnet during transport and resorption in partial melts [similar to kinetic Fe isotope fractionations in xenocrystic olivine grains observed by (McCoy-West et al., 2018)], but this requires further exploration.

The two remaining samples from the SP (DDM163 and DDM309) have slightly positive $\Delta^{44}Ca_{grt\text{-}fsp}$. One of these samples has $\Delta^{44}Ca_{grt\text{-}fsp}$ too low compared to equilibrium DFT predictions at relevant temperatures (DDM163). The other (DDM309) appears to represent garnet-feldspar and garnet-cpx Ca isotopic equilibrium at appropriate temperatures (Table S4.9). Garnet in DDM309, like garnet in DDM342 (the only cpx-bearing sample with disequilibrium garnet $\Delta^{44}Ca$), also contains rounded inclusions of clinopyroxene, but differs in that clinopyroxene is highly abundant and surrounds the garnet grains, whereas garnet in DDM342 is efficiently separated from clinopyroxene, by regions approximately granoblastic plagioclase. The grain boundaries in this sample are highly enriched in Mg, which are seen to extend from clinopyroxene grains (looking at X-ray maps for the thin section), delineating plagioclase grains and gathering around resorbing garnet. The increased diffusion length-scales for clinopyroxene-derived species (*e.g.* Fe, Mg) necessary for garnet growth in DDM342 may thus lead to the observed Ca isotope effects,. Previous work has shown that Fe and Mg diffusion in high-grade metamorphic rocks can transport Ca, even up its own chemical gradients (Grant, 1988), and so multi-component diffusion (Watkins et al., 2014, 2011) may be important to consider.

A similar mechanism is envisaged for excessively light $\Delta^{44}Ca_{opx\text{-}fsp}$ and $\Delta^{44}Ca_{opx\text{-}cpx}$, where diffusion towards the growing orthopyroxene would enrich it in light Ca isotopes (but this would be during heating as opposed to during cooling, as suggested for garnet). During clockwise heating, orthopyroxene formation could potentially be affected by diffusion-limitations during growth and become isotopically lighter than at equilibrium. However, none of the analyzed samples from the IVZ contain orthopyroxene.

During isobaric cooling, as suggested for the SP and NC (Davis et al., 2003; Harley, 2016), orthopyroxene is destabilized and may get isotopically heavier (as suggested by almost all of our NC samples) at the expense of garnet growth. However, orthopyroxene-bearing xenolith samples from the Slave Province have excessively-light orthopyroxene, which suggests that samples with similar cooling histories can have disequilibrium $\Delta^{44}Ca_{opx\text{-}mineral}$ in opposite directions [perhaps because of the higher (UHT) temperatures reached in the NC].

This could also be a potential manifestation of variability caused by multi-component diffusion. Ca isotope fractionation in silicate liquids depends strongly on the direction of its diffusion in composition-space [*e.g.* counter-diffusion of Na increases both Ca diffusion rates and $\Delta^{44}Ca$, whereas counter-diffusion of SiO_2 leads to the opposite effects (Watkins et al., 2014)], but these effects have not yet been explored for Fe and Mg. Another potential effect stems from a pressuredependency for the partitioning of Ca between garnet and plagioclase (Smit et al., 2013), but most of our samples (other than our eclogite samples) have similar pressures of ~1.0 ± 0.2 GPa.

Many aspects of the large Ca isotope fractionations we observe in high-temperature metamorphic rocks and minerals (with a δ^{44}Ca range twice as large as previously observed in terrestrial samples), however, remain enigmatic and warrant further investigation. In-situ analyses (*e.g.* by SIMS), for example, would be greatly beneficial to our understanding of high-temperature metamorphic and igneous processes, and would not necessitate very high precisions, given the magnitude of the effects.

4.7.6. Comments on partial-melting and δ^{44}Ca as a tracer

Partial-melting and subsequent melt-loss may have also affected our samples. This process is often associated with granulite/UHT facies samples (Cesare et al., 2009; Ferrero et al., 2018; White and Powell, 2002) and has been inferred for the early evolution of many of the samples analyzed in this study (Antonelli et al., 2018). Although not implicated by our diffusion modeling (the necessary diffusivities are too low), the generation and subsequent extraction of partial-melts may explain some of the early δ^{44}Ca variability in our samples (see main text, Section 4.3). It is currently too difficult, however, to adequately separate this process from subsequent metamorphic processes, but several of our samples and DFT predictions suggest that magmatic differentiation should lead to measureable whole-rock δ^{44}Ca effects.

Previous studies have also used δ^{44}Ca variability in mantle rocks to constrain carbonate subduction over time, where negative δ^{44}Ca shifts are interpreted as direct incorporation of carbonate sediments (Chen et al., 2018; Huang et al., 2011; S. Huang et al., 2010; Kang et al., 2017, 2016; Liu et al., 2017) and positive δ^{44}Ca shifts have been interpreted as recording interactions with fluids that have precipitated carbonates before interacting with the rocks (Chen et al., 2018). However, it is unlikely that linear mixing models using δ^{44}Ca as a tracer hold great validity, due to (i) the highly-variable kinetic fractionations (*e.g.* > ~1.5‰) associated with carbonate precipitation (Fantle and Tipper, 2014), (ii) the unknown quantities of hydrothermal vs. sedimentary carbonates in the subducting package, (iii) the unknown kinetic/unmixing effects associated with subduction-zone metamorphism, and (iv) the unconstrained effects of diffusion, crystallization, and partial melting in the mantle.

Fluid losses during subduction (*e.g.* John et al., 2012) could also be important. The role of variable fluid budgets during high-T magmatic and metamorphic Ca isotope fractionation, however, still remains underexplored. Given the general relationship between isotopic fractionation and magma viscosity (Watkins et al., 2017), it is likely that increasing volatile contents also leads to decreased kinetic Ca isotope fractionations (D_{44}/D_{40} values closer to unity), which could help explain why kinetic Ca isotope effects are so much larger in granulites than in previously observed high-T rocks and minerals.

4.7.7. Supplementary figures and tables

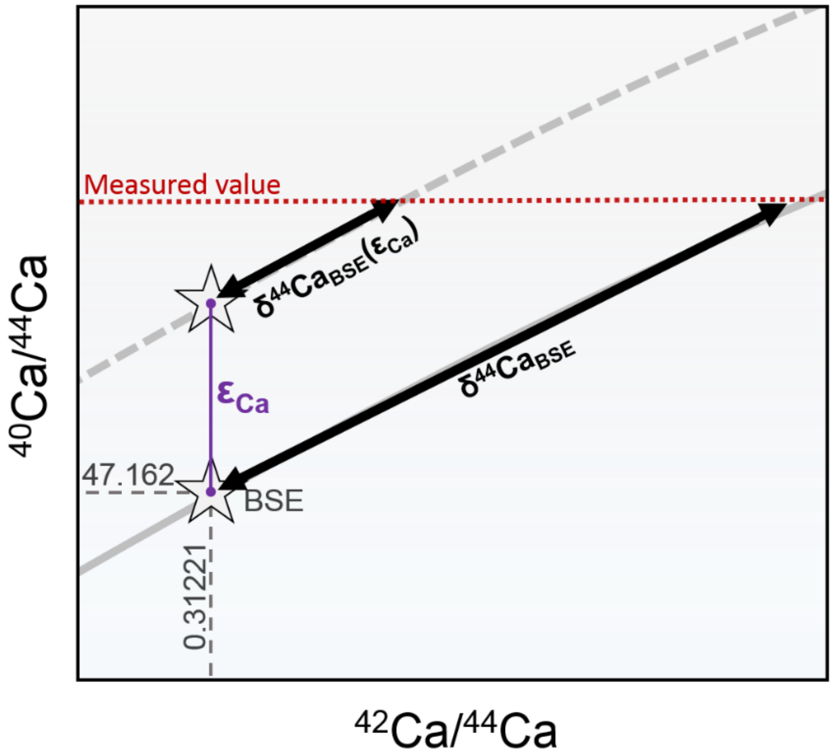

Fig. S4.1. Schematic diagram of radiogenic Ca (ε_{Ca}) correction for δ^{44}Ca analysis by TIMS.

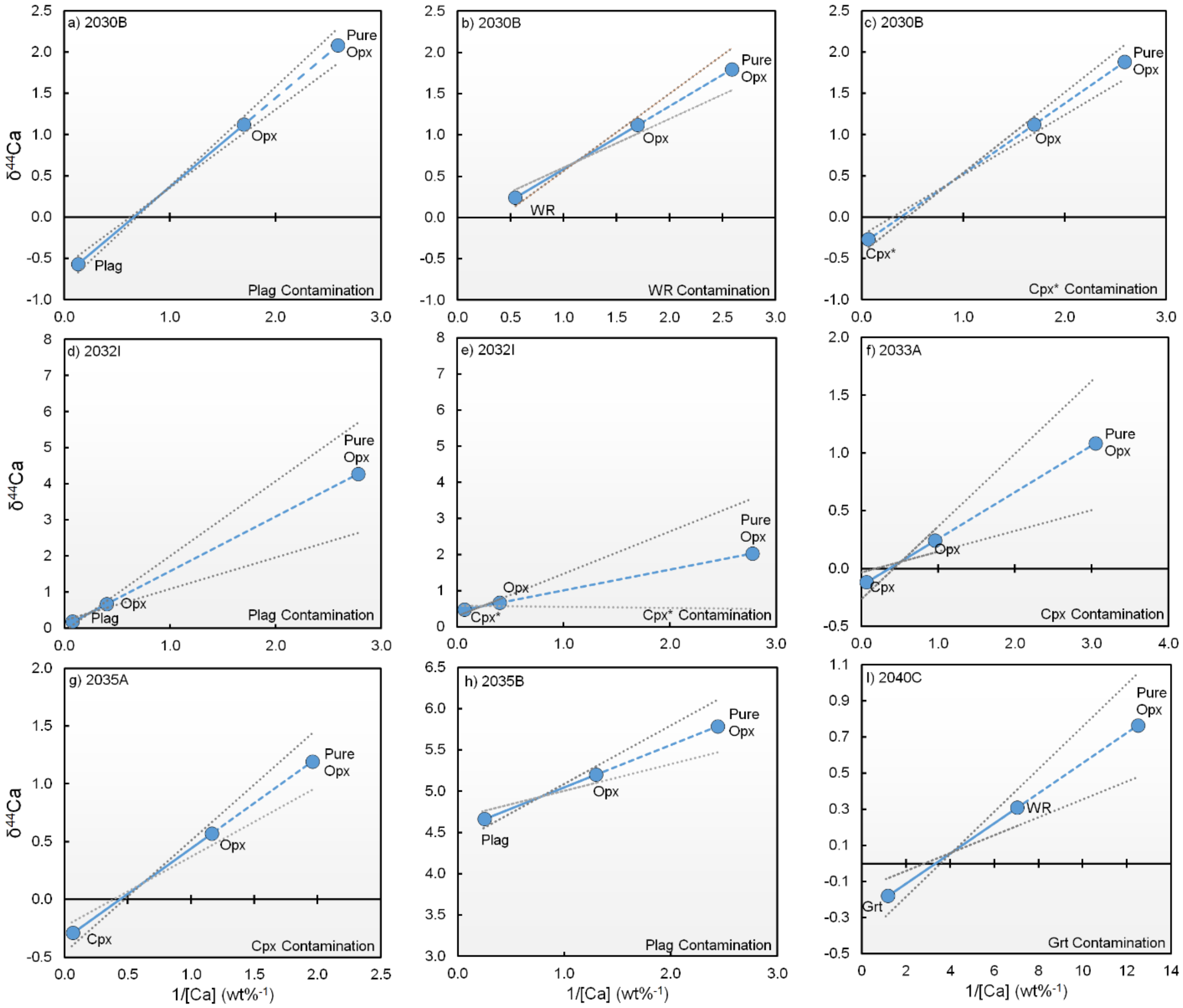

Fig. S4.2a-i. Unmixing calculations for orthopyroxene separates. [Ca] (wt%) is from TIMS or EPMA (for pure-opx). Uncertainties for pure-opx range from ~0.2 to~1.5‰ with an average of ~0.5‰. Errors envelops are calculated using the long term 2SD uncertainties on our δ^{44}Ca measurements (±0.1‰).

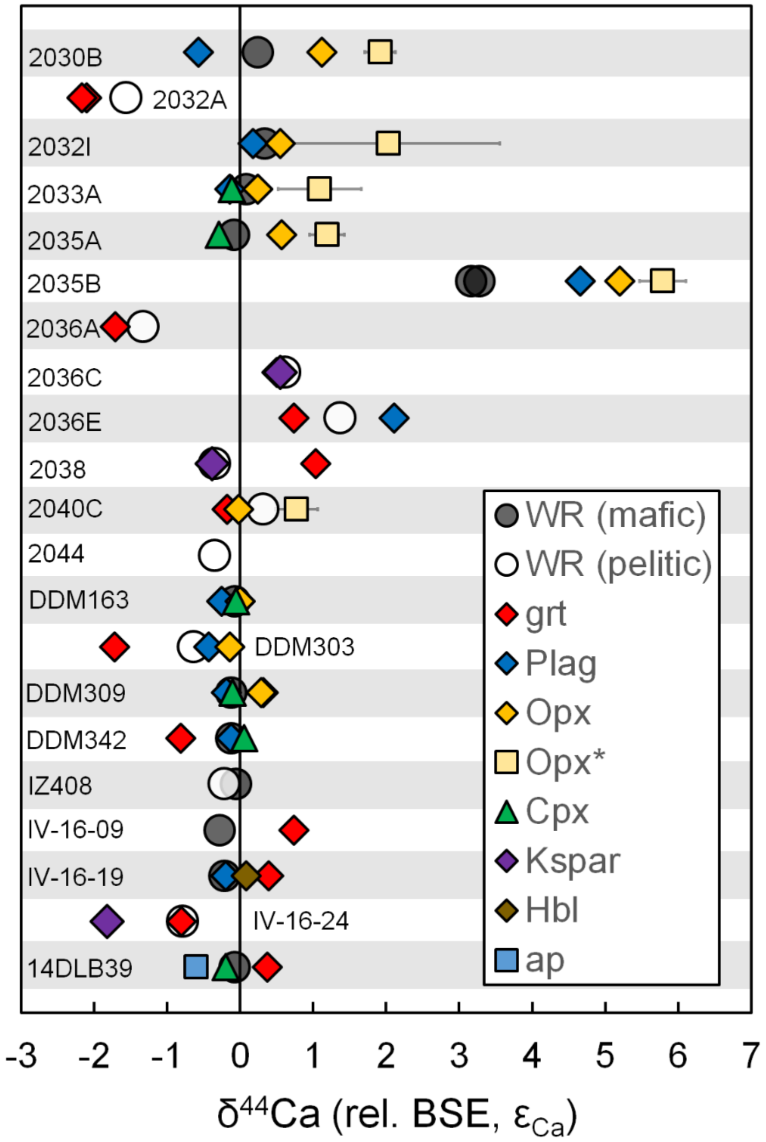

Fig. S4.3. Ca isotope compositions (δ^{44}Ca) of minerals and whole rocks in this study (n=66) versus sample-number. K-feldspar separates are slightly perthitic to mesoperthitic.

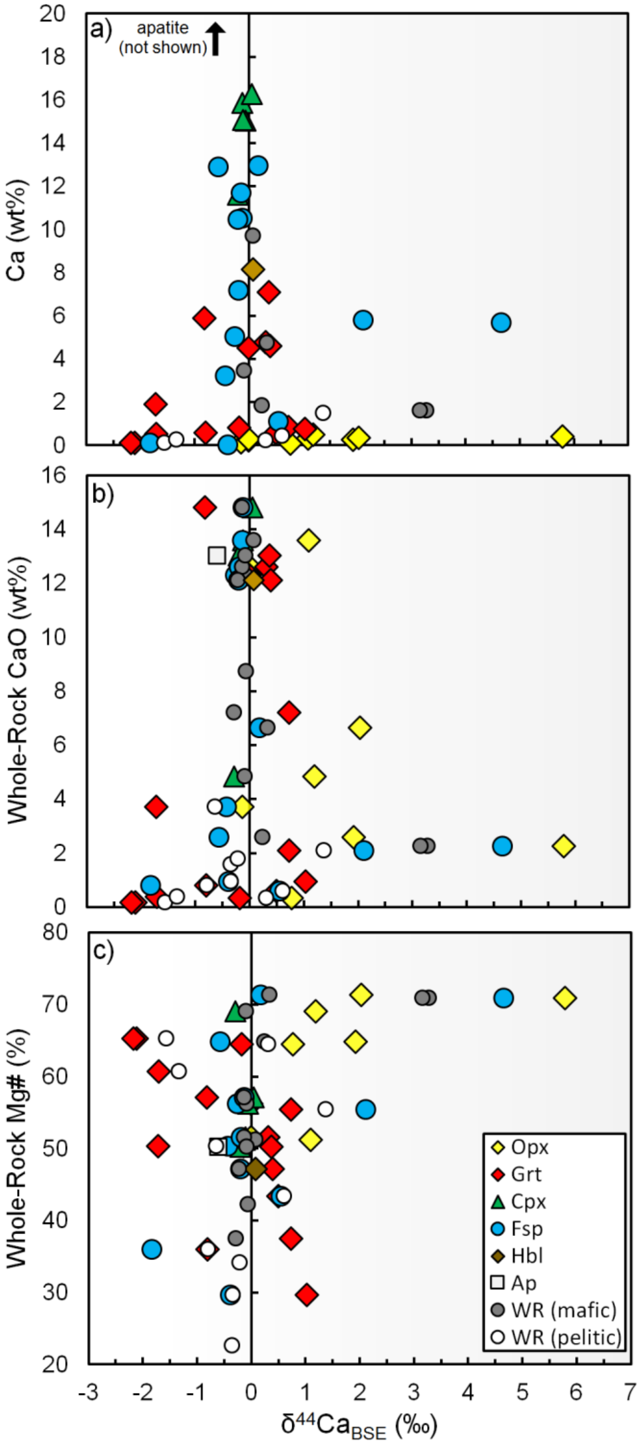

Fig. S4.4. Ca isotope compositions (δ^{44}Ca) of minerals and whole rocks in this study (n=66) versus (a) Ca (wt%) [by EPMA (minerals) and/or XRF (whole-rocks)], (b) whole-rock CaO (wt%), and (c) whole-rock Mg# (%) [defined as molar MgO/(MgO+FeO)]. In both figures, orthopyroxene values are from unmixed calculations.

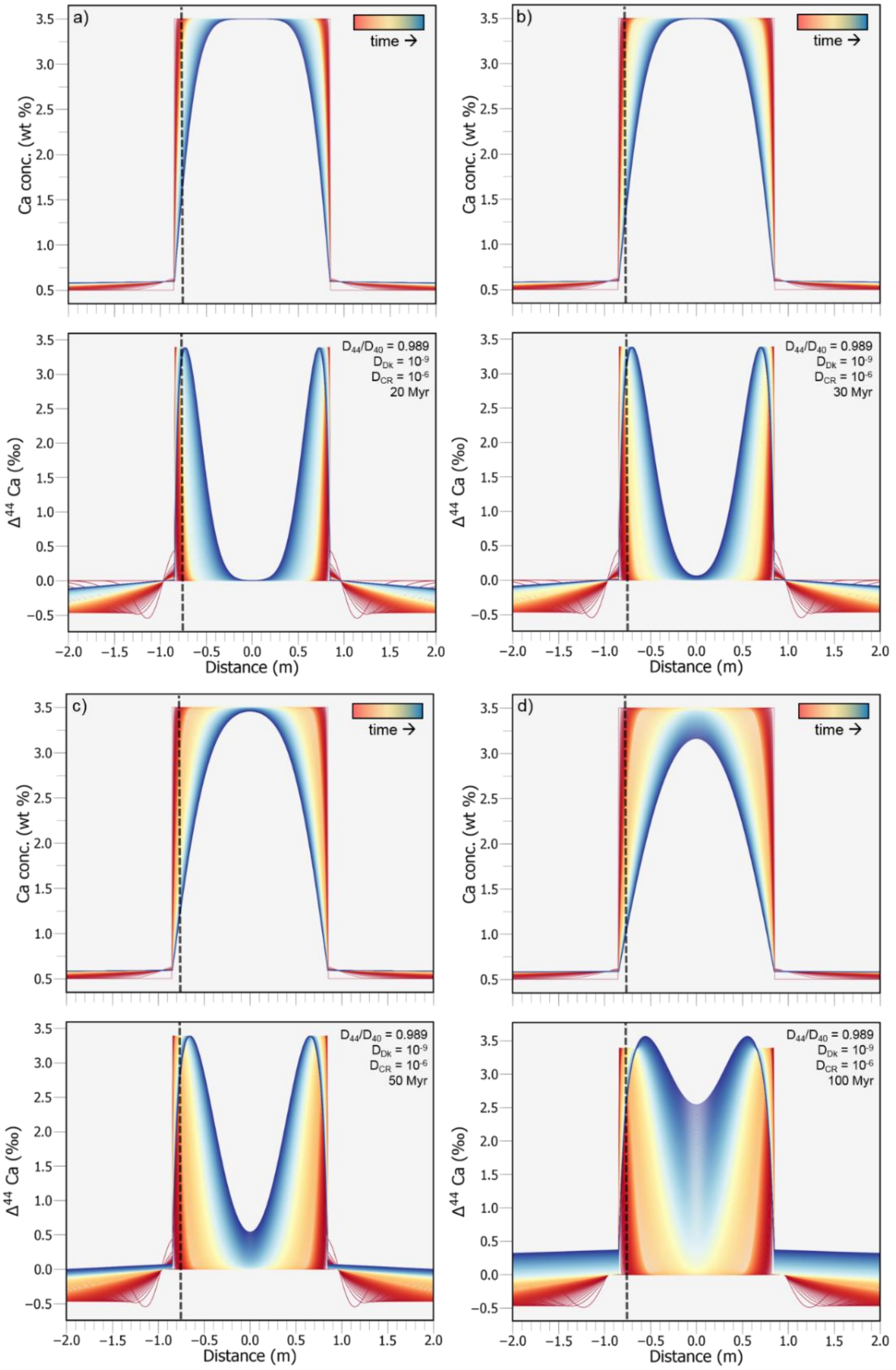

Fig. S4.5. Numerical diffusion model results for spatial-variations in Ca concentration and Δ^{44}Ca over time, as relevant to the center (2035A) and edge (2035B) of our metabasic dike samples from the Napier Complex. **(a)** 20 Myr, **(b)** 30 Myr, **(c)** 50 Myr, **(d)** 100 Myr.

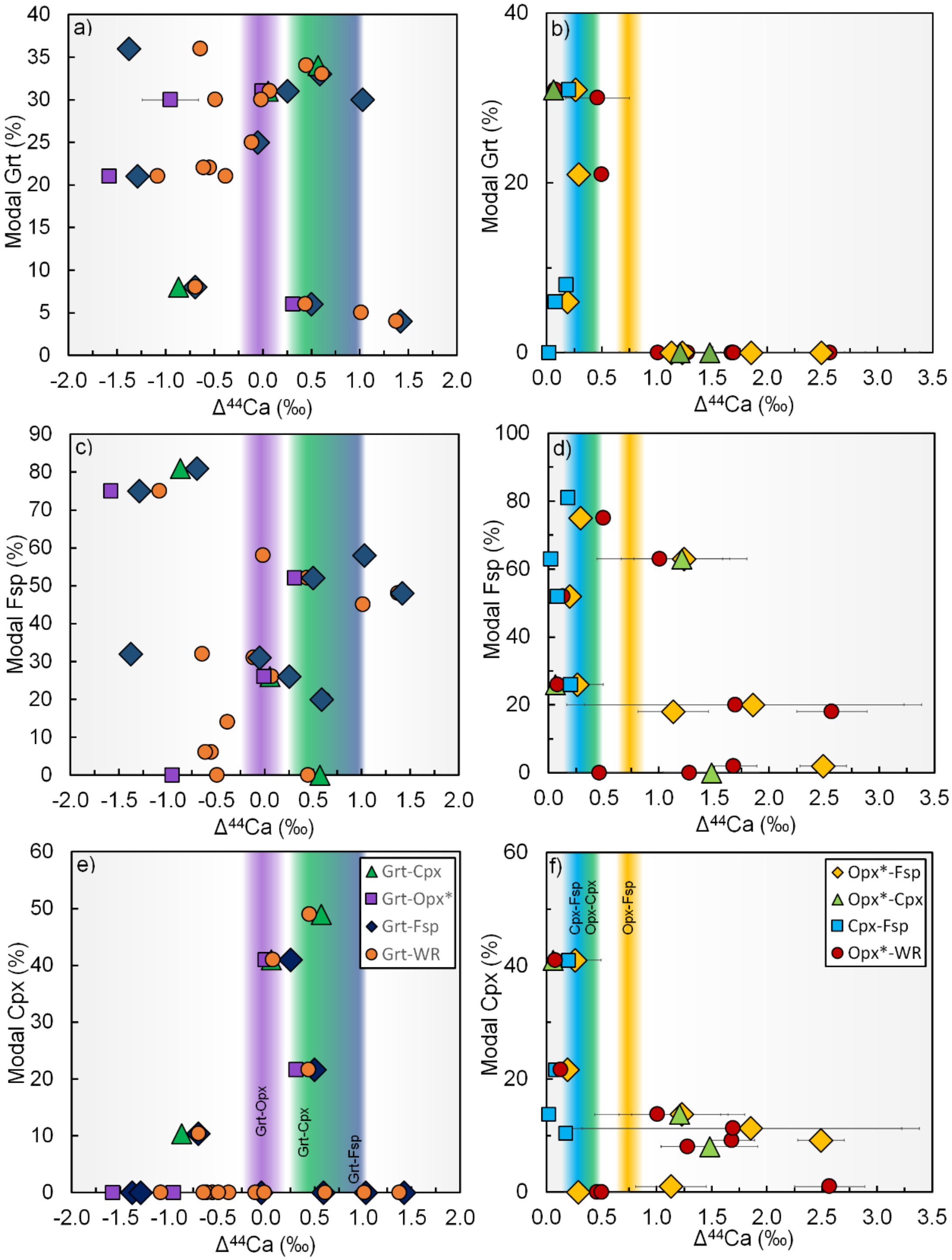

Fig. S4.6. Inter-mineral Ca isotope variability (Δ^{44}Ca) *vs.* modal mineralogy. (a,b) Modal garnet, (c,d) modal feldspar, (e,f) modal clinopyroxene abundances. Colored bands reflect equilibrium predictions at 800-900 °C.

Table S4.1. Modal mineralogy estimates (from optical, X-ray map, and BSE image analyses) (Antonelli et al., 2018).

	2030B	**2032A**	**2032I**	**2033A**	**2035A**	**2035B**	**2036A**	**2036C**	**2036E**	**2038**	**2040C**
Plag	2	-	20	63	-	18	-	6	25	9	-
Cpx	9	-	11	14	8	1	-	-	-	-	-
Opx	89	1	68	23	58	80	-	-	-	-	60
Grt	-	22	-	-	-	-	21	25	36	4	30
Sil	-	6	-	-	-	-	7	11	1	1	-
Qtz	-	?	-	-	-	-	36	33	20	47	10
Crd	-	46	-	-	-	-	20	-	7	-	-
Spr	-	19	-	-	-	-	-	-	-	-	-
Ol	-	-	-	-	16	-	-	-	-	-	-
Hbl	-	-	-	-	14	-	-	-	-	-	-
Bt	1	-	-	-	3	1	-	-	4	-	-
Kspar*	-	6	-	-	-	-	14	25	7	39	-
Ap	-	-	0.6	-	-	-	0.2	-	-	-	-
Spl	-	-	-	-	-	-	1	-	-	-	-
Opqs	0.4	0.1	0.1	0.1	0.5	0.4	0.4	0.5	0.5	0.0	0.2
Rt	-	-	-	-	-	-	-	-	-	-	-

	2044	**DDM163**	**DDM303**	**DDM309**	**DDM342**	**IV-16-09**	**IV-16-19**	**IV-16-24**	**IZ408L**	**IZ408M**	**14DLB39**
Plag	16	26	65	52	81	45	20	-	21	41	-
Cpx	-	41	-	22	10	-	-	-	-	-	49
Opx	1	2	1	16	-	-	-	-	-	-	-
Grt	-	31	21	6	8	5	33	30	-	-	34
Sil	-	-	-	-	-	-	-	1	-	-	-
Qtz	42	-	-	-	-	37	-	7	75	-	13
Crd	-	-	-	-	-	-	-	4	-	-	-
Spr	-	-	-	-	-	-	-	-	-	-	-
Ol	-	-	-	-	-	-	-	-	-	-	-
Hbl	1	-	-	2	-	-	47	-	3	53	-
Bt	-	-	2	-	-	11	-	-	-	-	-
Kspar*	40	-	10	-	-	-	-	58	-	-	-
Ap	-	-	-	-	-	-	-	-	-	-	2
Spl	-	-	-	-	-	-	-	-	-	-	-
Opqs	0.0	0.2	1.0	1.8	0.2	1.0	0.8	0.9	0.1	6.1	-
Rt	-	-	-	-	-	-	-	-	-	-	1.7

**K-spar is dominantly perthitic*

Table S4.2. Bulk-rock chemical compositions (XRF) from (Antonelli et al., 2018).

Sample	**2030B**	**2032A**	**2032I**	**2033A**	**2035A**	**2035B**	**2036A**	**2036C**
SiO_2	48.5	65.0	58.2	46.6	45.1	58.6	67.0	60.7
TiO_2	0.3	0.9	0.5	0.1	0.8	0.6	0.8	0.9
Al_2O_3	5.9	19.3	8.0	20.5	4.6	8.3	17.3	19.8
FeO	19.6	6.1	10.4	10.0	18.2	11.1	5.9	8.3
MgO	20.3	6.4	14.5	5.9	22.8	15.2	5.1	3.6
CaO	2.6	0.2	6.6	13.6	4.8	2.3	0.4	0.6
Na_2O	0.4	0.6	0.2	1.5	0.4	1.9	0.8	1.6
K_2O	0.05	0.81	0.10	0.25	0.90	0.61	1.86	3.58
MnO	0.3	0.1	0.2	0.2	0.3	0.2	0.1	0.1
Mg#	64.9	65.3	71.3	51.3	69.1	71.0	60.7	43.4
A/CNK	1.08	8.93	0.63	0.75	0.44	1.05	4.33	2.60
K/Ca	0.02	5.54	0.02	0.02	0.22	0.32	5.69	6.93

Sample	**2036E**	**2038**	**2040C**	**2044**	**DDM163***	**DDM303***	**DDM309**	**DDM309***
SiO_2	51.1	76.2	48.2	74.3	48.9	53.7	47.1	49.4
TiO_2	0.8	0.1	0.5	0.2	0.4	0.0	1.3	1.3
Al_2O_3	15.2	13.8	8.6	13.6	15.5	24.3	13.7	15.8
FeO	15.9	0.7	19.7	2.1	11.8	6.9	13.0	11.2
MgO	11.1	0.2	20.1	0.4	8.5	3.9	12.8	6.7
CaO	2.1	1.0	0.3	1.6	12.3	3.7	10.1	12.6
Na_2O	1.0	2.3	0.0	2.8	2.2	5.8	1.3	2.7
K_2O	1.00	5.79	0.004	4.87	0.07	1.69	0.27	0.21
MnO	0.2	0.0	0.2	0.0	0.2	0.1	0.2	0.2
Mg#	55.4	29.7	64.5	22.6	56.3	50.3	63.7	51.6
A/CNK	2.33	1.18	13.81	1.06	0.59	1.34	0.66	0.57
K/Ca	0.55	7.08	0.003	3.56	0.01	0.53	0.03	0.02

Sample	**DDM342***	**IV-16-09**	**IV-16-19**	**IV-16-24**	**IZ408-L**	**IZ408-M**	**14DLB39**
SiO_2	48.5	66.4	42.5	51.4	90.8	45.0	44.1
TiO_2	0.4	0.9	1.8	1.7	0.1	3.2	2.1
Al_2O_3	28.1	16.5	20.7	24.9	5.4	14.6	16.2
FeO	3.3	5.3	13.5	13.5	0.4	17.2	14.3
MgO	2.4	1.8	6.7	4.3	0.1	7.1	8.1
CaO	14.8	7.2	12.1	0.8	1.8	8.7	13.0
Na_2O	2.4	0.4	1.6	1.2	1.3	2.7	1.3
K_2O	0.13	1.33	0.75	2.00	0.13	0.75	0.06
MnO	0.0	0.1	0.2	0.2	0.0	0.3	0.2
Mg#	57.1	37.5	47.2	36.0	34.2	42.3	50.2
A/CNK	0.91	1.08	0.81	4.45	0.99	0.69	0.63
K/Ca	0.01	0.21	0.07	2.89	0.08	0.10	0.005

Table S4.3. In-situ chemical compositions of major minerals. Garnet, plagioclase, and K-feldspar values are from (Antonelli et al., 2018).

	2030B	**2032A**	**2032I**	**2033A**	**2035A**	**2035B**	**2036A**	**2036C**	**2036E**	**2038**	**2040C**
Plagioclase											
SiO_2	45.0		45.9	47.6		57.8		64.2	58.7	62.1	
TiO_2	-		0.01	-		0.02		0.01	0.03	-	
Al_2O_3	35.1		35.5	33.7		26.6		21.6	26.7	24.3	
Fe_2O_3	0.15		0.09	0.13		0.15		0.04	0.05	0.02	
CaO	18.1		18.1	16.4		8.0		3.1	8.1	4.8	
Na_2O	1.3		1.1	2.1		6.7		7.9	6.3	8.6	
K_2O	0.05		0.02	0.20		0.26		2.22	0.31	0.26	
Total	99.6		100.8	100.0		99.4		99.0	100.2	100.1	
An%	88.4		89.8	80.0		39.2		15.4	40.7	23.3	
Ab%	11.3		10.1	18.8		59.2		71.3	57.5	75.2	
Orth%	0.3		0.1	1.2		1.5		13.3	1.8	1.5	
Garnet/clinopyroxene											
		Grt		*Cpx*			*Grt*	*Grt*	*Grt*	*Grt*	*Grt*
SiO_2		40.6		50.4			40.6	39.6	40.8	38.4	40.3
TiO_2		0.03		0.52			0.06	0.04	0.06	0.05	0.02
Al_2O_3		23.1		4.1			22.6	22.7	23.1	22.0	22.3
FeO		22.9		10.9			23.3	24.0	21.7	30.5	23.6
MgO		13.6		11.2			13.6	13.0	13.5	7.3	12.9
CaO		0.2		22.2			0.7	0.8	1.2	1.1	1.2
Na_2O		-		0.4			< D.L.	0.01	0.005	-	0.003
K_2O		-		0.004			0.003	0.001	0.004	-	-
MnO		0.2		0.26			0.5	0.2	0.3	0.9	0.5
Cr_2O_3		-		0.04			-	-	-	0.00	-
Total		100.7		100.1			101.3	100.4	100.7	100.1	100.8
En%		-		33.7			-	-	-	-	-
Fs%		-		18.4			-	-	-	-	-
Wo%		-		47.9			-	-	-	-	-
Alm %		48.1		-			47.1	48.1	45.5	66.7	48.0
Pyr %		51.0		-			49.8	49.1	50.6	28.4	47.9
Grs %		0.4		-			2.0	2.2	3.1	3.0	3.1
Spsr %		0.5		-			1.1	0.5	0.7	2.0	1.1
Orthopyroxene/K-Feldspar											
	Opx		*Opx*	*Opx*	*Opx*	*Opx*	*Kspar*	*Kspar*		*Kspar*	*Opx*
SiO_2	51.3		54.4	50.8	52.8	54.4	63.7	64.2		64.1	48.8
TiO_2	0.23		0.10	0.16	0.13	0.12	-	0.04		-	0.19
Al_2O_3	3.6		1.8	2.2	3.5	1.7	19.0	19.1		19.1	10.8
FeO	19.5		17.8	28.4	17.2	16.8	-	-		-	17.6
MgO	24.2		25.3	17.2	25.0	26.1	-	-		-	21.9
CaO	0.54		0.46	0.46	0.71	0.57	0.26	0.31		0.05	0.11
Na_2O	0.009		0.011	0.015	0.014	0.017	2.0	2.4		1.0	0.00
K_2O	0.001		0.003	0.002	0.003	0.003	13.9	13.1		15.4	0.002
MnO	0.36		0.33	0.60	0.30	0.27	-	-		-	0.14
Cr_2O_3	0.35		0.28	0.02	0.11	0.22	-	-		-	0.496
Total	100.1		100.4	99.8	99.7	100.2	98.9	99.1		99.7	100.1
En%	66.8		71.1	51.4	71.1	72.7	-	-		-	68.8
Fs%	32.4		28.0	47.6	27.4	26.2	-	-		-	31.0
Wo%	0.8		0.9	1.0	1.5	1.1	-	-		-	0.2
An%	-		-	-	-	-	1.2	1.6		0.3	-
Ab%	-		-	-	-	-	17.7	21.3		9.1	-
Orth%	-		-	-	-	-	81.1	77.1		90.7	-

Table S4.3. (Continued).

	2044	DDM163	DDM303	DDM309	DDM342	IV-16-09	IV-16-19	IV-16-24	IZ408-L	IZ408-M	14DLB39
	Plag	*Plag*	*Plag*	*Plag*	*Plag*	*Plag*	*Plag*	*Kspar*	*Plag*	*Plag*	
SiO_2	61.4	60.3	63.0	55.3	50.1	45.2	48.8	61.9	66.2	56.2	
TiO_2	-	-	-	0.01	-	-	-	-	-	-	
Al_2O_3	24.4	26.0	23.8	28.1	32.8	35.8	33.0	18.9	21.4	28.2	
Fe_2O_3	0.17	0.03	0.03	0.07	0.06	0.03	0.38	-	0.17	0.09	
CaO	5.2	7.1	4.5	10.1	14.7	18.2	14.6	0.16	1.4	9.2	
Na_2O	8.0	7.5	8.9	5.5	3.0	1.1	2.9	1.9	10.6	6.1	
K_2O	0.77	0.33	0.35	0.34	0.17	0.01	0.16	14.1	0.25	0.09	
Total	99.9	101.1	100.6	99.5	100.8	100.4	99.8	97.0	100.0	100.0	
An%	25.3	33.5	21.4	49.3	72.5	90.0	72.8	0.8	6.5	45.1	
Ab%	70.2	64.6	76.6	48.7	26.5	10.0	26.3	16.7	92.1	54.3	
Orth%	4.5	1.9	2.0	2.0	1.0	0.1	0.9	82.5	1.4	0.5	
	Kspar	*Grt*	*Grt*	*Grt*	*Grt*	*Grt*	*Grt*	*Grt*			*Grt*
SiO_2	63.8	39.6	40.3	38.7	39.8	38.0	39.1	39.3			39.8
TiO_2	-	0.13	0.02	0.16	0.13	0.02	0.10	0.02			0.08
Al_2O_3	19.0	22.0	22.7	21.8	22.2	21.4	21.2	21.7			21.7
FeO	-	23.6	22.5	26.9	21.3	29.9	24.3	28.6			21.7
MgO	-	8.8	12.3	6.0	8.9	3.2	7.7	9.3			6.9
CaO	0.11	6.3	2.7	6.7	8.2	6.7	6.5	0.8			9.9
Na_2O	1.3	0.02	0.04	0.02	0.02	-	-	-			-
K_2O	14.7	< D.L.	< D.L.	0.01	<D.L.	-	-	0.004			0.01
MnO	-	0.5	0.3	0.8	0.4	1.0	1.0	0.4			0.4
Cr_2O_3	-	-	-	-	-	0.01	0.01	0.04			0.00
Y_2O_3	-	-	-	-	-	-	0.01	0.01			0.02
Total	99.1	101.0	100.8	101.2	101.0	100.2	99.8	100.2			100.5
Alm %	-	49.0	46.8	56.7	44.0	66.1	51.2	61.5			46.0
Pyr %	-	32.9	45.5	23.1	33.1	12.7	29.1	35.5			26.2
Grs %	-	17.1	7.2	18.5	22.1	18.9	17.4	2.3			26.9
Spsr %	-	1.1	0.6	1.8	0.8	2.3	2.1	0.8			0.9
An%	0.6	-	-	-	-	-	-	-			-
Ab%	12.1	-	-	-	-	-	-	-			-
Orth%	87.3	-	-	-	-	-	-	-			-
SiO_2	47.9	53.3	54.2	50.6							
TiO_2	0.07	0.05	0.03	0.08							
Al_2O_3	2.3	3.0	2.9	2.7							
FeO	37.5	19.9	16.8	27.9							
MgO	11.6	23.2	25.3	17.3							
CaO	0.15	0.33	0.21	0.43							
Na_2O	0.007	0.026	0.019	0.030							
K_2O	0.001	0.001	0.001	0.005							
MnO	0.43	0.12	0.07	0.35							
Cr_2O_3	0.002	0.03	0.15	0.03							
Total	100.0	99.9	99.7	99.4							
En%	35.5	67.0	72.5	52.1							
Fs%	64.2	32.3	27.1	47.0							
Wo%	0.33	0.68	0.42	0.92							
	Hbl	*Cpx*		*Cpx*	*Cpx*		*Hbl*				*Omph*
SiO_2	38.6	52.0		52.1	50.8		41.1				53.7
TiO_2	3.24	0.53		0.54	0.75		2.57				0.16
Al_2O_3	13.4	4.7		4.9	6.1		13.7				7.9
FeO	16.0	7.2		7.2	6.5		13.8				6.1
MgO	15.4	12.5		12.3	12.2		11.7				11.8
CaO	0.01	21.1		21.1	22.8		11.4				16.2
Na_2O	0.1	1.6		1.7	0.9		2.1				3.7
K_2O	8.91	0.001		0.001	0.001		0.99				0.02
MnO	0.04	0.05		0.06	0.03		0.12				0.03
Cr_2O_3	0.003	0.06		0.06	0.02		0.01				0.03
H_2O	1.93	-		-	-		2.01				-
Total	97.6	99.8		99.9	100.1		99.4				99.7
En%	-	39.5		39.1	37.9		-				-
Fs%	-	12.7		12.8	11.2		-				-
Wo%	-	47.8		48.2	50.8		-				-

Table S4.4. Mineral separate compositions (ICP-OES). Ca and K values in feldspar, garnet, and whole-rocks are from (Antonelli et al., 2018).

		Ca (wt%)	Mg (wt%)	Fe (wt%)	Na (wt%)	K (wt%)
Apatite	14DLB39	13.00	0.60	5.21	0.01	0.10
Clinopyroxene	2035A	13.34	8.65	6.69	0.02	0.40
Feldspar	2032I	11.41	0.75	0.69	0.27	0.75
	2035B	3.49	0.92	0.84	0.55	3.51
	2036C	0.49	-0.08	-0.20	10.39	2.38
	2038	0.89	0.01	0.03	8.65	2.70
	DDM303	2.66	0.89	0.41	0.76	5.02
	IV-16-24	0.56	0.04	0.19	3.76	2.41
Garnet	14DLB39	7.72	4.46	17.51	0.01	0.13
	2032A	0.09	5.99	12.05	0.02	0.01
	2036A	0.49	8.14	15.17	0.05	0.00
	2036C	0.51	7.04	19.61	0.00	-0.02
	2038	0.70	4.41	23.68	0.02	0.00
	DDM303	1.73	8.40	18.77	0.00	0.02
	IV-16-24	0.47	4.96	10.17	0.08	0.03
Orthopyroxene	2032I	2.30	10.77	7.66	0.06	0.06
	2035A	0.82	15.22	14.60	0.09	0.05
	2035B	0.64	14.06	12.67	0.07	0.30
	DDM163	0.54	14.90	14.05	0.04	0.08
	DDM303	3.04	11.82	6.19	0.36	0.24
	DDM309	0.97	12.77	12.11	0.15	0.09
WR	14DLB39	9.72	5.47	12.55	0.03	1.02
	2032I	4.99	9.26	8.38	0.08	0.14
	2035A	3.12	10.43	7.70	0.75	0.36
	2035B	1.32	8.07	6.99	0.51	1.45
	2036A	0.16	2.76	3.80	1.39	0.23
	2036C	0.30	2.12	4.86	2.48	0.72
	2038	0.73	0.12	0.56	5.38	1.94
	2044	1.17	0.18	1.58	4.11	2.26
	DDM309	7.04	7.84	10.50	0.19	0.95
	IV-16-09	5.78	1.30	5.11	1.26	0.27
	IV-16-24	0.62	3.03	12.01	1.68	0.89
	IZ408-L	1.33	0.06	0.25	0.10	0.97
	IZ408-M	6.94	5.07	15.16	0.62	2.03

Table S4.5. Ca isotope measurements (by TIMS) and Ca concentrations by TIMS, XRF (whole rocks), and EPMA (minerals). ε_{Ca} values are relative to $^{40}Ca/^{44}Ca = 47.156$ and come from (Antonelli et al., 2018). All values reported to bulk-silicate earth. Estimated 2SD uncertainties for $\delta^{44}Ca$ and $\delta^{44}Ca_{\varepsilon Ca}$ are ±0.1‰ and ±0.14‰, respectively. Estimated 2SD uncertainties for unmixed orthopyroxene (details in methods) are reported for each sample.

		n	**$\delta^{44}Ca$ (‰)**	**ε_{Ca}**	**$\delta^{44}Ca_{\varepsilon Ca}$ (‰)**	**$\delta^{44}Ca_{\varepsilon Ca,\ unmixed}$ (‰)**	**Ca (wt %)†**	**Ca (wt%)‡**
2030B	WR	2	0.05	-	0.24	-	1.8	1.9
	Opx	2	0.90	-	1.12	1.92 ± 0.21	0.6	0.3
	Plag	2	-0.76	3.1	-0.57	-	7.8	12.9
2032A	WR	2	-9.19	76.8	-1.56	-	0.04	0.1
	Grt	2	-6.48	-	-2.11	-	0.1	0.1
	Grt B	2	-6.54	42.4	-2.17	-	0.1	0.1
2032I	WR	2	0.34	-	0.34	-	4.7	4.8
	Opx	5	0.55	-	0.55	2.03 ± 1.53	2.5	0.4
	Plag	3	0.18	2.0	0.18	-	12.7	13.0
2033A	WR	2	0.08	-	0.08	-	9.0	9.7
	Cpx	2	-0.12	-	-0.12	-	14.5	15.9
	Opx	2	0.24	-	0.24	1.09 ± 0.57	1.0	0.3
	Plag	2	-0.14	2.3	-0.14	-	11.5	11.7
2035A	WR	2	-0.22	2.4	-0.09	-	3.5	3.5
	Cpx	2	-0.42	-	-0.29	-	14.6	15.5
	Opx	2	0.45	-	0.57	1.19 ± 0.24	0.9	0.5
2035B	WR	3	3.04	3.5	3.28	-	1.5	1.6
	WR B	2	2.92	3.5	3.16	-	1.5	1.6
	Opx	3	4.96	-	5.20	5.79 ± 0.32	0.8	0.4
	Plag	3	4.44	3.3	4.66	-	4.0	5.7
2036A	WR	2	-5.35	39.6	-1.33	-	0.2	0.3
	Grt	2	-3.23	15.3	-1.71	-	0.5	0.5
	Kspar	2	-14.69	-	-	-	0.4	0.2
2036C	WR	2	-3.12	36.3	0.61	-	0.3	0.4
	Grt	2	-0.73	12.6	0.50	-	0.6	0.6
	Kspar	2	-5.37	58.0	0.55	-	0.7	1.1
2036E	WR	2	0.76	6.9	1.37	-	1.2	1.5
	Grt	2	0.40	4.3	0.73	-	0.7	0.9
	Plag	2	1.78	-	2.11	-	5.3	5.8
2038	WR	2	-3.96	34.1	-0.35	-	0.7	0.7
	Grt	2	-0.37	14.1	1.03	-	0.7	0.8
	Kspar	2	-4.65	40.7	-0.39	-	0.9	0.04
2040C	WR	2	-0.88	12.5	0.31	-	0.1	0.2
	Grt	2	-1.41	12.5	-0.18	-	0.8	0.8
	Opx	2	-1.25	-	-0.02	0.77 ± 0.29	0.1	0.1

† Determined by TIMS; ‡ determined by XRF (WRs) or EPMA (minerals); $\delta^{44}Ca$ (ε_{Ca}) are based on unspiked Ca isotope measurements of the same aliquot; samples with unmeasured ε_{Ca} have $\delta^{44}Ca$ (ε_{Ca}) corrected to measured minerals from the same rock, taking into account K/Ca.

Table S4.5. (Continued).

		n	δ^{44}Ca (‰)	ε_{Ca}	$\delta^{44}\mathrm{Ca}_{\varepsilon Ca}$ (‰)	$\delta^{44}\mathrm{Ca}_{\varepsilon Ca,\ unmixed}$ (‰)	Ca (wt %)†	Ca (wt%)‡
2044	WR	2	-1.74	14.9	-0.35	-	1.2	1.1
DDM163	WR	-	-	-	-0.08	-	-	-
	Cpx	2	-0.06	-	-0.06	-	13.7	15.1
	Grt	2	-0.01	0.4	-0.01	-	4.4	4.5
	Opx	3	0.00	-	0.00	-	0.6	0.2
	Plag	3	-0.26	-	-0.26	-	5.0	5.0
DDM303	WR	-	-	-	-0.64	-	-	-
	Grt	2	-1.84	2.4	-1.72	-	1.7	1.9
	Opx	2	-0.26	-	-0.14	-	3.2	0.1
	Plag	2	-0.55	-	-0.43	-	3.0	3.2
DDM309	WR	-	-	-	-0.13	-	-	-
	Cpx	2	-0.11	-	-0.11	-	15.0	15.1
	Grt	2	0.31	-0.3	0.31	-	4.5	4.8
	Opx	3	0.00	-	0.00	-	1.1	0.3
	Plag	3	-0.19	-	-0.19	-	6.1	7.2
DDM342	WR	-	-	-	-0.13	-	-	-
	Cpx	2	0.05	-	0.05	-	14.3	16.3
	Grt	2	-0.82	1.8	-0.82	-	5.1	5.9
	Plag	2	-0.13	-	-0.13	-	10.2	10.5
IZ408	Mel	2	-0.06	1.0	-0.06	-	6.4	6.2
	Leuc	2	-0.22	1.4	-0.22	-	1.3	1.3
IV-16-09	WR	2	-0.29	0.9	-0.29	-	5.4	5.1
	Grt	2	0.73	1.5	0.73	-	6.4	4.8
IV-16-19	WR	1	-0.22	1.0	-0.22	-	8.6	
	Grt	2	0.39	0.7	0.39	-	4.3	4.6
	Hbl	2	0.08	-	0.08	-	8.1	8.1
	Plag	2	-0.20	-	-0.20	-	13.2	10.5
IV-16-24	WR	1	-0.97	2.9	-0.79	-	0.6	0.6
	Grt	3	-0.92	2.3	-0.80	-	0.5	0.6
	Kspar	2	-2.26	4.2	-1.83	-	0.6	0.1
14DLB39	WR	-	-	-	-0.08	-	-	-
	Ap	2	-0.61	-	-0.61	-	14.4	39.6
	Cpx	2	-0.20	-	-0.20	-	12.6	11.6
	Grt	2	0.37	1.1	0.37	-	7.2	7.1

† Determined by TIMS; ‡ determined by XRF (WRs) or EPMA (minerals); δ^{44}Ca (ε_{Ca}) are based on unspiked Ca isotope measurements of the same aliquot; samples with unmeasured ε_{Ca} have δ^{44}Ca (ε_{Ca}) corrected to measured minerals from the same rock, taking into account K/Ca.

Table S4.6. Calcium isotope composition of analyzed standards (by TIMS).

	Type	δ^{44}Ca (‰)	2SD (abs)		Type	δ^{44}Ca (‰)	2SD (abs)
SRM915a	WR	-0.85	0.06	**W2A**	WR	0.08	0.04
	WR	-0.93	0.05		WR	-0.05	0.05
	WR	-1.04	0.12		WR	0.14	0.03
	WR	-0.76	0.04		WR	0.04	0.03
	WR	-1.21	0.05		WR	0.07	0.04
	WR	-0.90	0.04		WR	-0.04	0.04
	WR	-0.87	0.03		WR	-0.04	0.05
	WR	-1.08	0.03		**Average**	**0.03**	-
	WR	-1.01	0.04		**2SE**	**0.06**	(n=7)
	WR	-0.92	0.03				
	WR	-0.90	0.05	**DNC-1**	WR	-0.17	0.08
	WR	-1.00	0.02		WR	-0.15	0.03
	WR	-1.05	0.03		WR	-0.15	0.03
	WR	-0.98	0.04		WR	0.09	0.07
	WR	-1.02	0.04		WR	-0.13	0.03
	WR	-0.86	0.05		WR	-0.10	0.04
	Average	**-0.96**	-		WR	-0.05	0.08
	2SE	**0.05**	(n=16)		WR	-0.02	0.08
					Average	**-0.09**	-
Wardsci Dunite	WR	0.92	0.03		**2SE**	**0.06**	(n=8)
	WR	0.98	0.03				
	WR	0.98	0.12				
	WR	1.01	0.05				
	WR	0.81	0.03				
	WR	0.99	0.05				
	WR	0.99	0.05				
	Average	**0.95**	-				
	2SE	**0.05**	(n=7)				

all measurements reported relative to bulk silicate earth (BSE)

Table S4.7. Ca isotope measurements by MC-ICP-MS.

		$\mu^{42/44}$Ca (ppm)	2SE (abs)	$\mu^{43/44}$Ca (ppm)	2SE (abs)	$\mu^{46/44}$Ca (ppm)	2SE (abs)	$\mu^{48/44}$Ca (ppm)	2SE (abs)	Δ^{48}Ca' (ppm)	2SE (abs)	44Ca (V)	n
2030B	Plag	364	48	168	19	-321	54	-655	97	-14	12	25.6	10
	WR	-5	47	-6	22	15	30	24	78	15	14	27	10
2035A	WR	63	54	28	27	52	69	-125	75	9	12	27	10
2035B	WR	-1426	41	-696	18	1440	79	2847	77	198.5	8.3	24	8
DDM303	Grt	840	64	415	32	-820	150	-1580	120	-102	19	10	10
	Opx	68	25	35	11	-35	97	-152	61	-51	16	15	10
	Plag	94	12	43.7	5.6	-120	65	-168	23	21	12	16	10
IV-16-19	Grt	-180	32	-93	17	248	63	330	53	9.4	9	31	10
	Plag	99	37	45	17	-20	110	-124	87	15.4	8.4	29	10
Stillwater	Opx	-430	22	-212.6	8.5	476	26	790	41	29.6	7.5	27	10
	Plag	-71	61	-39	28	73	80	140	110	24.4	8.7	29	10
Exp.	Glass	-134	14	-43	12	180	110	221	36	-15	17	21	3
	Plag	1082	39	541	22	-960	120	-2060	61	-153	15	20	7

All data reported relative to SRM915b; Δ^{48}Ca' is $\mu^{48/44}$Ca deviation (in ppm) from predicted equilibrium value based on measured $\mu^{42/44}$Ca (see main text). All means are weighted by 2SE of individual data.

Table S4.8. Calculated RPFRs (1000lnβ) values, coordination, and Ca-O bond lengths from our DFT calculations, using force-constant and phonon-based† PBE differentials.

		force-constant 1000lnβ (1000 K)	Coord.	Mean Bond-length (Å)	
Diopside	-	1.23	8	2.529	
	Doubled c	1.28	8	2.529	
	Full C2/c cell, 2c	1.31	8	2.529	
Enstatite	Ca:Mg = 1:15	1.72	6	2.3649	*7th Ca-O bond at 2.66Å
	Ca:Mg = 1:15, 2c	1.73	6	2.3649	*7th Ca-O bond at 2.66Å
	Ca:Mg = 1:31, 2c	1.84	6	2.3445	*7th Ca-O bond at 2.67Å
	Ca:Mg = 1:63, quad cell	**1.85**	6	2.343	*7th Ca-O bond at 2.68Å
Forsterite	Ca:Mg = 1:7, M2 sub	1.82	6	2.3314	
	Ca:Mg = 1:15, 2a	2.10	6	2.2975	
	Ca:Mg = 1:31, 2a & c	**2.08**	6	2.3010	
	Ca:Mg = 1:63, 4a & 2c	2.11	6	2.2977	
Garnet	Grossular	1.74	8	2.4288	
	Ca:Mg = 1:11 (pyr)	2.00	8	2.3797	
	Ca:Mg = 1:23 (pyr, FC)	**2.03**	8	2.3784	
	Ca:Fe = 1:11 (alm, FM)	**1.85**	8	2.3876	
	Ca:Mn = 1:11 (sps, FM)	**1.83**	8	2.3999	
Plagioclase	Anorthite	**1.08**	6	2.4608	*7th Ca-O bond at ~2.9-3.0Å
	An50 (v1)	**0.98**	6	2.4871	*7th Ca-O bond at 2.97-3.00Å for all Ca sites
	An50 (v2)	1.03	6	2.4740	*7th Ca-O bond at 2.84Å for half of Ca sites
	An50 (v3)	1.01	6	2.4723	*7th Ca-O bond at 2.92Å for half of Ca sites
Apatite	Fluorapatite	1.21†	6	2.4205	Ca1, *7-10th Ca-O neighbors at 2.84Å; Ca2, 5O+1F, and *7th Ca-O bond at 2.80Å
Lime (CaO)	(CaO]	1.51†	6	2.4158	
Fluorite (CaF_2)	(CaF_2)	1.34†	8	2.3818	

Assumed scale-factor of 1.06 for PBE, †indicates phonon-based estimates.

Table S4.9. Inter-mineral Δ^{44}Ca measurements and temperature-estimates, based on our DFT simulations, excluding samples with negative garnet-mineral Δ^{44}Ca and orthopyroxene-mineral/whole-rock Δ^{44}Ca > ~1‰, along with Ca-in-opx, Fe-Mg, and literature estimates for temperature in the various samples/terranes.

	$\Delta^{44}\mathrm{Ca}_{\mathrm{opx\text{-}fsp}}$	$\Delta^{44}\mathrm{Ca}_{\mathrm{opx\text{-}cpx}}$	$\Delta^{44}\mathrm{Ca}_{\mathrm{opx\text{-}grt}}$	$\Delta^{44}\mathrm{Ca}_{\mathrm{grt\text{-}fsp}}$	$\Delta^{44}\mathrm{Ca}_{\mathrm{grt\text{-}cpx}}$	$\Delta^{44}\mathrm{Ca}_{\mathrm{cpx\text{-}fsp}}$	$\Delta^{44}\mathrm{Ca}_{\mathrm{Ap\text{-}grt}}$	$\Delta^{44}\mathrm{Ca}_{\mathrm{Ap\text{-}cpx}}$
2032I	0.37	-	-	-	-	-	-	-
2033A	0.38	0.36	-	-	-	0.02	-	-
2035B	0.54	-	-	-	-	-	-	-
2038	-	-	-	1.42	-	-	-	-
2040C	-	-	0.16	-	-	-	-	-
DDM163	0.26	0.06	0.01	0.25	0.05	0.20	-	-
DDM309	0.19	0.11	-0.31	0.50	0.42	0.08	-	-
IV-16-19	-	-	-	0.59	-	-	-	-
IV-16-24	-	-	-	1.03	-	-	-	-
14DLB39	-	-	-	-	0.57	-	-0.98	-0.41

	T (Opx-Fsp)	T (Opx-Cpx)	T (Opx-Grt)	T (Grt-Fsp)	T (Grt-Cpx)	T (Cpx-Fsp)	T (Ap-Grt)	T (Ap-Cpx)
2032I	1165	-	-	-	-	-	-	-
2033A	1150	**950**	-	-	-	> 1500	-	-
2035B	1000	-	-	-	-	-	-	-
2038	-	-	-	500-550	-	-	-	-
2040C	-	-	N/A	-	-	-	-	-
DDM163	1450	> 1500	-	> 1400	> 1500	**800**	-	-
DDM309	> 1500	> 1500	500	**850-1100**	**760 -1025**	1350	-	-
IV-16-19	-	-	-	**800-1000**	-	-	-	-
IV-16-24	-	-	-	650-725	-	-	-	-
14DLB39	-	-	-	-	**650-850**	-	**475-650**	< 400

	T (Ca-in-opx)	T (Fe-Mg)	T (est.)		excl. samples	T (Ca-in-opx)	T (Fe-Mg)	T (est.)
2032I	868	-	900		2030B	899	-	900
2033A	879	-	900		2032A	-	-	900
2035B	909	-	900		2035A	961	-	900
2038		-	900		2036A	-	-	900
2040C	635	-	900		2036C	-	-	900
DDM163	817	760-840	-		2036E	-	-	900
DDM309	868	840-880	-		2044	710	-	900
IV-16-19	-	-	1000		DDM303	737	>770	-
IV-16-24	-	-	1020-1050’, > 870[†]		DDM342	-	> 870	-
14DLB39	-	-	700[‡]		IV-16-09	-	-	700-750[†]
					IZ-408	-	-	700-750[†]

Values in bold indicate agreement with other temperature estimates, within ±50°C; temperatures are in °C and Δ^{44}Ca are in ‰; [†]regional estimates from (Redler et al., 2012) based on Fe-Mg exchange thermometry, ‘regional values from Ti-in-zircon (Ewing et al., 2013; Pape et al., 2016), [‡]Fe-Mg estimate from (Weller et al., 2016). Ca-in-opx temperatures are based on [Ca] content of the m2-site and are mainly applicable to ultramafic rocks (Brey and Kohler, 1990). Regional temperature estimates for the location of our samples within the Napier Complex (900°C) are from (Mitchell and Harley, 2017). Temperature uncertainties are discussed in the main text, and are best for Opx-Fsp and Grt-Fsp (± ~50-75°C), intermediate for Opx-Cpx, Grt-Cpx, and Ap-Grt (± ~100°C), worst for Cpx-Fsp (± ~200°C), and unresolvable for Opx-Grt and Ap-Cpx.

Chapter 5

Ca isotopes indicate rapid disequilibrium crystal growth in volcanic and sub-volcanic systems

5.1. Overview

Large discrepancies between absolute crystal ages and (much shorter) time-scales for crystallization and cooling in volcanic systems suggest that volcanic eruptions are commonly triggered by short-lived injections of fresh magma into otherwise rigid crystal mush reservoirs. In turn, this implies that reservoirs with large/geophysically-observable fractions of liquid magma represent short-lived ephemeral states that potentially constitute imminent eruption hazards. Many of the proxies used to constrain cooling histories in magmatic crystals, however, depend on relatively unconstrained assumptions for crystal growth rates, which have been observed to vary by many orders of magnitude in magmatic systems. Similarly, exotic textures such as multiple layers of perpendicularly-oriented crystals growing on wall-rocks ("comb-layers") and around xenoliths ("orbicules") in magma reservoirs/conduits are suggested to result from short episodes of rapid disequilibrium crystal growth, yet rates remain poorly constrained in analogous systems. Here, we exploit disequilibrium Ca isotope fractionations in order to constrain growth rates for phenocryst crystallization and for crystallization of orbicular/comb-layers in sub-volcanic systems. We find that Ca isotopic compositions in a majority of our phenocrystic (and cumulate gabbro) mineral separates ($\delta^{44}Ca_{BSE}$ of -0.47 to +0.50‰) are consistent with equilibrium fractionation and growth rates of < ~1-4 cm/yr. Plagioclase phenocrysts from the 1915 Mt. Lassen rhyodacite eruption, along with orbicule and comb-layers from various locations in Northern California, however, have disequilibrium Ca isotopic compositions (down to $\Delta^{44}Ca$ = -0.3‰) consistent with rapid disequilibrium growth at rates greater than ~6-15 cm/yr. These rates are twenty to fifty times faster than commonly assumed for volcanic phenocrysts in decompressing magmas (up to ~0.3 cm/yr), but consistent with previous estimates for rapid crystal growth (based on plagioclase textures) during orbicule and comb-layer formation by depressurization crystallization in superheated magmas (~ 10cm/yr). In concert with crystal-size distribution (CSD) and maximum crystal-size analyses, our estimates indicate timescales of ~5 to ~30 days for growth of Mt. Lassen plagioclase phenocrysts and one to two months for individual comb and orbicule layers. These results lend weight to a growing body of evidence suggesting that magmatic crystals can form quickly and be stored at cool temperatures for a dominant fraction of their lifetimes. Our Ca isotopic data also suggest that comb-layers generally grow at faster rates than orbicule-rims, potentially due to larger temperature gradients during crystallization. We also present data for plagioclase phenocrysts and glass separates from rapidly-cooled experimental tonalites, confirming that very large disequilibrium Ca isotope effects (greater than ~2‰) can occur in rapidly-cooled silicic magmas, and indicating that increased volatile contents lead to decreasing $\Delta^{44}Ca_{plag-glass}$ fractionation, but not necessarily due to decreased Ca isotopic diffusivity differences (*e.g.* D_{44}/D_{40}). These results imply that Ca isotopes can be used to quantify growth rates in mixed phenocryst populations and understand cooling timescales at various stages of magma crystallization, given the future development of enhanced phenocryst separation or in-situ analysis techniques. Our experimental data suggest that the youngest/smallest phenocryst populations within a sample, which are likely to crystallize rapidly within erupted/degassed lava flows, are likely to preserve the largest disequilibrium Ca isotope signatures.

5.2. Introduction

Understanding the processes and time-scales leading to volcanic eruptions is of great importance to modern society. The nature and frequency of volcanic eruptions depends intimately on the competition between several magmatic processes including magma recharge, volatile exsolution, and crystallization. The eruptibility of a given magma generally depends on temperature, crystallinity, H_2O, and bubble contents (*e.g.* Burgisser and Bergantz, 2011; Gelman et al., 2013; Huber et al., 2012). A large body of work has recently suggested that injection of fresh melts into highly-crystallized sub-volcanic slushes is responsible for re-mobilizing previously formed crystals and triggering volcanic eruptions in a wide-variety of settings (Annen, 2009; Bachmann et al., 2007; Bachmann and Bergantz, 2008; Burgisser and Bergantz, 2011; Cooper and Kent, 2014; Davis et al., 2012; Druitt et al., 2012; Gelman et al., 2013; Huber et al., 2012; Karlstrom et al., 2012; Rubin et al., 2017). The implication of these findings is that sub-volcanic magma bodies spend the majority of their lifetimes in a dominantly crystalline/low-temperature state (*aka* “cold-storage”), which is sporadically interrupted by episodes of magmatic recharge leading to relatively-rapid partial-melting, mobilization, and eruption of mixed-population phenocrystic magmas (*e.g.* Cooper and Kent, 2014; Rubin et al., 2017).

Evidence for this process rests dominantly on the order-of-magnitude differences in absolute ages among phenocrysts and the much shorter amounts of time they are expected to have spent at high temperatures (Cooper, 2006; Cooper and Kent, 2014; Rubin et al., 2017; Schmitt, 2011). The amount of time that crystals spend above their liquidus temperatures can be constrained either by (i) diffusion modeling of trace-element zoning in magmatic crystals (*e.g.* Rubin et al., 2017), or (ii) crystal-size distribution (CSD) analyses coupled with estimates of crystallization rates (*e.g.* Brugger and Hammer, 2010; Cooper and Kent, 2014). These constraints suggest that crystals generally spend less than ~1% of their lifetimes (years to centuries) above liquidus temperatures, in spite of having much longer residence times within sub-volcanic systems (10-100 Kyr). Crystal growth rates in magmatic systems, however, are predicted to vary by over three orders of magnitude (Hammer and Rutherford, 2002; Shea and Hammer, 2013) , which can lead to relatively large uncertainties for estimates requiring crystal growth rates as an input parameter (*e.g.* cooling time-scales and temperature histories from CSD analyses). Additionally, estimates derived from mobile element diffusion profiles, such as Li (*e.g.* Rubin et al., 2017), could potentially be susceptible to cryptic late-stage metamorphic processes caused by fluid circulation at low-temperatures.

Orbicular rocks and comb-layers are thought to form in devolatilizing super-heated magmas during rapid crystallization of minerals onto xenoliths and wall-rocks within magmatic conduits (McCarthy et al., 2016; McCarthy and Müntener, 2017, 2016; Ort, 1992; Vernon, 1985). As such, they represent a connection between sub-volcanic magma chambers and the deeper-seated plutons which feed them. The different layers, which generally have similar mineral proportions and bulk compositions, are thought to form during injection of fresh-magmas into pipe-like conduits, which also serve to remove vestiges of evolving melt that would otherwise lead to compositional variations between the layers (McCarthy and Müntener, 2017). Thus orbicules and comb-layers, similar to tree rings, should preserve information regarding the conditions during various events throughout the lifetime of a given orbicule/magmatic conduit, thereby providing a link to cycles of rejuvenation/eruption in volcanic systems.

Here, we exploit the predicted fractionation between isotopes of calcium during rapid crystal growth (Watkins et al., 2017; Watson and Müller, 2009) in order to independently constrain growth rates in a variety of volcanic and plutonic settings. Compared to other proxies, Ca isotopes provide a unique advantage for addressing growth rates because they are more likely to record primary conditions attending crystal growth and less likely to be affected by post-crystallization processes such as re-heating, metamorphism, and/or diffusional relaxation, due to the low diffusivity of Ca within minerals (*e.g.* Dohmen and Milke, 2010; Grove et al., 1984; Hudgins et al., 2011; Madlakana and Stevens, 2018; Morse, 1984; Smit et al., 2013; Vielzeuf et al., 2007). The isotopic fractionations that generally accompany diffusion in silicate liquids (*e.g.* Richter et al., 2009, 2003, 1999, Watkins et al., 2014, 2011, 2009) should therefore be recorded with higher fidelity by Ca than by elements with higher diffusivities and smaller relative isotopic mass differences (*e.g.* Mg and Fe), making Ca isotopes a potentially useful new tool for investigating initial crystallization histories in magmatic crystal populations.

5.3. Samples and methods

Given that disequilibrium Ca isotopic signatures are predicted to increase with increasing growth rates (relative to Ca diffusivity) (Watkins et al., 2017; Watson and Müller, 2009), we target phenocrystic volcanic rocks from fast-cooled geologically-recent mafic to rhyolitic lava flows, as well as magmatic orbicule and comb-layer samples thought to form during rapid disequilibrium crystallization in sub-volcanic conduits (*e.g.* McCarthy and Müntener, 2017).

5.3.1. Volcanic phenocrysts

We analyze phenocrysts of plagioclase, amphibole, olivine, and clinopyroxene along with matrix materials from four rhyolitic rocks and one basalt. The rhyolitic samples come from recent (< 20 Ka) lava flows in Northern California: a rhyodacite from the 1915 Mt. Lassen eruption (02DLA-1), two samples from the Mono Valley Craters (MLV-6 and 93MLV-49), and one sample from Black Butte (BButte)]. The basaltic sample was collected from Lunar Crater Volcanic Field, Nevada (Lunar Crater). We also analyze orthopyroxene, clinopyroxene, and plagioclase separates from a slowly-crystallized cumulate gabbro (STL-100) in the Stillwater Complex, Montana (see SM for petrologic descriptions and previous work on the samples).

5.3.2. Orbicules and comb-layers

We micro-drilled subsamples from two magmatic orbicules, the larger orbicule sample is a ~10 cm diameter seven-layer dioritic orb collected from Emerald Bay, Sierra Nevada (Echo Lake Granodiorite), from which we cut twenty-two separate mm-size subsections from the edge of the core to the rim of the orbicule, along with two cm-sized samples representing the bulk inner core and outer (inter-orbicule) matrix material. The second analyzed orbicule comes from a silicic Archean pluton at Boogardie Station, Mount Magnet Shire, Western Australia. This orb is slightly smaller (~7 cm diameter), and consists of two major layers surrounding a dioritic core. We analyzed the bulk inner-core, the outer-core, and the two outer orbicule layers (see SM).

We took a different sampling approach by focusing on plagioclase in and around gabbro-dioritic orbicules and comb-layers collected at Fisher Lake, Sierra Nevada. We extracted plagioclase separates from orbicules, comb layers, inter-orbicule matrix, and related host-rocks by mechanical and magnetic separation techniques (*See SM and* McCarthy et al., 2016). The subsamples consist of plagioclase separated from a total of twelve comb-layers, two orbicule cores, three orbicule rims, four inter-orb matrices, and two orbicule host-rocks (country-rocks) in the area (see SM).

5.3.3. Experimental tonalites

Plagioclase and glass were manually-separated from three different simplified tonalite crystallization experiments (NCASH system), performed at ETH-Zurich. The three samples have the same approximate chemical compositions, as well as heating and cooling trajectories, but contain variable amounts of dissolved water (1, 1.5, and 2 wt%, see SM). The initial oxide and hydroxide powders were mixed together, cold-pressed in canisters, and held at 1200°C and 200 MPa for 24 hours before isobarically cooling to 650°C in ~10 minutes, resulting in the crystallization of plagioclase, and then cooled further to atmospheric PT conditions in ~15 hours [more details are available in (Tripoli et al., 2016)].

The two samples with lower H_2O show two distinct populations of phenocrysts (albitic *vs.* anorthitic plagioclase), indicating that they were also partially crystallized during the initial 24 hours (details in SM). However, the various phenocryst populations could not be separated for individual analyses using available methods, and all of our isotopic results represent variable combinations of the different phenocryst populations within our samples.

5.3.4. Ca isotope and chemical measurements

Ca concentrations and isotopic compositions are measured at the University of California, Berkeley, using a Thermofisher Triton thermal-ionization mass spectrometer (TIMS). We start by dissolving the whole-rock and mineral separates in combinations of concentrated hydrofluoric, perchloric, and 6N hydrochloric acid refluxed at 130 C for a minimum duration of one week. We then evaporate the samples to dryness under flowing N_2, check for complete dissolution, and redissolve in 3N nitric acid. We use a ^{42}Ca-^{48}Ca double-spike technique paired with established column chemistry methods [Eichrom DGA resin (Simon et al., 2009)] to monitor isotopic fractionation and to separate Ca from our dissolved samples, respectively. Aliquots of purified Ca (~3 µg) are then loaded onto rhenium filaments, coated with phosphoric acid, heated to a dull red glow, before loading into the mass spectrometer. Several standards (including USGS standards W2a and DNC-1, SRM915a, and an internal dunite standard), which are the same as reported in (Antonelli et al., 2019b), were also measured after being put through the same procedures as our samples. A majority of our data include duplicate analyses with average differences between duplicates of only ~0.06‰ (for Emerald Lake 'OG' samples) and ~0.05‰ (for phenocrystic samples). Taking into account long-term reproducibility on our standards, we conservatively report an average 2SD uncertainty of ~0.1‰. Nevertheless, we suspect our internal reproducibility in a given session is better than ~0.06‰. All of our Ca isotopic data are reported relative to bulk silicate earth (BSE) composition with ^{40}Ca/^{44}Ca = 47.162 at ^{42}Ca/^{44}Ca = 0.31221, but would be shifted by -0.13‰ if using the proposed BSE value of (Antonelli et al., 2018), which still requires further verification before application across the board to all measurements.

Major element compositions for phenocrystic (Table S5.1) and Emerald Bay orbicule minerals were measured by EPMA (Table S5.2), and dissolved aliquots from the Emerald Bay subsections were also analyzed for Fe, Mg, Ca, Na, and K concentrations by ICP-OES at the University of California, Berkeley (See SM, Table S5.3). Whole-rock and plagioclase major-element compositions for several Fisher Lake plagioclase separates come from (McCarthy et al., 2016; McCarthy and Müntener, 2017, 2016).

5.3.5. Crystal-size distribution (CSD) analyses

CSD analyses were performed on four out of five natural phenocrystic samples by slicing large slabs (~10-20 cm) with three perpendicular orientations through the hand-samples and then generating high-resolution images of each slice on a flat-bed scanner. These are also accompanied by CSD analyses of thin-section Ca and Al maps (generated using EPMA, Fig. S5.1), which helps to characterize the smaller-sized phenocryst populations not easily discernable in hand-specimen scans. We use a machine-learning approach called Trainable Weka Segmentation to efficiently mask phenocrysts in the images, and then use the CSDCorrections program to get best-fit estimates for the sizes and shapes of crystals in three dimensions (see SM for details). This method has been successfully applied in several previous studies (*e.g.* Brugger and Hammer, 2010; Cooper and Kent, 2014).

5.4. Results

5.4.1. Ca isotope results

5.4.1.1. Natural and experimental phenocrysts

Our results indicate that plagioclase from volcanic phenocrysts has lighter δ^{44}Ca (-0.41 to -0.24‰) than plagioclase separated from cumulate gabbro (-0.18‰) (Fig. 5.1a). We also find that plagioclase phenocrysts are isotopically lighter than bulk matrix ($\Delta^{44}\mathrm{Ca}_{\mathrm{plag\text{-}mtx}}$, defined $\delta^{44}\mathrm{Ca}_{\mathrm{plag}}$ - $\delta^{44}\mathrm{Ca}_{\mathrm{mtx}}$, ranging from ~0.0 to -0.2‰), whereas mafic minerals (including clinopyroxene, amphibole, and olivine) are isotopically heavier ($\Delta^{44}\mathrm{Ca}_{\mathrm{min\text{-}mtx}}$ ranging from ~0.0 to +0.3‰, Fig. 5.1b), but we do not observe any obvious trends between calcium isotopes and major mineral compositions.

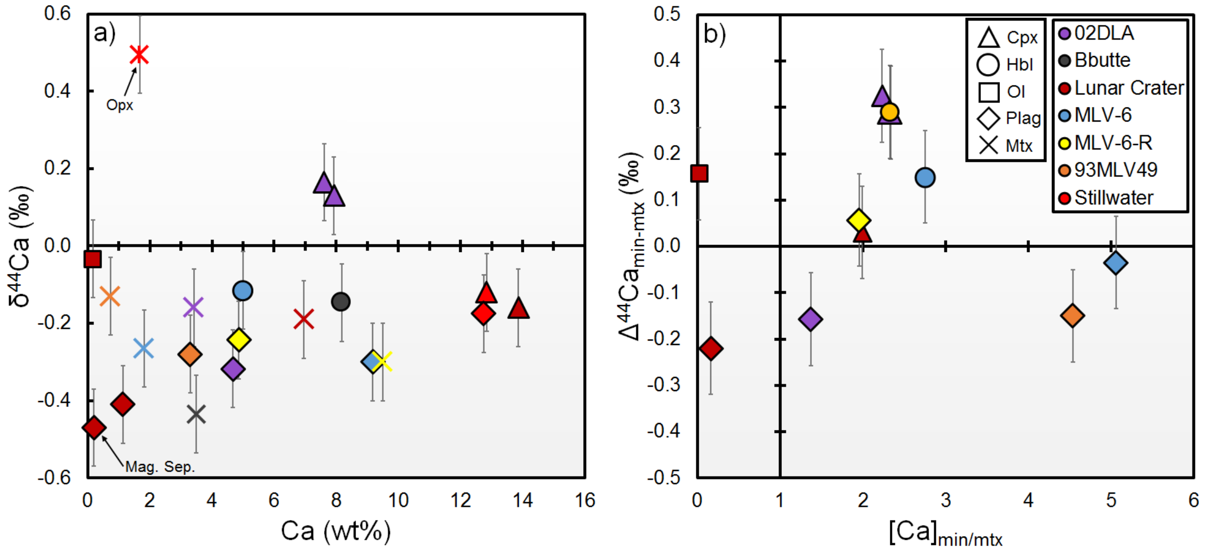

Fig. 5.1. Ca isotope compositions in natural phenocrysts and cumulate samples. In **(a)** we show δ^{44}Ca results for mineral and matrix separates versus measured Ca concentrations (by TIMS) and in **(b)** we show the Ca isotopic differences between minerals and matrix versus the mineral-melt Ca distribution coefficient. Mafic minerals are isotopically heavier than the melt whereas plagioclase is isotopically lighter. Error bars represent long-term 2SD uncertainties on δ^{44}Ca (±0.1‰).

A rough magnetic separation of magnetite grains in our Lunar Crater sample has the same Ca isotopic composition as plagioclase separates, indicating probable contamination by plagioclase inclusions in the magnetite separate. In the cumulate gabbro sample, which was shown to have equilibrium triple-isotope Ca (Δ^{48}Ca') and reasonable Δ^{44}Ca$_{\text{opx-plag}}$ temperatures (Antonelli et al., 2019b), clinopyroxene and orthopyroxene have δ^{44}Ca of -0.12‰ and +0.50‰, respectively (Table S5.4).

By contrast, the experimental plagioclase phenocrysts can have Δ^{44}Ca$_{\text{plag-mtx}}$ as large as ~ -2.2‰, which is an order of magnitude larger than observed in natural samples (Fig. 5.2a,b) which may be related to the high cooling rates/growth rates in the experiments. We find that maximum fractionations are expressed at lower water contents (~1 wt%), whereas increasing water to 1.5 and 2 wt% (plus small amounts of CO_2, see SM) leads to smaller Δ^{44}Ca$_{\text{plag-mtx}}$ fractionations of -1.0‰ and -0.3‰, respectively (Fig. 5.2). Although we are unable to independently estimate the proportion of crystals and isotopic composition of the bulk system, the observation that residual glass gets isotopically heavier as phenocryst populations become isotopically lighter (Fig.5.2a) suggests that the experimental capsules behaved as a closed system (*i.e.*, no diffusion of Ca into or out of the capsules).

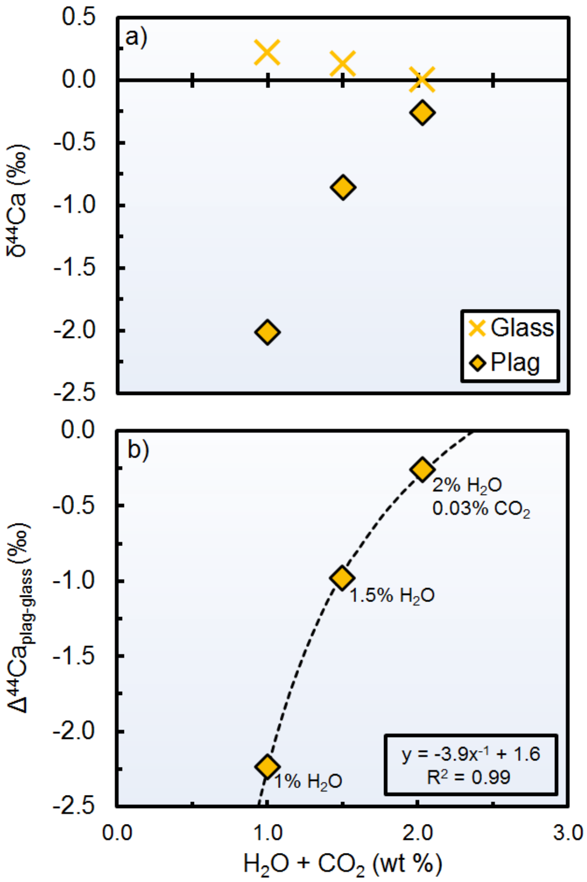

Fig. 5.2. Ca isotopic compositions of glass and plagioclase phenocryst separates versus H_2O + CO_2 contents for tonalite crystallization experiments. **(a)** Anti-correlation between the δ^{44}Ca of glass versus plagioclase. **(b)** Experiments with lower dissolved H_2O yield larger Ca isotopic fractionations. Pressure-temperature-time paths and bulk-compositions (other than volatile contents) are the same for all samples (see SM). Error bars are smaller than the symbols.

The sample with the highest water content (3-1) also has the most homogenous crystal populations (~An_{25}), whereas the other samples have more-strongly bimodal populations of anorthitic plagioclase (~An_{65}) over-grown and surrounded by smaller crystals of albitic (~An_{25}) plagioclase. At present, it is uncertain whether the large disequilibrium effects are caused by the initial crystallization of anorthite at high temperatures or the subsequent growth of albitic plagioclase during rapid cooling, but this may be addressed by mass balance constraints, enhanced separation techniques, and/or development of in-situ techniques in future work.

5.4.1.2. Orbicules and comb-layers

The subsections extracted from orbicule layers (Fig. 5.3a,b) have δ^{44}Ca ranging from 0.0 to -0.5‰, which are generally anti-correlated with Ca concentration differences across layers (Fig. 5.3c). The δ^{44}Ca variations across subsections also tend to be positively correlated with changes in [Fe] and [Mg] (Fig. 5.3d), suggesting a mineralogical control for a majority of the observed isotopic variations, given that ferromagnesian minerals are predicted to be isotopically heavier than plagioclase at equilibrium (Antonelli et al., 2019b).

The bulk isotopic composition of the Emerald Bay inter-orbicule matrix (-0.2‰) is heavier than the core and all the orbicule layers except one (OG-4), which has δ^{44}Ca of ~0.0‰ (Fig. 5.3c, Table S5.5). Compiling the spatial derivatives for δ^{44}Ca, [Ca], [Fe], and [Mg] between adjacent orbicule layers (Fig. S5.3) we are able to identify two regions within the orb where large changes in Ca isotope composition are not accompanied by changes in [Fe] and [Mg] (at the core/comb-layer interface and in 'layer 2', as delineated in Fig. S5.4). This suggests a kinetic control on δ^{44}Ca changes in these layers. The specified regions, however, do not appear to have plagioclase with significantly different anorthite-component (An%), compared to other layers in the orbicule (Fig. S5.4), whereas the orbicule matrix has significantly lower An than the orbicule layers (~An_{49}).

The smaller Archean-aged diorite orbicule from Boogardie Station, Australia was found to have bulk δ^{44}Ca ranging from -0.3 to 0.0‰ across different layers, with lighter values in the amphibole-poor core and heavier values in the amphibole rich comb-layer and outer layer (See SM, Fig. S5), also suggesting a mineralogical control for the δ^{44}Ca variations.

To more effectively exclude isotopic differences caused by variations in mineral abundances, we obtained clean plagioclase separates from orbicule layers, orbicule cores, comb-layers, inter-orb matrices, and host/country rocks obtained from the Fisher Lake pluton (McCarthy et al., 2016) (Fig. 5.4a). We find that plagioclase separates from comb-layers and orb-layers have restricted solid-solution compositions (~An_{87}) that are much higher than in the other samples (An_{55}-An_{85}, Fig. 5.4a), similar to the difference we observe between orb-layers and matrix in our Emerald Bay orbicule.

The separates have a relatively large δ^{44}Ca range (from -0.1 to -0.5‰) with comb-layers and orbicule-rims generally having more negative δ^{44}Ca than host-rocks, inter-orb matrices, and orbicule-cores with similar mineralogies, excluding olivine-norite sample AM-09 (see SM, Fig. 5.4b). We also find that plagioclase separates from comb-layers (grown on wall-rocks) tend to be isotopically lighter than those from orbicule layers grown around xenoliths (by up to ~0.25‰, Fig. 5.4a).

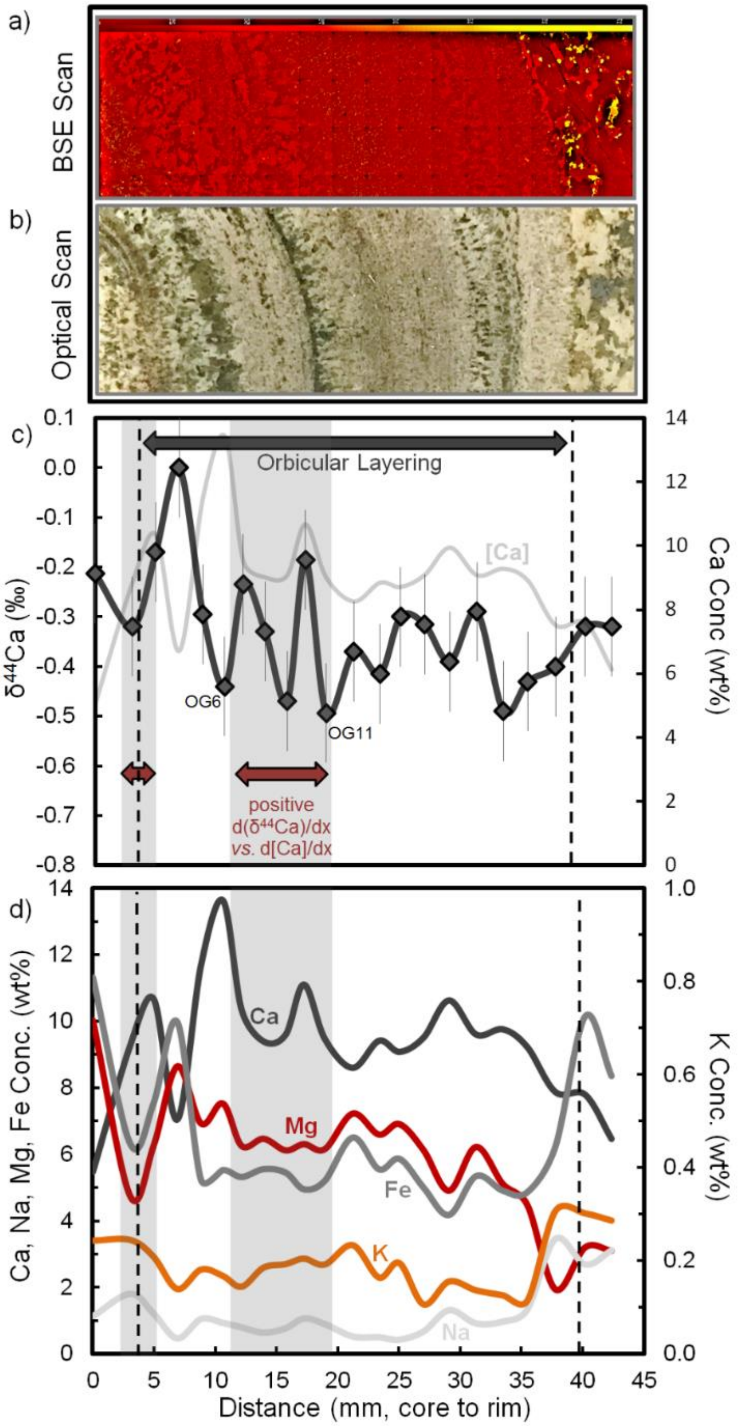

Fig. 5.3. Back-scattered electron and optical maps for Emerald Bay orbicule accompanied by δ^{44}Ca and ICP-OES cation concentrations (Ca, Na, Mg, Fe, and K) from micro-drilled sub-samples across various layers (n=22). Grey bands indicate regions where spatial derivatives for δ^{44}Ca and [Ca] are not anti-correlated, and changes in [Fe] and [Mg] are not correlated with δ^{44}Ca (see Fig. S5.2 and Fig. S5.3).

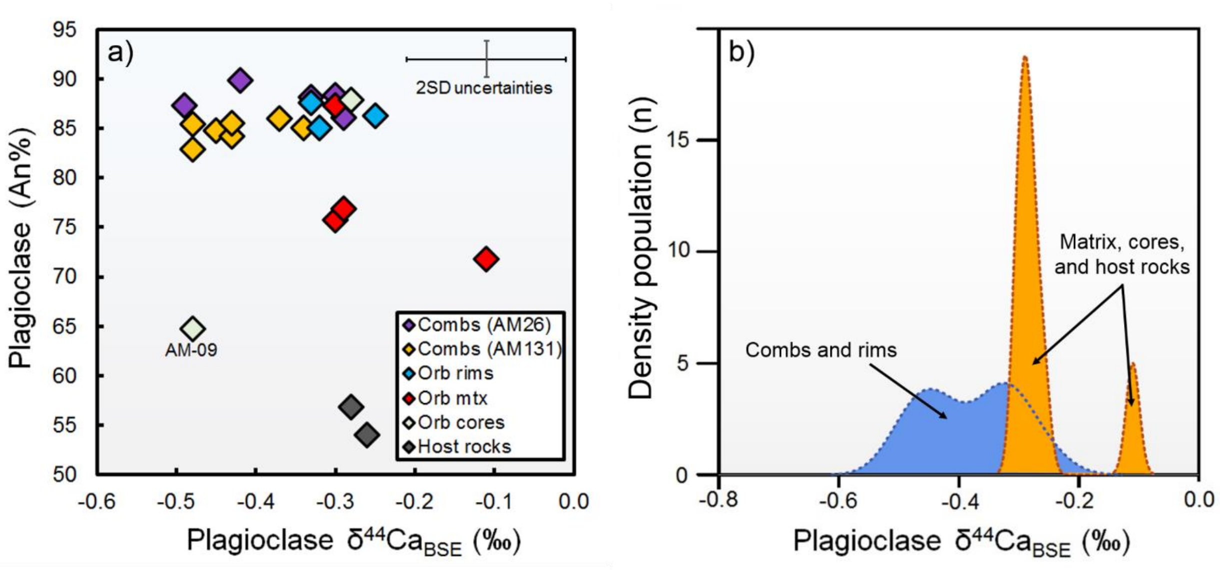

Fig. 5.4. Ca isotopic compositions in plagioclase separates from orbicules, comb-layers, and related rocks. In **(a)** we show plagioclase δ^{44}Ca compositions versus anorthite % of plagioclase separates (calculated from TIMS Ca concentrations). In **(b)** we show the kernel density functions for δ^{44}Ca, demonstrating that comb-layers and orbicule-rims (blue) have lighter plagioclase Ca isotopic compositions than other rock-types from the same location (orange). We exclude orb-core sample AM-09 from **(b)** on the basis that it represents a different primary lithology (olivine-norite, instead of hornblende-gabbro).

5.4.2. Crystal-size distribution results

Applying CSD analyses to our optical scans (Fig. 5.5) and thin-section Ca (and Al) maps (Figs. S5.1 and S5.8) from four of our natural phenocrystic samples (excluding Lunar Crater due to low phenocryst abundance), we find that the phenocryst populations are generally bimodal, with one sample (MLV-6) suggesting three distinct populations of plagioclase (Fig. 5.5d and Fig. S5.8d). The slopes from CSD analyses (left panels in the figures) are generally equal to -1/Rt where R is the growth rate and t is the cooling time-scale (Jerram et al., 2018). The large crystals suggest generally similar slopes from sample to sample, ranging from -5 to -20 (Fig. 5.5), while those for the smaller sized phenocrysts much steeper, ranging from approximately -500 to -1000 (Fig. S5.8) as a likely result of shorter time-scales for growth (with potentially faster growth rates), relative to the larger crystals.

The y-intercepts of CSD analyses are generally proportional to I/R where I is the crystal nucleation rate (*e.g.* Jerram et al., 2018). Intercepts for our larger crystals range from ~5.5 to ~7.5 (right panels in Fig. 5.5), whereas smaller-sized phenocryst populations have higher intercepts, ranging from ~20 to ~25 (Fig. S5.8). Assuming the same growth rates would thus suggest that smaller phenocrysts nucleated faster than larger phenocrysts, which also holds true when comparing the two populations of larger phenocrysts present in MLV-6 (Fig. 5.5d).

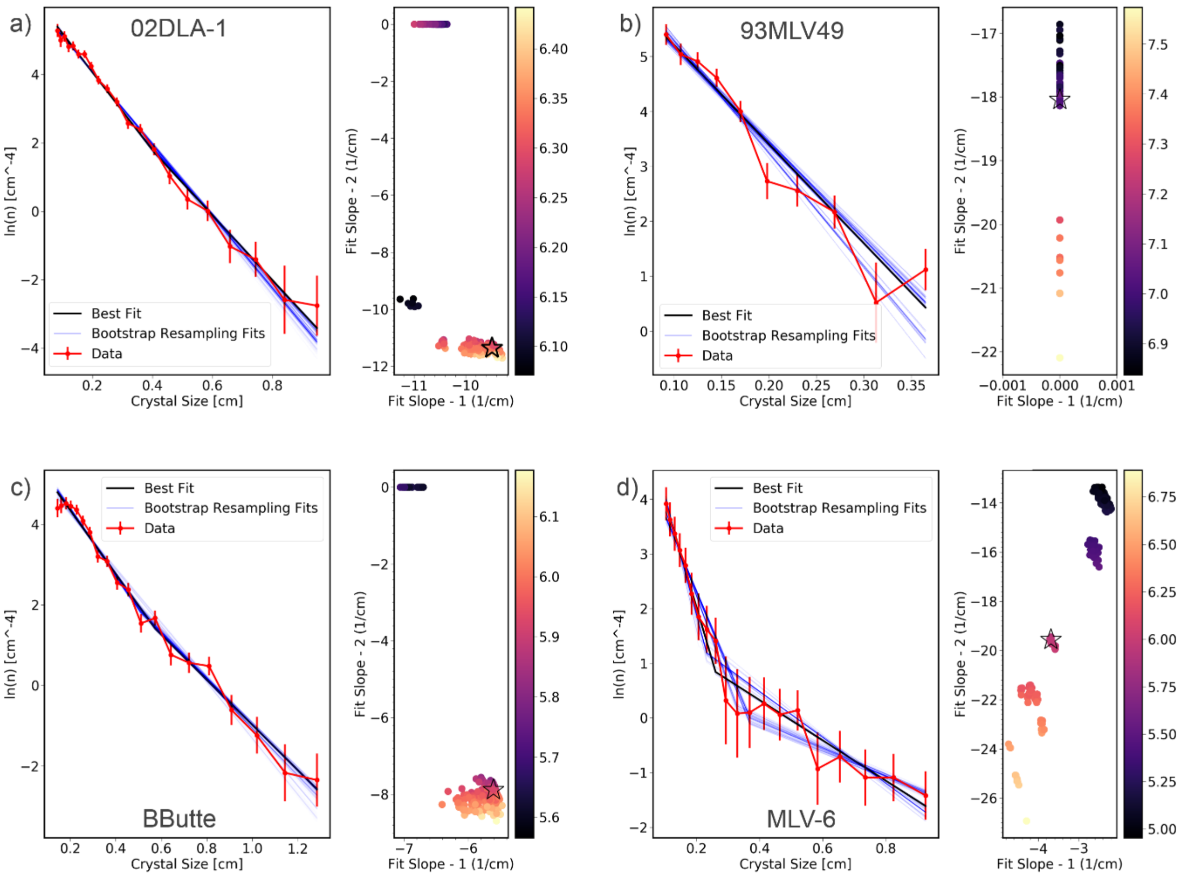

Fig. 5.5. Crystal size-distribution results for phenocrystic plagioclase or amphibole (BButte) in natural samples. The left panel in each figure shows the number density of phenocrysts of each size, whereas the right panel shows best fit slopes (for up to two different slopes) from bootstrap re-sampling methods, with colors depicting y-intercept values for the regressions. Black stars denote best-fit values for slopes. See SM for details and Fig. S5.8 for CSD results from thin-section element maps.

5.5. Discussion

5.5.1. Crystal growth-rate model

CSD analyses provide constraints on the product of growth rate and crystallization timescale for the natural rhyolitic samples. A standard approach to interpreting CSD data is to assume rates for phenocryst growth to obtain constraints on cooling/crystallization time scales (*e.g.* Cooper and Kent, 2014). Our Ca isotope data can provide additional information on crystallization time scales when used in conjunction with our CSD analyses.

Two important questions must be answered before proceeding with growth rate modeling: (i) What are the mineral-melt Δ^{44}Ca values at equilibrium? And (ii), how are the different phenocryst populations in CSD data represented by our mineral separations?

Although few data exist on equilibrium mineral-melt Δ^{44}Ca [partially due to the lack of Mossbauer isotopes (*e.g.* Blanchard et al., 2015; Dauphas et al., 2012) but also due to a lack of experimental constraint], a recent study by (Zhang et al., 2018) suggests that equilibrium clinopyroxene-melt and plagioclase-melt fractionations are very small in a slowly crystallizing basaltic lava lake (0.07

± 0.05 and -0.12 ± 0.06‰, respectively, at 1000 K). Our data suggest that clinopyroxene and plagioclase phenocrysts from Lunar Crater and 02DLA-1 are in approximate Ca isotope equilibrium with each other [based on the $\Delta^{44}Ca_{cpx\text{-}plag}$ thermometer of (Antonelli et al., 2019b) with values tabulated in Table S5.4], where plagioclase is slightly negative and clinopyroxene is slightly positive compared to the matrix. In agreement with (Zhang et al., 2018), and our Ca isotope measurements from a slowly cooled cumulate gabbro (Stillwater Complex, Table S5.4), this suggests that reduced partition function ratios (RPFRs, *e.g.* the affinity for heavy *vs.* light isotopes in a single phase) for both mafic and rhyolitic silicate melts are likely to be intermediate to those of clinopyroxene and plagioclase, and that equilibrium effects between plagioclase and melt are likely to be second-order to potential kinetic effects.

This assertion is also supported by samples where plagioclase and matrix have the same $\delta^{44}Ca$, especially because kinetic deviations during crystal growth are predicted to create increasingly negative $\delta^{44}Ca$ in most plagioclase (as well as in amphibole and clinopyroxene, where Ca is generally compatible (Watson and Müller, 2009). Although no ab-initio predictions have been made for amphiboles due to the complicated crystal structures, measurements of amphibole in this study and in high-T metamorphic rocks (Antonelli et al., 2019b), as well as in granites (Ryu et al., 2011), suggest similar $\delta^{44}Ca$ compositions to clinopyroxene. Thus amphibole, like clinopyroxene, perhaps has a slight enrichment in heavy Ca isotopes relative to melt at equilibrium. As such, amphibole phenocrysts from our various samples (see Fig. 5.1b) are also suggestive of approximate Ca isotope equilibrium during crystal growth.

The phenocryst separates were obtained by crushing in an impact mortar and picking clean grains, which is likely to result in a large bias towards populations of larger phenocrysts. The relative modal proportions of large to small crystals in the different samples varies from ~0.2 (MLV-6) to ~1.1 (02DLA-1) (Table S5.7). Nevertheless, it is likely that a dominant portion of our mineral separates come from the larger crystals and that our growth rate estimates (next section) correspond to populations of phenocrysts visible by stereoscopic microscope.

The model linking Ca isotopic disequilibria to crystal growth rates, schematically depicted in Fig. 5.6 (Watson and Müller, 2009), assumes 1-D steady-state growth conditions with constant dV/dt for growing crystals. Attainment of the predicted steady-state solutions depends on boundary-layer thicknesses relative to the crystal-sizes, with small boundary layers favoring quicker development of steady-state growth conditions. For a BL thickness of 200 μm, crystals require ~1cm of growth before reaching steady state (Watson and Müller, 2009). If steady state was not reached in our samples, this would indicate that the fractionations were not fully expressed, and that our growth rates would serve as minimum estimates.

In general, isotopic fractionation in this model, which assumes no surface kinetic effects (*e.g.* DePaolo, 2011), depends on: (i) crystal growth-rates relative to Ca diffusivity (R/D), (ii) isotopic differences in Ca diffusion coefficients (D_{44}/D_{40}) (iii) mineral-melt Ca distribution coefficients, and (iv) boundary-layer (BL) thicknesses around the growing crystals (Watson and Müller, 2009). Assuming development of steady-state boundary layers during crystal growth, the $\delta^{44}Ca$ deviation from equilibrium ($\Delta^{44}Ca$) derived in (Watson and Müller, 2009) is given by:

$$\Delta^{44}Ca = 10^3\left(1-\frac{D_{40}}{D_{44}}\right)\frac{R\times BL}{D_{40}}(1-K) \qquad \text{(Eq. 5.1)}$$

where D_{40} and D_{44} are the diffusivities of ^{40}Ca and ^{44}Ca in the melt, respectively, R is the crystal growth rate, BL is the boundary layer thickness, and K is the Ca distribution coefficient in the mineral *vs.* the melt. Thicker BLs, higher distribution coefficients, lower Ca diffusivities, and larger differences in isotope-specific diffusivities (D_{44}/D_{40}), lead to lower growth rate estimates for a given degree of isotopic fractionation.

Using our $\Delta^{44}Ca_{min-mtx}$ measurements and conservative estimates for (ii) through (iv), we estimate R/D for the various samples (Fig. 5.7) assuming no equilibrium fractionation between plagioclase and melt, and report growth rates relative to a Ca diffusivity of 10 cm^2/yr. Although Ca diffusivity varies depending on volatile abundances and bulk magma compositions, this diffusivity value is reinforced by several studies of anhydrous diffusion in dacitic liquids at high temperature (*e.g.* ~*1300*°C, Watkins et al., 2014), and by diffusion in hydrous magmas at lower temperatures, where H_2O increases diffusivity but decreasing temperature serves to counter-act this effect. The value is also in accordance with Ca diffusivities in dry mafic silicate liquids at ~1250°C (Hofmann and Magaritz, 1977), or at ~800°C, when enhanced by 2.5 orders of magnitude due to the presence of water (Watson, 1981).

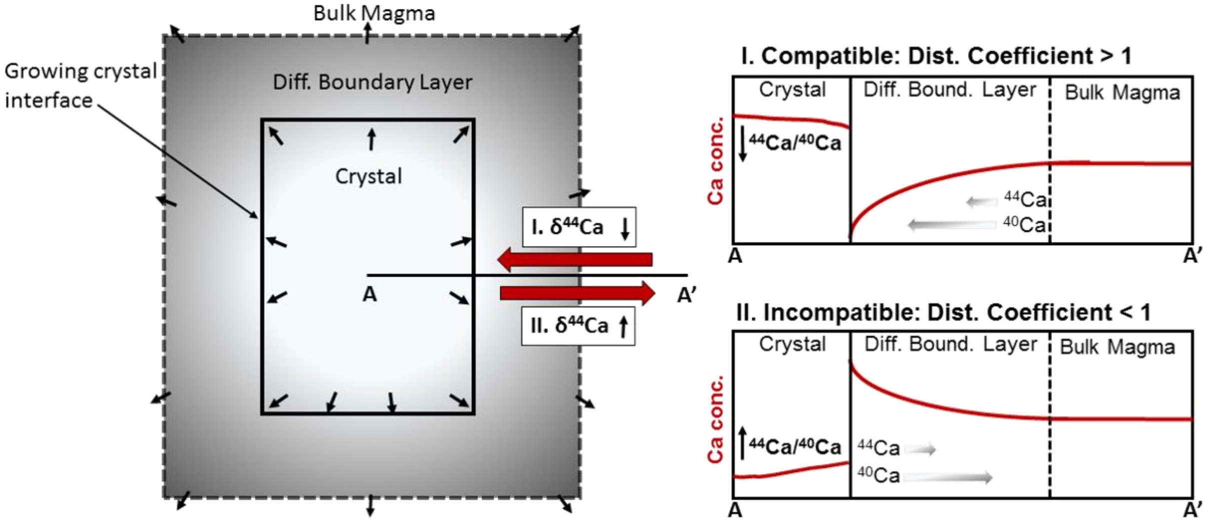

Fig. 5.6. Conceptual diagram for disequilibrium Ca isotope fractionation during rapid crystal growth, as described in (Watson and Müller, 2009). The kinetic effects are the result of isotopic rate differences for Ca diffusion through a chemically-distinct boundary-layer developed around growing crystals. For minerals where Ca is compatible (*e.g.* plagioclase, clinopyroxene, amphibole) faster growth leads to increasingly negative deviations from isotopic equilibrium (top right panel), whereas the opposite is true for minerals where Ca is strongly incompatible (*e.g.* olivine, bottom right panel).

Out of the relevant parameters, average mineral-melt Ca distribution coefficients are the easiest to measure. This was accomplished by analyzing the ratio of Ca concentrations in mineral separates *vs.* bulk matrix/glass by TIMS (chosen instead of EPMA values, to better account for potential effects of impurities/mixed-populations in our mineral separations). Ca diffusivities and D_{44}/D_{40} are also well-constrained from high-T diffusion experiments in silicate liquids of various composition (Richter et al., 2009, 2003, 1999, Watkins et al., 2014, 2011, 2009).

Ca isotopic fractionation during diffusion through silicate liquids (*e.g.* D_{44}/D_{40}) is observed to increase with increasing magma viscosities [*e.g.* magma $SiO_2 + Al_2O_3$], but can also depends on the direction of Ca diffusion with respect to other components (*e.g.* Watkins et al., 2014), temperature gradients across liquids (*e.g.* Huang et al., 2010; Richter et al., 2009), and the isotopic compositions themselves [*e.g.* 'isotopic self-diffusion' (Watkins et al., 2014)]. Due to the associated complexities, we save the incorporation of these additional effects for future work.

The effects of volatiles on Ca isotope fractionation during diffusion in silicate liquids also remain relatively unconstrained. All else being equal, greater isotopic fractionation during crystal growth results from higher values for R/D. Our experimental samples with lower H_2O contents and greater Δ^{44}Ca (Fig. 5.2), therefore, may have had higher R/D during crystallization. This implies that either (i) Ca diffusivities decrease, or that (ii) crystal growth rates increase with decreasing H_2O. Given the general relationships between element diffusivity and volatile contents, the former interpretation is more likely.

Without further constraints on isotopic composition of the bulk-system, modal percentages of glass and phenocrysts, and/or CSD analyses (which would give us crystal growth-rates from the known cooling timescales), however, it is hard to determine whether volatiles affected isotopic diffusivity ratios (D_{44}/D_{40}) on top of affecting Ca diffusivity. Differences in boundary-layer thicknesses with increasing H_2O could also contribute to the observed Δ^{44}Ca variability, with larger boundary layers generally favored by higher viscosities (and increasingly static conditions) (Watson and Müller, 2009).

Taken at face value, however, a $D_{44}/D_{40} > 0.995$ (*e.g.* closer to unity) would require unreasonably large growth rates for most of our samples (including the experimental samples, which probably grew at rates ~50 cm/yr, given the time-scales for heating and cooling and assuming an average crystal size of ~1 mm). The approximate growth-rate in the experimental samples is nicely reproduced, however, assuming a D_{44}/D_{40} of 0.980, in accordance with anhydrous diffusion experiments with ~90wt% $SiO_2 + Al_2O_3$ (Watkins et al., 2017), but with slightly larger boundary layers (150-200 μm) than shown in Fig. 5.7a. Although ~100 μm is suggested as a maximum BL limit in most natural dynamic systems (Lu et al., 1995), these boundary layer values are not unreasonable given the high viscosities and probable lack of fluid dynamic processes within the experimental capsules. This observation may hint that H_2O does not greatly change D_{44}/D_{40}, despite increasing overall Ca diffusivities, which has also recently been concluded for Li isotope diffusion in wet silicic melts (Holycross et al., 2018) *vs.* dry silicic melts (Richter et al., 2003).

Therefore, we estimate D_{44}/D_{40} from anhydrous high-T diffusion experiments (Watkins et al., 2017), where fractionation factors decrease from ~0.996 to ~0.980 along a trend of increasing magma $SiO_2 + Al_2O_3$ (from ~50 to ~90 wt%). The experimental samples, natural rhyolitic samples, large orbicule from Emerald Bay, and plagioclase separates from Fisher Lake orbicular (and related) samples, have measured host-matrix $SiO_2 + Al_2O_3$ of ~88, ~86, ~71, and ~61 wt%, respectively (Table S5.1, shown in Fig. S5.6). These imply D_{44}/D_{40} values of ~0.981, ~0.991, and ~0.994 for our rhyolitic, Fisher Lake, and Emerald Bay samples, respectively. Given the uncertainties, however, we use D_{44}/D_{40} of 0.980 for our phenocrystic samples (excluding Lunar Crater) and 0.990 for our orbicule and comb-layer samples, but show the effects of higher D_{44}/D_{40} (relevant to diffusion in basaltic liquids) in Fig. S5.7 for comparison.

5.5.2. Crystal growth-rate estimates

Including only the orbicule sub-sections where mineralogical controls on δ^{44}Ca can be excluded (grey bands in Fig. 5.3, bold values in Table S5.5), we generally find that our orbicule and comb-layer samples suggest faster growth rates than our phenocrysts (Fig. 5.7, Table S5.8), with speeds up to ~25 cm/yr (minimum values of ~6 to ~15 cm/yr, taking into account the lower limits of our 2SE uncertainties on the averages). Given that our plagioclase separates may also contain late-stage interstitial plagioclase (grown closer to equilibrium), it is likely that the disequilibrium $\Delta^{44}Ca_{plag\text{-}mtx}$ signatures we measure are minimum values for fast-grown plagioclase within the samples. The minimum rate required to generate measurable $\delta^{44}Ca$ effects in rhyolites, assuming a distribution coefficient of ~1.5, is about 4 cm/yr, which decreases to 1 cm/yr for minerals with distribution coefficients higher than ~4.

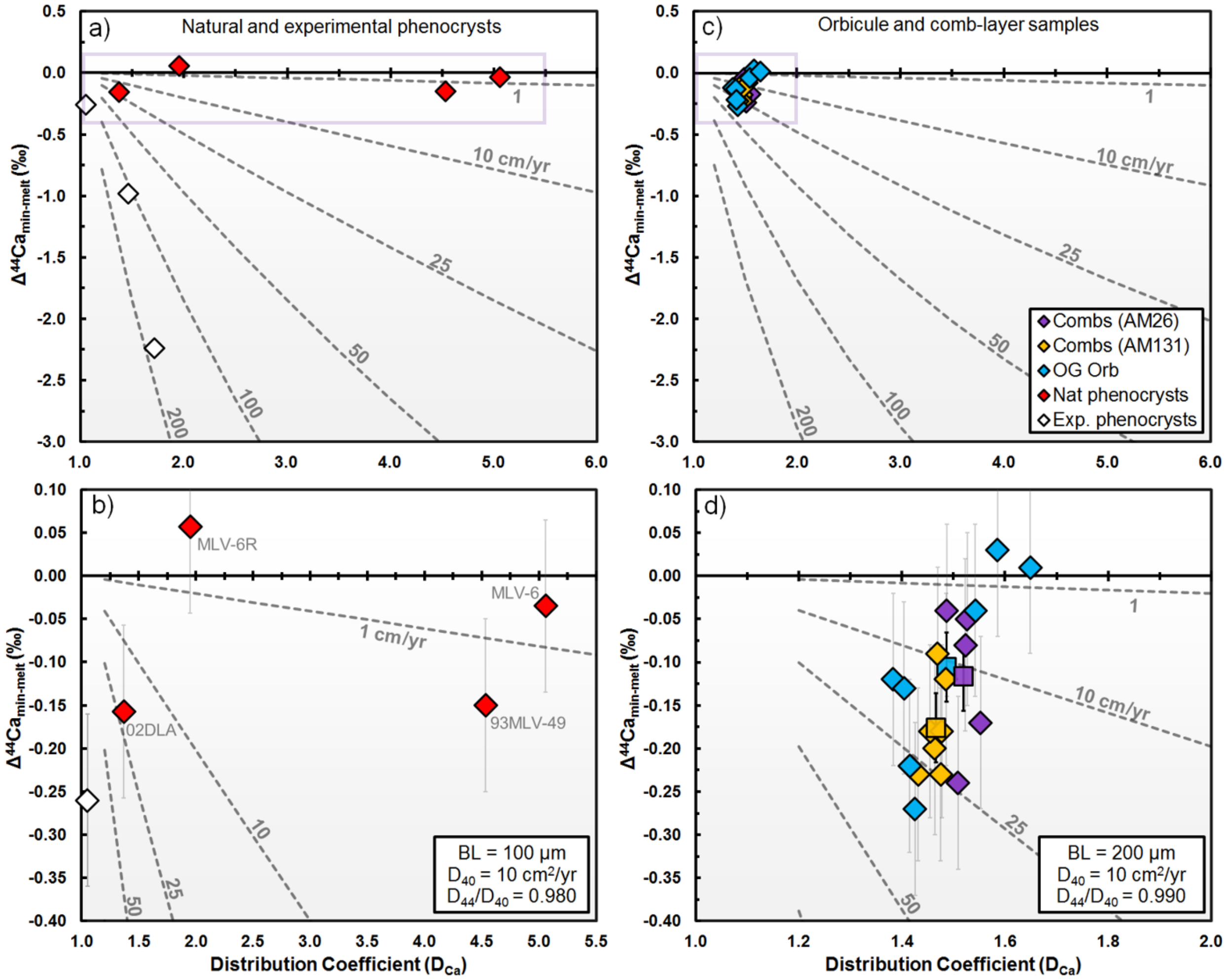

Fig. 5.7. Sample-matrix $\Delta^{44}Ca$ *vs.* Ca distribution coefficients for analyzed plagioclase separates from **(a,b)** natural and experimental phenocryst samples along with **(c,d)** separates from orbicule and comb-layer samples (Emerald Bay and Fisher Lake) with dashed contours representing predictions for various crystal growth rates, based on the model of (Watson and Müller, 2009). In **(a,b)**, we use D_{44}/D_{40} = 0.980, and boundary-layer (BL) thickness of 100 μm (suggested as maximum values in dynamic systems by (Lu et al., 1995), although boundary layers in experimental phenocrysts may be slightly larger (up to ~200 μm). In **(c,d)**, D_{44}/D_{40} = 0.990, equivalent to silicate liquids with SiO_2 + Al_2O_3 = ~65 wt%, and we use larger BL sizes of 200 μm (to account for the larger crystals). Rate estimates are directly proportional to BL thicknesses, thus ½ a given BL thicknesses would lead to double the required growth rate. Regions delineated by purple squares in (a) and (c) correspond to the axis limits for panels (b) and (d), respectively. The distribution coefficients for Emerald Bay orbicule samples (OG samples) are for the bulk sub-sections relative to orbicule matrix. Average values and 2SE for AM26, AM131, and OG sample (Emerald Bay) are represented by colored squares with bold error bars in panel (d).

Two of our plagioclase phenocrysts cannot be distinguished from their matrix materials, thus indicating growth rates of less than ~4 and ~1 cm/yr (MLV-6R and MLV-6, respectively). One sample (93MLV-49) shows a small yet resolvable δ^{44}Ca difference suggesting minimum growth rates ~0.7 cm/yr, and one sample (02DLA-1) suggests rapid plagioclase growth rates (minimum of ~7 cm/yr) (Fig. 5.7b).

Our clinopyroxene and amphibole samples (not shown in Fig. 5.7) are likely to be at mineral-melt equilibrium, thereby suggesting growth rates less than ~4 cm/yr. Our single olivine sample has lower δ^{44}Ca than would be predicted by equilibrium at relevant temperatures (Antonelli et al., 2019b), yet fast-growth is modeled to lead to to positive disequilibrium fractionations, due to the highly incompatible nature of Ca in olivine (see Fig. 5.6). This observation is difficult to explain if the olivine separate is not contaminated by Ca from plagioclase or clinopyroxene. Given a clean separation, the low values could potentially be due to surface-kinetic effects during olivine growth (*e.g.* DePaolo, 2011), but it is more likely that the olivine separates weren't completely pure.

Comparing our estimates to previous work, we find that our slowest growth rates (for plagioclase in MLV-6 and MLV-6R, along with clinopyroxene in 02DLA-1 and amphiboles in BButte and MLV-6) are generally consistent with previous estimates for decompressing magmas (~0.3 cm/yr) (*e.g.* Brugger and Hammer, 2010; Cooper and Kent, 2014). Plagioclase phenocrysts with δ^{44}Ca resolvable from their matrix (93MLV-49 and 02DLA-1), however, suggest rates ~2 and ~20 times faster than commonly assumed for phenocryst growth, respectively. These values are high but not unreasonable, given the high crystallization rates observed in supercooled experimental magmas (Shea and Hammer, 2013), upon which previous growth-rate estimates in orbicules and comb-layers (~10 cm/yr) were based (McCarthy and Müntener, 2016). These growth rates compare quite favorably to our estimates and support the combination of parameters used in Fig. 5.7c,d.

Although our BL values (~200 um) for the orbicule models are larger than suggested for dynamic silicate systems (Lu et al., 1995), maximum BL sizes in static/viscous systems can equal up to half of a crystal's diameter (Kerr, 1995). Given that some of our natural phenocrysts can range up to ~0.6 cm, and orbicule diameters are much larger, the BL thickness we use in Fig. 5.7c,d is only slightly conservative. All else being equal, BL thickness is directly proportional to isotopic fractionation, such that a 20 μm BL would require growth rates ten times faster than a 200 μm BL. Our estimates, therefore, can generally be taken as lower limits for crystal growth rates in the various samples, but variability caused by different BL thicknesses and chemical compositions (*e.g.* lower Al_2O_3 relative to bulk melt) requires further exploration.

5.5.3. Crystallization time scales

Combining our crystal growth-rate estimates for plagioclase in 02DLA-1 and 93MLV-49 (minimum growth rates of 7 cm/yr and 0.7cm/yr, respectively) with the slopes from our CSD analyses, we find that plagioclase phenocrysts in these samples are likely to have grown in ~5 days and ~29 days, respectively (Table S5.8). Given that there is likely to be a significant contribution from smaller-sized phenocryst populations, this represents an average value for the different populations. Previous work on Mt. Lassen samples indicate that plagioclase microphenocrysts and microlites were likely to have grown much faster (during magmatic rejuvenation) than the larger phenocrysts which were pre-existing (Salisbury et al., 2008). The Deadman's Dome sample (93MLV-49) comes from a ~650 year old lava flow with zircons (up to 200 Ka) that are estimated to have spent less than 1 Kyr above ~800°C. Our data suggest that rejuvenation of the magmatic system, which spent most of its lifetime at low temperatures, could have led to the rapid disequilibrium growth of plagioclase for a period of ~1 month, during supercooling of the injected magmas.

For the orbicule and comb-layer samples (with minimum growth rates ranging from 6-15 cm/yr) we could not apply CSD analyses, but based on the sizes of the largest comb-layers (up to ~1 cm) this suggests growth timescales on the order of 20-50 days. Performing a similarly simple estimate based on the maximum crystal sizes in our natural phenocryst samples leads to time scales 2-6 times longer than when using more-accurate CSD slopes (Table S5.8).

For samples with growth rates too small to cause Ca isotopic disequilibrium (such as Black Butte and MLV-6), we make the common assumption of 0.3 cm/yr for growth rates (*e.g.* Brugger and Hammer, 2010; Cooper and Kent, 2014). We find that the amphibole phenocrysts in BButte yield a time-scale of ~200 days, while the two distinct populations of plagioclase phenocrysts in MLV-6 yield ~330 days and ~60 days for the larger and smaller crystals, respectively (assuming the same growth rate). In the Mt. Lassen sample (02DLA-1) clinopyroxene in approximate Ca isotopic equilibrium with melt suggests timescales of ~40 to ~90 days for crystallization (at 0.3 cm/yr, Table S5.8), in agreement with previous CSD work on plagioclase (Salisbury et al., 2008).

The populations of very small phenocrysts analyzed from thin section element maps (Fig. S5.8) give much shorter time scales for growth, ranging from ~5 hours for plagioclase microlites in 02DLA to ~3 days for microlites in MLV-6, assuming the same growth rates as used for the larger crystals, which likely indicates that they formed during rapid cooling within lava flows. Our experimental data suggest that these tpyes of phenocrysts may contain some of the strongest disequilibrium Ca isotopic signatures, but unfortunately they cannot be separated from other crystals using current methods.

5.5.4. Comments on magmatic orbicule and comb-layer formation

Since their first descriptions in the late 1700’s, a wide variety of mechanisms (*e.g.* Liesgang banding, magma mixing and immiscibility, metamorphism/metasomatism, and fluid-flow processes at the edges of cooling plutons) have been proposed for the formation of orbicular textures in magmatic rocks (Leveson, 1966; Moore and Lockwood, 1973; Poldervaart and Taubeneck, 1959; Sederholm, 1928). More recent work, however, suggests that comb-layers and common orbicule types (*e.g.* without oscillatory mineral zoning) form first by super-heating of rapidly rising magmas in melt-conduits [which serves to eliminate crystal condensation nuclei (Vernon, 1985)], followed by rapid crystallization around xenoliths and along wall-rocks during magmatic degassing [*e.g.* ‘decompression crystallization’ above ~2 kbar, (McCarthy and Müntener, 2016)].

The lack of igneous differentiation trends and more evolved rocks in most localities suggest that evolved melt is efficiently removed from the system, either by continuous ascent of melt or the injection of new pulses of fresh magma, allowing for crystallization of new orbicule-rims and comb-layers with compositions similar to preceding layers (McCarthy and Müntener, 2017). Higher anorthite contents in plagioclase comb-layers/orbicule-layers compared to orbicule matrix, cores, and country rocks (see Fig. 5.4a), also observed in previous studies (McCarthy and Müntener, 2016), suggest that orbicule and comb-layer formation occur at higher pressures/H_2O contents, most likely during the initial stages of magmatic degassing, while final crystallization of inter-orbicule cumulate matrix occurs at lower pressures/H_2O contents (*e.g.* McCarthy and Müntener, 2017).

The minimum growth rate estimates we obtain from this study, ranging from ~6 to ~15 cm/yr are in agreement with previous estimates for Fisher Lake orbicules and comb-layers [~10 cm/yr, (McCarthy and Müntener, 2016)], which were based on experimental relationships between degree of undercooling and plagioclase textures (Shea and Hammer, 2013). Therefore, our Ca isotopic constraints lend weight to recent orbicule and comb-layer formation models involving rapid crystallization (McCarthy et al., 2016; McCarthy and Müntener, 2017, 2016; Ort, 1992; Vernon, 1985). These suggest that orbicule-layers and comb layers generally grow in time-periods of one to two months, which implies similar time-scales for associated cycles of rejuvenation and crystallization caused by injection of fresh magma into sub-volcanic systems.

Our Ca isotope constraints, however, provide the additional insight that orbicule rims are likely to grow at slower rates than associated comb-layers, which may be a manifestation of larger temperature differences between the wall-rocks and crystallizing magmas (*e.g.* greater degrees of undercooling compared to the xenoliths, which may crystallize near-isothermally) or could alternatively suggest (i) relatively smaller boundary layers or (ii) relatively smaller isotopic diffusivity differences (D_{44}/D_{40}) for orbicules *vs.* comb-layers. Given that the layer sizes and magmatic compositions are similar for the orbicules and combs, our results are most consistent with faster growth rates (relative to diffusion rates) for comb-layers *vs.* orbicules, potentially as a result of larger temperature differences between wall-rocks and magmas within the conduits.

5.6. Conclusions

We show that significant disequilibrium Ca isotope effects can occur during growth of experimental and natural phenocrysts, orbicular-rocks, and comb-layers, in accordance with the predictions of (Watson and Müller, 2009). Very large Δ^{44}Ca effects (> 2‰) are possible in highly-viscous experimental melts with fast cooling-rates, which are observed to decrease with increasing H_2O abundances as a probable manifestation of increasing Ca diffusivities in the magma. This hypothesis, however, requires further confirmation (*e.g.* using CSD analyses and X-ray maps) in order to exclude potential H_2O-induced decreases in BL thickness or changes in isotopic fractionation factors (D_{44}/D_{40}) as causes for the observed Δ^{44}Ca variations. Rough estimates of the experimental crystal sizes and time-scales may indicate that H_2O does not have a large effect on the isotopic diffusivity ratio of Ca (D_{44}/D_{40}), in agreement with recent observations for Li diffusion in wet *vs.* dry rhyolitic magmas (Holycross et al., 2018).

Although the effects of volatiles on Ca isotope fractionation still remain poorly quantified, using reasonable estimates for the various parameters we show that crystal growth rates during formation of comb-layers and orbicule-layers are generally greater than 6-14 cm/yr, implying timescales of one to two months for the formation of individual layers. A majority of volcanic phenocrysts in our data-set suggest slower growth rates (< 1-4 cm/yr) at Ca isotopic equilibrium, but plagioclase phenocrysts from the 1915 Mt. Lassen rhyodacite eruption and the ~650 year old Deadman's Dome eruption have measurable disequilibrium $\Delta^{44}Ca_{plag-matrix}$ compositions consistent with minimum growth rates of ~7 and 0.7 cm/yr, respectively. In combination with CSD analyses, these growth rates imply time-scales of ~5 days and ~29 days for phenocryst crystallization in these systems. Although the absolute ages of our phenocrysts are not currently known, the calculated time-scales are almost certain to represent less than 1% of the absolute crystal ages, adding to a growing body of evidence that suggests volcanic phenocrysts are formed quickly and stored at relatively cold temperatures for extended periods of time prior to re-activation and volcanic eruption triggered by the injection of fresh magma into sub-volcanic systems.

5.7. Supplementary information

5.7.1. Sample descriptions and previous work

5.7.1.1. Volcanic and cumulate samples

Mt. Lassen (1915 eruption, 02DLA-1): Sample 02DLA-1 was collected from the 1915 dacite flow at the summit of Mt. Lassen, CA from a flow approximately 10-25 meters thick. The sample contains large (~0.6 cm) plagioclase phenocrysts, slightly smaller rounded clinopyroxene phenocrysts, Fe-oxides, and plagioclase microlites contained within a rhyodacitic matrix. Clinopyroxene can contain small inclusions of apatite and aluminosilicates. Modal phenocryst and microlite abundances are tabulated in Table S5.7 and an EPMA Ca map (of a 1-mm section) is available in Fig. S5.1a. Chemical compositions (measured by EPMA) for the major minerals and matrix in our volcanic samples are shown in Table S5.1. Samples from the same 1915 Mt. Lassen flow find the same ~three plagioclase populations and CSD characteristics as we do (Salisbury et al., 2008), concluding that the largest were pre-existing, while the medium-sized (micro-phenocrysts) and smallest phenocrysts (microlites) grew rapidly (based on textural evidence, *e.g.* swallowtail, acicular, and skeletal textures) during injection of new mafic magma into the Mt. Lassen magma chamber (which was likely to be significantly crystallized prior to rejuvenation). Seismic activity indicating rejuvenation of magmatic processes (*e.g.* intermittent steam blasts and formation of ~350m wide summit crater) began happening ~1 year prior to the eruption (Clynne, 1999), suggesting a maximum duration for growth of micro-phenocrysts and microlites (Salisbury et al., 2008) within the erupted lavas.

Mono Craters (93MLV-49 and MLV-6): Sample MLV-6 was collected from the southwest edge of the oldest rhyolite/rhyodacite flow in the Mono Craters chain (Long Valley, CA), which is ~50-100 m thick and has a best age estimate ~16 Ka [ref]. The sample consists of large irregular clinopyroxene phenocrysts, large plagioclase phenocrysts with high An cores ('plag-1' in Fig. S5.1e), smaller plagioclase microlites ('plag-2'), and abundant Fe-oxides, hosted within a rhyodacitic matrix.

Sample 93MLV-49 is from Deadman Dome (one of the Inyo domes), along the northwest caldera ring fault at Long Valley. The section is also ~50-100 m thick. Most zircon U-Th ages cluster around ~200 Ka, but the lava was only erupted ~650 years ago (Reid et al., 1997), implying long time-scales at temperatures below ~800°C (at which zircon dissolves fairly rapidly), and a maximum periods of ~1 Kyr at temperatures > 815°C, prior to eruption (Reid et al., 1997). The sample consists of very-fine grained/glassy rhyodacitic matrix hosting large plagioclase phenocrysts and microlites, along with euhedral to subhedral amphibole phenocrysts and smaller elongated amphibole microlites (Fig. S5.1b).

Black Butte: The Black Butte sample is from the southeast side of Black Butte (~10 km southwest of Mt. Shasta) and is the same sample analyzed in (Getty and Deaolo, 1995), from the quarry on the south side of black butte, ~0.7 km north of Siskiyom County Dump. Black Butte represents a series of overlapping dacite domes and flows on the west side of Mt Shasta (~600m tall). The lavas were erupted at about 10 Ka (Miller, 1978). It is hard to tell exactly how thick any one flow might be, but they are likely to be ~100 m. The sample is a hornblende andesite consisting of large hornblende phenocrysts, small plagioclase micro-phenocrysts and microlites, small Fe-oxides, and rare apatite grains (Fig. S5.1c) hosted in a rhyodacitic matrix. Samples for the area have been recently studied (McCanta et al., 2007), where they constrained (compositionally-uniform) plagioclase growth to maximum rates of 2.5×10^{-8} mm/s (equivalent to ~0.1 cm/yr) were estimated from the size of amphibole symplectite rims, assuming a depth for amphibole breakdown and ascent rate for the magma (McCanta et al., 2007).

Lunar Crater, NV: Our Lunar Crater sample was collected from the Lunar Crater Volcanic Field, National Monument, NV. The formations in the area (central Nevada), includes cinder cones, lava flows, elongated fissures, ash hills, and a ~130m volcanic crater (aka. Lunar Crater). The Lunar Crater flow (aa-type) from which our sample was collected is a more fluid alkali basalt with a flow thickness ~10m. The sample consists of large clinopyroxene phenocrysts with lower-Ca cores, along with smaller olivine grains with high-Fe rims, abundant plagioclase phenocrysts and microlites, and fine-grained Fe-oxides, hosted in a basaltic matrix (Fig. S5.1d). The flow from which our sample was collected likely represents “episode 4” magmatism with ages between ~35 to ~270 Ka (Valentine et al., 2017). Magmatism in the area is thought to result from rise of aesthenospheric mantle during basin-and-range extension, variably contaminated by continental crust and incorporating variable mantle compositions (*e.g.* HIMU *etc*.) (Valentine et al., 2017).

Stillwater Complex, MT: Our Stillwater sample was collected from the Stillwater Complex, MT, and was also studied by (DePaolo and Wasserburg, 1979), where it was denoted ‘STL-100’. The sample consists of equant 1-3 mm euhedral to subhedral orthopyroxene, clinopyroxene, and plagioclase grains with a strong cumulate texture. The age of the complex is ~2.7 Ga, and indicates slight contamination by ancient crustal materials ($\varepsilon_{Nd} = -3$) (DePaolo and Wasserburg, 1979). The complex consists of a lower section with layered cumulate ultramafic rocks (dunites, peridotites, and pyroxenites) and an upper part of layered mafic rocks (including gabbro, norite, anorthosite, and troctolite). The intrusion represents a large volume of mafic/ultramafic magma emplaced into the crust and fractionally crystallized over a period of ~ 100 Kyr (DePaolo and Wasserburg, 1979, *and references therein*).

5.7.1.2. Experimental tonalites (3-10, 3-9, and 3-1)

The three analyzed experimental samples come from tonalite crystallization experiments performed by B. Tripoli at ETH-Zurich for a PhD project regarding seismic detection of crystallization and bubble-growth in magmas (Tripoli et al., 2016). The samples were created by mixing oxide-powders, cold-pressing the resulting mixture in canisters, and then into placing them into a hot isostatic press. The approximate composition of the starting materials is 65 wt% SiO_2, 19 wt% Al_2O_3, 3 wt% CaO, 8 wt% Na_2O, with variable H_2O and CO_2 contents. The samples were heated to 1200°C (at 200 MPa) for 24 hours, isobarically cooled to ~650°C in ~10 minutes, and then depressurized and cooled back down to atmospheric conditions in ~15 hours. Water contents in the various samples (measured by Karl Fisher Titration) were ~1 wt%, ~1.5 wt%, and ~2 wt%, for samples 3-10, 3-9, and 3-1, respectively. A CO_2 source was only included in the starting materials for sample 3-1 (~2 wt% of added CO_2). Analyses of the final quenched glass from 3-1, however, shows only 0.03 wt% CO_2 (measured by coulometry), due to nucleation and growth of CO_2 bubbles during the experiment. Microprobe results for the crystals and matrix were also performed at ETH-Zurich and are reported in Table S5.1, where we assume that the composition of phenocrysts in sample 3-1 is the same as in an accompanying sample with approximately the same initial compositions and volatile contents (sample 3-3 from B. Tripoli's PhD dissertation).

The lower H_2O samples (3-10 and 3-9) have liquidus temperatures similar to 1200°C, implying that they were not fully molten at the onset of cooling. This is manifested by two populations of plagioclase phenocrysts in 3-10 and 3-9, and to a much smaller extent in 3-1, where larger grains have high-An cores and low-An rims and smaller grains are dominantly low-An. The relative abundances of the two phenocryst types and crystal size distributions, however, are currently unknown.

5.7.1.3. Orbicules, comb-layers, and related rocks

Emerald Bay orbicule (OG): The large (~10 cm) ~7 layer dioritic orbicule sample (OG) was collected in 2012 from the Echo Lake Granodiorite pluton, just below Eagle Lake, and above Emerald Bay, Lake Tahoe, CA (coordinates: 38.946236, -120.119780). The sample was found in association with comb layered hornblende gabbros and a variety of orbicules. The orbicule consists dominantly of a coarse-grained dioritic core surrounded by concentric layers of variably coarse to fine grained plagioclase combs, along with interstitial amphiboles and clinopyroxene, and contained within a dioritic matrix similar to the core but with lower Mg and Ca, and higher amounts of Fe-oxides. Ca concentrations of plagioclase across the orb (measured by EPMA), which decrease at the edge of the orb and into the matrix, are shown in Fig. S5.4 and tabulated, along with other mineral compositions, in Table S5.2. K-Ar ages of the Echo Lake pluton range from ~90 Ma for hornblende and ~75 Ma for biotite (Loomis, 1983).

Boogardie Station orbicule (AUS21): Sample AUS21 (displayed in Fig. S5.5) was purchased from a dealer, but comes from Boogardie Station, a quarry located ~20 km west of Mount Magnet, Mount Magnet Shire, Western Australia (coordinates: -28.06116,117.48503). The orbicules occur in a granodiorite to tonalite matrix, and consist of plagioclase, hornblende, and biotite, arranged radially around a core dominated by plagioclase. Among the oldest known orbicular rocks, the orbicules from this location are ~2.69 Gyr old (Bevan, 2004; Bevan and Bevan, 2009). The orbicules are hosted in an oval-shaped body, ~40 m wide and at least ~55 m long (Bevan, 2004). Our orbicule is approximately ~6 cm wide, rimmed by a thin layer of hornblende and biotite with minor plagioclase and Fe-oxides. Inside the rim, there is one major plagioclase comb-layer with abundant interstitial hornblende, the orbicule as a whole has a dioritic bulk composition largely composed of plagioclase and hornblende.

Fisher Lake orbicules and comb layers: The 23 plagioclase separates analyzed in our study come from orbicule cores, rims, matrix, host-rocks, and associated comb-layer sequences from the Fisher Lake pluton, CA, where repeating mm-thick comb layers can reach several meters in thickness and orbicules can have up to ~20 layers (McCarthy and Müntener, 2016). The separation technique was sawing/micro-sawing, crushing and sieving below 250µm, hand-magnet separation, and finally use of a Frantz magnetic separator to get (>98% pure) plagioclase separates. The crystallization sequence and mineralogy for most of the samples is plagioclase → orthopyroxene + clinopyroxene + oxides → amphiboles. Plagioclase has an elongate comb-textured habit and pyroxenes, oxides, and amphiboles are interstitial, though occasional orthopyroxene-clinopyroxene- and amphibole-comb textures are present (McCarthy and Müntener, 2016). Inter-orb matrix materials, from which we have four different samples, have gabbroic to diotiric bulk compositions and occasionally show pegmatitic textures. The ^{238}U-^{206}Pb zircon ages for the orbicule cores, matrices, and host-rocks overlap and range from 110-113 Ma (McCarthy et al., 2016). As the samples represent a shallow (~2 Kbar), volatile saturated system, H_2O contents of the melts are likely to be ~4 wt%, typical for arc magmas, and corroborated by high-An plagioclase compositions (McCarthy et al., 2016; McCarthy and Müntener, 2017, 2016).

Comb layer samples

AM26 is a three-layer plagioclase comb sequence, sample AM26-1 is the top of a comb layer, sample 2 is a complete layer, and samples 3-5 are one thick layer divided into three (from base to top). The layers are approximately ~1cm each.

AM131 is a four layer plagioclase comb sequence described in (McCarthy and Müntener, 2017), depicted in their Fig. 1f, and represents the last layers of a ~1 m-thick plagioclase + amphibole comb layer sequence which abruptly changes into vertical layering dominated by unoriented olivine and amphibole [(*e.g.* McCarthy and Müntener, 2016), in their Fig. 6, transition from 'Pulse 2' to 'Pulse 3']. These four layers are mineralogically the same, dominated by comb-textured plagioclase with minor amounts of interstitial pyroxenes, hornblende and oxides. Layers are ~1 cm wide, except Layer 3 which is ~0.2 cm wide. Samples AM-131-1 and AM-131-2 represent the base and top of Layer 1, respectively, while samples AM-131-3 and AM-131-4 come from Layer 2, sample AM-131-5 comes from Layer 3, and sample AM-131-6 and AM-131-7 come from Layer 4.

Orb cores

AM-09 represents the rarer type of orbicule core (hornblende-olivine-norite) only found in a specific location within the Fisher Lake pluton [(McCarthy et al., 2015), in their Fig. 3a and Fig. 6d]. The mineralogy of this sample, olivine + orthopyroxene + plagioclase + hornblende and minor phlogopite + edenitic hornblende replacing olivine is significantly distinct from other Fisher Lake lithologies, which are predominantly hornblende-diorites and hornblende-gabbros. Though this samples contains fresh euhedral plagioclase, the genetic relationship between this rare type of orbicule and the other lithologies is unclear. Fisher Lake Orbicule cores are also occasionally formed surrounding fragments of metamorphic rock (McCarthy et al., 2015), which are unlikely to share a common origin with other magmatic samples in the region.

AM-89 is a core of an orbicule found close to orbicule AM-100 (from which we analyzed the rims) and is a hornblende-gabbro xenolith [*e.g.* picture Fig.5h in (McCarthy et al., 2016)] which represents the main orbicule core population present at Fisher Lake.

Orb rims

AM89-rim represents the comb-textured layer of orb core AM-89, dominated by comb-textured plagioclase.

AM-100 has two orbicule-layers which represent a large majority of the orbicule-rim populations found at Fisher Lake (consisting of low-numbers of comb-textured plagioclase-dominated layers). The orb is about 3cm across. The two orbicule layers have a combined thickness of ~1cm, and are individually represented by samples AM-100-1 and AM-100-2.

Orb Matrices

The following four inter-orb matrix samples are mineralogically similar and consist of hornblende diorites and hornblende gabbros (where there is more amphibole and less pyroxene than in the diorites) with cumulate compositions dominated by amphibole and plagioclase: AM-43, AM-95, AM-101-MTX, and 'Pegmatite'.

Host Rocks

The following two host-rocks (*e.g.* country-rocks) samples are compositionally similar diorites which host the orbicular bodies at plutonic margins: AM-31 and AM-59. Sample AM-59 is featured in Fig. 3a of (McCarthy et al., 2015).

5.7.2. Crystal-size distribution (CSD) analyses

CSD analyses were obtained both from compiled scans of large (~10 cm) saw-cut sections and from small (~mm^2) areas of associated thin-sections with elemental abundances mapped by EPMA, excluding Lunar Crater. The samples were cut with three perpendicular orientations to better constrain sizes and shapes of crystals in three dimensions.

For 02DLA, we were able to quantify both plagioclase and clinopyroxene phenocrysts in the optical scans (Tables S5.7, S5.8). For the other samples we were only able to identify one type of phenocryst in the optical samples (plagioclase in samples MLV-6 and 93MLV49, and amphibole phenocrysts in BButte), but we are able to constrain populations of plagioclase too small to observe in all four sample, using our EPMA element maps (Ca, Al, Fe, Mg, Mn) to distinguish different minerals (Fig. S5.8).

For each sample section, we analyzed a high resolution scanned image using ImageJ/Fiji (http://fiji.sc/Fiji) to measure the crystal population. We used a machine learning toolkit - Trainable Weka Segmentation tool - to segment the image pixel-by-pixel. For each image, we first manually selected a representative examples of the image pixels with the crystals (*e.g.* plagioclase, clinopyroxene, or amphibole) as well as pixels representing the background. We then used these examples to train a machine learning classifier which was subsequently used for segmenting the whole image into either crystals or background. We validated the results of the machine learning algorithm manually and found that the results were very accurate with a sufficiently representative training dataset. The primary utility of our machine learning based methodology for tracing crystals in sections is that our semi-automated procedure is much faster and reproducible as compared to manual image analysis.

Using the segmented image, we used ImageJ to fit ellipses to each crystal, excluding very small crystals (less than a few pixel long) as well as edge crystals. We then imported the measurements into the CSD Corrections software (http://www.uqac.ca/mhiggins/csdcorrections.html) to perform stereology corrections and estimate the 3D crystal size distributions. In order to ensure that we have a large enough number of crystals for the 2D to 3D correction, we combined the segmentation results from each of the cut-sections of the sample to obtain an aggregate crystal size distribution. We used the py-earth python package (https://github.com/scikit-learn-contrib/py-earth) to perform single or multi-segment linear fits to the obtained CSD. The package implements a Multivariate Adaptive Regression Splines algorithm (Friedman, 1991) to fit search for optimal, sparse data representations, and decide whether a single or multiple piecewise linear functions are required to represent the CSD. In order to assess the sensitivity of the fit result, we performed 500 additional bootstrap re-sampling fits for each CSD by randomly excluding 2 data points. The results of these analyses are reported in Fig. 5.7, Fig S5.8, and Table S5.8.

5.7.3. Supplementary figures and tables

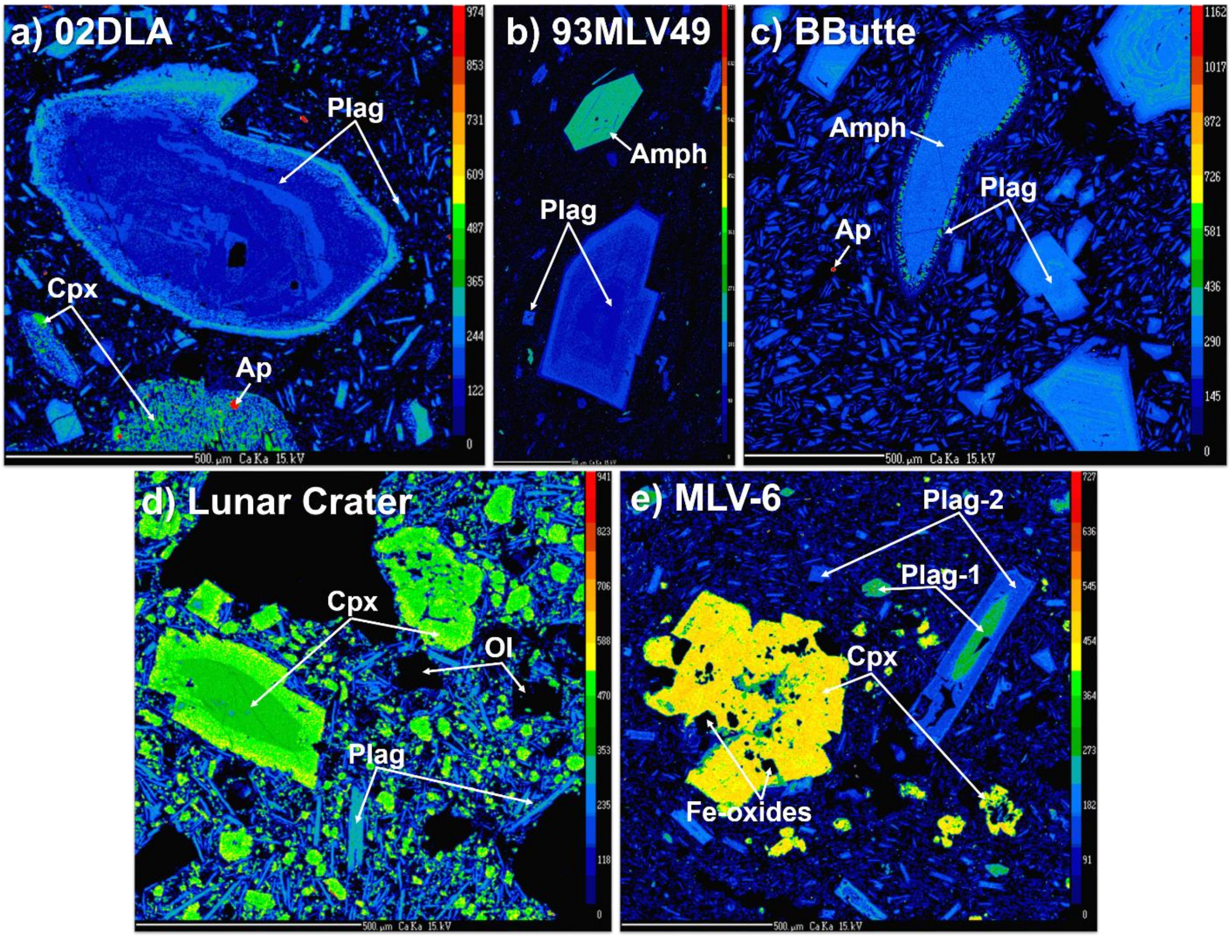

Fig. S5.1. Ca X-ray maps of select phenocrystic samples.

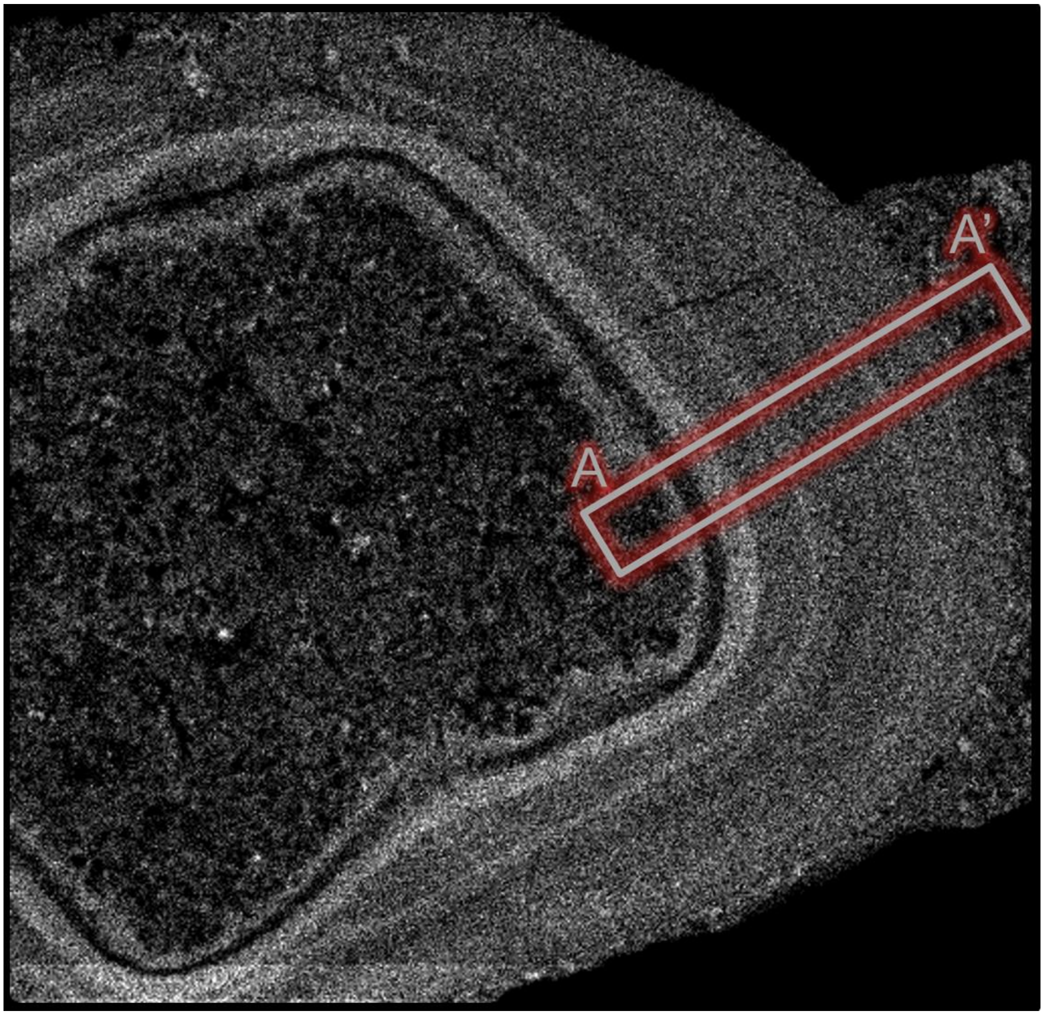

Fig. S5.2. Handheld micro-XRF Ca map of Emerald Bay orbicule (Courtesy of Cin-Ty Lee). Orb is ~10 cm wide. Approximate location of transect (A to A’) highlighted by red rectangle.

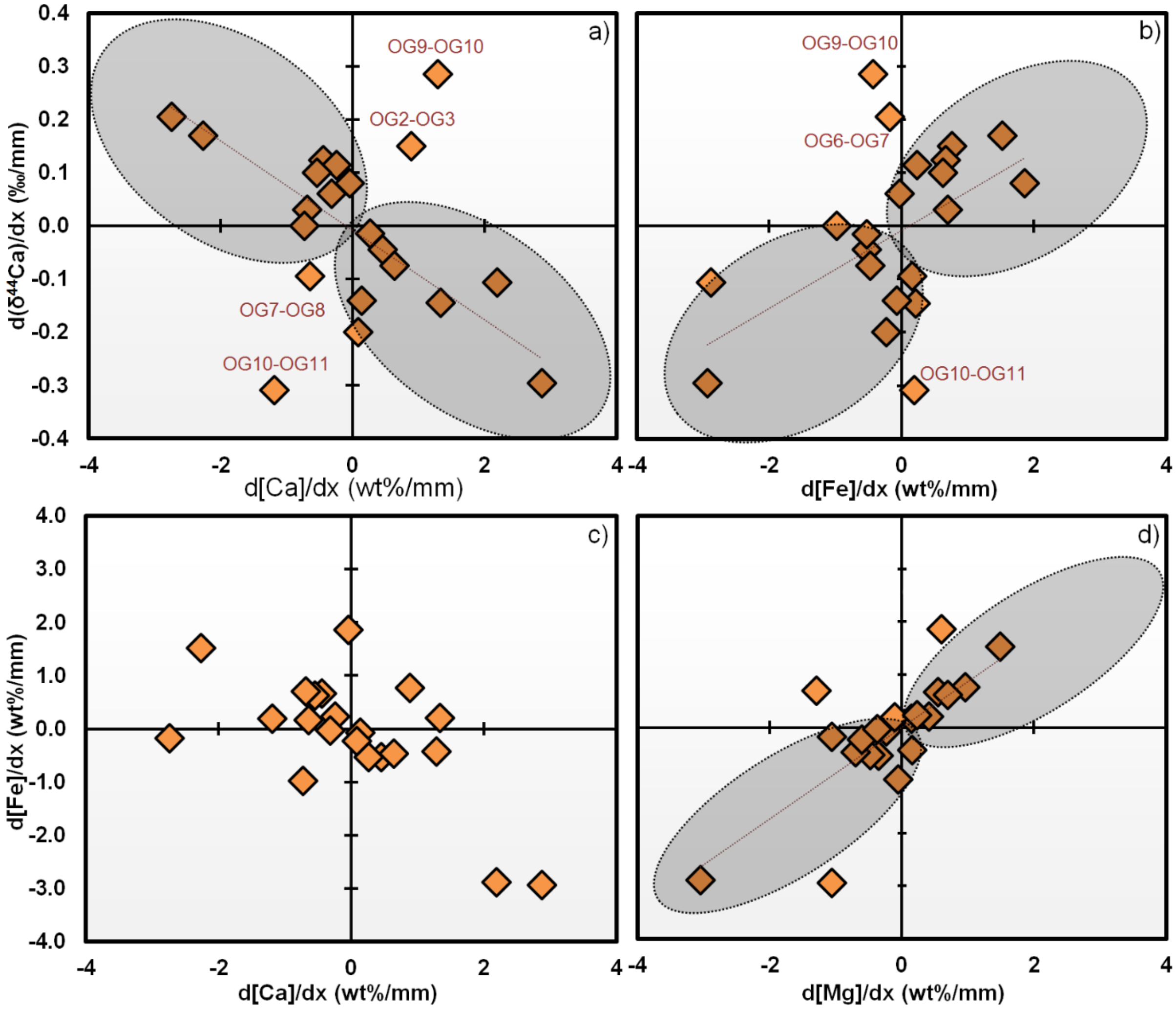

Fig. S5.3. d[δ^{44}Ca]/dx *vs.* d[conc.]/dx across OG orbicule layers, the width of the micro-drill (0.325 mm) was taken into account when calculating the distance between the center of adjacent samples. Outliers are labeled by sample numbers.

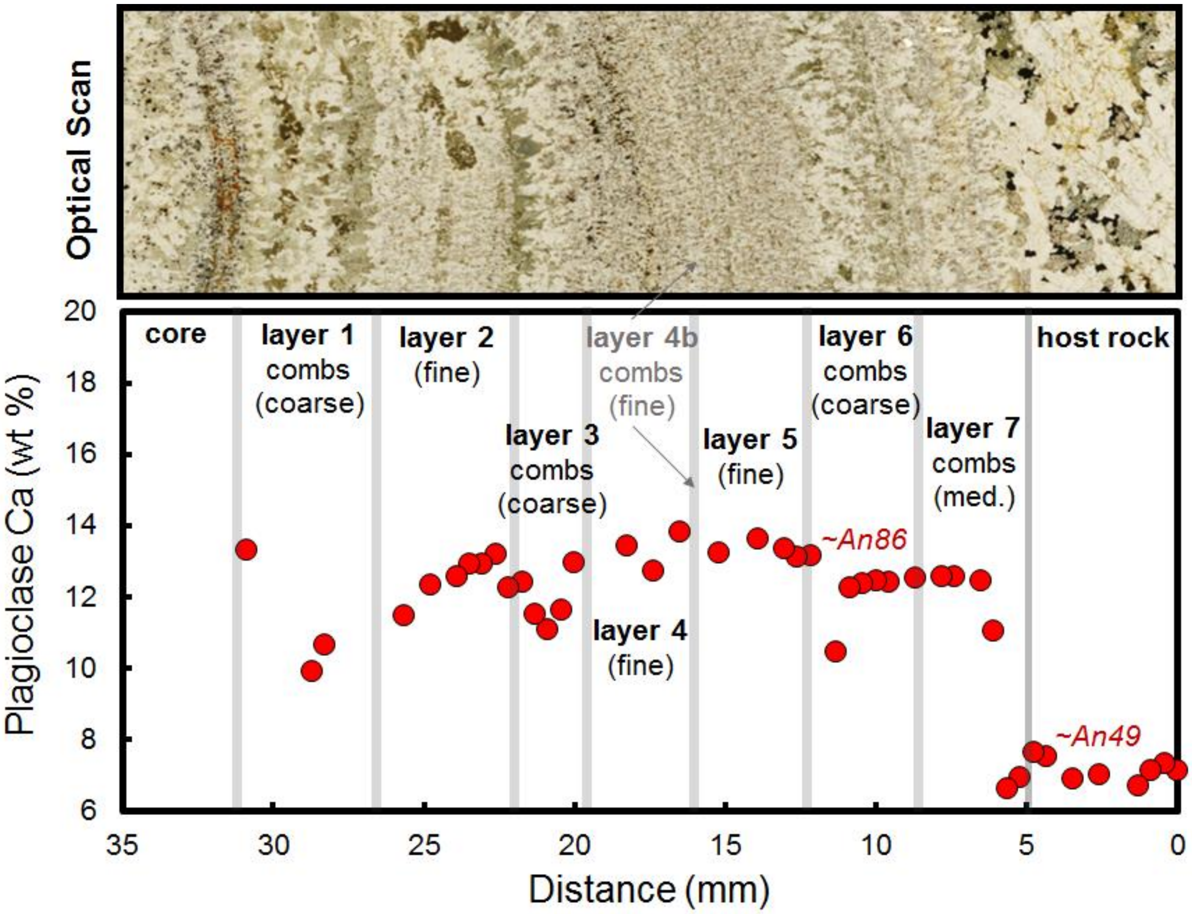

Fig. S5.4. Plagioclase compositions across the Emerald Bay orbicule. Optical scan of orbicule (top panel) and plagioclase Ca concentrations (wt%, by EPMA) (bottom panel).

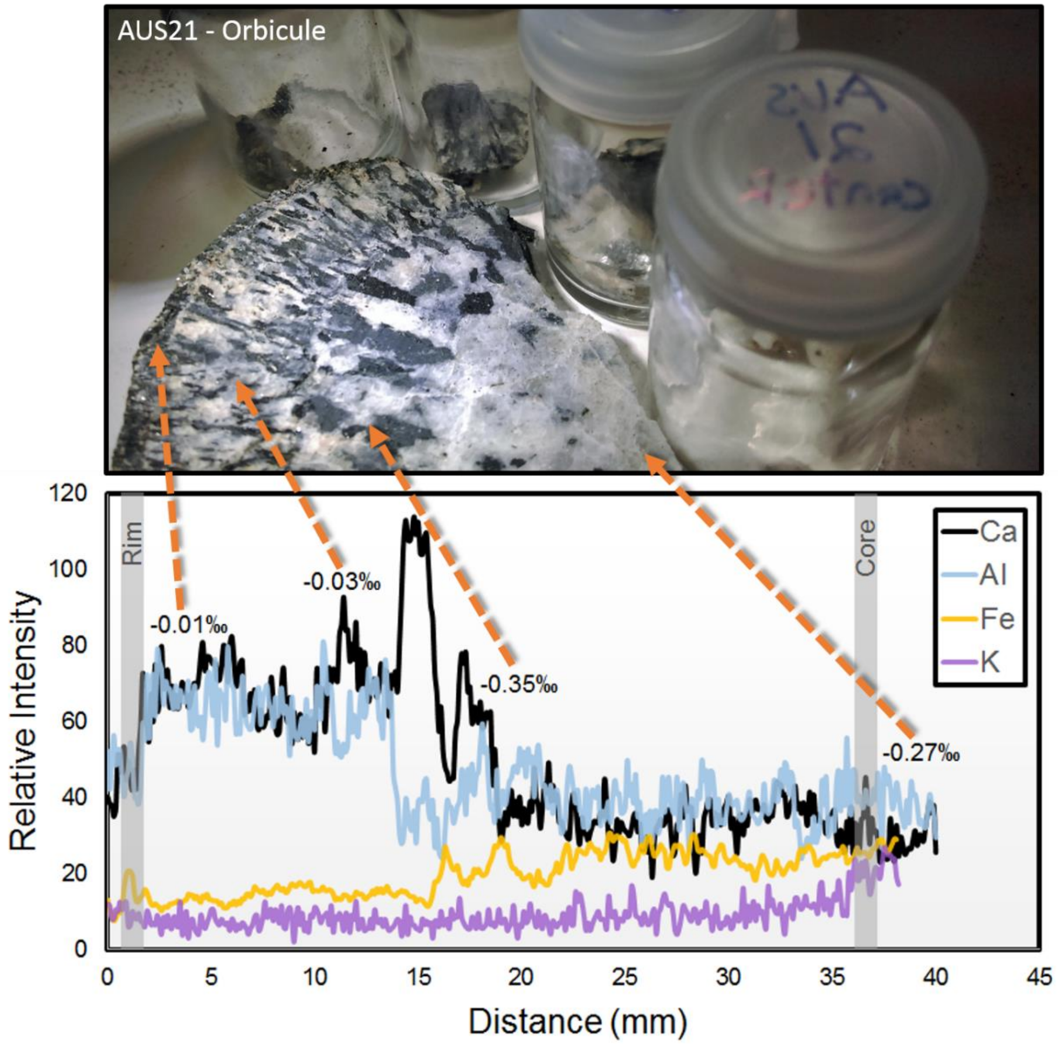

Fig. S5.5. Boogardie Station orb (AUS21) image, micro-XRF transect results, & δ^{44}Ca relative to BSE (black numbers with dashed orange arrows pointing to approximate sample location). Micro-XRF element transect results courtesy of Cin-Ty Lee.

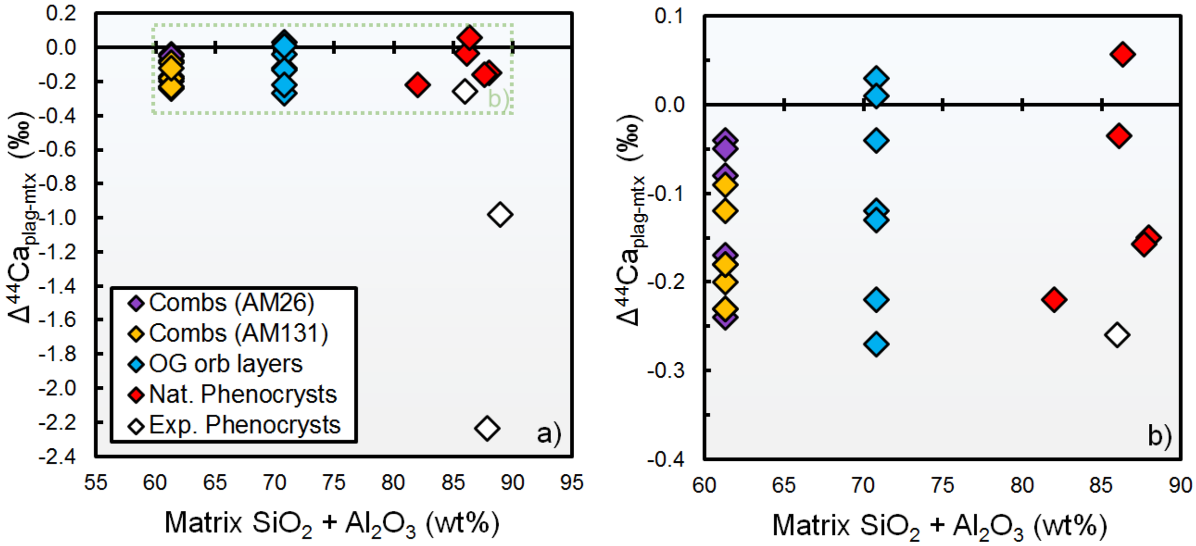

Fig. S5.6. Δ^{44}Ca vs. matrix $SiO_2 + Al_2O_3$ in phenocrystic and orbicular samples. Error bars. Only OG orbicular layers where changes in δ^{44}Ca are not correlated with changes in Fe and/or Mg are included (bold values in Table S5.5, see main text for discussion), in (b) we show a zoomed-in version of (a) delimited by the dashed green rectangle.

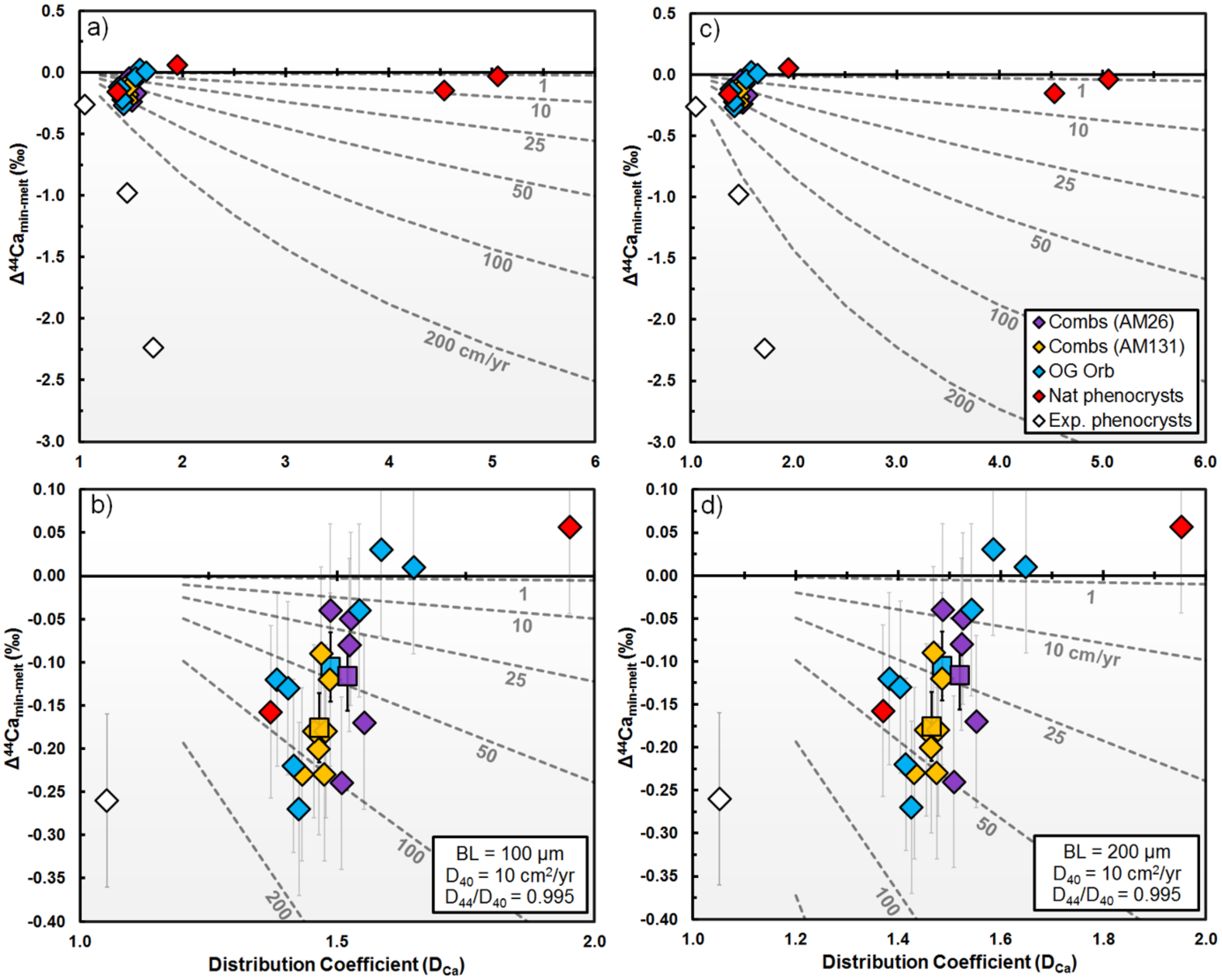

Fig. S5.7. Growth-rate estimates using the model of (Watson and Müller, 2009) with $D_{44}/D_{40} = 0.995$ (compared with same data as Fig. 5.7 of the main text). In (a,b) BL thicknesses are 100 µm, in (c,d) BL thicknesses are 200 µm.

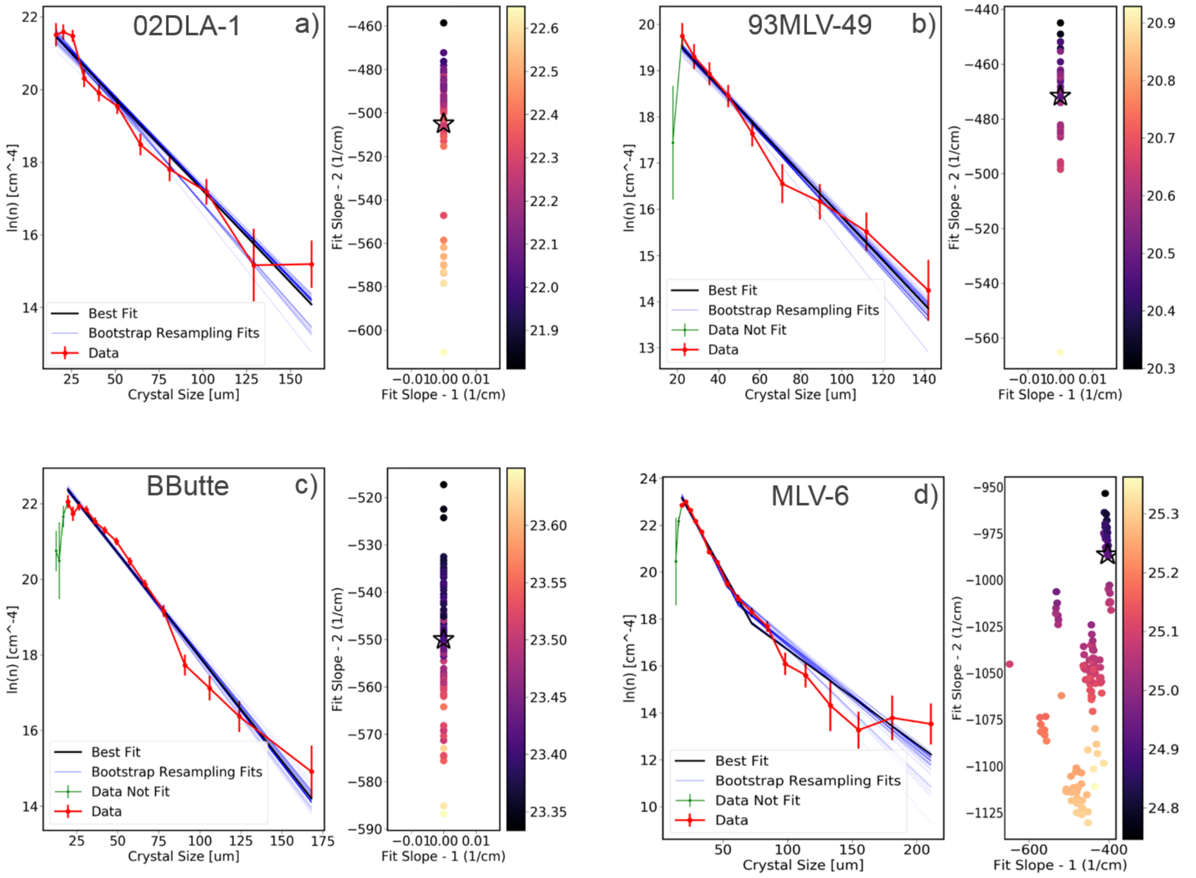

Fig. S5.8. Fine-grained plagioclase CSD analyses from thin-section element maps (*e.g.* Fig. S5.1). The left panel in each figure shows the number density of phenocrysts of each size, whereas the right panel shows best-fit slopes (for up to two different slopes) from bootstrap re-sampling methods, with colors depicting y-intercept values for the regressions. Black star represents best-fit values for slope and intercept.

Table S5.1. Major element data for phenocrystic samples.

	Volcanic samples						*Experimental samples*		
	B-Butte	93MLV-49	MLV-6	MLV-6-R	Lunar Cr.	02DLA-1	3-10	3-9	3-1*
<u>Matrix</u>	(n = 12)	(n = 17)	(n = 12)	(n = 12)	(n = 13)	(n = 14)	(n = 49)	(n = 16)	(n = 52)
SiO_2	74.1	73.3	72.8	71.9	53.4	72.5	72.6	70.0	68.7
Al_2O_3	14.5	14.6	13.3	14.4	28.7	15.1	15.2	18.9	17.3
MnO	0.01	0.05	0.02	<D.L	0.03	0.05	-	-	-
MgO	0.15	0.05	0.12	0.08	0.16	0.02	-	-	-
CaO	2.4	0.6	0.9	1.4	10.0	2.8	2.8	3.3	3.3
Na_2O	5.0	4.4	3.6	4.1	5.5	4.4	7.3	5.8	7.2
K_2O	1.5	5.4	5.2	4.9	1.3	2.6	-	-	-
TiO_2	0.16	0.12	0.27	0.27	0.22	0.11	-	-	-
FeO	0.39	1.19	0.83	0.54	1.13	0.33	-	-	-
BaO	0.03	0.08	0.03	0.04	0.17	0.06	-	-	-
H_2O (est)	1.8	0.2	3.0	2.4	n/a	1.9	2.2	2.0	3.5
Al_2O_3 + SiO_2	**89**	**88**	**86**	**86**	**82**	**88**	**88**	**89**	**86**
A/CNK (molar)	**1.02**	**1.03**	**1.02**	**1.00**	**1.00**	**1.00**	**0.90**	**1.22**	**0.96**
Mg# (molar %)	**41**	**8**	**20**	**21**	**21**	**8**	**-**	**-**	**-**
<u>Plagioclase</u>	(n = 25)	(n = 43)	(n = 19)	(n = 32)	(n = 24)†	(n = 32)	(n = 22)	(n = 7)	(n = 8)
SiO_2	50.8	62.3	52.1	52.6	50.8	59.2	53.6	52.6	24.4
Al_2O_3	30.1	22.5	29.6	28.4	30.4	25.0	29.8	30.3	68.7
Fe_2O_3	0.48	0.24	0.34	0.55	0.70	0.28	-	-	-
MnO	<D.L.	<D.L.	0.01	<D.L.	0.01	0.01	-	-	-
MgO	0.04	0.01	0.11	0.10	0.07	0.02	-	-	-
CaO	14.0	4.7	13.1	12.3	12.8	7.7	12.8	13.5	6.7
Na_2O	3.8	8.6	4.3	4.7	3.8	7.4	4.2	3.8	1.6
K_2O	0.08	1.45	0.22	0.28	0.35	0.61	-	-	-
TiO_2	0.00	<D.L.	0.07	0.08	0.10	0.02	-	-	-
An%	**66.6**	**21.3**	**62.1**	**58.1**	**63.7**	**35.2**	**63**	**67**	**70**
Ab%	**33.0**	**70.9**	**36.7**	**40.4**	**34.3**	**61.5**	**37**	**33**	**30**
Or%	**0.4**	**7.8**	**1.3**	**1.6**	**2.1**	**3.3**	**-**	**-**	**-**
<u>Plagioclase</u>	-	-	-	-	-	-	(n = 19)	(n = 52)	(n = 31)
SiO_2	-	-	-	-	-	-	71.3	69.5	70.8
Al_2O_3	-	-	-	-	-	-	17.9	18.5	18.9
CaO	-	-	-	-	-	-	3.4	4.1	3.4
Na_2O	-	-	-	-	-	-	6.0	5.7	5.9
An%	-	-	-	-	-	-	**24**	**28**	**24**
Ab%	-	-	-	-	-	-	**76**	**72**	**76**
<u>Clinopyroxene</u>	-	-	(n = 7)	-	(n = 7)	(n = 6)	-	-	-
SiO_2	-	-	48.0	-	48.7	51.4	-	-	-
Al_2O_3	-	-	5.8	-	7.5	4.0	-	-	-
Fe_2O_3	-	-	10.5	-	7.2	7.4	-	-	-
MnO	-	-	0.16	-	0.15	0.11	-	-	-
MgO	-	-	13.5	-	12.9	15.7	-	-	-
CaO	-	-	20.5	-	21.7	21.9	-	-	-
Na_2O	-	-	0.52	-	0.81	0.24	-	-	-
K_2O	-	-	<D.L.	-	0.01	<D.L.	-	-	-
TiO_2	-	-	1.65	-	1.27	0.42	-	-	-
Wo%	-	-	**44.0**	-	**48.6**	**44.8**	**-**	**-**	**-**
En%	**-**	**-**	**40.2**	**-**	**40.0**	**44.6**	**-**	**-**	**-**
Fs%	**-**	**-**	**15.8**	**-**	**11.3**	**10.6**	**-**	**-**	**-**

All data are reported in wt%. †measured by SEM on plagioclase grain mounts. *measured values on related sample 3-3, from B. Tripoli's PhD dissertation].

Table S5.1. (Continued). Major element data for phenocrystic samples.

	Volcanic samples						*Experimental samples*		
	B-Butte	93MLV-49	MLV-6	MLV-6-R	Lunar Cr.	02DLA-1	3-10	3-9	3-1*
Amphibole	*(n = 29)*	*(n = 1)*	*(n = 10)*	-	-	-	-	-	-
SiO_2	45.8	42.3	43.9	-	-	-	-	-	-
Al_2O_3	10.6	10.7	9.7	-	-	-	-	-	-
Fe_2O_3	12.9	15.6	17.6	-	-	-	-	-	-
MnO	0.14	0.46	0.28	-	-	-	-	-	-
MgO	15.8	12.4	12.0	-	-	-	-	-	-
CaO	11.2	10.7	11.9	-	-	-	-	-	-
Na_2O	2.1	2.6	2.3	-	-	-	-	-	-
K_2O	0.19	0.95	0.76	-	-	-	-	-	-
TiO_2	1.2	3.0	2.3	**-**	**-**	**-**	**-**	**-**	**-**
Olivine	-	-	*(n = 14)*	*(n = 36)*	*(n = 7)*	-	-	-	-
SiO_2	-	-	37.9	38.3	39.4	-	-	-	-
Al_2O_3	-	-	0.03	0.04	0.37	-	-	-	-
FeO	-	-	22.5	22.9	18.8	-	-	-	-
MnO	-	-	0.35	0.38	0.25	-	-	-	-
MgO	-	-	39.7	39.2	45.4	-	-	-	-
CaO	-	-	0.23	0.21	0.31	-	-	-	-
TiO_2	-	-	0.03	0.03	0.15	-	-	-	-
Fo%	-	-	**75.3**	**74.8**	**80.6**	-	-	-	-
Fa%	**-**	**-**	**24.0**	**24.5**	**18.7**	**-**	**-**	**-**	**-**
Ca-Ol %	**-**	**-**	**0.3**	**0.3**	**0.4**	**-**	**-**	**-**	**-**

All data are reported in wt%.

Table S5.2. Orbicule and comb-layer mineral compositions (by EPMA) including Emerald Bay orb transect (matrix-to-core) and comb-layer mineral data from (McCarthy and Müntener, 2017, 2016).

	Distance (mm)	SiO_2	TiO_2	Cr_2O_3	Al_2O_3	FeO	MnO	MgO	CaO	Na_2O	K_2O	Total
OG Transect												
Ab	0.0	55.3	<D.L.	<D.L.	28.4	0.2	<D.L.	0.0	10.0	5.7	0.2	99.8
	0.4	55.5	<D.L.	<D.L.	29.3	0.3	<D.L.	<D.L.	10.2	5.9	0.2	101.5
	0.9	53.8	0.0	<D.L.	29.2	0.3	0.06	<D.L.	10.0	6.0	0.4	99.7
	1.3	53.8	0.0	0.004	28.6	0.3	<D.L.	0.0	9.4	6.1	0.3	98.6
	2.6	55.0	0.0	0.009	27.8	0.2	0.02	0.0	9.8	5.5	0.3	98.7
	3.5	55.3	0.0	0.001	28.5	0.3	<D.L.	0.0	9.7	5.7	0.1	99.6
	4.3	52.5	0.0	<D.L.	28.1	0.3	<D.L.	0.0	10.5	5.1	0.3	96.7
	4.8	53.4	0.0	0.023	28.1	0.3	0.02	0.0	10.7	4.8	0.3	97.7
	5.2	56.1	0.0	0.014	27.6	0.2	<D.L.	0.0	9.7	5.5	0.3	99.4
	5.7	57.1	0.0	0.021	27.8	0.2	0.02	0.0	9.2	6.0	0.4	100.8
An	6.1	47.3	<D.L.	0.004	32.6	1.4	<D.L.	0.1	15.4	2.3	0.1	99.2
	6.5	45.3	<D.L.	<D.L.	34.9	0.6	<D.L.	0.0	17.4	1.7	0.0	99.9
	7.4	45.6	<D.L.	0.004	35.5	0.3	0.03	0.0	17.6	1.3	0.0	100.4
	7.8	45.5	0.0	<D.L.	34.8	0.8	0.03	0.7	17.6	1.2	0.0	100.7
	8.7	45.5	0.0	<D.L.	34.9	0.4	<D.L.	<D.L.	17.5	1.4	0.0	99.6
	9.6	45.2	0.0	0.010	34.4	0.5	0.04	0.0	17.4	1.4	0.0	99.0
	10.0	44.9	0.0	<D.L.	35.5	0.4	0.02	0.0	17.4	1.6	0.0	99.9
	10.4	47.5	0.0	<D.L.	35.2	0.4	0.02	0.0	17.3	1.4	0.0	101.9
	10.9	46.4	0.0	0.012	35.0	0.3	0.01	0.0	17.2	1.9	0.0	100.8
	11.3	49.7	<D.L.	0.001	32.0	0.3	<D.L.	0.0	14.7	3.0	0.1	99.8
	12.2	43.8	0.0	<D.L.	35.5	0.3	<D.L.	0.0	18.4	0.9	0.0	99.0
	12.6	43.3	<D.L.	<D.L.	35.2	0.3	<D.L.	<D.L.	18.3	0.9	0.0	98.0
	13.0	44.6	<D.L.	<D.L.	36.4	0.3	<D.L.	0.0	18.7	0.9	0.0	100.9
	13.9	43.5	0.0	0.016	37.1	0.5	<D.L.	<D.L.	19.1	0.5	0.0	100.6
	15.2	45.0	<D.L.	0.018	36.5	0.3	<D.L.	0.0	18.5	1.1	0.0	101.5
	16.5	43.2	0.0	0.008	36.3	0.3	0.00	<D.L.	19.4	0.4	0.0	99.7
	17.4	45.2	<D.L.	0.005	34.5	1.3	<D.L.	0.4	17.8	0.7	0.0	100.0
	18.3	43.0	<D.L.	<D.L.	35.7	0.4	<D.L.	0.0	18.8	0.8	0.0	98.7
	20.0	44.6	<D.L.	0.000	35.6	0.4	<D.L.	0.0	18.1	1.0	0.0	99.7
	20.4	46.7	<D.L.	0.007	33.6	0.3	0.00	0.0	16.3	1.9	0.0	98.8
	20.9	48.0	0.0	0.015	33.6	0.3	0.02	0.0	15.5	2.6	0.1	100.2
	21.3	47.8	0.0	0.004	33.7	0.4	0.00	0.0	16.1	2.2	0.1	100.3
	21.7	43.5	0.0	0.003	34.2	0.3	0.00	0.0	17.4	1.3	0.0	96.8
	22.2	45.0	<D.L.	0.008	37.0	0.4	<D.L.	0.0	17.2	1.5	0.0	101.1
	22.6	44.4	0.0	<D.L.	35.7	0.3	0.02	0.0	18.5	1.0	0.0	100.0
	23.0	44.6	0.0	0.003	37.1	0.4	0.02	0.0	18.1	1.2	0.0	101.5
	23.5	45.0	0.0	0.001	35.5	0.4	0.05	0.0	18.1	1.1	0.0	100.3
	23.9	44.0	0.0	<D.L.	34.2	0.4	<D.L.	0.0	17.6	1.2	0.0	97.5
	24.8	45.8	0.0	0.004	34.2	0.4	<D.L.	0.0	17.3	1.5	0.0	99.1
	25.7	47.8	<D.L.	0.002	34.4	0.5	0.05	0.0	16.1	2.5	0.1	101.5
	28.3	47.8	<D.L.	0.003	32.2	0.3	0.00	0.0	14.9	2.9	0.1	98.2
	28.7	50.2	0.0	0.029	30.4	0.4	0.01	0.0	13.9	2.8	0.1	97.9
	30.9	43.8	<D.L.	0.010	36.0	0.2	0.01	0.0	18.6	0.7	0.0	99.4
Opx	3.0	52.5	0.2	0.009	1.2	21.3	0.55	23.3	0.8	0.00	<D.L.	99.8
	7.0	53.6	0.2	<D.L.	1.1	17.7	0.36	26.2	0.5	0.01	0.0	99.8
	9.1	53.4	0.1	0.011	0.9	17.5	0.36	27.1	0.4	0.01	<D.L.	99.8
	16.1	54.3	0.1	<D.L.	1.7	13.4	0.23	30.4	0.5	-0.01	0.0	100.6
	17.0	53.6	0.1	0.024	1.6	12.4	0.28	29.9	0.3	0.02	0.0	98.2
	17.8	54.5	0.1	0.009	1.9	11.6	0.22	30.9	0.4	-0.01	<D.L.	99.6
	25.2	55.9	0.1	<D.L.	0.9	17.0	0.30	29.0	0.3	0.02	0.0	103.7
	30.4	53.2	0.1	<D.L.	1.2	14.5	0.39	28.3	0.7	0.01	<D.L.	98.4
	31.7	52.7	0.1	0.012	2.5	11.6	0.32	29.5	0.3	0.02	0.0	97.1
	32.2	54.4	0.1	<D.L.	1.6	12.8	0.40	30.1	0.4	0.02	0.0	99.8
Cpx	1.7	50.9	0.3	<D.L.	1.5	10.1	0.24	15.0	19.7	0.26	<D.L.	98.0
	29.6	54.7	0.3	0.019	2.1	6.7	0.17	16.9	21.7	0.32	0.1	103.0
Hbl	26.1	47.2	1.9	0.048	10.4	10.0	0.04	16.8	11.7	1.40	0.0	100.2
	26.5	44.0	2.0	0.052	10.8	10.9	0.11	15.0	11.8	1.38	0.0	96.8
	27.0	44.6	2.2	0.137	10.0	11.8	0.14	14.8	11.8	1.50	0.0	97.9
	29.1	46.1	2.4	0.041	10.5	11.6	0.09	15.7	11.7	1.57	0.0	100.6

All values are from single analyses.

Table S5.2. (Continued). Orbicule and comb-layer mineral compositions (by EPMA) including Emerald Bay orb transect (matrix-to-core) and comb-layer mineral data from (McCarthy and Müntener, 2017, 2016).

		SiO_2	TiO_2	Cr_2O_3	Al_2O_3	FeO	MnO	MgO	CaO	Na_2O	K_2O	Total
AM131 Combs												
An	A	48.8	-	-	32.0	0.3	-	-	15.9	2.6	0.1	99.6
	B	49.8	-	-	31.3	0.3	-	-	15.1	3.0	0.1	99.5
	C	48.2	-	-	32.7	0.3	<D.L.	<D.L.	16.5	2.3	0.1	100.1
Opx	A	54.2	0.2	0.007	0.9	19.8	0.43	24.5	0.8	0.01	<D.L.	100.8
	B	54.3	0.2	0.006	0.9	19.9	0.42	24.4	0.8	0.02	<D.L.	100.9
	C	54.2	0.2	0.006	0.9	19.4	0.41	24.8	0.7	0.01	<D.L.	100.7
Hbl	A	44.6	2.8	0.005	9.6	12.0	0.14	14.1	11.8	1.6	0.8	97.5
	C	45.3	2.6	0.015	9.7	10.9	0.12	14.6	11.9	1.6	0.8	97.5
Cpx	A	53.1	0.4	0.012	1.7	7.5	0.18	14.9	22.5	0.29	<D.L.	100.6
	B	52.6	0.5	0.020	2.1	8.4	0.19	15.1	21.3	0.30	<D.L.	100.4
	C	52.6	0.5	0.013	2.0	7.5	0.19	14.8	22.5	0.29	<D.L.	100.5
AM09 Core												
An	OC	52.0	<D.L.	0.004	29.9	0.2	0.01	0.1	13.1	4.09	<D.L.	99.5
Opx	OC	54.4	0.1	0.025	1.3	17.1	0.48	26.7	0.5	0.02	<D.L.	100.6

Table S5.3. Emerald Bay orbicule subsample bulk-chemistry by XRF[†] and ICP-OES (converted to oxide values).

	width (mm)	CaO	K_2O	MgO	Na_2O	FeO	SiO_2	TiO_2	Al_2O_3
OG Core[†]	-	7.3	0.36	12.1	1.6	11.1	51.9	0.7	14.7
OG-1	1.98	7.7	0.29	16.6	1.5	14.6	-	-	-
OG-2	1.49	13.0	0.30	7.9	2.4	8.1	-	-	-
OG-3	1.68	14.9	0.25	10.4	1.6	9.7	-	-	-
OG-4	1.53	9.9	0.17	14.3	0.6	12.8	-	-	-
OG-5	1.71	16.4	0.22	11.5	1.4	6.7	-	-	-
OG-6	1.21	19.1	0.20	12.5	1.3	7.1	-	-	-
OG-7	1.20	14.5	0.17	10.4	1.1	6.8	-	-	-
OG-8	1.72	13.2	0.22	10.7	0.9	7.1	-	-	-
OG-9	1.24	13.4	0.23	10.1	1.0	7.0	-	-	-
OG-10	1.11	15.5	0.25	10.5	1.4	6.4	-	-	-
OG-11	1.65	13.3	0.23	10.2	1.2	6.7	-	-	-
OG-12	2.25	12.0	0.28	12.0	0.7	8.4	-	-	-
OG-13	1.36	13.2	0.20	10.9	0.7	7.1	-	-	-
OG-14	1.37	12.7	0.23	11.5	0.6	7.5	-	-	-
OG-15	1.91	13.3	0.13	10.2	0.9	6.4	-	-	-
OG-16	1.60	14.9	0.19	8.1	1.8	5.4	-	-	-
OG-17	2.16	13.4	0.16	10.3	1.2	6.9	-	-	-
OG-18	1.58	13.7	0.15	8.5	1.3	6.3	-	-	-
OG-19	1.76	12.9	0.14	7.4	1.8	6.3	-	-	-
OG-20	2.17	11.0	0.37	3.2	4.7	8.0	-	-	-
OG-21	2.05	10.9	0.36	5.3	3.6	13.1	-	-	-
OG-22	1.60	9.1	0.35	5.1	4.2	10.8	-	-	-
OG Matrix[†]	-	9.4	0.35	4.7	3.5	9.5	51.3	1.3	19.5

All values are in (wt%), micro-drill width ~0.325 mm.

Table S5.4. δ^{44}Ca, [Ca], and Δ^{44}Ca temperatures in phenocrysts and matrix, analyzed by TIMS.

		sample	n	δ^{44}Ca (‰)	Ca (wt%)	Δ^{44}Ca$_{\text{min-mtx}}$ (‰)	Ca$_{\text{min/mtx}}$	Δ^{44}Ca$_{\text{min-plag}}$ (‰)	Δ^{44}Ca Temp (˚C)
Mono Craters	MLV-6	Hbl	2	-0.12	4.99	0.15	2.75	0.19	-
		Mtx	2	-0.27	1.82	-	-	-	-
		Mtx - R	2	-0.30	4.86	-	-	-	-
		Plag	2	-0.30	9.18	-0.04	5.06	-	-
		Plag - R	3	-0.24	9.50	0.06	1.95	-	-
	93MLV49	Mtx	2	-0.13	0.73	-	-	-	-
		Plag	2	-0.28	3.30	-0.15	4.53	-	-
								-	
Mt. Lassen	02DLA	Cpx	2	0.17	7.61	0.33	2.23	0.48	550 ± 200
		Cpx-2	3	0.13	7.93	0.29	2.32	0.45	600 ± 200
		Mtx	2	-0.16	3.41	-	-	-	-
		Plag	4	-0.32	4.67	-0.16	1.37	-	-
Black Butte	Bbutte	Hbl	3	-0.15	8.18	0.29	2.34	-	-
		Mtx	2	-0.44	3.50	-	-	-	-
National Monument, NV	Lunar Crater	Cpx	2	-0.16	13.87	0.03	1.99	0.25	875 ± 250
		Mag. sep	1	-0.47	0.20	-0.28	-	-	-
		Mtx	2	-0.19	6.96	-	-	-	-
		Ol	3	-0.03	0.17	0.16	0.02	0.38	> 1250
		Plag	4	-0.41	1.13	-0.22	0.16	-	-
Stillwater Complex	STL-100	Cpx	2	-0.12	12.84	-	-	0.06	> 900
		Opx	2	0.50	1.67	-	-	0.67	800 ± 100
		Plag	2	-0.18	12.75	-	-	-	-
Exp. tonalites	3-10	Gls	3	0.22	2.35	-	-	-	-
		Plag	3	-2.02	4.03	-2.24	1.71	-	-
	3-9	Gls	2	0.13	2.11	-	-	-	-
		Plg	2	-0.86	3.08	-0.98	1.46	-	-
	3-1	Gls	2	0.00	2.50	-	-	-	-
		Plg	2	-0.26	2.63	-0.26	1.05	-	-

Δ^{44}Ca Temperatures are based on mineral-plag equilibrium estimates from (Antonelli et al., 2019b).

Table S5.5. δ^{44}Ca and [Ca] in bulk orbicule subsamples and plagioclase separates from Fisher Lake, analyzed by TIMS. Emerald Bay orb (OG samples), Boogardie Station Orb (Aus21). Bold values indicate samples where δ^{44}Ca is not a function of [Fe] or [Mg] (see main text, Fig. 5.3, and Fig. S5.2).

		n	δ^{44}Ca (‰)	2SD	Ca (wt%)			n	δ^{44}Ca (‰)	2SD	Ca (wt%)
Plagioclase separates						Whole-rock separates					
Comb	AM-26-1	1	-0.29	0.03	11.81	*Orb Core*	OG Inner mtx	2	-0.37	0.04	4.99
	AM-26-2	1	-0.49	0.04	11.98						
	AM26-3	1	-0.33	0.03	12.10	*Orb Host*	OG Outer mtx	2	-0.20	0.04	6.89
	AM26-4	1	-0.30	0.03	12.12						
	AM26-5	1	-0.42	0.03	12.33	*Orb layers*	OG 1	2	-0.17	0.03	5.06
							OG 2	2	**-0.32**	0.04	8.85
Comb Layers	AM131-1	1	-0.45	0.04	11.63		**OG 3**	2	**-0.17**	0.04	10.35
	AM131-2	1	-0.43	0.04	11.55		OG 4	2	0.00	0.03	6.71
	AM131-3	1	-0.34	0.04	11.67		OG 5	2	-0.30	0.04	11.52
	AM131-4	1	-0.43	0.05	11.74		OG 6	2	-0.44	0.04	13.43
	AM131-5	1	-0.48	0.04	11.72		**OG 7**	2	**-0.24**	0.04	9.50
	AM131-6	1	-0.48	0.04	11.37		**OG 8**	2	**-0.33**	0.03	9.01
	AM131-7	1	-0.37	0.04	11.80		**OG 9**	2	**-0.47**	0.04	9.08
							OG 10	2	**-0.19**	0.03	10.67
Orb Cores	AM-09	1	-0.48	0.04	8.88		**OG 11**	2	**-0.42**	0.04	9.00
	AM-89	1	-0.28	0.04	12.06		OG 12	2	-0.37	0.03	8.26
							OG 13	2	-0.42	0.04	8.85
Orb Rims	AM-89-rim	1	-0.33	0.04	12.02		OG 14	2	-0.30	0.03	8.71
	AM-100-1	1	-0.32	0.04	11.67		OG 15	2	-0.32	0.04	9.08
	AM-100-2	1	-0.25	0.04	11.84		OG 16	2	-0.39	0.04	9.94
							OG 17	2	-0.29	0.03	9.08
Orb Matrices	AM-43	1	-0.30	0.04	11.98		OG 18	2	-0.49	0.03	9.28
	AM-95	1	-0.30	0.04	10.39		OG 19	2	-0.51	0.04	8.91
	AM-101-MTX	1	-0.29	0.03	10.54		OG 20	2	-0.40	0.03	7.51
	Pegmatite	1	-0.11	0.04	9.86		OG 21	2	-0.32	0.03	7.59
							OG 22	2	-0.32	0.03	6.13
Host Rocks	AM-31	1	-0.26	0.04	7.41						
	AM-59	1	-0.28	0.03	7.80	*Aus21*	Inner Core	2	-0.27	0.05	3.26
							Outer Core	2	-0.35	0.04	5.41
							Comb layer	2	-0.03	0.03	5.67
							Outer Layer	2	-0.01	0.05	5.25

All samples reported relative to bulk-silicate earth (BSE).

Table S5.6. $\delta^{18}O$ from (McCarthy et al., 2016) and measured $\delta^{44}Ca$ in plagioclase separates from Fisher Lake, CA.

		Plag $\delta^{44}Ca$ (‰)	An (%)	Plag $\delta^{18}O$ (‰)	Hbl $\delta^{18}O$ (‰)	Hbl $\delta^{18}O$ (‰)	Zrcn $\delta^{18}O$ (‰)	Zrcn $\delta^{18}O$ (‰)
Comb Layers	AM-26-1	-0.29	86.1	-	-	-	-	-
	AM-26-2	-0.49	87.3	-	-	-	-	-
	AM26-3	-0.33	88.2	-	-	-	-	-
	AM26-4	-0.30	88.4	-	-	-	-	-
	AM26-5	-0.42	89.9	-	-	-	-	-
Comb Layers	AM131-1	-0.45	84.7	-	-	-	-	-
	AM131-2	-0.43	84.2	-	6.4	6.0	-	-
	AM131-3	-0.34	85.0	8.3	7.1	-	-	-
	AM131-4	-0.43	85.5	8.3	-	-	-	-
	AM131-5	-0.48	85.4	7.5	-	-	-	-
	AM131-6	-0.48	82.9	7.5	-	-	-	-
	AM131-7	-0.37	86.0	7.5	-	-	-	-
Orb Cores	AM-09	-0.48	64.7	8.1	-	-	-	-
	AM-89	-0.28	87.9	7.6	6.2	7.1	6.4	7.1
Orb Rims	AM-89-rim	-0.33	87.6	-	-	-	-	-
	AM-100-1	-0.32	85.1	-	-	-	-	-
	AM-100-2	-0.25	86.3	-	-	-	-	-
Orb Matrices	AM-43	-0.30	87.3	7.6	-	-	-	-
	AM-95	-0.30	75.7	7.7	6.7	-	6.0	6.9
	AM-101-MTX	-0.29	76.8	-	-	-	-	-
	Pegmatite	-0.11	71.8	-	-	-	-	-
Host Rocks	AM-31	-0.26	54.0	7.3	-	-	-	-
	AM-59	-0.28	56.9	-	-	-	6.5	7.0

Table S5.7. Modal phenocrysts abundances from optical scans (combined multiple whole rock sections >7 cm) and thin-section element maps (see Fig. S5.1).

	Mineral	Modal % (optical scans)	Modal % (X-ray maps) incl. large crystals	excl. large crystals	Ratio (large/small)
02DLA-1	Plag	7.4	40.2	6.7	1.1
02DLA-1	Cpx	5.0	-	-	-
93MLV49	Plag	1.9	26.0	3.3	0.6
Bbutte	Amph	3.9	32.0 *(plag)*	-	-
MLV-6	Plag	2.5	13.4	13.4	0.2

Table S5.8. Crystal growth-rates and cooling time-scale estimates based on CSD of optical scans (Fig. 5.7) and thin section element maps (Fig. S5.8) and on largest crystal sizes.

	mineral	slope-1	slope-2	intercept	Growth rate (cm/yr)	required time (days)	[slope-2] required time (days)	Largest crystal (cm)
Optical Scans								
02DLA-1	Plag	-9.49	-11.4	6.34	7	5	5	0.6
93MLV49	Plag	-18	-	7.01	0.7	29	-	0.3
Bbutte	Amph	-5.61	-7.88	5.93	*0.3*	*217*	154	0.6
MLV-6	Plag	-3.69	-19.6	5.95	*0.3*	*330*	62	0.6
02DLA	Cpx	-14.3	-29	0.83	*0.3*	*85*	42	0.3
Thin section maps								
02DLA-1	Plag	-505	-	22.3	4	0.2	-	-
93MLV49	Plag	-472	-	20.5	1	0.8	-	-
Bbutte	Plag	-550	-	23.5	*0.3*	2.2	-	-
MLV-6	Plag	-403	-987	24.9	*0.3*	3.0	1.2	-
Largest-crystal estimates								
Am26	Plag	-	-	-	7	53	-	1.0
Am131	Plag	-	-	-	15	25	-	1.0
OG	Plag	-	-	-	6	24	-	0.3
02DLA-1	Plag	-	-	-	7	31	-	-
93MLV49	Plag	-	-	-	0.7	157	-	-
Bbutte	Amph	-	-	-	*0.3*	730	-	-
MLV-6	Plag	-	-	-	*0.3*	730	-	-
02DLA-1	Cpx	-	-	-	*0.3*	365	-	-

References

Alexander, R.J., Harper, G.D., Bowman, J.R., 1993. Oceanic Faulting and Fault-Controlled Subseafloor Hydrothermal Alteration in the Sheeted Dike Complex of the Josephine Ophiolite. J. Geophys. Res. Earth 98, 9731–9759. https://doi.org/10.1029/92JB01413

Algeo, T.J., Luo, G.M., Song, H.Y., Lyons, T.W., Canfield, D.E., 2015. Reconstruction of secular variation in seawater sulfate concentrations. Biogeosciences 12, 2131–2151. https://doi.org/10.5194/bg-12-2131-2015

Allègre, C.J., Louvat, P., Gaillardet, J., Meynadier, L., Rad, S., Capmas, F., 2010. The fundamental role of island arc weathering in the oceanic Sr isotope budget. Earth Planet. Sci. Lett. 292, 51–56. https://doi.org/10.1016/j.epsl.2010.01.019

Amini, M., Eisenhauer, A., Böhm, F., Fietzke, J., Bach, W., Garbe-Schönberg, D., Rosner, M., Bock, B., Lackschewitz, K.S., Hauff, F., 2008. Calcium isotope (d44/40Ca) fractionation along hydrothermal pathways, Logatchev field (Mid-Atlantic Ridge, 14 45 N). Geochim. Cosmochim. Acta 72, 4107–4122. https://doi.org/10.1016/j.gca.2008.05.055

Amini, M., Eisenhauer, A., Böhm, F., Holmden, C., Kreissig, K., Hauff, F., Jochum, K.P., 2009. Calcium isotopes (d44/40Ca) in MPI-DING reference glasses, USGS rock powders and various rocks: Evidence for Ca isotope fractionation in terrestrial silicates. Geostand. Geoanalytical Res. 33, 231–247. https://doi.org/10.1111/j.1751-908X.2009.00903.x

André, L., Deutsch, S., 1986. Magmatic 87Sr/86Sr relicts in hydrothermally altered quartz diorites (Brabant Massif, Belgium) and the role of epidote as a Sr filter. Contrib. to Mineral. Petrol. 92, 104–112. https://doi.org/10.1007/BF00373968

Annen, C., 2009. From plutons to magma chambers: Thermal constraints on the accumulation of eruptible silicic magma in the upper crust. Earth Planet. Sci. Lett. 284, 409–416. https://doi.org/10.1016/j.epsl.2009.05.006

Antonelli, M.A., DePaolo, D.J., Chacko, T., Grew, E.S., Rubatto, D., 2018. Radiogenic Ca isotopes confirm post-formation K depletion of lower crust. Geochemical Perspect. Lett. *(re-submitted with revisions)*

Antonelli, M.A., Mittal, T., McCarthy, A., Tripoli, B.A., Watkins, J.M., DePaolo, D.J., 2019a. Ca isotopes indicate rapid disequilibrium crystal growth in volcanic and sub-volcanic systems. Earth Planet. Sci. Lett. *(in prep.)*

Antonelli, M.A., Pester, N.J., Brown, S.T., DePaolo, D.J., 2017. Effect of paleoseawater composition on hydrothermal exchange in midocean ridges. Proc. Natl. Acad. Sci. 114, 201709145. https://doi.org/10.1073/pnas.1709145114

Antonelli, M.A., Schiller, M., Schauble, E.A., Mittal, T., DePaolo, D.J., Chacko, T., Grew, E.S., Tripoli, B., 2019b. Kinetic and equilibrium Ca isotope effects in high-T rocks and minerals. Earth Planet. Sci. Lett. *(submitted)*

Aradóttir, E.S.P., Sigfússon, B., Sonnenthal, E.L., Björnsson, G., Jónsson, H., 2013. Dynamics of basaltic glass dissolution - Capturing microscopic effects in continuum scale models. Geochim. Cosmochim. Acta 121, 311–327. https://doi.org/10.1016/j.gca.2013.04.031

Aranovich, L.Y., Makhluf, a. R., Manning, C.E., Newton, R.C., Touret, J.L.R., 2016. Fluids, Melting, Granulites and Granites: A Controversy - Reply to the Commentary of J.D. Clemens, I.S. Buick and G. Stevens. Precambrian Res. 278, 400–404. https://doi.org/10.1016/j.precamres.2016.03.020

Aulbach, S., Krauss, C., Creaser, R.A., Stachel, T., Heaman, L.M., Matveev, S., Chacko, T., 2010. Granulite sulphides as tracers of lower crustal origin and evolution: An example from the Slave craton, Canada. Geochim. Cosmochim. Acta 74, 5368–5381. https://doi.org/10.1016/j.gca.2010.06.005

Bach, W., Humphris, S.E., 1999. Relationship between the Sr and O isotope compositions of hydrothermal fluids and the spreading and magma-supply rates at oceanic spreading centers. Geology 27, 1067–1070. https://doi.org/10.1130/0091-7613(1999)027<1067:RBTSAO>2.3.CO

Bachmann, O., Bergantz, G.W., 2008. Rhyolites and their source mushes across tectonic settings. J. Petrol. 49, 2277–2285. https://doi.org/10.1093/petrology/egn068

Bachmann, O., Miller, C.F., de Silva, S.L., 2007. The volcanic-plutonic connection as a stage for understanding crustal magmatism. J. Volcanol. Geotherm. Res. 167, 1–23. https://doi.org/10.1016/j.jvolgeores.2007.08.002

Barker, a. K., Coogan, L. a., Gillis, K.M., 2010. Insights into the behaviour of sulphur in mid-ocean ridge axial hydrothermal systems from the composition of the sheeted dyke complex at Pito Deep. Chem. Geol. 275, 105–115. https://doi.org/10.1016/j.chemgeo.2010.05.003

Bartoli, O., 2017. Phase equilibria modelling of residual migmatites and granulites: An evaluation of the melt-reintegration approach. J. Metamorph. Geol. 35, 919–942. https://doi.org/10.1111/jmg.12261

Bartoli, O., Acosta-Vigil, A., Ferrero, S., Cesare, B., 2016. Granitoid magmas preserved as melt inclusions in high-grade metamorphic rocks. Am. Mineral. 101, 1543–1559. https://doi.org/10.2138/am-2016-5541CCBYNCND

Bernasconi, S.M., Meier, I., Wohlwend, S., Brack, P., Hochuli, P.A., Bläsi, H., Wortmann, U.G., Ramseyer, K., 2017. An evaporite-based high-resolution sulfur isotope record of Late Permian and Triassic seawater sulfate. Geochim. Cosmochim. Acta 204, 331–349. https://doi.org/10.1016/j.gca.2017.01.047

Berndt, M.E., Seyfried, W.E., Janecky, D.R., 1989. Plagioclase and epidote buffering of cation ratios in mid-ocean ridge hydrothermal fluids: Experimental results in and near the supercritical region. Geochim. Cosmochim. Acta 53, 2283–2300. https://doi.org/10.1016/0016-7037(89)90351-7

Berndt, M.E., Seyfried, W.E.J., Beck, J.W., 1988. Hydrothermal alteration processes at midocean ridges: Experimental and theoretical constraints from Ca and Sr exchange reactions and Sr isotopic ratios. J. Geophys. Res. 93, 4573. https://doi.org/10.1029/JB093iB05p04573

Berner, R. a., Kothavala, Z., 2001. Geocarb III: A revised model of atmospheric CO2 over phanerozoic time. Am. J. Sci. 301, 182–204. https://doi.org/10.2475/ajs.294.1.56

Bethke, C.M., 2008. Geochemical and Biogeochemical Reaction Modeling, 2nd ed, Geochemical and Biogeochemical Reaction Modeling. Cambridge Univeristy Press, New York. https://doi.org/10.1017/CBO9781107415324.004

Bevan, J.C., 2004. Archaean orbicular granitoids from Boogardie, near Mt Magnet, in: Western Australia: Dynamic Earth: Past, Present and Future: Geological Society of Australia.

Bevan, J.C., Bevan, A.W.R., 2009. Nature and origin of the orbicular granodiorite from Boogardie Station, Western Australia. Aust. Gemmol. 23, 373–432.

Bickle, M.J., Teagle, D. a H., 1992. Strontium alteration in the Troodos ophiolite: implications for fluid fluxes and geochemical transport in mid-ocean ridge hydrothermal systems. Earth Planet. Sci. Lett. 113, 219–237. https://doi.org/10.1016/0012-821X(92)90221-G

Bigeleisen, J., Mayer, M.G., 1947. Calculation of Equilibrium Constants for Isotopic Exchange Reactions. J. Chem. Phys. 15, 261–267. https://doi.org/10.1063/1.1746492

Bischoff, J.L., Rosenbauer, R.J., 1983. A note on the chemistry of seawater in the range 350 -500 C. Geochim. Cosmochim. Acta 47, 139–144. https://doi.org/10.1016/0016-7037(83)90098-4

Bischoff, J.L., Seyfried, W.E.J., 1978. Hydrothermal chemistry of seawater from 25 degrees to 350 degrees C. Am. J. Sci. 278, 838–860. https://doi.org/10.2475/ajs.278.6.838

Blanchard, M., Dauphas, N., Hu, M.Y., Roskosz, M., Alp, E.E., Golden, D.C., Sio, C.K., Tissot, F.L.H., Zhao, J., Gao, L., Morris, R. V., Fornace, M., Floris, a., Lazzeri, M., Balan, E., 2015. Reduced partition function ratios of iron and oxygen in goethite. Geochim. Cosmochim. Acta 151, 19–33. https://doi.org/10.1016/j.gca.2014.12.006

Blättler, C.L., Higgins, J.A., 2014. Calcium isotopes in evaporites record variations in Phanerozoic seawater SO4 and Ca. Geology 42, 711–714. https://doi.org/10.1130/G35721.1

Bourg, I.C., Richter, F.M., Christensen, J.N., Sposito, G., 2010. Isotopic mass dependence of metal cation diffusion coefficients in liquid water. Geochim. Cosmochim. Acta 74, 2249–2256. https://doi.org/10.1016/j.gca.2010.01.024

Brey, G.P., Kohler, T., 1990. Geothermobarometry in 4-phase lherzolites .2. New thermobarometers, and practical assessment of existing thermobarometers. J. Petrol. 31, 1353–1378.

Brown, M., 2007. Metamorphic Conditions in Orogenic Belts: A Record of Secular Change. Int. Geol. Rev. 49, 193–234. https://doi.org/10.2747/0020-6814.49.3.193

Brown, M., 2006. Duality of thermal regimes is the distinctive characteristics of plate tectonics since the Neoarchean. Geology 34, 961–964. https://doi.org/10.1130/G22853A.1

Brown, M., 2002. Retrograde processes in migmatites and granulites revisited. J. Metamorph. Geol. 20, 25–40. https://doi.org/10.1046/j.0263-4929.2001.00362.x

Brugger, C.R., Hammer, J.E., 2010. Crystal size distribution analysis of plagioclase in experimentally decompressed hydrous rhyodacite magma. Earth Planet. Sci. Lett. 300, 246–254. https://doi.org/10.1016/j.epsl.2010.09.046

Burgisser, A., Bergantz, G.W., 2011. A rapid mechanism to remobilize and homogenize highly crystalline magma bodies. Nature 471, 212–217. https://doi.org/10.1038/nature09799

Butterfield, D.A., Jonasson, I.R., Massoth, G.J., Feely, R.A., Roe, K.K., Embley, R.E., Holden, J.F., McDuff, R.E., Lilley, M.D., Delaney, J.R., 1997. Seafloor eruptions and evolution of hydrothermal fluid chemistry. Philos. Trans. R. Soc. A Math. Phys. Eng. Sci. 355, 369–386. https://doi.org/10.1098/rsta.1997.0013

Butterfield, D.A., Massoth, G.J., 1994. Geochemistry of north Cleft segment vent fluids: Temporal changes in chlorinity and their possible relation to recent volcanism. J. Geophys. Res. Solid Earth 99, 4951–4968. https://doi.org/10.1029/93JB02798

Butterfield, D.A., Massoth, G.J., McDuff, R.E., Lupton, J.E., Lilley, M.D., 1990. Geochemistry of hydrothermal fluids from Axial Seamount hydrothermal emissions study vent field, Juan de Fuca Ridge: Subseafloor boiling and subsequent fluid-rock interaction. J. Geophys. Res. 95, 12895. https://doi.org/10.1029/JB095iB08p12895

Butterfield, D.A., McDuff, R.E., Mottl, M.J., Lilley, M.D., Lupton, J.E., Massoth, G.J., 1994. Gradients in the composition of hydrothermal fluids from the Endeavour segment vent field: Phase separation and brine loss. J. Geophys. Res. Solid Earth 99, 9561–9583. https://doi.org/10.1029/93JB03132

Campbell, A.C., Palmer, M.R., Klinkhammer, G.P., Bowers, T.S., Edmond, J.M., Lawrence, J.R., Casey, J.F., Thompson, G., Humphris, S., Rona, P., Karson, J.A., 1988. Chemistry of hot springs on the Mid-Atlantic Ridge. Nature 335, 514–519. https://doi.org/10.1038/335514a0

Canfield, D.E., 2004. The evolution of the Earth surface sulfur reservoir. Am. J. Sci. 304, 839–861. https://doi.org/10.2475/ajs.304.10.839

Carlson, W.D., 2006. Rates of Fe, Mg, Mn, and Ca diffusion in garnet. At. Mineral. 91, 1–11. https://doi.org/10.2138/am.2006.2043

Carlson, W.D., 2002. Scales of disequilibrium and rates of equilibration during metamorphism. Am. Mineral. 87, 185–204. https://doi.org/10.2138/am-2002-2-301

Caro, G., Papanastassiou, D. a., Wasserburg, G.J., 2010. 40K-40Ca isotopic constraints on the oceanic calcium cycle. Earth Planet. Sci. Lett. 296, 124–132. https://doi.org/10.1016/j.epsl.2010.05.001

Castro, A., Corretgé, L.G., El-Biad, M., El-Hmidi, H., Ferńndez, C., Patĩo Douce, A.E., 2000. Experimental constraints on Hercynian anatexis in the Iberian Massif, Spain. J. Petrol. 41, 1471–1488. https://doi.org/10.1093/petrology/41.10.1471

Castro, A., Patiño Douce, A.E., Corretgé, L.G., De La Rosa, J.D., El-Biad, M., El-Hmidi, H.H., 1999. Origin of peraluminous granites and granodiorites, Iberian massif, Spain: An experimental test of granite petrogenesis. Contrib. to Mineral. Petrol. 135, 255–276. https://doi.org/10.1007/s004100050511

Cesare, B., Ferrero, S., Salvioli-Mariani, E., Pedron, D., Cavallo, A., 2009. “Nanogranite” and glassy inclusions: The anatectic melt in migmatites and granulites. Geology 37, 627–630. https://doi.org/10.1130/G25759A.1

Charlou, J.., Donval, J.., Douville, E., Jean-Baptiste, P., Radford-Knoery, J., Fouquet, Y., Dapoigny, A., Stievenard, M., 2000. Compared geochemical signatures and the evolution of Menez Gwen (37°50′N) and Lucky Strike (37°17′N) hydrothermal fluids, south of the Azores Triple Junction on the Mid-Atlantic Ridge. Chem. Geol. 171, 49–75. https://doi.org/10.1016/S0009-2541(00)00244-8

Charlou, J.., Donval, J.., Fouquet, Y., Jean-Baptiste, P., Holm, N., 2002. Geochemistry of high H2 and CH4 vent fluids issuing from ultramafic rocks at the Rainbow hydrothermal field (36°14′N, MAR). Chem. Geol. 191, 345–359. https://doi.org/10.1016/S0009-2541(02)00134-1

Charlou, J.L., Fouquet, Y., Donval, J.P., Auzende, J.M., Jean-Baptiste, P., Stievenard, M., Michel, S., 1996. Mineral and gas chemistry of hydrothermal fluids on an ultrafast spreading ridge: East Pacific Rise, 17° to 19°S (Naudur cruise, 1993) phase separation processes controlled by volcanic and tectonic activity. J. Geophys. Res. Solid Earth 101, 15899–15919. https://doi.org/10.1029/96JB00880

Chen, C., Liu, Y., Feng, L., Foley, S.F., Zhou, L., Ducea, M.N., Hu, Z., 2018. Calcium isotope evidence for subduction-enriched lithospheric mantle under the northern North China Craton. Geochim. Cosmochim. Acta 238, 55–67. https://doi.org/10.1016/j.gca.2018.06.038

Chopra, R., Richter, F.M., Bruce Watson, E., Scullard, C.R., 2012. Magnesium isotope fractionation by chemical diffusion in natural settings and in laboratory analogues. Geochim. Cosmochim. Acta 88, 1–18. https://doi.org/10.1016/j.gca.2012.03.039

Clemens, J.D., Buick, I.S., Stevens, G., 2016. Fluids, melting, granulites and granites: A commentary. Precambrian Res. 278, 394–399. https://doi.org/10.1016/j.precamres.2016.01.001

Clynne, M.A., 1999. A complex magma mixing origin for rocks erupted in 1915, Lassen Peak, California. J. Petrol. 40, 105–132. https://doi.org/10.1093/petroj/40.1.105

Coggon, R.M., Teagle, D.A.H., Smith-Duque, C.E., Alt, J.C., Cooper, M.J., 2010. Reconstructing Past Seawater Mg/Ca and Sr/Ca from Mid-Ocean Ridge Flank Calcium Carbonate Veins. Science (80-.). 327, 1114–1117. https://doi.org/10.1126/science.1182252

Coogan, L. a., Dosso, S., 2012. An internally consistent, probabilistic, determination of ridge-axis hydrothermal fluxes from basalt-hosted systems. Earth Planet. Sci. Lett. 323–324, 92–101. https://doi.org/10.1016/j.epsl.2012.01.017

Coogan, L. a., Dosso, S.E., 2015. Alteration of ocean crust provides a strong temperature dependent feedback on the geological carbon cycle and is a primary driver of the Sr-isotopic composition of seawater. Earth Planet. Sci. Lett. 415, 38–46. https://doi.org/10.1016/j.epsl.2015.01.027

Coogan, L.A., 2009. Altered oceanic crust as an inorganic record of paleoseawater Sr concentration. Geochemistry, Geophys. Geosystems 10.

https://doi.org/10.1029/2008GC002341

Cooper, K., 2006. Crystal ages and timescales of magma reservoir processes. Geochim. Cosmochim. Acta 70, A111–A111. https://doi.org/10.1016/j.gca.2006.06.135

Cooper, K.M., Kent, A.J.R., 2014. Rapid remobilization of magmatic crystals kept in cold storage. Nature 506, 480–483. https://doi.org/10.1038/nature12991

Crowe, S.A., Paris, G., Katsev, S., Jones, C., Kim, S.-T., Zerkle, A.L., Nomosatryo, S., Fowle, D.A., Adkins, J.F., Sessions, A.L., Farquhar, J., Canfield, D.E., 2014. Sulfate was a trace constituent of Archean seawater. Science (80-.). 346, 735–739. https://doi.org/10.1126/science.1258966

Dauphas, N., Roskosz, M., Alp, E.E., Golden, D.C., Sio, C.K., Tissot, F.L.H., Hu, M.Y., Zhao, J., Gao, L., Morris, R. V., 2012. A general moment NRIXS approach to the determination of equilibrium Fe isotopic fractionation factors: Application to goethite and jarosite. Geochim. Cosmochim. Acta 94, 254–275. https://doi.org/10.1016/j.gca.2012.06.013

Davis, J.W., Coleman, D.S., Gracely, J.T., Gaschnig, R., Stearns, M., 2012. Magma accumulation rates and thermal histories of plutons of the Sierra Nevada batholith, CA. Contrib. to Mineral. Petrol. 163, 449–465. https://doi.org/10.1007/s00410-011-0683-7

Davis, W.J., Canil, D., MacKenzie, J.M., Carbno, G.B., 2003. Petrology and U–Pb geochronology of lower crustal xenoliths and the development of a craton, Slave Province, Canada. Lithos 71, 541–573. https://doi.org/10.1016/S0024-4937(03)00130-0

DePaolo, D.J., 2011. Surface kinetic model for isotopic and trace element fractionation during precipitation of calcite from aqueous solutions. Geochim. Cosmochim. Acta 75, 1039–1056. https://doi.org/10.1016/j.gca.2010.11.020

DePaolo, D.J., 2006. Isotopic effects in fracture-dominated reactive fluid-rock systems. Geochim. Cosmochim. Acta 70, 1077–1096. https://doi.org/10.1016/j.gca.2005.11.022

DePaolo, D.J., 2004. Calcium Isotopic Variations Produced by Biological, Kinetic, Radiogenic and Nucleosynthetic Processes. Rev. Mineral. Geochemistry 55, 255–288. https://doi.org/10.2138/gsrmg.55.1.255

DePaolo, D.J., Manton, W.I., Grew, E.S., Halpern, M., 1982. Sm–Nd, Rb–Sr and U–Th–Pb systematics of granulite facies rocks from Fyfe Hills, Enderby Land, Antarctica. Nature 298, 614–618. https://doi.org/10.1038/298614a0

DePaolo, D.J., Wasserburg, G.J., 1979. Sm-Nd age of the Stillwater complex and the mantle evolution curve for neodymium. Geochim. Cosmochim. Acta 43, 999–1008. https://doi.org/10.1016/0016-7037(79)90089-9

Dickson, J. a D., 2002. Fossil Echinoderms As Monitor of the Mg/Ca Ratio of Phanerozoic Oceans. Science (80-.). 298, 1222–1224. https://doi.org/10.1126/science.1075882

Dohmen, R., Milke, R., 2010. Diffusion in Polycrystalline Materials: Grain Boundaries, Mathematical Models, and Experimental Data. Rev. Mineral. Geochemistry 72, 921–970. https://doi.org/10.2138/rmg.2010.72.21

Druitt, T.H., Costa, F., Deloule, E., Dungan, M., Scaillet, B., 2012. Decadal to monthly timescales of magma transfer and reservoir growth at a caldera volcano. Nature 482, 77–80. https://doi.org/10.1038/nature10706

Edmond, J.M., Campbell, A.C., Palmer, M.R., Klinkhammer, G.P., German, C.R., Edmonds, H.N., Elderfield, H., Thompson, G., Rona, P., 1995. Time series studies of vent fluids from the TAG and MARK sites (1986, 1990) Mid-Atlantic Ridge: a new solution chemistry model and a mechanism for Cu/Zn zonation in massive sulphide orebodies. Geol. Soc. London, Spec. Publ. 87, 77–86. https://doi.org/10.1144/GSL.SP.1995.087.01.07

Elcombe, M.M., Pryor, A.W., 1970. The lattice dynamics of calcium fluoride. J. Phys. C Solid State Phys. https://doi.org/10.1088/0022-3719/3/3/002

Elderfield, H., Schultz, a., 1996. Mid-Ocean Ridge Hydrothermal Fluxes and the Chemical Composition of the Ocean. Annu. Rev. Earth Planet. Sci. 24, 191–224. https://doi.org/10.1146/annurev.earth.24.1.191

Elderfield, H., Wheat, C.G., Mottl, M.J., Monnin, C., Spiro, B., 1999. Fluid and geochemical transport through oceanic crust: a transect across the eastern flank of the Juan de Fuca Ridge. Earth Planet. Sci. Lett. 172, 151–165. https://doi.org/10.1016/S0012-821X(99)00191-0

Engebretson, D.C., Kelley, K.P., Cashman, H.J., Richards, M.A., 1992. 180 Million Years of Subduction. GSA Today.

Ewing, T.A., Hermann, J., Rubatto, D., 2013. The robustness of the Zr-in-rutile and Ti-in-zircon thermometers during high-temperature metamorphism (Ivrea-Verbano Zone, northern Italy). Contrib. to Mineral. Petrol. https://doi.org/10.1007/s00410-012-0834-5

Ewing, T.A., Rubatto, D., Hermann, J., 2014. Hafnium isotopes and Zr/Hf of rutile and zircon from lower crustal metapelites (Ivrea-Verbano Zone, Italy): Implications for chemical differentiation of the crust. Earth Planet. Sci. Lett. 389, 106–118. https://doi.org/10.1016/j.epsl.2013.12.029

Fantle, M.S., Tipper, E.T., 2014. Calcium isotopes in the global biogeochemical Ca cycle: Implications for development of a Ca isotope proxy. Earth-Science Rev. 129, 148–177. https://doi.org/10.1016/j.earscirev.2013.10.004

Farquhar, J., Chacko, T., Ellis, D.J., 1996. Preservation of oxygen isotope compositions in granulites from Northwestern Canada and Enderby Land, Antarctica: implications for high-temperature isotopic thermometry. Contrib. to Mineral. Petrol. 125, 213–224. https://doi.org/10.1007/s004100050217

Farver, J.R., Yund, R.A., 1995. Grain-Boundary Diffusion of Oxygen, Potassium and Calcium in Natural and Hot-Pressed Feldspar Aggregates. Contrib. to Mineral. Petrol. 118, 340–355. https://doi.org/10.1007/s004100050019

Feng, C., Qin, T., Huang, S., Wu, Z., Huang, F., 2014. First-principles investigations of equilibrium calcium isotope fractionation between clinopyroxene and Ca-doped orthopyroxene. Geochim. Cosmochim. Acta 143, 132–142. https://doi.org/10.1016/j.gca.2014.06.002

Ferrero, S., Godard, G., Palmieri, R., Wunder, B., Cesare, B., 2018. Partial melting of ultramafic granulites from Dronning Maud Land, Antartica: constraints from melt inclusions and thermodynamic modeling. Am. Mineral. 103, 610–622. https://doi.org/10.2138/am-2018-6214

Fonneland-Jorgensen, H., Furnes, H., Muehlenbachs, K., Dilek, Y., 2005. Hydrothermal alteration and tectonic evolution of an intermediate- to fast-spreading back-arc oceanic crust: Late Ordovician Solund-Stavfjord ophiolite, western Norway. Isl. Arc 14, 517–541. https://doi.org/10.1111/j.1440-1738.2005.00481.x

Foustoukos, D.I., Pester, N.J., Ding, K., Seyfried, W.E., 2009. Dissolved carbon species in associated diffuse and focused flow hydrothermal vents at the Main Endeavour Field, Juan de Fuca Ridge: Phase equilibria and kinetic constraints. Geochemistry, Geophys. Geosystems 10, n/a-n/a. https://doi.org/10.1029/2009GC002472

Foustoukos, D.I.I., Seyfried, W.E.E., 2007. Quartz solubility in the two-phase and critical region of the NaCl–KCl–H2O system: Implications for submarine hydrothermal vent systems at 9°50′N East Pacific Rise. Geochim. Cosmochim. Acta 71, 186–201. https://doi.org/10.1016/j.gca.2006.08.038

Friedman, J., 1991. Multivariate adaptive regression splines. Ann. Stat. 19, 1–67.

Frost, B.R., Chacko, T., 1989. The Granulite Uncertainty Principle: Limitations on Thermobarometry in Granulites. J. Geol. 97, 435–450. https://doi.org/10.1086/629321

Gaffin, S., 1987. Ridge volume dependence on seafloor generation rate and inversion using long term sealevel change. Am. J. Sci. https://doi.org/10.2475/ajs.287.6.596

Gallant, R.M., Von Damm, K.L., 2006. Geochemical controls on hydrothermal fluids from the Kairei and Edmond Vent Fields, 23°-25°S, Central Indian Ridge. Geochemistry, Geophys. Geosystems 7, n/a-n/a. https://doi.org/10.1029/2005GC001067

Gao, P., Zheng, Y.F., Zhao, Z.F., 2016. Experimental melts from crustal rocks: A lithochemical constraint on granite petrogenesis. Lithos 266–267, 133–157. https://doi.org/10.1016/j.lithos.2016.10.005

García-Arias, M., 2018. Decoupled Ca and Fe + Mg content of S-type granites: An investigation on the factors that control the Ca budget of S-type granites. Lithos 318–319, 30–46. https://doi.org/10.1016/j.lithos.2018.08.004

Garcia-Arias, M., Stevens, G., 2017. Phase equilibrium modelling of granite magma petrogenesis: A. An evaluation of the magma compositions produced by crystal entrainment in the source. Lithos 277, 131–153. https://doi.org/10.1016/j.lithos.2016.09.028

Garrity, K.F., Bennett, J.W., Rabe, K.M., Vanderbilt, D., 2014. Pseudopotentials for high-throughput DFT calculations. Comput. Mater. Sci. https://doi.org/10.1016/j.commatsci.2013.08.053

Gelman, S.E., Gutiérrez, F.J., Bachmann, O., 2013. On the longevity of large upper crustal silicic magma reservoirs. Geology 41, 759–762. https://doi.org/10.1130/G34241.1

German, C.R., Seyfried, W.E., 2014. Hydrothermal Processes, 2nd ed, The Oceans and Marine

Geochemistry. Elsevier Ltd. https://doi.org/10.1016/B978-0-08-095975-7.00607-0

Getty, S.R., Deaolo, D.J., 1995. Quaternary geochronology using the UThPb method. Geochim. Cosmochim. Acta 59, 3267–3272. https://doi.org/10.1016/0016-7037(95)00197-8

Giannozzi, P., Baroni, S., Bonini, N., Calandra, M., Car, R., Cavazzoni, C., Ceresoli, D., Chiarotti, G.L., Cococcioni, M., Dabo, I., Dal Corso, A., De Gironcoli, S., Fabris, S., Fratesi, G., Gebauer, R., Gerstmann, U., Gougoussis, C., Kokalj, A., Lazzeri, M., Martin-Samos, L., Marzari, N., Mauri, F., Mazzarello, R., Paolini, S., Pasquarello, A., Paulatto, L., Sbraccia, C., Scandolo, S., Sclauzero, G., Seitsonen, A.P., Smogunov, A., Umari, P., Wentzcovitch, R.M., 2009. QUANTUM ESPRESSO: A modular and open-source software project for quantum simulations of materials. J. Phys. Condens. Matter 21. https://doi.org/10.1088/0953-8984/21/39/395502

Giletti, B.J., 1994. Isotopic Equilibrium/Disequilibrium and Diffusion Kinetics in Feldspars, in: Parsons, I. (Ed.), Feldspars and Their Reactions. Springer Netherlands, Dordrecht, pp. 351–382. https://doi.org/10.1007/978-94-011-1106-5_9

Gillis, K.M., Coogan, L. a., 2011. Secular variation in carbon uptake into the ocean crust. Earth Planet. Sci. Lett. 302, 385–392. https://doi.org/10.1016/j.epsl.2010.12.030

Gothmann, A.M., Stolarski, J., Adkins, J.F., Schoene, B., Dennis, K.J., Schrag, D.P., Mazur, M., Bender, M.L., 2015. Fossil corals as an archive of secular variations in seawater chemistry since the Mesozoic. Geochim. Cosmochim. Acta 160, 188–208. https://doi.org/10.1016/j.gca.2015.03.018

Grant, S.M., 1988. Diffusion models for corona formation in metagabbros from the Western Grenville Province, Canada. Contrib. to Mineral. Petrol. 98, 49–63. https://doi.org/10.1007/BF00371909

Green, E.C.R., White, R.W., Diener, J.F.A., Powell, R., Holland, T.J.B., Palin, R.M., 2016. Activity–composition relations for the calculation of partial melting equilibria in metabasic rocks. J. Metamorph. Geol. 34, 845–869. https://doi.org/10.1111/jmg.12211

Griffith, E.M., Schauble, E.A., Bullen, T.D., Paytan, A., 2008. Characterization of calcium isotopes in natural and synthetic barite. Geochim. Cosmochim. Acta 72, 5641–5658. https://doi.org/10.1016/j.gca.2008.08.010

Grimaud, D., Michard, A., Michard, G., 1984. Composition chimique et composition isotopique du strontium dans les eaux hydrothermales sous-marines de la dosale Est Pacifique a 13° Nord. C. R. Acad. Sc. Paris 299, 865–870.

Grove, T.L., Baker, M.B., Kinzler, R.J., 1984. Coupled CaAl-NaSi diffusion in plagioclase feldspar: Experiments and applications to cooling rate speedometry. Geochim. Cosmochim. Acta. https://doi.org/10.1016/0016-7037(84)90391-0

Gudbrandsson, S., Wolff-Boenisch, D., Gislason, S.R., Oelkers, E.H., 2011. An experimental study of crystalline basalt dissolution from 2pH11 and temperatures from 5 to 75 C. Geochim. Cosmochim. Acta 75, 5496–5509. https://doi.org/10.1016/j.gca.2011.06.035

Guernina, S., Sawyer, E.W., 2003. Large-scale melt-depletion in granulite terranes: An example from the Archean Ashuanipi subprovince of Quebec. J. Metamorph. Geol. 21, 181–201.

https://doi.org/10.1046/j.1525-1314.2003.00436.x

Hacker, B.R., Kelemen, P.B., Behn, M.D., 2015. Continental Lower Crust. Annu. Rev. Earth Planet. Sci. 43, 167–205. https://doi.org/10.1146/annurev-earth-050212-124117

Halevy, I., Peters, S.E., Fischer, W.W., 2012. Sulfate Burial Constraints on the Phanerozoic Sulfur Cycle. Science (80-.). 337, 331–334. https://doi.org/10.1126/science.1220224

Halverson, G.P., Dudás, F.Ö., Maloof, A.C., Bowring, S. a., 2007. Evolution of the 87Sr/86Sr composition of Neoproterozoic seawater. Palaeogeogr. Palaeoclimatol. Palaeoecol. 256, 103–129. https://doi.org/10.1016/j.palaeo.2007.02.028

Hammer, J.E., Rutherford, M.J., 2002. An experimental study of the kinetics of decompression-induced crystallization in silicic melt. J. Geophys. Res. Solid Earth 107, ECV 8-1-ECV 8-24. https://doi.org/10.1029/2001JB000281

Harley, S.L., 2016. A matter of time: The importance of the duration of UHT metamorphism. J. Mineral. Petrol. Sci. 111, 50–72. https://doi.org/10.2465/jmps.160128

Haymon, R.M., Kastner, M., 1986. Caminite : A new magnesium-hydroxide-sulfate-hydrate mineral found in a submarine hydrothermal deposit, East Pacific Rise , 21'N. Am. Mineral. 71, 819–825.

He, Y., Wang, Y., Zhu, C., Huang, S., Li, S., 2016. Mass-Independent and Mass-Dependent Ca Isotopic Compositions of Thirteen Geological Reference Materials Measured by Thermal Ionisation Mass Spectrometry. Geostand. Geoanalytical Res. 1–20. https://doi.org/10.1111/ggr.12153

Hermann, J., Rubatto, D., 2014. Subduction of Continental Crust to Mantle Depth: Geochemistry of Ultrahigh-Pressure Rocks. Geochemistry of Ultrahigh-Pressure Rocks, 2nd ed, Treatise on Geochemistry: Second Edition. Elsevier Ltd. https://doi.org/10.1016/B978-0-08-095975-7.00309-0

Hofmann, A.W., Magaritz, M., 1977. Diffusion of Ca, Sr, Ba, and Co in a basalt melt: Implications for the geochemistry of the mantle. J. Geophys. Res. 82, 5432–5440. https://doi.org/10.1029/JB082i033p05432

Holycross, M.E., Watson, E.B., Richter, F.M., Villeneuve, J., 2018. Diffusive fractionation of Li isotopes in wet, silicic melts. Geochemical Perspect. Lett. 39–42. https://doi.org/10.7185/geochemlet.1807

Horie, K., Hokada, T., Hiroi, Y., Motoyoshi, Y., Shiraishi, K., 2012. Contrasting Archaean crustal records in western part of the Napier Complex, East Antarctica: New constraints from SHRIMP geochronology. Gondwana Res. 21, 829–837. https://doi.org/10.1016/j.gr.2011.08.013

Horita, J., Zimmermann, H., Holland, H.D., 2002. Chemical evolution of seawater during the Phanerozoic: Implications from the record of marine evaporites. Geochim. Cosmochim. Acta 66, 3733–3756. https://doi.org/10.1016/S0016-7037(01)00884-5

Huang, F., Chakraborty, P., Lundstrom, C.C.C., Holmden, C.E., Glessner, J.J.G.J.G., Kieffer, S.W., Lesher, C.E.E., 2010. Isotope fractionation in silicate melts by thermal diffusion.

Nature 464, 396–400. https://doi.org/10.1038/nature08840

Huang, S., Farkaš, J., Jacobsen, S.B., 2011. Stable calcium isotopic compositions of Hawaiian shield lavas: Evidence for recycling of ancient marine carbonates into the mantle. Geochim. Cosmochim. Acta 75, 4987–4997. https://doi.org/10.1016/j.gca.2011.06.010

Huang, S., Farkaš, J., Jacobsen, S.B., 2010. Calcium isotopic fractionation between clinopyroxene and orthopyroxene from mantle peridotites. Earth Planet. Sci. Lett. 292, 337–344. https://doi.org/10.1016/j.epsl.2010.01.042

Huber, C., Bachmann, O., Dufek, J., 2012. Crystal-poor versus crystal-rich ignimbrites: A competition between stirring and reactivation. Geology 40, 115–118. https://doi.org/10.1130/G32425.1

Hudgins, J.A., Spray, J.G., Hawkes, C.D., 2011. Element diffusion rates in lunar granulitic breccias: Evidence for contact metamorphism on the Moon. Am. Mineral. 96, 1673–1685. https://doi.org/10.2138/am.2011.3640

Janecky, D.R., Seyfried, W.E., 1983. The solubility of magnesium-hydroxide-sulfate-hydrate in seawater at elevated temperatures and pressures. Am. J. Sci. 283, 831–860. https://doi.org/10.2475/ajs.283.8.831

Jerram, D.A., Dobson, K.J., Morgan, D.J., Pankhurst, M.J., 2018. The Petrogenesis of Magmatic Systems: Using Igneous Textures to Understand Magmatic Processes, Volcanic and Igneous Plumbing Systems. Elsevier Inc. https://doi.org/10.1016/B978-0-12-809749-6.00008-X

John, T., Gussone, N., Podladchikov, Y.Y., Bebout, G.E., Dohmen, R., Halama, R., Klemd, R., Magna, T., Seitz, H.M., 2012. Volcanic arcs fed by rapid pulsed fluid flow through subducting slabs. Nat. Geosci. 5, 489–492. https://doi.org/10.1038/ngeo1482

Kaercher, P., Militzer, B., Wenk, H.-R., 2014. Ab initio Calculations of Elastic Constants of Plagioclase feldespars. Am. Mineral. 99, 2344–2352. https://doi.org/10.2138/am-2014-4796

Kagoshima, T., Sano, Y., Takahata, N., Maruoka, T., Fischer, T.P., Hattori, K., 2015. Sulphur geodynamic cycle. Sci. Rep. 5, 8330. https://doi.org/10.1038/srep08330

Kang, J.T., Ionov, D.A., Liu, F., Zhang, C.L., Golovin, A. V., Qin, L.P., Zhang, Z.F., Huang, F., 2017. Calcium isotopic fractionation in mantle peridotites by melting and metasomatism and Ca isotope composition of the Bulk Silicate Earth. Earth Planet. Sci. Lett. 474, 128–137. https://doi.org/10.1016/j.epsl.2017.05.035

Kang, J.T., Zhu, H.L., Liu, Y.F., Liu, F., Wu, F., Hao, Y.T., Zhi, X.C., Zhang, Z.F., Huang, F., 2016. Calcium isotopic composition of mantle xenoliths and minerals from Eastern China. Geochim. Cosmochim. Acta 174, 335–344. https://doi.org/10.1016/j.gca.2015.11.039

Karlstrom, L., Rudolph, M.L., Manga, M., 2012. Caldera size modulated by the yield stress within a crystal-rich magma reservoir. Nat. Geosci. 5, 402–405. https://doi.org/10.1038/ngeo1453

Kawahata, H., Kusakabe, M., Kikuchi, Y., 1987. Strontium, oxygen, and hydrogen isotope geochemistry of hydrothermally altered and weathered rocks in DSDP Hole 504B, Costa Rica Rift. Earth Planet. Sci. Lett. 85, 343–355. https://doi.org/10.1016/0012-

821X(87)90132-4

Kawahata, H., Nohara, M., Ishizuka, H., Hasebe, S., Chiba, H., 2001. Sr isotope geochemistry and hydrothermal alteration of the Oman ophiolite. J. Geophys. Res. Solid Earth 106, 11083–11099. https://doi.org/10.1029/2000JB900456

Keller, L.M., Wirth, R., Rhede, D., Kunze, K., Abart, R., 2008. Asymmetrically zoned reaction rims: Assessment of grain boundary diffusivities and growth rates related to natural diffusion-controlled mineral reactions. J. Metamorph. Geol. 26, 99–120. https://doi.org/10.1111/j.1525-1314.2007.00747.x

Kelly, N.M., Harley, S.L., 2005. An integrated microtextural and chemical approach to zircon geochronology: Refining the Archaean history of the Napier Complex, east Antarctica. Contrib. to Mineral. Petrol. 149, 57–84. https://doi.org/10.1007/s00410-004-0635-6

Kelsey, D.E., Hand, M., 2015. On ultrahigh temperature crustal metamorphism: Phase equilibria, trace element thermometry, bulk composition, heat sources, timescales and tectonic settings. Geosci. Front. 6, 311–356. https://doi.org/10.1016/j.gsf.2014.09.006

Kerr, R.C., 1995. Convective crystal dissolution. Contrib. to Mineral. Petrol. 121, 237–246. https://doi.org/10.1007/BF02688239

Kristall, B., Jacobson, A.D., Hurtgen, M.T., 2017. Modeling the paleo-seawater radiogenic strontium isotope record: A case study of the Late Jurassic-Early Cretaceous. Palaeogeogr. Palaeoclimatol. Palaeoecol. 472, 163–176. https://doi.org/10.1016/j.palaeo.2017.01.048

Kuhn, T., Herzig, P.M., Hannington, M.D., Garbe-Schönberg, D., Stoffers, P., 2003. Origin of fluids and anhydrite precipitation in the sediment-hosted Grimsey hydrothermal field north of Iceland. Chem. Geol. 202, 5–21. https://doi.org/10.1016/S0009-2541(03)00207-9

Kumagai, H., Nakamura, K., Toki, T., Morishita, T., Okino, K., Ishibashi, J.I., Tsunogai, U., Kawagucci, S., Gamo, T., Shibuya, T., Sawaguchi, T., Neo, N., Joshima, M., Sato, T., Takai, K., 2008. Geological background of the Kairei and Edmond hydrothermal fields along the Central Indian Ridge: Implications of their vent fluids'distinct chemistry. Geofluids 8, 239–251. https://doi.org/10.1111/j.1468-8123.2008.00223.x

Kump, L.R., 2008. The role of seafloor hydrothermal systems in the evolution of seawater composition during the Phanerozoic, in: Magma to Microbe: Modeling Hydrothermal Processes at Oceanic Spreading Centers. pp. 275–283. https://doi.org/10.1029/178GM14

Kump, L.R., Seyfried, W.E., 2005. Hydrothermal Fe fluxes during the Precambrian: Effect of low oceanic sulfate concentrations and low hydrostatic pressure on the composition of black smokers. Earth Planet. Sci. Lett. 235, 654–662. https://doi.org/10.1016/j.epsl.2005.04.040

Kunz, B.E., Regis, D., Engi, M., 2018. Zircon ages in granulite facies rocks: decoupling from geochemistry above 850 °C? Contrib. to Mineral. Petrol. 173, 1–21. https://doi.org/10.1007/s00410-018-1454-5

Kusiak, M. a., Whitehouse, M.J., Wilde, S.A., Dunkley, D.J., Menneken, M., Nemchin, A. a., Clark, C., 2013. Changes in zircon chemistry during Archean UHT metamorphism in the Napier Complex, Antarctica. Am. J. Sci. 313, 933–967. https://doi.org/10.2475/09.2013.05]

Langtangen, H.P., Linge, S., 2017. Finite Difference Computing with PDEs, Texts in Computational Science and Engineering. Springer International Publishing, Cham. https://doi.org/10.1007/978-3-319-55456-3

LaTourrette, T., Wasserburg, G.J., Fahey, A.J., 1996. Self diffusion of Mg, Ca, Ba, Nd, Yb, Ti, Zr, and U in haplobasaltic melt. Geochim. Cosmochim. Acta 60, 1329–1340. https://doi.org/10.1016/0016-7037(96)00015-4

Lear, C.H., Elderfield, H., Wilson, P. a., 2003. A Cenozoic seawater Sr/Ca record from benthic foraminiferal calcite and its application in determining global weathering fluxes. Earth Planet. Sci. Lett. 208, 69–84. https://doi.org/10.1016/S0012-821X(02)01156-1

Leveson, D.J., 1966. Orbicular Rocks: A Review. Geol. Soc. Am. Bull. 77, 409–426.

Liu, F., Li, X., Wang, G., Liu, Y., Zhu, H., Kang, J., Huang, F., Sun, W., Xia, X., Zhang, Z., 2017. Marine Carbonate Component in the Mantle Beneath the Southeastern Tibetan Plateau: Evidence From Magnesium and Calcium Isotopes. J. Geophys. Res. Solid Earth 122, 9729–9744. https://doi.org/10.1002/2017JB014206

Loomis, A.A., 1983. Geology of the Fallen Leaf Lake 15’ quadrangle, El Dorado County, California. Calif. Div. Mines Geol.

Lowenstein, T.K., Hardie, L. a., Timofeeff, M.N., Demicco, R. V., 2003. Secular Variation in seawater Chemistry and the origin of calcium chloride basinal brines. Geology 31, 857–860.

Lowenstein, T.K., Kendall, B., Anbar, a. D., 2013. The Geologic History of Seawater, 2nd ed, Treatise on Geochemistry: Second Edition. Elsevier Ltd. https://doi.org/10.1016/B978-0-08-095975-7.00621-5

Lu, F., Anderson, A.T., Davis, A.M., 1995. Diffusional Gradients at the Crystal / Melt Interface and Their Effect on the Compositions of Melt Inclusions. J. Geol. 103, 591–597.

Madlakana, N., Stevens, G., 2018. Plagioclase disequilibrium induced during fluid-absent biotite-breakdown melting in metapelites. J. Metamorph. Geol. https://doi.org/10.1111/jmg.12429

Magna, T., Gussone, N., Mezger, K., 2015. The calcium isotope systematics of Mars. Earth Planet. Sci. Lett. 430, 86–94. https://doi.org/10.1016/j.epsl.2015.08.016

Marshall, B.D., DePaolo, D.J., 1989. Calcium isotopes in igneous rocks and the origin of granite. Geochim. Cosmochim. Acta 53, 917–922. https://doi.org/10.1016/0016-7037(89)90036-7

Marshall, B.D., DePaolo, D.J., 1982. Precise age determinations and petrogenetic studies using the KCa method. Geochim. Cosmochim. Acta 46, 2537–2545. https://doi.org/10.1016/0016-7037(82)90376-3

McCanta, M.C., Rutherford, M.J., Hammer, J.E., 2007. Pre-eruptive and syn-eruptive conditions in the Black Butte, California dacite: Insight into crystallization kinetics in a silicic magma system. J. Volcanol. Geotherm. Res. 160, 263–284. https://doi.org/10.1016/j.jvolgeores.2006.10.004

McCarthy, A., Müntener, O., 2017. Mineral growth in melt conduits as a mechanism for igneous layering in shallow arc plutons: mineral chemistry of Fisher Lake orbicules and comb layers (Sierra Nevada, USA). Contrib. to Mineral. Petrol. 172, 1–32. https://doi.org/10.1007/s00410-017-1371-z

McCarthy, A., Müntener, O., 2016. Comb layering monitors decompressing and fractionating hydrous mafic magmas in subvolcanic plumbing systems (Fisher Lake, Sierra Nevada, USA). J. Geophys. Res. Solid Earth 121, 8595–8621. https://doi.org/10.1002/2016JB013489

McCarthy, A., Müntener, O., Bouvier, A.S., Baumgartner, L., 2016. Melt extraction zones in shallow arc plutons: Insights from fisher lake orbicules (Sierra Nevada, Western USA). J. Petrol. 57, 2011–2052. https://doi.org/10.1093/petrology/egw068

McCoy-West, A.J., Fitton, J.G., Pons, M.L., Inglis, E.C., Williams, H.M., 2018. The Fe and Zn isotope composition of deep mantle source regions: Insights from Baffin Island picrites. Geochim. Cosmochim. Acta 238, 542–562. https://doi.org/10.1016/j.gca.2018.07.021

McCulloch, M.T., Gregory, R.T., Wasserburg, G.J., Taylor, H.P., 1981. Sm-Nd, Rb-Sr, and 18O/16O isotopic systematics in an oceanic crustal section: Evidence from the Samail Ophiolite. J. Geophys. Res. Solid Earth 86, 2721–2735. https://doi.org/10.1029/JB086iB04p02721

Méheut, M., Lazzeri, M., Balan, E., Mauri, F., 2007. Equilibrium isotopic fractionation in the kaolinite, quartz, water system: Prediction from first-principles density-functional theory. Geochim. Cosmochim. Acta 71, 3170–3181. https://doi.org/10.1016/j.gca.2007.04.012

Michard, G., Albarède, F., Michard, A., Minster, J.-F., Charlou, J.-L., Tan, N., 1984. Chemistry of solutions from the 13°N East Pacific Rise hydrothermal site. Earth Planet. Sci. Lett. 67, 297–307. https://doi.org/10.1016/0012-821X(84)90169-9

Miller, C.D., 1978. Holocene pyroclastic-flow deposits from Shastina and Black Butte, west of Mount Shasta, California. J. Res. U.S. Geol. Surv. 6, 611–624.

Mills, R.D., Simon, J.I., DePaolo, D.J., 2018. Calcium and neodymium radiogenic isotopes of igneous rocks: Tracing crustal contributions in felsic magmas related to super-eruptions and continental rifting. Earth Planet. Sci. Lett. 495, 242–250. https://doi.org/10.1016/j.epsl.2018.05.017

Mitchell, R.J., Harley, S.L., 2017. Zr-in-rutile resetting in aluminosilicate bearing ultra-high temperature granulites: Refining the record of cooling and hydration in the Napier Complex, Antarctica. Lithos 272–273, 128–146. https://doi.org/10.1016/j.lithos.2016.11.027

Moore, J.G., Lockwood, J.P., 1973. Origin of Comb Layering and Orbicular Structure, Sierra Nevada Batholith, California. Geol. Soc. Am. Bull. 84, 1–20. https://doi.org/10.1130/0016-7606(1973)84<1:OOCLAO>2.0.CO;2

Morse, S.A., 1984. Cation diffusion in plagioclase feldspar. Science (80-.). https://doi.org/10.1126/science.225.4661.504

Mottl, M.J., Wheat, C.G., 1994. Hydrothermal circulation through mid-ocean ridge flanks: Fluxes of heat and magnesium. Geochim. Cosmochim. Acta 58, 2225–2237.

https://doi.org/10.1016/0016-7037(94)90007-8

Moynier, F., Yin, Q.-Z., Schauble, E., 2011. Isotopic evidence of Cr partitioning into Earth's core. Science 331, 1417–1420. https://doi.org/10.1126/science.1199597

Muehlenbachs, K., Furnes, H., Fonneland, H.C., Hellevang, B., 2003. Ophiolites as faithful records of the oxygen isotope ratio of ancient seawater: the Solund-Stavfjord Ophiolite Complex as a Late Ordovician example. Geol. Soc. London, Spec. Publ. 218, 401–414. https://doi.org/10.1144/GSL.SP.2003.218.01.20

Nicoli, G., Stevens, G., Moyen, J.F., Vezinet, A., Mayne, M., 2017. Insights into the complexity of crustal differentiation: K2O-poor leucosomes within metasedimentary migmatites from the Southern Marginal Zone of the Limpopo Belt, South Africa. J. Metamorph. Geol. 35, 999–1022. https://doi.org/10.1111/jmg.12265

Olsen, M.B., Schiller, M., Krot, A.N., Bizzarro, M., 2013. Magnesium isotope evidence for single stage formation of CB chondrules by colliding planetesimals. Astrophys. J. 776, L1. https://doi.org/10.1088/2041-8205/776/1/L1

Ono, S., Shanks, W.C., Rouxel, O.J., Rumble, D., 2007. S-33 constraints on the seawater sulfate contribution in modern seafloor hydrothermal vent sulfides. Geochim. Cosmochim. Acta 71, 1170–1182. https://doi.org/10.1016/j.gca.2006.11.017

Ort, M.H., 1992. Orbicular volcanic rocks of Cerro Panizos: their origin and implications for orb formation. Geol. Soc. Am. Bull. 104, 1048–1058. https://doi.org/10.1130/0016-7606(1992)104<1048:OVROCP>2.3.CO;2

Palin, R.M., White, R.W., Green, E.C.R., 2016. Partial melting of metabasic rocks and the generation of tonalitic–trondhjemitic–granodioritic (TTG) crust in the Archaean: Constraints from phase equilibrium modelling. Precambrian Res. 287, 73–90. https://doi.org/10.1016/j.precamres.2016.11.001

Pape, J., Mezger, K., Robyr, M., 2016. A systematic evaluation of the Zr-in-rutile thermometer in ultra-high temperature (UHT) rocks. Contrib. to Mineral. Petrol. 171, 1–20. https://doi.org/10.1007/s00410-016-1254-8

Patiño Douce, a E., Beard, J.S., 1995. Dehydrations-melting of Biotite Gneiss ans Quarz Amphibolite from 3 to 15 kbar. J. Petrol. 36, 707–738.

Pehrsson, S.J., Chacko, T., Pilkington, M., Villeneuve, M.E., Bethune, K., 2000. Anton terrane revisited: Late Archean exhumation of a moderate pressure granulite terranc in the Western Slave Province. Geology 28, 1075–1078. https://doi.org/10.1130/0091-7613(2000)28<1075:ATRLAE>2.0.CO;2

Perdew, J.P., Burke, K., Ernzerhof, M., 1996. Generalized Gradient Approximation Made Simple. Phys. Rev. Lett. 77, 3865–3868. https://doi.org/10.1103/PhysRevLett.77.3865

Pester, N.J., Ding, K., Seyfried, W.E., 2015. Vapor–liquid partitioning of alkaline earth and transition metals in NaCl-dominated hydrothermal fluids: An experimental study from 360 to 465°C, near-critical to halite saturated conditions. Geochim. Cosmochim. Acta 168, 111–132. https://doi.org/10.1016/j.gca.2015.07.028

Pester, N.J., Ding, K., Seyfried, W.E., 2014. Magmatic eruptions and iron volatility in deep-sea hydrothermal fluids. Geology 42, 255–258. https://doi.org/10.1130/G35079.1

Pester, N.J., Reeves, E.P., Rough, M.E., Ding, K., Seewald, J.S., Seyfried, W.E., 2012. Subseafloor phase equilibria in high-temperature hydrothermal fluids of the Lucky Strike Seamount (Mid-Atlantic Ridge, 37°17′N). Geochim. Cosmochim. Acta 90, 303–322. https://doi.org/10.1016/j.gca.2012.05.018

Pester, N.J., Rough, M., Ding, K., Seyfried, W.E., 2011. A new Fe/Mn geothermometer for hydrothermal systems: Implications for high-salinity fluids at 13°N on the East Pacific Rise. Geochim. Cosmochim. Acta 75, 7881–7892. https://doi.org/10.1016/j.gca.2011.08.043

Pester, N.J., Syverson, D.D., Higgins, J.A., Seyfried, W.E.J., 2016. Ca and Sr isotope Systematics in mid-ocean ridge hydrothermal fluids, in: Abstract V53E-02, Fall Meeting, AGU, San Francisco, CA. p. 1.

Peters, M., Strauss, H., Farquhar, J., Ockert, C., Eickmann, B., Jost, C.L., 2010. Sulfur cycling at the Mid-Atlantic Ridge: A multiple sulfur isotope approach. Chem. Geol. 269, 180–196. https://doi.org/10.1016/j.chemgeo.2009.09.016

Pickering, J.M., Johnston, A.D., 1998. Fluid-absent melting behavior of a two-mica metapelite: Experimental constraints on the origin of Black Hills granite. J. Petrol. 39, 1787–1804. https://doi.org/10.1093/petroj/39.10.1787

Poldervaart, A., Taubeneck, W.H., 1959. Layered intrusions of Willow Lake type. Bull. Geol. Soc. Am. https://doi.org/10.1130/0016-7606(1959)70[1395:LIOWLT]2.0.CO;2

Pownall, J.M., Hall, R., Armstrong, R.A., Forster, M.A., 2014. Earth's youngest known ultrahigh-temperature granulites discovered on Seram, eastern Indonesia. Geology 42, 279–282. https://doi.org/10.1130/G35230.1

Prokoph, A., Shields, G.A., Veizer, J., 2008. Compilation and time-series analysis of a marine carbonate d18O, d13C, 87Sr/86Sr and d34S database through Earth history. Earth-Science Rev. 87, 113–133. https://doi.org/10.1016/j.earscirev.2007.12.003

Rapp, R.P., Watson, E.B., Miller, C.F., 1991. Partial melting of amphibolite/eclogite and the origin of Archean trondhjemites and tonalites. Precambrian Res. 51, 1–25. https://doi.org/10.1016/0301-9268(91)90092-O

Rausch, S., Böhm, F., Bach, W., Klügel, A., Eisenhauer, A., 2013. Calcium carbonate veins in ocean crust record a threefold increase of seawater Mg/Ca in the past 30 million years. Earth Planet. Sci. Lett. 362, 215–224. https://doi.org/10.1016/j.epsl.2012.12.005

Redler, C., Johnson, T.E., White, R.W., Kunz, B.E., 2012. Phase equilibrium constraints on a deep crustal metamorphic field gradient: Metapelitic rocks from the Ivrea Zone (NW Italy). J. Metamorph. Geol. 30, 235–254. https://doi.org/10.1111/j.1525-1314.2011.00965.x

Reeves, E.P., Seewald, J.S., Saccocia, P., Bach, W., Craddock, P.R., Shanks, W.C., Sylva, S.P., Walsh, E., Pichler, T., Rosner, M., 2011. Geochemistry of hydrothermal fluids from the PACMANUS, Northeast Pual and Vienna Woods hydrothermal fields, Manus Basin, Papua New Guinea. Geochim. Cosmochim. Acta 75, 1088–1123. https://doi.org/10.1016/j.gca.2010.11.008

Reid, M.R., Coath, C.D., Harrison, T.M., Mckeegan, K.D., 1997. Prolonged residence times for the youngest rhyolites associated with Long Valley Caldera : 230Th- 238U ion microprobe dating of young zircons. Earth Planet. Sci. Lett. 150, 27–39. https://doi.org/10.1016/S0012-821X(97)00077-0

Richter, F.M., Davis, A.M., DePaolo, D.J., Watson, E.B., 2003. Isotope fractionation by chemical diffusion between molten basalt and rhyolite. Geochim. Cosmochim. Acta 67, 3905–3923. https://doi.org/10.1016/S0016-7037(03)00174-1

Richter, F.M., Liang, Y., Davis, A.M., 1999. Isotope fractionation by diffusion in molten oxides. Geochim. Cosmochim. Acta 63, 2853–2861. https://doi.org/10.1016/S0016-7037(99)00164-7

Richter, F.M., Mendybaev, R.A., Christensen, J.N., Hutcheon, I.D., Williams, R.W., Sturchio, N.C., Beloso, A.D., 2006. Kinetic isotopic fractionation during diffusion of ionic species in water. Geochim. Cosmochim. Acta 70, 277–289. https://doi.org/10.1016/j.gca.2005.09.016

Richter, F.M., Watson, E.B., Mendybaev, R., Dauphas, N., Georg, B., Watkins, J., Valley, J., 2009. Isotopic fractionation of the major elements of molten basalt by chemical and thermal diffusion. Geochim. Cosmochim. Acta 73, 4250–4263. https://doi.org/10.1016/j.gca.2009.04.011

Rowley, D.B., 2002. Rate of plate creation and destruction: 180 Ma to present. Geol. Soc. Am. Bull. 114, 927–933. https://doi.org/10.1130/0016-7606(2002)114<0927:ROPCAD>2.0.CO;2

Rubin, A.E., Cooper, K.M., Till, C.B., Kent, A.J.R., Costa, F., Bose, M., Gravley, D., Deering, C., Cole, J., 2017. Rapid cooling and cold storage in a silicic magma reservoir recorded in individual crystals. Science (80-.). 356, 1154–1156. https://doi.org/10.1126/science.aam8720

Rudnick, R.L., Gao, S., 2014. Composition of the Continental Crust, in: Treatise on Geochemistry. Elsevier Ltd., pp. 1–64. https://doi.org/http://dx.doi.org/10.1016/B0-08-043751-6/03016-4

Rudnick, R.L., McLennan, S.M., Taylor, S.R., 1985. Large ion lithophile elements in rocks from high-pressure granulite facies terrains. Geochim. Cosmochim. Acta 49, 1645–1655. https://doi.org/10.1016/0016-7037(85)90268-6

Ryu, J.S., Jacobson, A.D., Holmden, C., Lundstrom, C., Zhang, Z., 2011. The major ion, d44/40Ca, d44/42Ca, and d26/24Mg geochemistry of granite weathering at pH=1 and T=25 C: Power-law processes and the relative reactivity of minerals. Geochim. Cosmochim. Acta 75, 6004–6026. https://doi.org/10.1016/j.gca.2011.07.025

Salisbury, M.J., Bohrson, W.A., Clynne, M.A., Ramos, F.C., Hoskin, P., 2008. Multiple plagioclase crystal populations identified by crystal size distribution and in situ chemical data: Implications for timescales of magma chamber processes associated with the 1915 eruption of Lassen Peak, CA. J. Petrol. 49, 1755–1780. https://doi.org/10.1093/petrology/egn045

Saunderson, D.H., Peckham, G.E., 1971. The lattice dynamics of calcium oxide. J. Phys. C Solid

State Phys. https://doi.org/10.1088/0022-3719/4/14/016

Sawyer, E.W., 2014. The inception and growth of leucosomes: Microstructure at the start of melt segregation in migmatites. J. Metamorph. Geol. 32, 695–712. https://doi.org/10.1111/jmg.12088

Schauble, E.A., 2011. First-principles estimates of equilibrium magnesium isotope fractionation in silicate, oxide, carbonate and hexaaquamagnesium(2+) crystals. Geochim. Cosmochim. Acta 75, 844–869. https://doi.org/10.1016/j.gca.2010.09.044

Schauble, E.A., Ghosh, P., Eiler, J.M., 2006. Preferential formation of 13C–18O bonds in carbonate minerals, estimated using first-principles lattice dynamics. Geochim. Cosmochim. Acta 70, 2510–2529. https://doi.org/10.1016/j.gca.2006.02.011

Schiller, M., Gussone, N., Wombacher, F., 2016. High Temperature Geochemistry and Cosmochemistry, in: Calcium Stable Isotope Geochemistry. pp. 223–245. https://doi.org/10.1007/978-3-540-68953-9

Schiller, M., Paton, C., Bizzarro, M., 2012. Calcium isotope measurement by combined HR-MC-ICPMS and TIMS. J. Anal. At. Spectrom. 27, 38–49. https://doi.org/10.1039/C1JA10272A

Schmitt, A.K., 2011. Uranium Series Accessory Crystal Dating of Magmatic Processes. Annu. Rev. Earth Planet. Sci. 39, 321–349. https://doi.org/10.1146/annurev-earth-040610-133330

Sederholm, J.J., 1928. On Orbicular Granites: Spotted and Nodular Granites Etc., and on the Rapakivi Texture. Comm. Geol. Bull 83, 5–126.

Seyfried, W.E., Bischoff, J.L., 1981. Experimental seawater-basalt interaction at 300 C, 500 bars, chemical exchange, secondary mineral formation and implications for the transport of heavy metals. Geochim. Cosmochim. Acta 45, 135–147. https://doi.org/10.1016/0016-7037(81)90157-5

Seyfried, W.E., Bischoff, J.L., 1979. Low temperature basalt alteration by sea water: an experimental study at 70 C and 150 C. Geochim. Cosmochim. Acta 43, 1937–1947. https://doi.org/10.1016/0016-7037(79)90006-1

Seyfried, W.E., Pester, N.J., Ding, K., Rough, M., 2011. Vent fluid chemistry of the Rainbow hydrothermal system (36°N, MAR): Phase equilibria and in situ pH controls on subseafloor alteration processes. Geochim. Cosmochim. Acta 75, 1574–1593. https://doi.org/10.1016/j.gca.2011.01.001

Seyfried, W.E., Seewald, J.S., Berndt, M.E., Ding, K., Foustoukos, D.I., 2003. Chemistry of hydrothermal vent fluids from the Main Endeavour Field, northern Juan de Fuca Ridge: Geochemical controls in the aftermath of June 1999 seismic events. J. Geophys. Res. Solid Earth 108. https://doi.org/10.1029/2002JB001957

Shea, T., Hammer, J.E., 2013. Kinetics of cooling- and decompression-induced crystallization in hydrous mafic-intermediate magmas. J. Volcanol. Geotherm. Res. 260, 127–145. https://doi.org/10.1016/j.jvolgeores.2013.04.018

Shikazono, N., Holland, H.D., 1983. The partitioning of strontium between anhydrite and aqueous solutions from 150 to 250 C. Econ. Geol. Monogr 5, 320–328.

Simon, J.I., DePaolo, D.J., Moynier, F., 2009. Calcium Isotope Composition of Meteorites, Earth, and Mars. Astrophys. J. 702, 707–715. https://doi.org/10.1088/0004-637X/702/1/707

Skjerlie, K.P., Johnston, A.D., 1996. Vapour absent melting from 10-20 kbar of crustal rock that contain multiple hydrous phase: implications for anatexis in the deep to very deep continental crust and active continental margins. J. Petrol. 37, 661–691.

Skjerlie, K.P., Johnston, A.D., 1993. Fluid-absent melting behavior of an F-rich tonalitic gneiss at mid-crustal pressures: Implications for the generation of anorogenic granites. J. Petrol. 34, 785–815. https://doi.org/10.1093/petrology/34.4.785

Skjerlie, K.P., Johnston, A.D., 1992. Vapor-absent melting at 10 kbar of a biotite- and amphibole-bearing tonalitic gneiss-Implications for the generation of A-type granites-Comment and Reply.pdf. Geology 20, 263–266. https://doi.org/10.1130/0091-7613(1992)020<0263:VAMAKO>2.3.CO

Skjerlie, K.P., Patiño Douce, A.E., Johnston, A.D., 1993. Fluid absent melting of a layered crustal protolith: implications for the generation of anatectic granites. Contrib. to Mineral. Petrol. 114, 365–378. https://doi.org/10.1007/BF01046539

Smit, M.A., Scherer, E.E., Mezger, K., 2013. Peak metamorphic temperatures from cation diffusion zoning in garnet. J. Metamorph. Geol. 31, 339–358. https://doi.org/10.1111/jmg.12024

Spear, F.S., Spear, F.S., 1993. Metamorphic phase equilibria and pressure-temperature-time paths, Vol. 1. ed. Washington, DC: Mineralogical Society of America.

Staudigel, H., 2013. Chemical Fluxes from Hydrothermal Alteration of the Oceanic Crust, 2nd ed, Treatise on Geochemistry: Second Edition. Elsevier Ltd. https://doi.org/10.1016/B978-0-08-095975-7.00318-1

Stepanov, A.S., Hermann, J., Korsakov, A. V., Rubatto, D., 2014. Geochemistry of ultrahigh-pressure anatexis: Fractionation of elements in the Kokchetav gneisses during melting at diamond-facies conditions. Contrib. to Mineral. Petrol. 167, 1–25. https://doi.org/10.1007/s00410-014-1002-x

Stepanov, A.S., Hermann, J., Rubatto, D., Korsakov, A. V., Danyushevsky, L. V., 2016. Melting history of an ultrahigh-pressure paragneiss revealed by multiphase solid inclusions in garnet, Kokchetav massif, Kazakhstan. J. Petrol. 57, 1531–1554. https://doi.org/10.1093/petrology/egw049

Steuber, T., Veizer, J., 2002. Phanerozoic record of plate tectonic control of seawater chemistry and carbonate sedimentation. Geology 30, 1123–1126. https://doi.org/10.1130/0091-7613(2002)030<1123:PROPTC>2.0.CO;2

Teagle, D., Bickle, M.J., Alt, J.C., 2003. Recharge flux to ocean-ridge black smoker systems: A geochemical estimate from ODP Hole 504B. Earth Planet. Sci. Lett. 210, 81–89. https://doi.org/10.1016/S0012-821X(03)00126-2

Teagle, D.A.H., Alt, J.C., Chiba, H., Humphris, S.E., Halliday, A.N., 1998. Strontium and oxygen isotopic constraints on fluid mixing, alteration and mineralization in the TAG hydrothermal deposit. Chem. Geol. 149, 1–24. https://doi.org/10.1016/S0009-

2541(98)00030-8

Tostevin, R., Turchyn, A. V., Farquhar, J., Johnston, D.T., Eldridge, D.L., Bishop, J.K.B., McIlvin, M., 2014. Multiple sulfur isotope constraints on the modern sulfur cycle. Earth Planet. Sci. Lett. 396, 14–21. https://doi.org/10.1016/j.epsl.2014.03.057

Tripoli, B.A., Cordonnier, B., Zappone, A., Ulmer, P., 2016. Effects of crystallization and bubble nucleation on the seismic properties of magmas. Geochemistry, Geophys. Geosystems. https://doi.org/10.1002/2015GC006123

Turchyn, A. V., Alt, J.C., Brown, S.T., DePaolo, D.J., Coggon, R.M., Chi, G., Bédard, J.H., Skulski, T., 2013. Reconstructing the oxygen isotope composition of late Cambrian and Cretaceous hydrothermal vent fluid. Geochim. Cosmochim. Acta 123, 440–458. https://doi.org/10.1016/j.gca.2013.08.015

Turner, F.J., 1981. Metamorphic petrology: Mineralogical, field, and tectonic aspects. McGraw-Hill Companies.

Urey, H.C.C., 1946. The Thermodynamic Properties of Isotopic Substances.

Valentine, G.A., Cortés, J.A., Widom, E., Smith, E.I., Rasoazanamparany, C., Johnsen, R., Briner, J.P., Harp, A.G., Turrin, B., 2017. Lunar Crater volcanic field (Reveille and Pancake Ranges, Basin and Range Province, Nevada, USA). Geosphere 13, 391–438. https://doi.org/10.1130/GES01428.1

Vavra, G., Gebauer, D., Schmid, R., Compston, W., 1996. Multiple zircon growth and recrystallization during polyphase late carboniferous to triassic metamorphism in granulites of the Ivrea Zone (Southern Alps): An ion microprobe (SHRIMP) study. Contrib. to Mineral. Petrol. 122, 337–358. https://doi.org/10.1007/s004100050132

Vernon, R.H., 1985. Possible role of superheated magma in the formation of orbicular granitoids. Geology 13, 843–845. https://doi.org/10.1130/0091-7613(1985)13<843:PROSMI>2.0.CO;2

Vielzeuf, D., Baronnet, A., Perchuk, A.L., Laporte, D., Baker, M.B., 2007. Calcium diffusivity in alumino-silicate garnets: An experimental and ATEM study. Contrib. to Mineral. Petrol. 154, 153–170. https://doi.org/10.1007/s00410-007-0184-x

Von Damm, K.. L., Edmond, J.. M., Grant, B., Measures, C.. I., Walden, B., Weiss, R.. F., 1985. Chemistry of submarine hydrothermal solutions at 21 °N, East Pacific Rise. Geochim. Cosmochim. Acta 49, 2197–2220. https://doi.org/10.1016/0016-7037(85)90222-4

Von Damm, K.L., 2004. Evolution of the hydrothermal system at East Pacific Rise 9º50´N: Geochemical evidence for changes in the upper oceanic crust, in: German, C.R., Lindsay, J., Parson, L.M. (Eds.), Mid-Ocean Ridges: Hydrothermal Interactions Between the Lithosphere and Oceans. American Geophysical Union, Washington DC, pp. 285–305.

Von Damm, K.L., 2000. Chemistry of hydrothermal vent fluids from 9°-10°N, East Pacific Rise: “Time zero,” the immediate posteruptive period. J. Geophys. Res. Solid Earth 105, 11203–11222. https://doi.org/10.1029/1999JB900414

Von Damm, K.L., Bray, A.M., Buttermore, L.G., Oosting, S.E., 1998. The geochemical controls on vent fluids from the Lucky Strike vent field, Mid-Atlantic Ridge. Earth Planet. Sci. Lett.

160, 521–536. https://doi.org/10.1016/S0012-821X(98)00108-3

Von Damm, K.L., Parker, C.M., Gallant, R.M., Loveless, J.P., 2002. Chemical Evolution of Hydrothermal Fluids From EPR 21° N: 23 Years Later in a Phase Separating World, in: American Geophysical Union, Fall Meeting. https://doi.org/2002AGUFM.V61B1365V

Voshage, H., Hunziker, J.C., Hofmann, A.W., Zingg, A., 1987. A Nd and Sr isotopic study of the Ivrea zone, Southern Alps, N-Italy. Contrib. to Mineral. Petrol. 97, 31–42. https://doi.org/10.1007/BF00375212

Wang, W., Zhou, C., Qin, T., Kang, J.T., Huang, S., Wu, Z., Huang, F., 2017. Effect of Ca content on equilibrium Ca isotope fractionation between orthopyroxene and clinopyroxene. Geochim. Cosmochim. Acta 219, 44–56. https://doi.org/10.1016/j.gca.2017.09.022

Watkins, J.M., Clemens, J.D., Treloar, P.J., 2007. Archaean TTGs as sources of younger granitic magmas: Melting of sodic metatonalites at 0.6-1.2 GPa. Contrib. to Mineral. Petrol. 154, 91–110. https://doi.org/10.1007/s00410-007-0181-0

Watkins, J.M., DePaolo, D.J., Huber, C., Ryerson, F.J., 2009. Liquid composition-dependence of calcium isotope fractionation during diffusion in molten silicates. Geochim. Cosmochim. Acta 73, 7341–7359. https://doi.org/10.1016/j.gca.2009.09.004

Watkins, J.M., DePaolo, D.J., Ryerson, F.J., Peterson, B.T., 2011. Influence of liquid structure on diffusive isotope separation in molten silicates and aqueous solutions. Geochim. Cosmochim. Acta 75, 3103–3118. https://doi.org/10.1016/j.gca.2011.03.002

Watkins, J.M., DePaolo, D.J., Watson, E.B., 2017. Kinetic Fractionation of Non-Traditional Stable Isotopes by Diffusion and Crystal Growth Reactions. Rev. Mineral. Geochemistry 82, 85–125. https://doi.org/10.2138/rmg.2017.82.4

Watkins, J.M., Liang, Y., Richter, F., Ryerson, F.J., DePaolo, D.J., 2014. Diffusion of multi-isotopic chemical species in molten silicates. Geochim. Cosmochim. Acta 139, 313–326. https://doi.org/10.1016/j.gca.2014.04.039

Watson, E.B., 1981. Diffusion in magmas at depth in the Earth: he effects of pressure and dissolved H2O. Earth Planet. Sci. Lett. 52, 291–301.

Watson, E.B., Müller, T., 2009. Non-equilibrium isotopic and elemental fractionation during diffusion-controlled crystal growth under static and dynamic conditions. Chem. Geol. 267, 111–124. https://doi.org/10.1016/j.chemgeo.2008.10.036

Weller, O.M., St-Onge, M.R., Rayner, N., Waters, D.J., Searle, M.P., Palin, R.M., 2016. U–Pb zircon geochronology and phase equilibria modelling of a mafic eclogite from the Sumdo complex of south-east Tibet: Insights into prograde zircon growth and the assembly of the Tibetan plateau. Lithos 262, 729–741. https://doi.org/10.1016/j.lithos.2016.06.005

White, R.W., Powell, R., 2002. Melt loss and the preservation of granulite facies mineral assemblages. J. Metamorph. Geol. 20, 621–632. https://doi.org/10.1046/j.1525-1314.2002.00206.x

Widanagamage, I.H., Schauble, E.A., Scher, H.D., Griffith, E.M., 2014. Stable strontium isotope fractionation in synthetic barite. Geochim. Cosmochim. Acta 147, 58–75.

https://doi.org/10.1016/j.gca.2014.10.004

Yakymchuk, C., Brown, M., 2014. Consequences of open-system melting in tectonics. J. Geol. Soc. London. 171, 21–40. https://doi.org/10.1144/jgs2013-039

Yang, J., Xu, Z., Li, Z., Xu, X., Li, T., Ren, Y., Li, H., Chen, S., Robinson, P.T., 2009. Discovery of an eclogite belt in the Lhasa block, Tibet: A new border for Paleo-Tethys? J. Asian Earth Sci. 34, 76–89. https://doi.org/10.1016/j.jseaes.2008.04.001

Young, E.D., Galy, A., 2004. The Isotope Geochemistry and Cosmochemistry of Magnesium. Rev. Mineral. Geochemistry 55, 197–230. https://doi.org/10.2138/gsrmg.55.1.197

Young, E.D., Galy, A., Nagahara, H., 2002. Kinetic and equilibrium mass-dependant isotope fractionation laws in nature and their geochemical and cosmochemical significance. Geochim. Cosmochim. Acta 66, 1095–1104. https://doi.org/10.1016/S0016-7037(01)00832-8

Zeebe, R.E., 2012. History of Seawater Carbonate Chemistry, Atmospheric CO2, and Ocean Acidification. Annu. Rev. Earth Planet. Sci. 40, 141–165. https://doi.org/10.1146/annurev-earth-042711-105521

Zhang, H., Wang, Y., He, Y., Teng, F.-Z., Jacobsen, S.B., Helz, R.T., Marsh, B.D., Huang, S., 2018. No measurable calcium isotopic fractionation during crystallization of Kilauea Iki lava lake. Geochemistry, Geophys. Geosystems. https://doi.org/10.1029/2018GC007506

Zhao, X., Zhang, Z., Huang, S., Liu, Y., Li, X., Zhang, H., 2017. Coupled extremely light Ca and Fe isotopes in peridotites. Geochim. Cosmochim. Acta 208, 368–380. https://doi.org/10.1016/j.gca.2017.03.024